Theoretical and numerical investigation in biomechanics and biotribology: from the musculoskeletal multibody modelling to the *in silico* wear assessment of human synovial replacements

Alessandro Sicilia

UNIVERSITY OF SALERNO

DEPARTMENT OF INDUSTRIAL ENGINEERING

Ph.D. Course in Industrial Engineering
Curriculum in Mechanical Engineering
XXXVIII Cycle

Theoretical and numerical investigation in biomechanics and biotribology: from the musculoskeletal multibody modelling to the *in silico* wear assessment of human synovial replacements

Supervisor
Prof. Alessandro Ruggiero

Ph.D. student
Alessandro Sicilia

Scientific Referees
Prof. Lorenza Mattei
Prof. Federico Colombo

Ph.D. Course Coordinator
Prof. Massimo De Santo

List of papers

Ruggiero, A. and Sicilia, A. (2022). Synovial Lubrication Modeling of Total Hip Replacements Using Musculoskeletal Multibody Dynamics. *Industrial Tribology*, CRC Press, 167-207.

Ruggiero, A. and Sicilia, A. (2024). Total Hip Replacement Response to a Variation of the Radial Clearance Through In Silico Models. *Mechanical Engineering in Biomedical Applications: Bio-3D Printing, Biofluid Mechanics, Implant Design, Biomaterials, Computational Biomechanics, Tissue Mechanics*, Scrivener Publishing, 185-229.

Sicilia, A., De Stefano, M. and Ruggiero, A. (2024). From Marker Trajectories to Muscular Activations: A Musculoskeletal Multibody Model Considering Compliant Tendon Behaviour. In *International Tribology Symposium of IFToMM*, Springer Nature Switzerland, 468-478.

Sicilia, A. and Ruggiero, A. (2025). A Fractal Rough surfaces' Mixed Lubrication model considering Boundary Element Method deformation. *Tribology International*, 111210.

Sicilia, A. and Ruggiero, A. (2026). Simulating the transient dynamics of line-contact Elasto-Hydrodynamic Lubricated systems by solving a Differential Algebraic Equation set. *Journal of Tribology*, 148(4), 044102.

Summary

List of figures

List of tables

Abstract

This Ph.D. work is based on the investigation of the phenomena involved in the bio-tribology of the synovial replacements. The synovial joints are the natural articulations of the human body linking two bones, providing minimum friction and ensuring a high range of motion between them.

When the natural joint suffers from articular diseases, a surgical procedure of replacement is often required: the artificial implant realized with biomaterials that is going to substitute the unhealthy joint has to guarantee the same functionality of the replaced one while ensuring the maximum duration and then the minimum implant wear.

Hence, an accurate tribological characterization of the prosthesis is needed; the scientific community is going to move from the experimental characterization (*in vitro*) to a numerical simulative one (*in silico*), in order to have fast and cheap computational tools during the design and the wear prediction phase: this aspect requires a deep knowledge of the physical/mathematical description of the problem.

With these foundations, this Ph.D. work is moving following two parallel investigations regarding in particular the Total Hip Replacement:

- the assembling of a multibody model capable of simulating the inverse kinematics and the inverse dynamics of musculoskeletal systems, in order to have a generator of tribological configurations (load and relative motion) for the analyzed joint due to a selected musculoskeletal motion;
- the realization of a tribological model able to simulate the lubrication/contact regime of the analyzed tribo-system in terms of lubricant/contact pressure, surfaces' deformation and separation, wear depth, load and friction torque due to a certain relative motion between the articulated surfaces.

The developed numerical models related to both the investigations are conceived in Matlab® computational environment and have to communicate in order to obtain a global tool that characterizes the biotribological performance of a synovial replacement due to an overall musculoskeletal physical activity.

The main goal is to provide the basis of the numerical modelling in this framework and to make the realized codes more and more accurate by adopting advanced numerical techniques (non-linear solvers, minimization, Finite Difference Method, Finite Element Method, Boundary Element Method, random fractals generator, Differential Algebraic Equations, etc.) and by the validation with respect to experimental/*in vivo* measurements or empirical benchmarks.

Introduction

This work finds its motivations and practical applicability into the context of the wear assessment of human prostheses.

It is established that nowadays the need of the replacement of an unhealthy human articulation is growing among the population and across the ages, in fact it is required by both elderly and young people, where the first are mainly subjected to articular pathologies or simply ageing, while the seconds, especially high-performance athletes, are stressed by intense physical activities: in both cases the articular pathology could lead to the articulation non-functionality, pain and related diseases, reason why a complete or partial substitution of the unhealthy joint with an artificial implant is often necessary through a surgical procedure. Furthermore, the implanted prosthesis is subjected to wear during its functioning over its life, so there could be the possibility of a revision surgery in order to restore the implant surfaces, so the period between the replacement and the revision surgeries has to be maximised, of course based on investigations depending on the particular patient (Ciccarelli *et al.*, 2024).

It is evident the cruciality of the role played by the tribological phenomena governing the implant conjugated surfaces' interaction: the complex of contact, lubrication, roughness, relative motion, load, surface geometry, texture, material mechanical response and so on, is decisive with respect to the resulting implant wear and so to the prosthesis duration, then, it is mandatory to analyse these phenomena both in the design and the verification phases concerning the prosthesis study (Fisher and Dowson, 1991).

In order to highlight the tribological framework in which the artificial joints work, the natural lubrication of the human articulations is discussed in the following.

The human articulations are the linking between conjugated bones, then they are responsible for the skeleton integrity and also for its mobility. The surfaces of the bones linked by the articulation are covered by cartilage, i.e., a connective tissue in which some constituting cells called chondrocytes are responsible for the production of collagen fibers; the latter are filaments made of proteins (the collagen) characterised by high traction resistance, so, based on their density in the cartilage and on their orientation with respect to the conjugated surfaces, three types of human joints are discriminated (Nordin and Frankel, 2001) (Figure 1):

- *Fibrous joints*
  They are characterised by a high collagen fibers density mostly oriented normally with respect to the conjugated bony surfaces, so the bones linked by a fibrous joint are substantially fixed, i.e., there is no relative motion between them; examples of human fibrous joints arethe sutures between the skull bones and the lower tibiofibular junction rigidly connecting the tibia to the fibula;
- *Cartilaginous joints*
  They are characterised by a lower collagen fibers density than the fibrous joints, so they allow a limited relative motion between the linked bones; examples of human cartilaginous joints are the intervertebral disks and the manubriosternal joint which give the necessary mobility to, respectively, the spine and the thoracic cage;
- *Synovial joints*
  They are the human joints offering the highest Range of Motion (RoM) between the linked bones, thanks to a cavity separating the surfaces and filled by the synovial fluid, i.e., the natural lubricant of the articulation, and to the mostly tangential orientation of the collagen fibers with respect to the conjugated surfaces, which are able to absorb the shear stresses produced by the sliding surfaces; example of synovial joints are the high RoM articulations of the upper limb, e.g., shoulder, elbow and wrist, and of the lower limb, e.g., hip, knee and ankle.

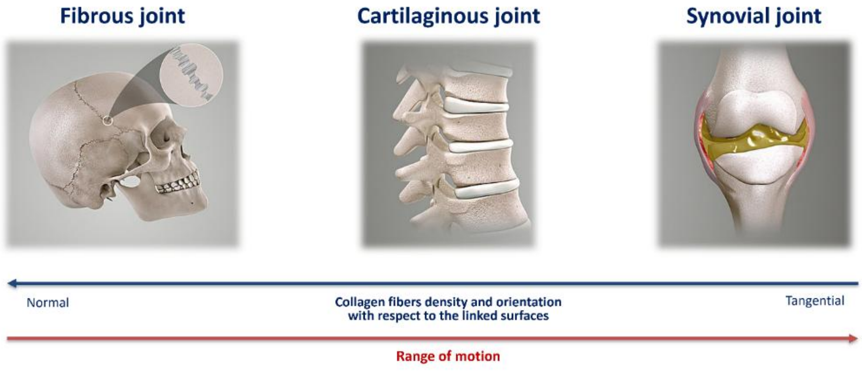

Figure 1 *Human joints typology*

The articular cartilage covering the bones linked by a synovial joint shows a stratified structure (Figure 2) in which, going from the superficial zone exposed to the cavity towards the bone, the collagen fibers increase in density and tilt their inclination orienting mostly normally with respect to the underlying bone in the deep zone, so that here the calcification occurs, i.e., the transition from cartilage tissue to bony structure. The space separating the cartilage conjugated surfaces is surrounded by the synovial membrane which, thanks to the cartilage porosity, supplies the synovial fluid to the cavity, so it provides for its lubrication and nutrition and also it is able to expel waste products outside the synovial environment. The whole synovial joint structure is kept in position by ligaments connecting the bones.

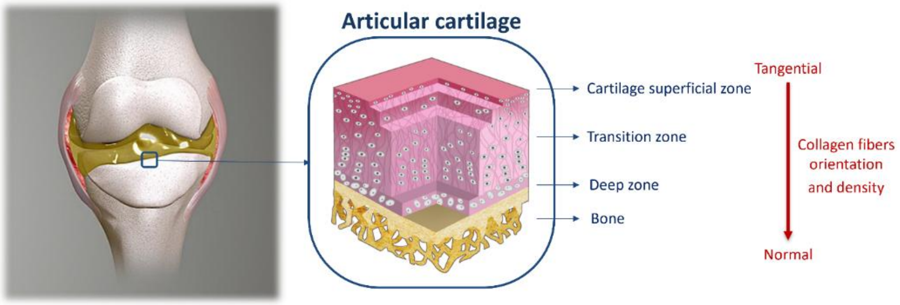

Figure 2 *Articular cartilage structure*

The natural lubrication of the synovial joint (Figure 3) is governed by complex lubrication regimes which combine in space and time providing a very low friction coefficient and establishing the synovial joint as a very effective tribo-system in the framework of the human musculoskeletal system (Dumbleton, 1981; Nordin and Frankel, 2001).

The main classification distinguishes the full-film and the boundary lubrications modes, where the first ones are generated when the surfaces are completely separated by the synovial fluid lubricant meatus and the second ones work at the cartilage-to-cartilage contact level.

In the full-film mode the articular surface lubrication is given by:

- the relative motion between the surfaces which can be tangential (sliding effect) or normal (squeeze effect); in this case the Hydrodynamic Lubrication (HL) results in the lubricant pressure rise due to the sliding fluid carried along the converging zones of the meatus and to the surfaces' approaching motion that squeezes the lubricant out of the contact;
- the deformability of the cartilage bulk; when the load acting on the articulation increases, the synovial lubricant pressure becomes so high that it deforms the articular cartilage providing the survival of an ultra-thin lubricant film that ensures the surfaces' separation and the minimum friction, establishing the so-called Elasto-Hydrodynamic Lubrication (EHL).

The full-film synovial lubrication modes are governed by the lubricant rheological properties (in particular its viscosity) and by the relative motion; when the load acting on the articulation is too high or the surfaces' relative motion is too slow, other lubrication mechanisms depending on the chemical properties of the synovial fluid take place in the so-called Boundary Lubrication; the synovial fluid is an ultrafiltrate from blood and its constituents, in particular the hyaluronic acid macromolecules and the lubricin proteins, provide the lubrication effect:

- in the Mixed Lubrication (ML) regime, when the cartilage surfaces touch due to the too high load that breaks the continuity of the synovial fluid meatus, the direct cartilage-to-cartilage contact does not really happens because of a layer of lubricin coming from the synovial fluid that covers the cartilage surfaces and sticks to it, ensuring the lubrication effect even in this highly loaded configuration;
- a particular synovial Boundary Lubrication (BL) mode is the Boosted one that occurs when the surfaces are approaching towards each other with high velocity; the high squeeze produced by the normal relative motion of the surfaces constrains the synovial lubricant to be filtrated within the porous cartilage matrix, where a chemical reaction between the synovial fluid hyaluronic acid and the cartilage collagen fibers produces a gel-like substance that is successively exudated during the weeping phase, i.e., the negative squeeze motion produced by the surfaces moving away from each other that sucks in the gel in the synovial cavity that goes to cover the cartilage surfaces increasing even more the lubrication effect during direct contact.

Thanks to the natural lubrication modes described above, the synovial joint is characterised by minimum friction and wear.

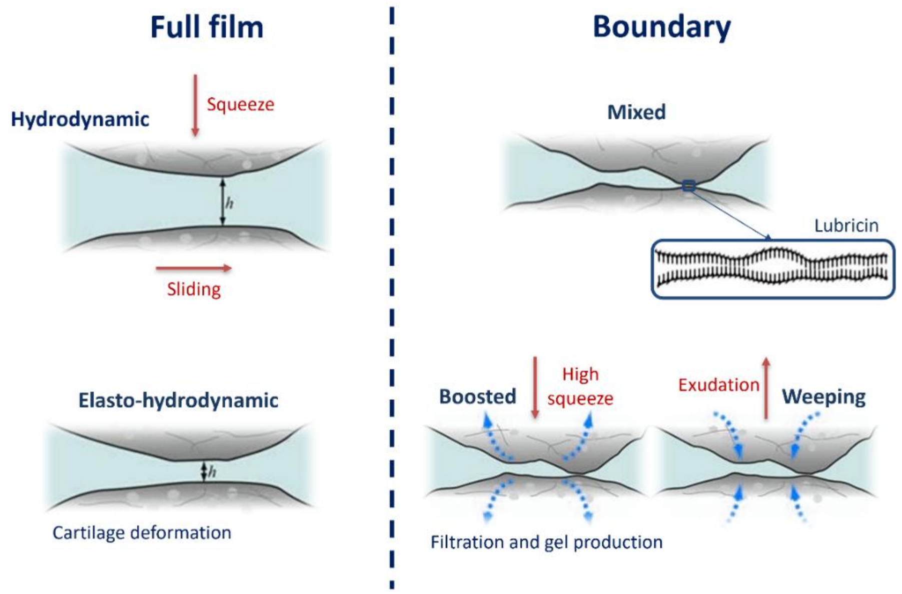

Figure 3 *Synovial lubrication mechanisms*

The above beautiful and effective natural lubrication modes are compromised when the cartilage deteriorates because of articular pathologies or ageing: the partial absence of cartilage in the synovial cavity turns into direct bone-to-bone contact and consequent wear, tissue inflammation, loss of mobility, pain and various disease: generally, a total or partial synovial replacement is needed (Figure 4). The replaced implant has to be designed and manufactured with biomaterials demonstrating biocompatibility with the articulation synovial environment and it has to guarantee stability, mobility, load carrying capacity, lubrication, low friction and low wear in order to enhance its longevity.

Figure 4 *Synovial prosthetics examples*

This work was based on the particular application represented by the Total Hip Replacement (THR).

The hip joint (Mattei *et al.*, 2011) is a synovial articulation linking the pelvis and the femur bones over a spherical-like surface (Figure 5), so it is a ball-socket or spherical joint allowing three relative rotations: defining the Anterior/Posterior x_{AP}, the Proximal/Distal y_{PD} and the Medial/Lateral z_{ML} hip axes, the three relative rotations are called respectively Adduction/Abduction θ_{AA}, Internal/External Rotation θ_{IER} and the Flexion/Extension θ_{FE}. During a physical activity moving the whole musculoskeletal system, each joint is subjected to a loading configuration resulting from the combination of inertial effects, external actions and muscular actions: in the hip case, the load supported by the joint (the norm of the vector composed by N_{AP}, N_{PD} and N_{ML}) is generally a multiple of the Body Weight (BW), e.g., 4-5 BW during a simple activity like walking or 6-10 BW during the running and even more during the jumping.

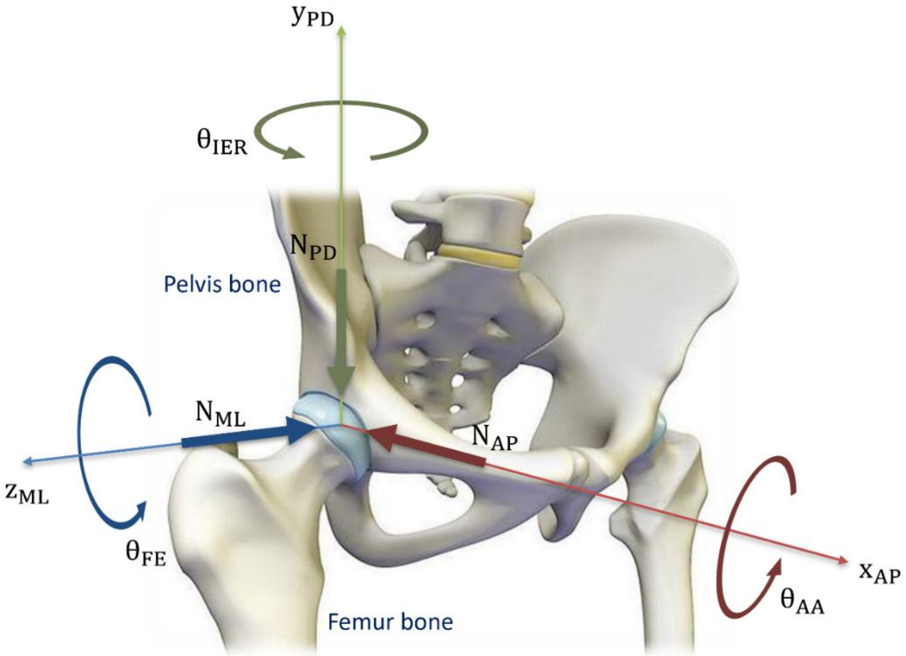

Figure 5 *Hip joint system*

The hip high RoM and intense loading make the hip joint a highly stressed articulation that provides for the stability and the mobility of the whole musculoskeletal system: as a consequence, also the THR is subjected to the same kinematics and dynamics conditions, so its tribological and mechanical design has a significant impact.

The THR (Figure 6) is composed by the acetabular cup fixed to the pelvis acetabulum through a metallic back and by the femoral head fixed to the femur through a metallic stem.

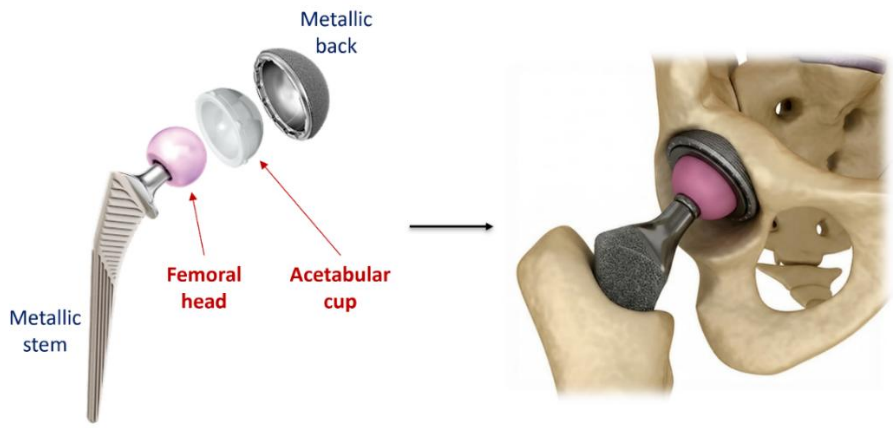

Figure 6 *Total Hip Replacement*

The biomaterials actually used in the framework of the Total Hip Arthroplasty (THA) regarding the conjugated surfaces of acetabular cup and femoral head are (Aherwar, Singh and Patnaik, 2015; Zivic *et al.*, 2017; Merola and Affatato, 2019):

- *Metallic*

  Titanium alloys (Ti), Cobalt-Chromium (Co-Cr) alloys and Stainless Steel (SS) are characterised by a moderate corrosion and wear resistance but the metal ions coming from the debris and spread through the synovial membrane could lead to osteolysis;
- *Polymeric*

  Ultra-High Molecular Weight PolyEthylene (UHMWPE) and Cross-Linked PolyEthylene (XLPE) are introduced thanks to the good wear resistance and mechanical properties that can be enhanced through polymer treatments;
- *Ceramic*

  Alumina, Zirconia, Zirconia-Toughened Alumina (ZTA) are well-known for the high hardness, toughness and very low wear rate, while presenting the risk of fracture.

Based on the particular subject age and activity level and also on the desired properties to give to the prosthesis, several choices can be made of both Hard-on-Hard or Hard-on-Soft implants typologies, e.g., Co-Cr head against UHMWPE cup, ZTA head against XLPE cup, etc. Clinical reports showed that Polyethylene and Ceramic solutions offer the best performance in terms of wear rate and longevity (Merola and Affatato, 2019).

Together with the clinical reports, information about the implants' wear rate can be obtained experimentally: the *in vitro* approach consists into simulating the loading and the relative of motion operating conditions referred to a THR through a tribometer, like the hip simulators (Figure 7) or basic reciprocatory and rotatory tribometers in both dry and wet conditions (Essner, Schmidig and Wang, 2005; Affatato *et al.*, 2009). The hip simulators have to be able to reproduce the spherical joint triaxial loading and motion and it can be run for millions of cycles in order to provide an estimation of the implant material loss over years; furthermore, other outputs can be obtained like the coefficient of friction and also topological measurements. The duration of the experiments and the complexity of the involved machines make the *in vitro* approach very reliable but at the same time very expensive from both time and money consumption points of view.

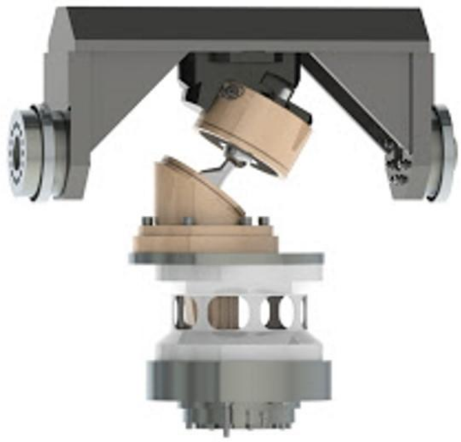

Figure 7 *Hip tribometer simulator*

With the growing performance of the calculators, the same operating conditions can be simulated numerically through the assembling of models describing the mathematics and the physics of the analysed phenomena: the *in silico* approach establishes as a very powerful approach theoretically able to simulate all the desired operating conditions and complex configurations while limited by the physical accuracy of the developed models and by the computing time depending on the particular calculator. The best possible outcome is represented by the cooperation between the *in silico* and the *in vitro* approaches, where the first ones can be validated by the second ones (Mattei *et al.*, 2011).

As discussed until now, it is clear that what happens at the interface between the conjugated surfaces of a joint is strictly related to the tribological state (lubrication, contact, wear, etc.) resulting from the joint operating conditions of loading and relative motion, while the latter are the result of the kinematics and the dynamics of the global mechanical system that the joint belongs to: then, from the *in silico* perspective, it would be very useful to develop numerical models that, starting from the kinematics of a musculoskeletal system, are able to provide the analysed joint operating conditions and then to elaborate them in order to simulate the tribology of the joint, so that the practical outcome of wear estimation can be conducted with a fully dedicated customizable computational tool (Figure 8).

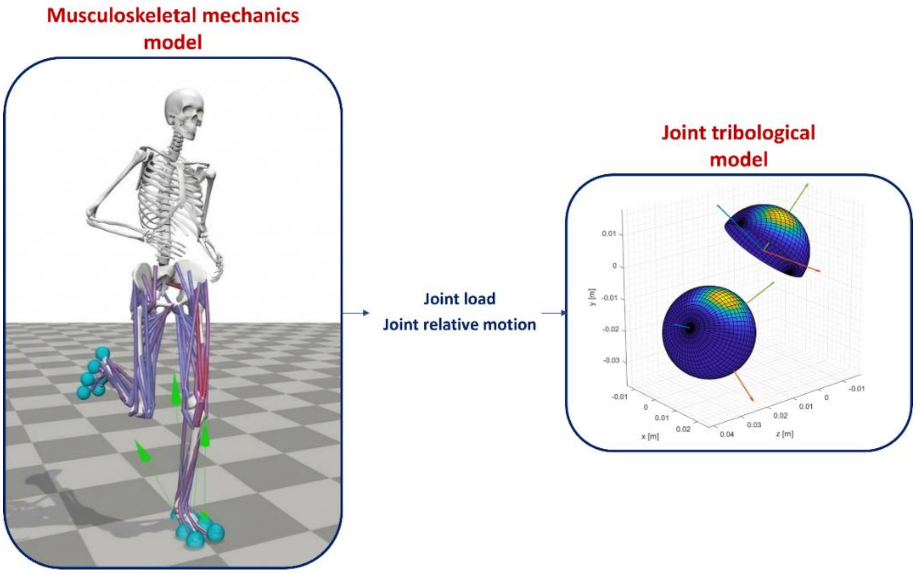

Figure 8 *In silico perspective for the joint wear estimation*

The above was the current objective of this work and it was characterised by the parallel study of the two related main topics, i.e., the development of musculoskeletal mechanics and joint tribological models: these topics are generally addressed by assembling Multi-Body kinematics and dynamics simulators and by numerically solving the Partial Differential Equations (PDE) related to the lubrication/contact of tribo-systems; the scientific literature in this framework made significant efforts to obtain reliable results and laid the foundation for other researchers to prosecute and deepen the investigations.

State of the art and proposed approaches

In this section, a review of the scientific literature associated to the presented framework is conducted and the approaches proposed by the author in this work are placed along the studies developments.

In order to introduce the significant scientific community achievements, the basic concepts regarding the analysed topics are qualitatively introduced in the following.

Starting from the mechanics models, the musculoskeletal system (Figure 9) can be viewed as a set of rigid bodies (the bones) linked by joints (the articulations), moved by actuators (the muscles) and subjected to external force fields (gravity, environmental actions like the ground reaction forces for the lower limb case, etc.); in this sense, the Multi-Body mechanical system is described by a set of equations that communicate in order to describe its configuration in terms of kinematics (position, velocity and acceleration) and dynamics (actuation forces and joint reactions).

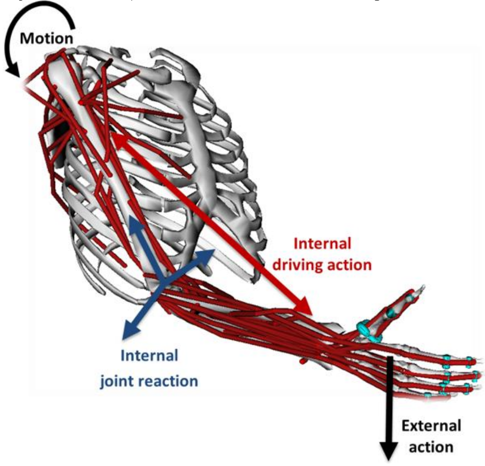

Figure 9 *Musculoskeletal system*

Once the Multi-Body system is defined through its Lagrangian coordinates $\mathbf{q}$, i.e., parameters able to describe its bodies' position and orientation in the space, and its Degrees of Freedom (DoF) $\mathbf{d}$, i.e., the independent coordinates that univocally determine the pose of the whole system, a set of constraint equations $\boldsymbol{\Phi}$ in (1) governs the relations between $\mathbf{q}$ and $\mathbf{d}$, based on the joints kinematical behaviour; furthermore, the Equation of Motion (EoM) $\mathbf{E}$ of the Multi-Body system in (1) relates the Lagrangian coordinates $\mathbf{q}$ and their time derivatives (velocities $\dot{\mathbf{q}}$ and accelerations $\ddot{\mathbf{q}}$) to the driving forces $\mathbf{f}$ and the joint reactions $\boldsymbol{\lambda}$ (Abdullah *et al.*, 2024).

$$\begin{cases} \mathbf{E}(\mathbf{q}, \dot{\mathbf{q}}, \ddot{\mathbf{q}}, \mathbf{f}, \boldsymbol{\lambda}) = \mathbf{0} \\ \boldsymbol{\Phi}(\mathbf{q}, \mathbf{d}) = \mathbf{0} \end{cases} \tag{1}$$

The process that leads to the evaluation over time of the DoF $\mathbf{d}$ knowing the driving forces $\mathbf{f}$ is the Forward Dynamics: in the applications like the ones analysed in this work where the driving forces $\mathbf{f}$ have to be evaluated by knowing the kinematics provided by the DoF $\mathbf{d}$, the solution of the constraint equations and of the EoM is given by the inverse dynamics (let note that in both verses the joint reactions $\boldsymbol{\lambda}$ and the Lagrangian coordinates $\mathbf{q}$ are outputs of the evaluation). When the analysed mechanical system is a musculoskeletal one, the driving forces are provided by the muscles, so the muscular actuation system has to be modelled in order to relate the generated forces to the muscle activation levels: since the number of muscles is redundant with respect to the possible movements offered by the articulations, the modelling of the muscular actuation system has to take into account a recruitment criterion that optimally decides what muscles and with which intensity have to activate to produce the known kinematics (Sharif Shourijeh, 2013).

The scientific literature produced several research in the framework of the biomechanics of musculoskeletal systems and the same was done in case of joint replacements; several research questions arose for a wide set of applications and in the following some significant examples are listed.

In (Quental *et al.*, 2013) the authors focused on the differences exhibited by an upper limb musculoskeletal system with reverse shoulder prosthesis with respect to an anatomical one: they investigated the shoulder replacement location and geometry effects on the resulting muscles' lengths, forces and joint reactions.

In (Schwarze *et al.*, 2013) the authors investigated the reliability of a Multi-Body model of the lower limb referred to people with above knee amputation equipped with a socket prosthesis: through the model they evaluated the loads acting at the socket interface level and compared them with the ones acquired by sensors applied on six subjects who were monitored during walking in gait laboratories.

In (Cosenza, Niola and Savino, 2018) the authors aimed to give the basis to the development of artificial hands by discussing the Multi-Body theory and the contact mechanics principles in the context of the hand grasping ability.

In (Silva, Pereira and Martins, 2011) the authors wanted to implement the physical tiredness into a Multi-Body model considering a fatigue tool into the used muscle model, considering its actuation force time history: with reference to the upper limb, they investigated how the muscles' activation increases over time and how the number of recruited muscles varies due to a force production capability loss.

In (Silva and Ambrósio, 2003) the authors provided a wide and comprehensive review of the main techniques and approaches to solve the inverse dynamics of musculoskeletal systems, describing the strategies to model the joint behaviour, the muscular tissue dynamics and the physiological recruitment criteria involved into the muscle force evaluation: they developed and tested a reliable full body musculoskeletal system moving with the gait kinematics.

In (Curtis, 2010) the authors demonstrated the potentials of the Multi-Body analysis to describe problems in the framework of the craniofacial biomechanics for both human and non-human applications focusing on the biting dynamics and its effects on the temporomandibular joint.

In (Duprey *et al.*, 2017) the authors listed and discussed several techniques to perform inverse kinematics optimizations, i.e., the evaluation of a musculoskeletal system DoF by knowing the trajectories of skin-applied markers, focusing on the reliability of the optimization tools with respect to the motion of the skin soft tissues the marker sensors are applied to, which generally provides errors during the calculation.

In (Huynh *et al.*, 2013) the authors exploited the Multi-Body simulations in the context of the seating systems comfort and of the surgical field, developing an interesting model of the human spine by considering the linked intervertebral discs as a series of revolute joints.

In (Quental, Folgado and Ambrosio, 2016) the authors analysed the optimization techniques to evaluate the redundant muscle forces: they moved from a static optimization, i.e., performed each time instant, to a dynamic optimization which considers the time history of the muscles' activation.

In (Quental *et al.*, 2018) the authors compared four different muscle modelling strategies based on the results of muscles' activation referred to an upper limb musculoskeletal system: they evaluated the reliability of the muscle models analysing *in vivo* muscles' activations and glenohumeral joint reactions finding satisfactory matchings and negligible differences regarding the different strategies.

With respect to the existing literature, the authors often focus on a couple of steps of the musculoskeletal simulation, since their aim is to provide deepening on the usage of a particular technique or modelling strategy or to investigate the consequences of a particular musculoskeletal property: in this context, the work proposed in this thesis aims to develop a comprehensive simulator that follows the whole path starting from marker trajectories and ending with muscle activations and joint reactions, i.e., the concatenation of inverse kinematics and inverse dynamics solvers within a self-made code that takes into account minimization strategies, non-linear constraint equation solvers, straight and curved muscle modelling, etc.; in the author opinion, this would constitute a useful computational tool providing the tribological operating conditions referred to a joint belonging to the system in terms of loading and sliding motion, strictly dependent on the particular musculoskeletal system properties given as input: basically, the developed Multi-Body code represent the biomechanics simulator needed to conduct a successive biotribological analysis (Ruggiero and Sicilia, 2020b, 2022a, 2022c); the code is written in Matlab® computational environment, so it is fully controllable and it can be easily modified to implement possible modelling advancements.

Again, the Multi-Body results interesting for the joint tribological design are the joint relative motion and load coming from the Lagrangian coordinates $\mathbf{q}$ and the joint reactions $\boldsymbol{\lambda}$: the basics of the tribological numerical evaluation in this framework rely on the HL Reynolds equation (Reynolds, 1886) in (2) which, in its original form, describes the lubricant pressure field p rising mechanisms within the meatus gap h due to the rigid surfaces' tangential velocities U and W (velocity vector $\mathbf{U}$), to the load N and to the lubricant viscosity μ (Figure 10).

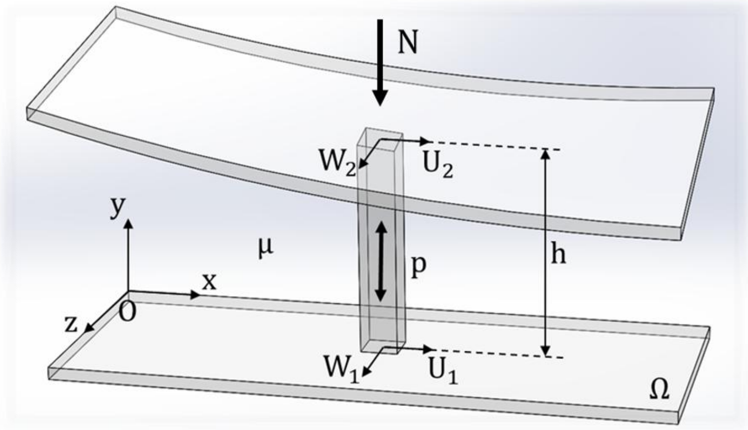

Figure 10 *Reynolds equation tribo-system reference frame*

Along the time t and over the analysed domain $\mathbf{x}$ (which is the contact plane xz), the gap h is the result of the geometrical gap g and the rigid normal approach between the surfaces δ, while the load N is instant by instant balanced by the fluid pressure p integral over the lubricated area Ω (Lombera Rodríguez and Tello, 2019) (eq. (2)); generally, the time-varying input of surfaces' tangential velocities $\mathbf{U}$ and load N are given and the rigid approach δ is unknown, but there are also applications where the latter is given, so, in that cases, the load balance equation is useless and it can be considered in a post-processing phase.

$$\begin{cases} \boldsymbol{\nabla}\cdot\left(\dfrac{h^3}{12\mu}\boldsymbol{\nabla}p\right) = \boldsymbol{\nabla}\cdot(h\mathbf{U}) + \dfrac{\partial h}{\partial t} \\ h(\mathbf{x},t) = g(\mathbf{x}) - \delta(t) \\ N(t) = \displaystyle\int_{\Omega} p(\mathbf{x},t)\,dA \end{cases} \tag{2}$$

Moving towards the tribology research, an equal wide effort can be observed in terms of investigated topics, modelling strategies to investigate more complex regimes and simulative numerical approaches.

In (Jin and Dowson, 1999) the authors developed a numerical model to simulate the HL of Hard-on-Hard hip joint replacements under walking operating conditions: they verified that a small lubricant film thickness survives thanks to the realisation of a dimple on the acetabular cup if it is deep and close to the direction of the resulting load.

In (Ramjee, 2008) the authors realised an HL model of the THR and they supplied it with the walking cycle operating conditions: they demonstrated that the squeeze effect due to the femoral head eccentricity within the acetabular cup is dominant with respect to the sliding effect provided by the relative angular motion; furthermore they verified that the THR during walking early undergoes in a contact configuration unless a better lubrication is provided by increasing the viscosity or the femoral head radius.

The high load acting on the THR suggests that the joint lubrication regime is not hydrodynamic, so EHL and ML models have to be developed; the consideration of the surfaces' deformability implies that a deformation contribution dependent on the pressure has to be included into the gap equation: this introduces a non-linearity into the Reynolds equation that has to be handled with numerical iterative solution methods. Before introducing some literature EHL and ML models, let see what deformation models are established in the THR context.

A Hard-on-Soft implant deformation can be evaluated by neglecting the deformability of the much harder material (that generally constitutes the femoral head bulk, which can be metallic or ceramic) with respect to the softer one (generally a polymeric material constituting the acetabular cup); in this case the deformation of the softer acetabular cup is evaluated assuming that it is everywhere proportional the to the local pressure through a constant coefficient depending on the cup mechanical and geometrical properties: this deformation model is generally called "constraint column" or "independent spring" model and it is widely used in literature for Ceramic/Metallic-on-Polymer implants (Jalali-Vahid and Jin, 2001; Jalali-Vahid *et al.*, 2001a, 2001b; Jalali-Vahid, Jin and Dowson, 2003).

Another local and proportional approach used in the framework of Hard-on-Soft implants is represented by the elastic foundation deformation models, which consider the softer surface as composed by a set of parallel springs, where the latter can show in general a different stiffness (Fregly, Bei and Sylvester, 2003; Halloran *et al.*, 2005; Pérez-González *et al.*, 2008; Mukras *et al.*, 2010; Srivastava, Christian and Higgs, 2021).

When the implant is composed by materials with similar mechanical responses, the local deformation is no longer given only by the local pressure, instead it is dependent also on the pressure acting on the surroundings; in this case two approaches are generally used:

- when the boundaries of the bulks are very far away from the conjugated interface, then the implant bodies can be viewed as half-spaces, which the interface deformation is the result of a convolution of the acting pressure field; in the THR case the convolution has to be adapted to the spherical geometry of the prosthesis (Evans and Hughes, 2000; Jagatia and Jin, 2001; Wang and Jin, 2004b, 2004a, 2008; Wang *et al.*, 2009; Gao, Dowson and Hewson, 2015);
- when no geometrical assumption can be made on the implant bodies, it is necessary to conduct a Finite Element Method (FEM) simulation, which gives accurate deformation results at the expense of a heavy computational burden due to the full spatial

discretization of the implant bulks even if the lubrication calculus is performed over the interface (Jagatia and Jin, 2001; Halloran *et al.*, 2005).

Once the deformation model is chosen and implemented into the EHL Reynolds solver, the simulations can be conducted to answer to several scientific questions.

In (Wang and Jin, 2008) the authors developed an EHL model for metal-on-metal THR investigating the effects of the acetabular cup inclination and of the lubricant viscosity on the implant tribological outcomes.

In (Gao *et al.*, 2009) the authors built a metal-on-metal EHL simulator considering walking operating conditions and they investigated the position of the highly deformed gap within the acetabular cup; moreover, they demonstrated that during walking a significant squeeze effect is given by the load horizontal components, i.e., the Anterior/Posterior and the Medial-Lateral ones.

In (Udofia and Jin, 2003) the authors validated their EHL solver for metal-on-metal THR by comparing the resulting minimum film thickness with respect to the one obtained with empirical formulas gained from experimental characterizations.

While the EHL models give information about the full-film lubrication of the implants, the ML mode has to be taken into account, because, even during a simple musculoskeletal activity like walking, the THR shows direct contact zones: the numerical modelling has to consider the possibility that in some zones of the analysed domain the gap can close and there the dry contact pressure takes place; furthermore, in this configuration the implant wear becomes severe and it needs to be estimated.

In (Wang and Jin, 2004a) the authors investigated the size of the contact area response to a variation of the lubricating fluid viscosity in the context of metal-on-UHMWPE implant.

In (Wang, Wang and Sun, 2010) the authors developed a ML numerical model for THR with complex spherical-based geometries to predict their wear.

Generally, the wear modelling of the THR implant is devoted to the Archard law, which assumes that the local wear depth rate is proportional to the product between the contact pressure and the sliding velocity through a wear factor depending on the coupling, where the latter is generally found empirically by hip simulators and used as a constant for the simulations: it is worth to underline that some authors propose the modification of the wear factor as a function of several parameters to take into account further wear properties like:

- (Gao, Dowson and Hewson, 2015) proposing the wear factor dependency on the ratio between the lubricant film thickness and the arithmetical roughness in order to investigate the wear of lubricated contacts, providing high wear when the surfaces' gap get close to the coupling roughness;

- (Liu *et al.*, 2021) proposing a modification of the wear law taking into account the effects of the UHMWPE THRs multidirectional sliding producing different responses due to the orientation of the polymers chains and the role of the frictional work and the contact pressure with respect to the material loss.

Moving away from the spherical geometry of the THR tribo-system, the scientific literature tried several approaches to address the ML problem, in order to solve two different phenomena in the same domain, i.e., full film lubrication and Dry Contact Mechanics (DCM).

In (Zhu and Hu, 1999; Hu *et al.*, 2001; Zhu, 2007) the authors observed that the lubrication Reynolds equation in EHL regime provides a steady-state pressure field similar to the DCM solution for the same operating conditions when the film thickness goes to zero: so, in order to model the ML regime, they wrote a reduced Reynolds equation in which the terms related to the lubricant flow, i.e., sliding and squeeze, are turned off when the surfaces' gap goes below a small tolerance.

Similarly, the authors in (Zhang *et al.*, 2019) used a single unified Reynolds equation valid for both the lubricated zones and the contact ones by switching off the lubricant properties to zero in correspondence of negative gap; furthermore, they considered surface forces due to Van der Waals interactions between the lubricant and the surfaces, hydration and electric double layer effects.

In (Zhang *et al.*, 2016) the authors studied the ML of rough surfaces using the average Reynolds approach, i.e., the asperity contact pressure is implemented into the Reynolds equation through pressure flow factors multiplying the flow terms that take into account the probability distribution related to the asperity contact events; they used the described approach to investigate the surface texture strategies on the friction coefficient of the rough tribo-system.

In order to address the ML numerical solution, especially for rough surfaces, a high grid resolution is needed to discretise the analysed domain: as a consequence, the iterative approaches chosen to numerically solve the problem have to be performant and manageable by the calculators.

In (Venner, 1992) the author laid the foundation to exploit the MultiGrid/MultiLevel techniques in the framework of EHL solutions; the MultiGrid approach is based on the differential equation solving on different grid resolution level: starting from the finer grids, fast iterative methods able to handle the high number of grid points are used to smooth the numerical residual, i.e., the distance from the numerical solution, then on the coarsest grid a heavy iterative method handling a poor number of grid points is used to break down the residual resulting in a fast convergence rate. Furthermore, the same approach is used to evaluate the half-space deformation convolution:

since the convolution is numerically a product between a dense matrix and a vector, the MultiLevel technique “anterpolates” the finest grid pressure down to the coarsest grid where the summation is executed over a poor number of grid points; then, the evaluated deformation is interpolated up to the finest grid. Then, the minimum film thickness is found, instead of the surfaces’ rigid approach, by executing an outer iterative cycle solving the load balance equation: this nested cycles approach, in which the outer cycle iterates on the approach solving the load balance equation and the inner one iterates on the lubricant pressure solving the Reynolds equation is widely used in this context.

In (Venner and Wijnant, 2005) the authors adapted the codes developed in (Venner, 1992) to the transient case, replacing the minimum film thickness with the surfaces’ rigid approach and including the approaching surfaces’ inertia into the load balance equation: with the same MultiGrid/MultiLevel and nested cycles techniques, the authors investigated the tribo-system response to a time-varying load input.

In (Almqvist, Almqvist and Larsson, 2004) the authors developed an EHL simulator in which the Reynolds equation and the gap composition equation involving the surfaces’ deformation are solved simultaneously by updating both the lubricant pressure and the film thickness according to a block logic that exploited fast iterative techniques, while the minimum film thickness was evaluated by the nested cycles approach; the authors validated their model by comparing their results with respect to the ones obtained by a commercial Computational Fluid Dynamics (CFD) software demonstrating very low deviations.

In (Goodyer and Berzins, 2006) the authors highlighted the differential/algebraic nature of the EHL problem and they used adaptive time-stepping techniques to simulate transient conditions, while at each time instant the MultiGrid/MultiLevel techniques and the nested cycles approach were adopted.

Interesting crossing between Multi-Body environbments and tribological systems were already addressed in the scientific literature in the framework of the forward dynamics analyses of mechanisms.

In (Askari *et al.*, 2014b) the authors modelled the artificial hip joint as a dry tribo-system where the two bodies (acetabular cup and femoral head) interacted by exchanging the contact force based on the surfaces’ interpenetration for the normal interaction and on the Coulomb friction force for the tangential interaction: they investigated the friction-induced vibrations of the implants and found that stick-slip phenomena occurring at the interface affect the joint wear.

In (Askari *et al.*, 2014a) the same authors in (Askari *et al.*, 2014b) used the previously developed model to investigate the squeaking noise in ceramic-on-ceramic THR during the walking cycle.

In (Flores, Ambrosio and Claro, 2004) the authors developed a Multi-Body model for the planar slider-crank mechanism in which the rod-slider revolute joint was characterised by a lubricated clearance, so, based on its eccentricity, it was able to develop internal forces due to the lubricant squeeze effect (coming from a particular analytical solution of the Reynolds equation) and to the contact interpenetration: they investigated the eccentricity orbit with respect to the ideal joint case, i.e., with no clearance.

In (Tian *et al.*, 2009) the authors used the same previous approach but, in addition, they introduced the flexible behaviour of the involved bodies and they compared their result with the rigid body case for several spatial mechanisms.

The contribution of the presented literature is summarised in the Table 1, where, for the cited references, information about the analysed tribo-system and the related adopted numerical modelling/strategies are given concisely.

Table 1 *Tribological modelling review*

Authors	System	Model
(Jin and Dowson, 1999; Ramjee, 2008)	THR	HL simulation revealing the need for EHL/ML simulator
(Jalali-Vahid and Jin, 2001; Jalali-Vahid *et al.*, 2001a, 2001b; Jalali-Vahid, Jin and Dowson, 2003)	THR	Proportional local deformation model suitable for Hard-on-Soft implants
(Fregly, Bei and Sylvester, 2003; Halloran *et al.*, 2005; Pérez-González *et al.*, 2008; Mukras *et al.*, 2010; Srivastava, Christian and Higgs, 2021)	THR	Elastic foundation deformation model suitable for Hard-on-Soft implants
(Evans and Hughes, 2000; Jagatia and Jin, 2001; Wang and Jin, 2004b, 2004a, 2008; Wang *et al.*, 2009; Gao, Dowson and Hewson, 2015)	THR	Half space deformation model suitable for both Hard-on-Soft and Hard-on-Hard implants
(Jagatia and Jin, 2001; Udofia and Jin, 2003; Halloran *et al.*, 2005; Wang and Jin, 2008; Gao *et al.*, 2009)	THR	FEM deformation model, most accurate but computationally heavy computation or software dependent

(Wang and Jin, 2004a; Wang, Wang and Sun, 2010)	THR	ML simulation implementing the contact pressure from the surface overlapping
(Zhu and Hu, 1999; Hu *et al.*, 2001; Zhu, 2007; Zhang *et al.*, 2019)	Rectangular system	ML simulation with the Reduced Reynolds equation
(Zhang *et al.*, 2016)	Rectangular system	ML simulation with the average Reynolds equation
(Venner, 1992; Venner and Wijnant, 2005; Goodyer and Berzins, 2006)	Rectangular system	EHL simulation with MultiGrid/MultiLevel startegies
(Almqvist, Almqvist and Larsson, 2004)	Rectangular system	EHL simulation with simultaneous pressure and gap update
(Flores, Ambrosio and Claro, 2004; Tian *et al.*, 2009; Askari *et al.*, 2014a, 2014b)	THR and basic mechanisms	DCM/HL simulation based on the Multi-Body modelling and on analytical forms of the fluid/contact forces

From the Table 1, it is evident the wide availability of numerical tools able to describe the tribological interaction between coupled surfaces under certain conditions; in this work, the objective was to try the main modelling strategies for both the THR and a general rectangular tribo-system referred to the EHL and ML regimes; in particular, the realised simulation codes are devoted to:

- the ML of the THR characterised by a proportional and local deformation model, in which the hip loads and the angular velocities input are supplied from the results of the Multi-Body musculoskeletal simulator presented above, so that an estimate of the implant wear can be obtained from a specific musculoskeletal kinematics (Ruggiero and Sicilia, 2020a, 2022c, 2024);
- the EHL of a ball-in-socket tribo-system where the deformation model is given by a compliance matrix obtained from a self-made FEM calculation avoiding the interface with a dedicated software (Ruggiero and Sicilia, 2021b, 2022b);
- the ML of a general rectangular tribo-system where the surfaces are modelled as half-spaces; in this case the couplings of ball against plane and rough surface against plane are analysed and the results were compared also to the respective dry regime outcomes coming from a described DCM simulator (Sicilia and Ruggiero, 2025);
- the transient EHL for a line-contact system composed by half-spaces in which the focus is oriented to the numerical strategy to solve the problem based on the assembling and the time marching of a DAE system (Sicilia and Ruggiero, 2026).

All the presented simulations were obtained by running codes written in Matlab® environment, so they are manageable, improvable and in continuous modelling progression.

At this point the simulative framework this work belongs to has been presented, so the works developed by the author in this context will be presented; this thesis contents are organised and structured along two main chapters as follows:

- in the Biomechanics chapter the detailed theory behind the code development is presented in the sections from 1.1 to 1.6, i.e., constrained rigid body kinematics, Multi-Body Lagrangian dynamics, muscular actuation modelling, optimization strategies, etc.; therefore, the simulations conducted with the assembled algorithm are presented in the section 1.7 referring to an upper limb and to a lower limb musculoskeletal system, where the latter moves following the gait cycle kinematics providing the hip tribological operating conditions of loads and angular velocities;
- in the Tribology chapter the techniques adopted to numerically model the HL, the EHL and the ML regimes are presented in the sections from 2.1 to 2.3; in particular, three deformation models were presented in the section 2.2 (spring, FEM and BEM) and several ML tools were introduced in the section 2.3, e.g., the DCM solver to obtain starting solution guess or to compare the ML results with, a fractal roughness generator and the strategies to numerically couple the lubrication and the contact equations; then, three simulations conducted with the described tools are presented in the section 2.4, referring in particular to the ML of the THR subjected to the Multi-Body simulator output conditions, the EHL of a ball-in-socket joint equipped with the developed FEM deformation model, the ML of a rectangular tribo-system (able to consider also rough surfaces) equipped with the BEM deformation model; finally, the last author advancement is presented in the section 2.5, regarding the transient EHL modelling where the coupling is regarded as a dynamical system described by states that evolve over time according to the numerical marching of the associated DAE system.

1. Biomechanics

In this chapter the Multi-Body theory necessary to address the inverse dynamics of the musculoskeletal system is presented; in the final section of this chapter, the simulation regarding the inverse dynamics of upper limb and lower limb systems are presented, where the latter simulation investigated the gait cycle kinematics providing the associated hip loads and relative motions necessary to supply the successive tribological investigations.

1.1. Rigid body kinematics formulation

The dynamics of a Multi-Body system is strictly related to its kinematics, so it is necessary to define the system's bodies configuration in the space.

Talking about rigid bodies with reference to the Figure 11, a local reference frame $\bar{x}_i\bar{y}_i\bar{z}_i$ is associated to each involved body i, it is fixed with the body and its origin is the body mass centre G_i (actually, the origin can be any point of the body, but choosing the centre of mass will lead to dynamical decoupling simplifications discussed in the next): the rigid body i configuration in the 3D space is given by the position and the orientation of its local reference frame with respect to a global reference frame $Oxyz$ (Shabana, 2020) (fixed in space and time) through a set of translational parameters, i.e., the position vector $\mathbf{t}_i$, and a set of rotational parameters, i.e., the orientation vector $\boldsymbol{\theta}_i$; all these information can be collected in the body Lagrangian coordinates vector $\mathbf{q}_i$ in the eq. (3).

$$\mathbf{q}_i = \begin{bmatrix} \mathbf{t}_i \\ \boldsymbol{\theta}_i \end{bmatrix} \tag{3}$$

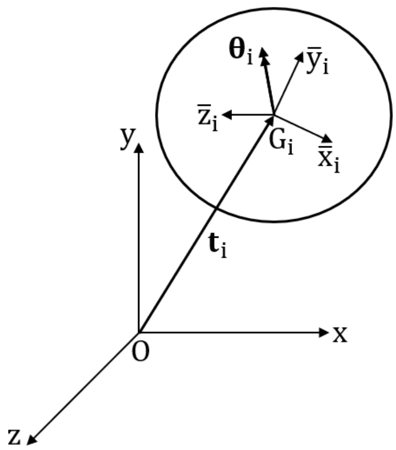

Figure 11 *Rigid body configuration in the 3D space*

While the 3D position is a straightforward definition, the 3D orientation has to be carefully defined. Generally, the aim is to characterize a mathematical formulation that relates a starting reference frame $0xyz$ to a rotated one $0\bar{x}\bar{y}\bar{z}$.

Among the several ways to describe 3D rotations, the most common approach is represented by the Euler angles (Shabana, 2020), which are 3 independent parameters that decompose the general frame rotation into the 3 successive basic rotations around the resulting frame axes according to a chosen order. For example, a general 3D rotation can be decomposed as in the Figure 12 into a rotation around the x axis by the angle α, followed by a rotation around the new axis y' by the angle β, lastly followed by a rotation around the new z'' axis by the angle γ: the 3 basic rotations are described by 3 rotation matrices depending on the 3 Euler angles α, β and γ, i.e., $\mathbf{R}_x$, $\mathbf{R}_y$ and $\mathbf{R}_z$, which the product in the chosen order provided the resulting rotation matrix $\mathbf{R}$ in the eq. (4).

$$\left.\begin{array}{l}\mathbf{R}_x(\alpha) = \begin{bmatrix} 1 & 0 & 0 \\ 0 & \cos\alpha & -\sin\alpha \\ 0 & \sin\alpha & \cos\alpha \end{bmatrix} \\ \mathbf{R}_y(\beta) = \begin{bmatrix} \cos\beta & 0 & \sin\beta \\ 0 & 1 & 0 \\ -\sin\beta & 0 & \cos\beta \end{bmatrix} \\ \mathbf{R}_z(\gamma) = \begin{bmatrix} \cos\gamma & -\sin\gamma & 0 \\ \sin\gamma & \cos\gamma & 0 \\ 0 & 0 & 1 \end{bmatrix}\end{array}\right. \rightarrow \mathbf{R}(\alpha,\beta,\gamma) = \mathbf{R}_x(\alpha)\mathbf{R}_y(\beta)\mathbf{R}_z(\gamma) \quad (4)$$

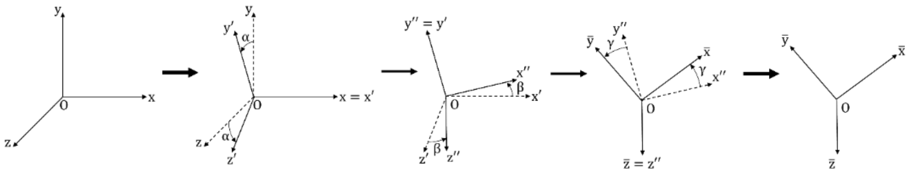

Figure 12 *Euler angles consecutive rotations*

Another strategy widely used in the context of 3D rotations is represented by the Euler parameters (Shabana, 2020) which allow to describe a general frame rotation performed in one step around an axis oriented as the unit vector $\hat{\mathbf{v}}$ by an angle Θ: the Euler parameters are 4 numbers that can be collected into a vector called unit quaternion; in this work the quaternion approach is chosen.

With reference to the Figure 13, going to the rotated reference frame $\mathrm{O}\overline{\mathrm{x}}\overline{\mathrm{y}}\overline{\mathrm{z}}$ from the starting one Oxyz rotating around the axis oriented as the unit vector $\hat{\mathbf{v}}$ by an angle Θ, the unit quaternion $\boldsymbol{\theta}$ is defined in the (5) as a function of $\hat{\mathbf{v}}$ and Θ; let note that the components of the unit vector $\hat{\mathbf{v}}$ are the same in both the reference frames and that the "unit" quaternion has unitary norm, so it is characterised by 3 independent information.

$$\boldsymbol{\theta}(\hat{\mathbf{v}},\Theta) = \begin{bmatrix} \cos\frac{\Theta}{2} \\ \hat{\mathbf{v}}\sin\frac{\Theta}{2} \end{bmatrix} \quad \rightarrow \quad \boldsymbol{\theta}^{\mathrm{T}}\boldsymbol{\theta} = 1 \tag{5}$$

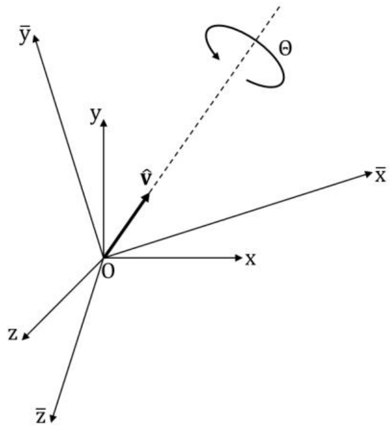

Figure 13 *Reference frame general rotation*

The unit quaternion $\boldsymbol{\theta}$ is often seen as a complex number with a real scalar part and a vector imaginary part, respectively, θ_{Re} and $\boldsymbol{\theta}_{\mathrm{Im}}$ (eq. (6)).

$$\begin{aligned} \theta_{\mathrm{Re}} &= \cos\frac{\Theta}{2} \\ \boldsymbol{\theta}_{\mathrm{Im}} &= \hat{\mathbf{v}}\sin\frac{\Theta}{2} \end{aligned} \quad \rightarrow \quad \boldsymbol{\theta} = \begin{bmatrix} \theta_{\mathrm{Re}} \\ \boldsymbol{\theta}_{\mathrm{Im}} \end{bmatrix} \tag{6}$$

Defining the 3D skew operator that turns a three-element vector $\mathbf{u}$ into its associated 3x3 skew matrix $\tilde{\mathbf{u}}$ and the 3x3 identity matrix $\mathbf{I}$, it is possible to define in (7) two important matrices related to the unit quaternion $\boldsymbol{\theta}$, i.e., $\mathbf{E}$ and $\bar{\mathbf{E}}$.

$$\tilde{\mathbf{u}} = \begin{bmatrix} 0 & -u_z & u_y \\ u_z & 0 & -u_x \\ -u_y & u_x & 0 \end{bmatrix} = -\tilde{\mathbf{u}}^T \qquad \begin{aligned} \mathbf{E}(\boldsymbol{\theta}) &= [-\boldsymbol{\theta}_{Im} \quad \theta_{Re}\mathbf{I} + \tilde{\boldsymbol{\theta}}_{Im}] \\ \bar{\mathbf{E}}(\boldsymbol{\theta}) &= [-\boldsymbol{\theta}_{Im} \quad \theta_{Re}\mathbf{I} - \tilde{\boldsymbol{\theta}}_{Im}] \end{aligned} \tag{7}$$

The rotation matrix $\mathbf{R}$ referred to the orientation transformation can be evaluated by knowing the unit quaternion $\boldsymbol{\theta}$: a vector $\bar{\mathbf{u}}$ which components are defined in the rotated reference frame $O\bar{x}\bar{y}\bar{z}$ can be rotated and evaluated in the starting reference frame Oxyz, where its components compose the vector $\mathbf{u}$ by the application of the rotation matrix $\mathbf{R}$ (eq. (8)).

$$\mathbf{R}(\boldsymbol{\theta}) = \mathbf{E}(\boldsymbol{\theta})\bar{\mathbf{E}}^T(\boldsymbol{\theta}) \;\rightarrow\; \mathbf{u} = \mathbf{R}(\boldsymbol{\theta})\bar{\mathbf{u}} \tag{8}$$

It's worth to note in (9) that the 3-column composing the rotation matrix are the unit vectors associated to the rotated reference frame $O\bar{x}\bar{y}\bar{z}$ written in the starting one; furthermore, the inverse operation that starting from the vector $\mathbf{u}$ leads to the vector $\bar{\mathbf{u}}$ requires the inverse of the rotation matrix $\mathbf{R}$.

$$\mathbf{u} = \mathbf{R}\bar{\mathbf{u}} = \begin{bmatrix} \hat{\bar{\mathbf{i}}} & \hat{\bar{\mathbf{j}}} & \hat{\bar{\mathbf{k}}} \end{bmatrix} \begin{bmatrix} \bar{u}_{\bar{x}} \\ \bar{u}_{\bar{y}} \\ \bar{u}_{\bar{z}} \end{bmatrix} \qquad \bar{\mathbf{u}} = \mathbf{R}^{-1}\mathbf{u} \tag{9}$$

Executing the product in (8) to evaluate the rotation matrix and substituting the quaternion real and imaginary parts, after algebraic manipulation the rotation matrix can be written in (10) also as a function of the rotation axis unit vector $\hat{\mathbf{v}}$ and the rotation angle Θ within the so-called Rodriguez formula (Shabana, 2020).

$$\mathbf{R}(\hat{\mathbf{v}}, \Theta) = \mathbf{I} + \tilde{\mathbf{v}}\sin\Theta + 2\tilde{\mathbf{v}}^2\sin^2\frac{\Theta}{2} \tag{10}$$

The inverse rotation in (9) can be seen as a rotation Θ executed around the axis oriented as $-\hat{\mathbf{v}}$ or as a rotation $-\Theta$ executed around the axis oriented as $\hat{\mathbf{v}}$: recalling the properties of a skew matrix, in both cases the Rodriguez formula demonstrates in (11) the orthogonality of the rotation matrix $\mathbf{R}$, which allows to write its inverse as its transposed.

$$\begin{aligned} &\mathbf{R}^{-1} = \mathbf{I} - \tilde{\mathbf{v}}\sin\Theta + 2\tilde{\mathbf{v}}^2\sin^2\frac{\Theta}{2} = \mathbf{R}^T \\ &\mathbf{R}\mathbf{R}^T = \mathbf{R}^T\mathbf{R} = \mathbf{I} \end{aligned} \tag{11}$$

The orthogonality of the rotation matrix $\mathbf{R}$, after a time differentiation, shows that the rotation matrix time derivative can be obtained in (12) by the product between $\mathbf{R}$ and, respectively, a skew matrix $\tilde{\boldsymbol{\omega}}$ for the left-product and a skew matrix $\tilde{\bar{\boldsymbol{\omega}}}$ for the right-product.

$$\begin{aligned} &\mathbf{R}\mathbf{R}^T = \mathbf{I} \;\rightarrow\; \dot{\mathbf{R}}\mathbf{R}^T + \mathbf{R}\dot{\mathbf{R}}^T = \mathbf{0} \;\rightarrow\; \dot{\mathbf{R}}\mathbf{R}^T = -\left(\dot{\mathbf{R}}\mathbf{R}^T\right)^T = \tilde{\boldsymbol{\omega}} \\ &\dot{\mathbf{R}} = \tilde{\boldsymbol{\omega}}\mathbf{R} \\ &\mathbf{R}^T\mathbf{R} = \mathbf{I} \;\rightarrow\; \dot{\mathbf{R}}^T\mathbf{R} + \mathbf{R}^T\dot{\mathbf{R}} = \mathbf{0} \;\rightarrow\; \mathbf{R}^T\dot{\mathbf{R}} = -\left(\mathbf{R}^T\dot{\mathbf{R}}\right)^T = \tilde{\bar{\boldsymbol{\omega}}} \end{aligned} \tag{12}$$

$\dot{\mathbf{R}} = \mathbf{R}\tilde{\bar{\boldsymbol{\omega}}}$

The vectors associated to the skew matrices $\tilde{\boldsymbol{\omega}}$ and $\tilde{\bar{\boldsymbol{\omega}}}$ are the angular velocity vectors of the transformation defined, respectively, in the starting reference frame Oxyz, i.e., $\boldsymbol{\omega}$, and in the rotated reference frame $O\bar{x}\bar{y}\bar{z}$, i.e., $\bar{\boldsymbol{\omega}}$: both the angular velocity vectors can be obtained in (13) from the quaternion time derivative $\dot{\boldsymbol{\theta}}$.

$$\begin{aligned} &\mathbf{G}(\boldsymbol{\theta}) = 2\mathbf{E}(\boldsymbol{\theta}) \;\; \rightarrow \;\; \boldsymbol{\omega}(\boldsymbol{\theta}, \dot{\boldsymbol{\theta}}) = \mathbf{G}(\boldsymbol{\theta})\dot{\boldsymbol{\theta}} = -\dot{\mathbf{G}}\boldsymbol{\theta} \quad \dot{\mathbf{G}} = \mathbf{G}(\dot{\boldsymbol{\theta}}) \\ &\bar{\mathbf{G}}(\boldsymbol{\theta}) = 2\bar{\mathbf{E}}(\boldsymbol{\theta}) \;\; \rightarrow \;\; \bar{\boldsymbol{\omega}}(\boldsymbol{\theta}, \dot{\boldsymbol{\theta}}) = \bar{\mathbf{G}}(\boldsymbol{\theta})\dot{\boldsymbol{\theta}} = -\dot{\bar{\mathbf{G}}}\boldsymbol{\theta} \quad \dot{\bar{\mathbf{G}}} = \bar{\mathbf{G}}(\dot{\boldsymbol{\theta}}) \end{aligned} \tag{13}$$

Two successive rotations identified by the quaternions $\boldsymbol{\theta}_1$ and $\boldsymbol{\theta}_2$ in this order, are equivalent to a global rotation identified by the quaternion $\boldsymbol{\theta}_3$ that can be evaluated in (14) by the definition of the quaternion Hamiltonian product 4x4 matrices $\mathbf{H}$ and $\bar{\mathbf{H}}$.

$$\begin{aligned} &\mathbf{H}(\boldsymbol{\theta}) = \begin{bmatrix} \theta_{\mathrm{Re}} & -\boldsymbol{\theta}_{\mathrm{Im}}^{\mathrm{T}} \\ \boldsymbol{\theta}_{\mathrm{Im}} & \theta_{\mathrm{Re}}\mathbf{I} + \tilde{\boldsymbol{\theta}}_{\mathrm{Im}} \end{bmatrix} = [\boldsymbol{\theta} \quad \bar{\mathbf{E}}^{\mathrm{T}}(\boldsymbol{\theta})] \quad \rightarrow \quad \boldsymbol{\theta}_3 = \mathbf{H}(\boldsymbol{\theta}_1)\boldsymbol{\theta}_2 \\ &\bar{\mathbf{H}}(\boldsymbol{\theta}) = \begin{bmatrix} \theta_{\mathrm{Re}} & -\boldsymbol{\theta}_{\mathrm{Im}}^{\mathrm{T}} \\ \boldsymbol{\theta}_{\mathrm{Im}} & \theta_{\mathrm{Re}}\mathbf{I} - \tilde{\boldsymbol{\theta}}_{\mathrm{Im}} \end{bmatrix} = [\boldsymbol{\theta} \quad \mathbf{E}^{\mathrm{T}}(\boldsymbol{\theta})] \quad \rightarrow \quad \boldsymbol{\theta}_3 = \bar{\mathbf{H}}(\boldsymbol{\theta}_2)\boldsymbol{\theta}_1 \end{aligned} \tag{14}$$

Like the rotation matrix, the Hamiltonian matrix is an orthogonal one, so its inverse is equal to its transposed (eq. (15)).

$$\begin{aligned} &\mathbf{H}\mathbf{H}^{\mathrm{T}} = \mathbf{I} \quad \rightarrow \quad \mathbf{H}^{\mathrm{T}}(\boldsymbol{\theta}_1)\boldsymbol{\theta}_3 = \boldsymbol{\theta}_2 \\ &\bar{\mathbf{H}}\bar{\mathbf{H}}^{\mathrm{T}} = \mathbf{I} \quad \rightarrow \quad \bar{\mathbf{H}}^{\mathrm{T}}(\boldsymbol{\theta}_2)\boldsymbol{\theta}_3 = \boldsymbol{\theta}_1 \end{aligned} \tag{15}$$

Another useful operation that will be exploited in the next is the quaternion conjugation: the conjugated quaternion $\bar{\boldsymbol{\theta}}$, obtained by changing the sign of the quaternion $\boldsymbol{\theta}$ imaginary part, is equivalent, as reported in (16), to the application of the conjugation matrix $\bar{\mathbf{C}}$ to the original quaternion $\boldsymbol{\theta}$.

$$\bar{\boldsymbol{\theta}} = \begin{bmatrix} \theta_{\mathrm{Re}} \\ -\boldsymbol{\theta}_{\mathrm{Im}} \end{bmatrix} = \begin{bmatrix} 1 & \mathbf{0}^{\mathrm{T}} \\ \mathbf{0} & -\mathbf{I} \end{bmatrix} \begin{bmatrix} \theta_{\mathrm{Re}} \\ \boldsymbol{\theta}_{\mathrm{Im}} \end{bmatrix} = \bar{\mathbf{C}}\boldsymbol{\theta} \tag{16}$$

In the context of the constraint equation writing, it will be also useful to evaluate the rotation angle Θ associated with a given quaternion $\boldsymbol{\theta}$ by knowing the rotation axis unit vector $\hat{\mathbf{v}}$, i.e., applying the $\langle\boldsymbol{\theta}\rangle$ angle operator defined in (17).

$$\Theta = \langle\boldsymbol{\theta}\rangle = 2\arctan\frac{\hat{\mathbf{v}}^{\mathrm{T}}\boldsymbol{\theta}_{\mathrm{Im}}}{\theta_{\mathrm{Re}}} \tag{17}$$

Executing in (18) the time differentiation of a quaternion $\boldsymbol{\theta}$ with constant unit vector $\hat{\mathbf{v}}$, its derivative with respect the angle Θ, $\boldsymbol{\theta}_\Theta$, is highlighted: it will be useful to evaluate the time derivative of the angle operator $\langle\boldsymbol{\theta}\rangle$.

$$\begin{aligned} &\dot{\boldsymbol{\theta}}(\hat{\mathbf{v}}, \Theta, \dot{\Theta}) = \frac{\dot{\Theta}}{2}\begin{bmatrix} -\sin\frac{\Theta}{2} \\ \hat{\mathbf{v}}\cos\frac{\Theta}{2} \end{bmatrix} = \boldsymbol{\theta}_\Theta\dot{\Theta} \quad \rightarrow \quad \boldsymbol{\theta}_\Theta(\hat{\mathbf{v}}, \Theta) = \frac{1}{2}\begin{bmatrix} -\sin\frac{\Theta}{2} \\ \hat{\mathbf{v}}\cos\frac{\Theta}{2} \end{bmatrix} \\ &\dot{\Theta} = \langle\dot{\boldsymbol{\theta}}\rangle = 4\,\boldsymbol{\theta}_\Theta^{\mathrm{T}}\dot{\boldsymbol{\theta}} \end{aligned} \tag{18}$$

Also the time derivative of $\boldsymbol{\theta}_{\Theta}$, i.e., $\dot{\boldsymbol{\theta}}_{\Theta}$ in (19), will be used in the context of the constraint equation writing.

$$\dot{\boldsymbol{\theta}}_{\Theta}\left(\hat{\mathbf{v}},\Theta,\dot{\Theta}\right) = -\frac{\dot{\Theta}}{4}\begin{bmatrix} \cos\frac{\Theta}{2} \\ \hat{\mathbf{v}}\sin\frac{\Theta}{2} \end{bmatrix} = -\frac{\dot{\Theta}}{4}\boldsymbol{\theta}(\hat{\mathbf{v}},\Theta) \quad (19)$$

Despite the fourth redundant information, the quaternion approach to describe 3D rotations is widely used in the context of mechanics thanks to their properties in (20) that lead to several simplifications (Shabana, 2020).

$$\begin{aligned}
&\mathbf{E}\mathbf{E}^{\mathrm{T}} = \bar{\mathbf{E}}\bar{\mathbf{E}}^{\mathrm{T}} = \mathbf{I}\\
&\mathbf{E}^{\mathrm{T}}\mathbf{E} = \bar{\mathbf{E}}^{\mathrm{T}}\bar{\mathbf{E}} = \mathbf{I} - \boldsymbol{\theta}\boldsymbol{\theta}^{\mathrm{T}}\\
&\mathbf{E}\boldsymbol{\theta} = \bar{\mathbf{E}}\boldsymbol{\theta} = \mathbf{0}\\
&\dot{\mathbf{E}}\dot{\boldsymbol{\theta}} = \dot{\bar{\mathbf{E}}}\dot{\boldsymbol{\theta}} = \mathbf{0}\\
&\mathbf{E}\dot{\bar{\mathbf{E}}}^{\mathrm{T}} = \dot{\mathbf{E}}\bar{\mathbf{E}}^{\mathrm{T}}\\
&\dot{\mathbf{G}}\mathbf{G}^{\mathrm{T}} = -\mathbf{G}\dot{\mathbf{G}}^{\mathrm{T}} = 2\tilde{\boldsymbol{\omega}}\\
&\dot{\bar{\mathbf{G}}}\bar{\mathbf{G}}^{\mathrm{T}} = -\bar{\mathbf{G}}\dot{\bar{\mathbf{G}}}^{\mathrm{T}} = 2\tilde{\bar{\boldsymbol{\omega}}}\\
&\boldsymbol{\theta}^{\mathrm{T}}\boldsymbol{\theta} = 1\\
&\dot{\boldsymbol{\theta}}^{\mathrm{T}}\boldsymbol{\theta} = 0
\end{aligned} \quad (20)$$

Once the orientation description strategy is chosen, the knowledge of the body i Lagrangian coordinates $\mathbf{q}_{\mathrm{i}}$ allows to evaluate the position of anything fixed to the body (Shabana, 2020): with reference to the Figure 14, if a point P fixed to the body is located by the vector $\bar{\mathbf{u}}$ in the local reference frame, then its position $\mathbf{r}$ in the global one is a nonlinear function of the body Lagrangian coordinates $\mathbf{q}_{\mathrm{i}}$ that can be determined in (21) by adding to the translation vector $\mathbf{t}_{\mathrm{i}}$ the vector $\bar{\mathbf{u}}$ rotated by the means of the quaternion $\boldsymbol{\theta}_{\mathrm{i}}$.

$$\mathbf{r}(\mathbf{q}_{\mathrm{i}}) = \mathbf{t}_{\mathrm{i}} + \mathbf{R}(\boldsymbol{\theta}_{\mathrm{i}})\bar{\mathbf{u}} \quad (21)$$

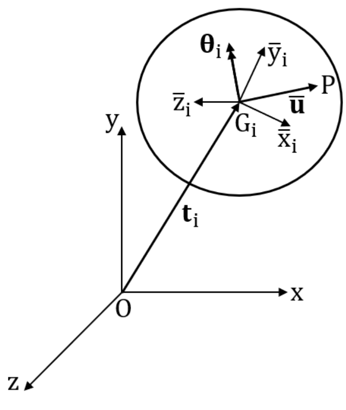

Figure 14 *Point fixed to a rigid body*

Furthermore, the velocity vector $\dot{\mathbf{r}}$ in the global reference frame of the point P can be obtained in (22) by time-differentiating its position introducing the local angular velocity skew matrix $\tilde{\bar{\boldsymbol{\omega}}}_\mathrm{i}$ (since P is fixed to the rigid body, its local position vector $\bar{\mathbf{u}}$ is constant).

$$\dot{\mathbf{r}} = \dot{\mathbf{t}}_\mathrm{i} + \mathbf{R}(\boldsymbol{\theta}_\mathrm{i})\tilde{\bar{\boldsymbol{\omega}}}_\mathrm{i}\bar{\mathbf{u}} \tag{22}$$

Recalling the skew matrices properties, the velocity of the point P in (23) results to be a linear combination of the body Lagrangian velocities $\dot{\mathbf{q}}_\mathrm{i}$, through a matrix $\mathbf{J}$ that depends on the Lagrangian coordinates $\mathbf{q}_\mathrm{i}$.

$$\begin{gathered} \tilde{\bar{\boldsymbol{\omega}}}_\mathrm{i}\bar{\mathbf{u}} = -\tilde{\bar{\mathbf{u}}}\bar{\boldsymbol{\omega}}_\mathrm{i} \quad \bar{\boldsymbol{\omega}}_\mathrm{i} = \bar{\mathbf{G}}(\boldsymbol{\theta}_\mathrm{i})\dot{\boldsymbol{\theta}}_\mathrm{i} \\ \dot{\mathbf{r}}(\mathbf{q}_\mathrm{i}, \dot{\mathbf{q}}_\mathrm{i}) = [\mathbf{I} \quad -\mathbf{R}(\boldsymbol{\theta}_\mathrm{i})\tilde{\bar{\mathbf{u}}}\bar{\mathbf{G}}(\boldsymbol{\theta}_\mathrm{i})] \begin{bmatrix} \dot{\mathbf{t}}_\mathrm{i} \\ \dot{\boldsymbol{\theta}}_\mathrm{i} \end{bmatrix} = \mathbf{J}(\mathbf{q}_\mathrm{i})\dot{\mathbf{q}}_\mathrm{i} \end{gathered} \tag{23}$$

In order to assemble the Multi-Body musculoskeletal system EoM, the Lagrangian coordinates $\mathbf{q}_\mathrm{i}$, velocities $\dot{\mathbf{q}}_\mathrm{i}$ and accelerations $\ddot{\mathbf{q}}_\mathrm{i}$ are needed: during an inverse dynamics analysis, the latter can be found by knowing the DoF time evolution through the solution of the so-called constraint equations.

1.2. Constrained kinematics

A Multi-Body system is given by a set of bodies linked by joints (Silva and Ambrósio, 2003); at the joint level the relative motion between the linked bodies occurs and, based on the joint behaviour, some relative movements are allowed while others are suppressed: the DoF of a Multi-Body system can be the joints' allowed movements that univocally determine the pose of the whole musculoskeletal system, so they are a set of parameters collected in the vector $\mathbf{d}$ that produce a particular set of the involved bodies Lagrangian coordinates $\mathbf{q}_\mathrm{i}$, for each body i; the latter are concatenated into a single column vector $\mathbf{q}$.

Given that a rigid body free to move in the space has 6 DoF (it needs of 3 independent translational parameters plus 3 independent rotational parameters to describe its pose), the Multi-Body system DoF number $\mathrm{n_D}$ is given in (24) by the number of DoF in absence of joints, i.e., in absence of kinematical constraints, so 6 times the number of bodies $\mathrm{n_B}$, minus the total number $\mathrm{n_C}$ of relative movements suppressed by the joints; as described previously, each body pose has to be described with respect to a global reference frame, which actually is the ground that needs to be considered as a body, so it is included into the bodies count but, since it has no mobility, the total mobility of the system in absence of joints is actually 6 times the bodies' number minus one (the ground).

$$\mathrm{n_D} = 6(\mathrm{n_B} - 1) - \mathrm{n_C} \tag{24}$$

In order to evaluate the bodies Lagrangian coordinates $\mathbf{q}$ (7 parameters for each body, due to the quaternion usage, excluding the ground), the number of constraint equations has to be equal to the total number of Lagrangian coordinates. In particular, the system of equations that represents the so-called position problem is composed by (Nikravesh and Gim, 1993; Oliveira, 2016):

- n_C constraint equations $\mathbf{C}$ imposing that the Lagrangian coordinates $\mathbf{q}$ evolve by avoiding the joints suppressed movements;
- n_D mobility equations $\mathbf{D}$ imposing that the Lagrangian coordinates $\mathbf{q}$ evolve by following the joints allowed movements, i.e., the DoF $\mathbf{d}$;
- $n_B - 1$ body equations $\mathbf{B}$ imposing that the Lagrangian coordinates $\mathbf{q}$ evolve by keeping the unitary norm of the moving bodies quaternions.

The total number of equations concatenated in (25) into a single vector $\mathbf{\Phi}$ is $7(n_B - 1)$ which is equal to the length of the Lagrangian coordinates vector: the position problem is a nonlinear well-posed equation system that can be solved with numerical iterative techniques to evaluate for each time t the Lagrangian coordinates $\mathbf{q}$ due to a given set of DoF $\mathbf{d}$.

$$\mathbf{d}(t) \;\rightarrow\; \mathbf{\Phi}(\mathbf{q},\mathbf{d}) = \begin{bmatrix} \mathbf{C}(\mathbf{q},\mathbf{d}) \\ \mathbf{D}(\mathbf{q},\mathbf{d}) \\ \mathbf{B}(\mathbf{q}) \end{bmatrix} = \mathbf{0} \;\rightarrow\; \mathbf{q}(t) \tag{25}$$

Generally, the constraint and the mobility equations, $\mathbf{C}$ and $\mathbf{D}$, are written as functions of the Lagrangian coordinates $\mathbf{q}$ and of the time t: in this work the dependence on the time t is strictly due to the DoF time evolution $\mathbf{d}(t)$.

The velocity problem is obtained in (26) by time-differentiating the position one, introducing the derivatives of the constraint, the mobility and the body equations with respect to the Lagrangian coordinates $\mathbf{q}$, i.e., $\mathbf{C_q}$, $\mathbf{D_q}$ and $\mathbf{B_q}$, and to the DoF $\mathbf{d}$, i.e., $\mathbf{C_d}$ and $\mathbf{D_d}$.

$$\begin{gathered} \dot{\mathbf{\Phi}}(\mathbf{q},\dot{\mathbf{q}},\mathbf{d},\dot{\mathbf{d}}) = \mathbf{\Phi_q}(\mathbf{q},\mathbf{d})\dot{\mathbf{q}} + \mathbf{\Phi_d}(\mathbf{q},\mathbf{d})\dot{\mathbf{d}} = \mathbf{0} \\ \dot{\mathbf{\Phi}}(\mathbf{q},\dot{\mathbf{q}},\mathbf{d},\dot{\mathbf{d}}) = \begin{bmatrix} \mathbf{C_q}(\mathbf{q},\mathbf{d}) \\ \mathbf{D_q}(\mathbf{q},\mathbf{d}) \\ \mathbf{B_q}(\mathbf{q}) \end{bmatrix} \dot{\mathbf{q}} + \begin{bmatrix} \mathbf{C_d}(\mathbf{q},\mathbf{d}) \\ \mathbf{D_d}(\mathbf{q},\mathbf{d}) \\ \mathbf{0} \end{bmatrix} \dot{\mathbf{d}} = \mathbf{0} \end{gathered} \tag{26}$$

The global equation system derivative with respect to the Lagrangian coordinates $\mathbf{\Phi_q}$ is the Jacobian of the position problem: it can be exploited in (27) in order to solve the nonlinear position problem with the iterative Newton method along the iterations k.

$$\mathbf{q}^{(k+1)} = \mathbf{q}^{(k)} - \left[\mathbf{\Phi_q}\left(\mathbf{q}^{(k)},\mathbf{d}\right)\right]^{-1} \mathbf{\Phi}\left(\mathbf{q}^{(k)},\mathbf{d}\right) \tag{27}$$

While the Lagrangian coordinates $\mathbf{q}$ need a nonlinear solver to be evaluated, the velocity problem in the unknown Lagrangian velocities $\dot{\mathbf{q}}$ is a linear problem that can be solved in (28) by inverting the Jacobian $\mathbf{\Phi_q}$ matrix.

$$\dot{\mathbf{q}} = -\left[\mathbf{\Phi_q}(\mathbf{q},\mathbf{d})\right]^{-1} \mathbf{\Phi_d}(\mathbf{q},\mathbf{d})\dot{\mathbf{d}} \tag{28}$$

The acceleration problem to evaluate the Lagrangian accelerations $\ddot{\mathbf{q}}$ requires a further time differentiation of the equations, introducing the time derivatives of the above matrices, i.e., $\dot{\mathbf{C}}_\mathbf{q}$, $\dot{\mathbf{D}}_\mathbf{q}$, $\dot{\mathbf{B}}_\mathbf{q}$, $\dot{\mathbf{C}}_\mathbf{d}$ and $\dot{\mathbf{D}}_\mathbf{d}$, and providing again a linear problem in (29) solvable by direct inversion.

$$\ddot{\mathbf{\Phi}} = \dot{\mathbf{\Phi}}_{\mathbf{q}}\dot{\mathbf{q}} + \mathbf{\Phi}_{\mathbf{q}}\ddot{\mathbf{q}} + \dot{\mathbf{\Phi}}_{\mathbf{d}}\dot{\mathbf{d}} + \mathbf{\Phi}_{\mathbf{d}}\ddot{\mathbf{d}} = \mathbf{0}$$

$$\ddot{\mathbf{\Phi}} = \begin{bmatrix} \dot{\mathbf{C}}_{\mathbf{q}} \\ \dot{\mathbf{D}}_{\mathbf{q}} \\ \dot{\mathbf{B}}_{\mathbf{q}} \end{bmatrix} \dot{\mathbf{q}} + \begin{bmatrix} \mathbf{C}_{\mathbf{q}} \\ \mathbf{D}_{\mathbf{q}} \\ \mathbf{B}_{\mathbf{q}} \end{bmatrix} \ddot{\mathbf{q}} + \begin{bmatrix} \dot{\mathbf{C}}_{\mathbf{d}} \\ \dot{\mathbf{D}}_{\mathbf{d}} \\ \mathbf{0} \end{bmatrix} \dot{\mathbf{d}} + \begin{bmatrix} \mathbf{C}_{\mathbf{d}} \\ \mathbf{D}_{\mathbf{d}} \\ \mathbf{0} \end{bmatrix} \ddot{\mathbf{d}} = \mathbf{0} \tag{29}$$

$$\ddot{\mathbf{q}} = -\mathbf{\Phi}_{\mathbf{q}}^{-1}\left(\dot{\mathbf{\Phi}}_{\mathbf{q}}\dot{\mathbf{q}} + \dot{\mathbf{\Phi}}_{\mathbf{d}}\dot{\mathbf{d}} + \mathbf{\Phi}_{\mathbf{d}}\ddot{\mathbf{d}}\right)$$

The overall kinematical problem leading from the DoF $\mathbf{d}$, $\dot{\mathbf{d}}$ and $\ddot{\mathbf{d}}$ to the Lagrangian coordinates $\mathbf{q}$, $\dot{\mathbf{q}}$ and $\ddot{\mathbf{q}}$ substantially requires the analytical form of the constraint and the mobility equations for each joint involved into the Multi-Body system and of the body equations for each body.

Practically, as reported in the eq. (30), for each joint J linking the bodies i and j, the associated constraint and mobility equations $\mathbf{C}_{\mathrm{J}}$ and $\mathbf{D}_{\mathrm{J}}$ depending on the related bodies Lagrangian coordinates $\mathbf{q}_{\mathrm{i}}$ and $\mathbf{q}_{\mathrm{j}}$ and on the joint DoF $\mathbf{d}_{\mathrm{J}}$ have to be characterised (Nikravesh and Gim, 1993) (let note that for each joint the sum of the constraint and the mobility equations numbers has to be equal to 6, which is the number of the free relative movements between the linked bodies in absence of the joint); furthermore, for each body i, the body equation B_{i} depending on the Lagrangian coordinates $\mathbf{q}_{\mathrm{i}}$ has to be written.

$$\begin{gathered} \mathbf{C}_{\mathrm{J}}\left(\mathbf{q}_{\mathrm{i}}, \mathbf{q}_{\mathrm{j}}, \mathbf{d}_{\mathrm{J}}\right) = \mathbf{0} \\ \mathbf{D}_{\mathrm{J}}\left(\mathbf{q}_{\mathrm{i}}, \mathbf{q}_{\mathrm{j}}, \mathbf{d}_{\mathrm{J}}\right) = \mathbf{0} \\ \mathrm{B}_{\mathrm{i}}\left(\mathbf{q}_{\mathrm{i}}\right) = 0 \end{gathered} \tag{30}$$

The time differentiation of the above equations will provide in (31) the matrices needed to solve the position and the velocity problem.

$$\begin{gathered} \mathbf{C}_{\mathbf{q}_{\mathrm{Ji}}}\dot{\mathbf{q}}_{\mathrm{i}} + \mathbf{C}_{\mathbf{q}_{\mathrm{Jj}}}\dot{\mathbf{q}}_{\mathrm{j}} + \mathbf{C}_{\mathbf{d}_{\mathrm{J}}}\dot{\mathbf{d}}_{\mathrm{J}} = \mathbf{0} \\ \mathbf{D}_{\mathbf{q}_{\mathrm{Ji}}}\dot{\mathbf{q}}_{\mathrm{i}} + \mathbf{D}_{\mathbf{q}_{\mathrm{Jj}}}\dot{\mathbf{q}}_{\mathrm{j}} + \mathbf{D}_{\mathbf{d}_{\mathrm{J}}}\dot{\mathbf{d}}_{\mathrm{J}} = \mathbf{0} \\ \mathrm{B}_{\mathbf{q}_{\mathrm{i}}}\dot{\mathbf{q}}_{\mathrm{i}} = 0 \end{gathered} \tag{31}$$

The further time differentiation of the found matrices will provide in (32) the matrices needed to solve the acceleration problem.

$$\begin{gathered} \dot{\mathbf{C}}_{\mathbf{q}_{\mathrm{Ji}}} = \frac{\mathrm{d}}{\mathrm{dt}}\left(\mathbf{C}_{\mathbf{q}_{\mathrm{Ji}}}\right) \quad \dot{\mathbf{C}}_{\mathbf{q}_{\mathrm{Jj}}} = \frac{\mathrm{d}}{\mathrm{dt}}\left(\mathbf{C}_{\mathbf{q}_{\mathrm{Jj}}}\right) \quad \dot{\mathbf{C}}_{\mathbf{d}_{\mathrm{J}}} = \frac{\mathrm{d}}{\mathrm{dt}}\left(\mathbf{C}_{\mathbf{d}_{\mathrm{J}}}\right) \\ \dot{\mathbf{D}}_{\mathbf{q}_{\mathrm{Ji}}} = \frac{\mathrm{d}}{\mathrm{dt}}\left(\mathbf{D}_{\mathbf{q}_{\mathrm{Ji}}}\right) \quad \dot{\mathbf{D}}_{\mathbf{q}_{\mathrm{Jj}}} = \frac{\mathrm{d}}{\mathrm{dt}}\left(\mathbf{D}_{\mathbf{q}_{\mathrm{Jj}}}\right) \quad \dot{\mathbf{D}}_{\mathbf{d}_{\mathrm{J}}} = \frac{\mathrm{d}}{\mathrm{dt}}\left(\mathbf{D}_{\mathbf{d}_{\mathrm{J}}}\right) \\ \dot{\mathrm{B}}_{\mathbf{q}_{\mathrm{i}}} = \frac{\mathrm{d}}{\mathrm{dt}}\left(\mathrm{B}_{\mathbf{q}_{\mathrm{i}}}\right) \end{gathered} \tag{32}$$

The found single contributions constitute the global kinematical problem into the Multi-Body space resumed in the eq. (33).

$$
\begin{aligned}
&\begin{bmatrix} \vdots \\ \mathbf{C}_{\mathrm{J}}(\mathbf{q}_{\mathrm{i}},\mathbf{q}_{\mathrm{j}},\mathbf{d}_{\mathrm{J}}) \\ \vdots \\ \mathbf{D}_{\mathrm{J}}(\mathbf{q}_{\mathrm{i}},\mathbf{q}_{\mathrm{j}},\mathbf{d}_{\mathrm{J}}) \\ \vdots \\ \mathrm{B}_{\mathrm{i}}(\mathbf{q}_{\mathrm{i}}) \\ \vdots \end{bmatrix} = \mathbf{0} \\
&\begin{bmatrix} & \vdots & & \vdots & \\ & \mathbf{C}_{\mathbf{q}_{\mathrm{Ji}}} & & \mathbf{C}_{\mathbf{q}_{\mathrm{Jj}}} & \\ & \vdots & & \vdots & \\ \cdots & \mathbf{D}_{\mathbf{q}_{\mathrm{Ji}}} & \cdots & \mathbf{D}_{\mathbf{q}_{\mathrm{Jj}}} & \cdots \\ & \vdots & & \vdots & \\ & \mathrm{B}_{\mathbf{q}_{\mathrm{i}}} & & \mathbf{0}^{\mathrm{T}} & \\ & \vdots & & \vdots & \end{bmatrix} \begin{bmatrix} \vdots \\ \dot{\mathbf{q}}_{\mathrm{i}} \\ \vdots \\ \dot{\mathbf{q}}_{\mathrm{j}} \\ \vdots \end{bmatrix} + \begin{bmatrix} & \vdots & \\ & \mathbf{C}_{\mathbf{d}_{\mathrm{J}}} & \\ & \vdots & \\ \cdots & \mathbf{D}_{\mathbf{d}_{\mathrm{J}}} & \cdots \\ & \vdots & \\ & \mathbf{0}^{\mathrm{T}} & \\ & \vdots & \end{bmatrix} \begin{bmatrix} \vdots \\ \dot{\mathbf{d}}_{\mathrm{J}} \\ \vdots \end{bmatrix} = \mathbf{0} \\
&\begin{bmatrix} & \vdots & & \vdots & \\ & \dot{\mathbf{C}}_{\mathbf{q}_{\mathrm{Ji}}} & & \dot{\mathbf{C}}_{\mathbf{q}_{\mathrm{Jj}}} & \\ & \vdots & & \vdots & \\ \cdots & \dot{\mathbf{D}}_{\mathbf{q}_{\mathrm{Ji}}} & \cdots & \dot{\mathbf{D}}_{\mathbf{q}_{\mathrm{Jj}}} & \cdots \\ & \vdots & & \vdots & \\ & \dot{\mathrm{B}}_{\mathbf{q}_{\mathrm{i}}} & & \mathbf{0}^{\mathrm{T}} & \\ & \vdots & & \vdots & \end{bmatrix} \begin{bmatrix} \vdots \\ \dot{\mathbf{q}}_{\mathrm{i}} \\ \vdots \\ \dot{\mathbf{q}}_{\mathrm{j}} \\ \vdots \end{bmatrix} + \begin{bmatrix} & \vdots & & \vdots & \\ & \mathbf{C}_{\mathbf{q}_{\mathrm{Ji}}} & & \mathbf{C}_{\mathbf{q}_{\mathrm{Jj}}} & \\ & \vdots & & \vdots & \\ \cdots & \mathbf{D}_{\mathbf{q}_{\mathrm{Ji}}} & \cdots & \mathbf{D}_{\mathbf{q}_{\mathrm{Jj}}} & \cdots \\ & \vdots & & \vdots & \\ & \mathrm{B}_{\mathbf{q}_{\mathrm{i}}} & & \mathbf{0}^{\mathrm{T}} & \\ & \vdots & & \vdots & \end{bmatrix} \begin{bmatrix} \vdots \\ \ddot{\mathbf{q}}_{\mathrm{i}} \\ \vdots \\ \ddot{\mathbf{q}}_{\mathrm{j}} \\ \vdots \end{bmatrix} + \cdots \\
&\ldots + \begin{bmatrix} & \vdots & \\ & \dot{\mathbf{C}}_{\mathbf{d}_{\mathrm{J}}} & \\ & \vdots & \\ \cdots & \dot{\mathbf{D}}_{\mathbf{d}_{\mathrm{J}}} & \cdots \\ & \vdots & \\ & \mathbf{0}^{\mathrm{T}} & \\ & \vdots & \end{bmatrix} \begin{bmatrix} \vdots \\ \dot{\mathbf{d}}_{\mathrm{J}} \\ \vdots \end{bmatrix} + \begin{bmatrix} & \vdots & \\ & \mathbf{C}_{\mathbf{d}_{\mathrm{J}}} & \\ & \vdots & \\ \cdots & \mathbf{D}_{\mathbf{d}_{\mathrm{J}}} & \cdots \\ & \vdots & \\ & \mathbf{0}^{\mathrm{T}} & \\ & \vdots & \end{bmatrix} \begin{bmatrix} \vdots \\ \ddot{\mathbf{d}}_{\mathrm{J}} \\ \vdots \end{bmatrix} = \mathbf{0}
\end{aligned}
\tag{33}
$$

1.3. Joints equations

In the following, the constraint and the mobility equations characterising the joints considered in this work are presented: they are the revolute joint, the cam joint, the spherical joint and the free joint.

During the writing of the equations some unit vectors will be used to describe translation/rotation axes (Nikravesh and Gim, 1993; Oliveira, 2016): these vectors will be defined in the so-called parent body reference frame which will be conventionally chosen as the body i, while the body j will be indicated as the child body.

1.3.1. *Revolute joint*

The revolute joint, reported in the Figure 15, linking the bodies i and j allows the relative rotation Θ_J, i.e., the single revolute joint DoF, around its joint axis oriented as the unit vector $\hat{\mathbf{v}}_J$; the joint is located by the vector $\bar{\mathbf{u}}_{Ji}$ in the body i reference frame and by the vector $\bar{\mathbf{u}}_{Jj}$ in the body j reference frame.

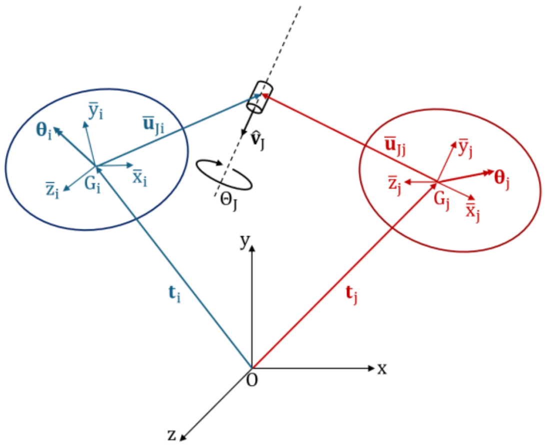

Figure 15 *Revolute joint scheme*

The 3 relative translations can be suppressed by 3 constraint equations in (34) that impose the equality of the global joint position whether written starting from the body i reference frame or from the j one.

$$\mathbf{t}_i + \mathbf{R}_i\bar{\mathbf{u}}_{Ji} = \mathbf{t}_j + \mathbf{R}_j\bar{\mathbf{u}}_{Jj} \tag{34}$$

The remaining 2 relative rotations can be suppressed by 2 constraint equations in (35) that impose the orthogonality, in the global reference frame, between the unit vector $\hat{\mathbf{v}}_J$ as if it belongs to the body j and a couple of orthogonal unit vectors $\hat{\mathbf{u}}_J$ and $\hat{\mathbf{w}}_J$ (unknown at the moment) as if they belong to the body i, by ensuring that the scalar product between orthogonal vectors is null.

$$(\mathbf{R}_j\hat{\mathbf{v}}_J)^T(\mathbf{R}_i\hat{\mathbf{u}}_J) = (\mathbf{R}_j\hat{\mathbf{v}}_J)^T(\mathbf{R}_i\hat{\mathbf{w}}_J) = 0 \tag{35}$$

Recalling that the unit vector $\hat{\mathbf{v}}_J$ has the same components in both the parent and the child bodies reference because of the single rotation allowed, the unit vectors $\hat{\mathbf{u}}_J$ and $\hat{\mathbf{w}}_J$ can be evaluated in (36), referring to the Figure 16, with the following steps:

- the known components of the unit vector $\hat{\mathbf{v}}_J$ can be used to evaluate its spherical angles θ_v and φ_v transformation with respect to the reference frame in which it is defined;

- the spherical angles θ_v and φ_v can be exploited to evaluate the rotation matrix $\mathbf{R}_v$ with the Euler angles approach that leads the $\hat{\mathbf{v}}_J$ reference frame x axis to align with the vector $\hat{\mathbf{v}}_J$ itself;
- by the definition of the rotation matrix, it is known that its 3 columns are the unit vectors associated to the rotated reference frame but written in the starting one, so its last 2 columns are the searched $\hat{\mathbf{u}}_J$ and $\hat{\mathbf{w}}_J$ unit vectors.

$$\hat{\mathbf{v}}_J = \begin{bmatrix} \cos\theta_v \cos\varphi_v \\ \sin\varphi_v \\ \sin\theta_v \cos\varphi_v \end{bmatrix} \qquad \begin{aligned} \theta_v &= \arctan\left(\frac{\hat{v}_{J_z}}{\hat{v}_{J_x}}\right) \\ \varphi_v &= \arctan\left(\frac{\hat{v}_{J_y}}{\sqrt{\hat{v}_{J_x}^2 + \hat{v}_{J_z}^2}}\right) \end{aligned} \tag{36}$$

$$\mathbf{R}_v = \mathbf{R}_y(-\theta_v)\mathbf{R}_z(\varphi_v) = [\hat{\mathbf{v}}_J \quad \hat{\mathbf{u}}_J \quad \hat{\mathbf{w}}_J]$$

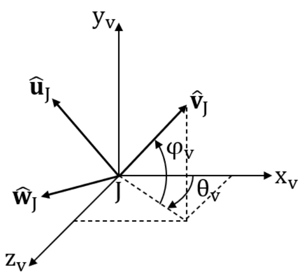

Figure 16 *Revolute joint triplet of orthogonal unit vectors*

The revolute joint mobility equation can be set by considering in (37) that the quaternion of the child body $\boldsymbol{\theta}_j$ can be obtained by the orientation of the parent body $\boldsymbol{\theta}_i$ followed by the relative rotation identified by the revolute joint angle Θ_J around its axis $\hat{\mathbf{v}}_J$: then, the relative quaternion can be evaluated by the way of the quaternion Hamiltonian product and it is known that its angle has to be equal to the revolute joint DoF through the angle operator.

$$\mathbf{H}_i^T\boldsymbol{\theta}_j = \begin{bmatrix} \cos\frac{\Theta_J}{2} \\ \hat{\mathbf{v}}_J \sin\frac{\Theta_J}{2} \end{bmatrix} \quad \rightarrow \quad \langle \mathbf{H}_i^T\boldsymbol{\theta}_j \rangle = \Theta_J \tag{37}$$

The residual of the found relationships can be arranged in (38) in order to obtain the revolute joint constraint and mobility equations.

$$\mathbf{d}_J = [\Theta_J] \qquad \mathbf{C}_J(\mathbf{q}_i, \mathbf{q}_j, \mathbf{d}_J) = \begin{bmatrix} \mathbf{t}_j + \mathbf{R}_j\bar{\mathbf{u}}_{Jj} - \mathbf{t}_i - \mathbf{R}_i\bar{\mathbf{u}}_{Ji} \\ \hat{\mathbf{v}}_J^T\mathbf{R}_j^T\mathbf{R}_i\hat{\mathbf{u}}_J \\ \hat{\mathbf{v}}_J^T\mathbf{R}_j^T\mathbf{R}_i\hat{\mathbf{w}}_J \end{bmatrix} = \mathbf{0} \tag{38}$$
$$\mathbf{D}_J(\mathbf{q}_i, \mathbf{q}_j, \mathbf{d}_J) = \langle \mathbf{H}_i^T\boldsymbol{\theta}_j \rangle - \Theta_J = \mathbf{0}$$

The first time derivative of the revolute joint equations leads to its contribution to the velocity problem. Let start with the constraint equations in (39).

$$\dot{\mathbf{C}}_{\mathrm{J}} = \begin{bmatrix} \dot{\mathbf{t}}_{\mathrm{j}} - \mathbf{R}_{\mathrm{j}}\tilde{\tilde{\mathbf{u}}}_{\mathrm{Jj}}\overline{\mathbf{G}}_{\mathrm{j}}\dot{\boldsymbol{\theta}}_{\mathrm{j}} - \dot{\mathbf{t}}_{\mathrm{i}} + \mathbf{R}_{\mathrm{i}}\tilde{\tilde{\mathbf{u}}}_{\mathrm{Ji}}\overline{\mathbf{G}}_{\mathrm{i}}\dot{\boldsymbol{\theta}}_{\mathrm{i}} \\ -\hat{\mathbf{v}}_{\mathrm{J}}^{\mathrm{T}}\mathbf{R}_{\mathrm{j}}^{\mathrm{T}}\mathbf{R}_{\mathrm{i}}\tilde{\mathbf{u}}_{\mathrm{J}}\overline{\mathbf{G}}_{\mathrm{i}}\dot{\boldsymbol{\theta}}_{\mathrm{i}} - \hat{\mathbf{u}}_{\mathrm{J}}^{\mathrm{T}}\mathbf{R}_{\mathrm{i}}^{\mathrm{T}}\mathbf{R}_{\mathrm{j}}\tilde{\mathbf{v}}_{\mathrm{J}}\overline{\mathbf{G}}_{\mathrm{j}}\dot{\boldsymbol{\theta}}_{\mathrm{j}} \\ -\hat{\mathbf{v}}_{\mathrm{J}}^{\mathrm{T}}\mathbf{R}_{\mathrm{j}}^{\mathrm{T}}\mathbf{R}_{\mathrm{i}}\tilde{\mathbf{w}}_{\mathrm{J}}\overline{\mathbf{G}}_{\mathrm{i}}\dot{\boldsymbol{\theta}}_{\mathrm{i}} - \hat{\mathbf{w}}_{\mathrm{J}}^{\mathrm{T}}\mathbf{R}_{\mathrm{i}}^{\mathrm{T}}\mathbf{R}_{\mathrm{j}}\tilde{\mathbf{v}}_{\mathrm{J}}\overline{\mathbf{G}}_{\mathrm{j}}\dot{\boldsymbol{\theta}}_{\mathrm{j}} \end{bmatrix} = \mathbf{0} \tag{39}$$

Highlighting in (40) the linear combination with respect to the Lagrangian and to the DoF velocities:

$$\dot{\mathbf{C}}_{\mathrm{J}} = \begin{bmatrix} -\mathbf{I} & \mathbf{R}_{\mathrm{i}}\tilde{\tilde{\mathbf{u}}}_{\mathrm{Ji}}\overline{\mathbf{G}}_{\mathrm{i}} \\ \mathbf{0} & -\hat{\mathbf{v}}_{\mathrm{J}}^{\mathrm{T}}\mathbf{R}_{\mathrm{j}}^{\mathrm{T}}\mathbf{R}_{\mathrm{i}}\tilde{\mathbf{u}}_{\mathrm{J}}\overline{\mathbf{G}}_{\mathrm{i}} \\ \mathbf{0} & -\hat{\mathbf{v}}_{\mathrm{J}}^{\mathrm{T}}\mathbf{R}_{\mathrm{j}}^{\mathrm{T}}\mathbf{R}_{\mathrm{i}}\tilde{\mathbf{w}}_{\mathrm{J}}\overline{\mathbf{G}}_{\mathrm{i}} \end{bmatrix} \begin{bmatrix} \dot{\mathbf{t}}_{\mathrm{i}} \\ \dot{\boldsymbol{\theta}}_{\mathrm{i}} \end{bmatrix} + \begin{bmatrix} \mathbf{I} & -\mathbf{R}_{\mathrm{j}}\tilde{\tilde{\mathbf{u}}}_{\mathrm{Jj}}\overline{\mathbf{G}}_{\mathrm{j}} \\ \mathbf{0} & -\hat{\mathbf{u}}_{\mathrm{J}}^{\mathrm{T}}\mathbf{R}_{\mathrm{i}}^{\mathrm{T}}\mathbf{R}_{\mathrm{j}}\tilde{\mathbf{v}}_{\mathrm{J}}\overline{\mathbf{G}}_{\mathrm{j}} \\ \mathbf{0} & -\hat{\mathbf{w}}_{\mathrm{J}}^{\mathrm{T}}\mathbf{R}_{\mathrm{i}}^{\mathrm{T}}\mathbf{R}_{\mathrm{j}}\tilde{\mathbf{v}}_{\mathrm{J}}\overline{\mathbf{G}}_{\mathrm{j}} \end{bmatrix} \begin{bmatrix} \dot{\mathbf{t}}_{\mathrm{j}} \\ \dot{\boldsymbol{\theta}}_{\mathrm{j}} \end{bmatrix} = \mathbf{0}$$

$$\mathbf{C}_{\mathbf{q}_{\mathrm{Ji}}} = \begin{bmatrix} -\mathbf{I} & \mathbf{R}_{\mathrm{i}}\tilde{\tilde{\mathbf{u}}}_{\mathrm{Ji}}\overline{\mathbf{G}}_{\mathrm{i}} \\ \mathbf{0} & -\hat{\mathbf{v}}_{\mathrm{J}}^{\mathrm{T}}\mathbf{R}_{\mathrm{j}}^{\mathrm{T}}\mathbf{R}_{\mathrm{i}}\tilde{\mathbf{u}}_{\mathrm{J}}\overline{\mathbf{G}}_{\mathrm{i}} \\ \mathbf{0} & -\hat{\mathbf{v}}_{\mathrm{J}}^{\mathrm{T}}\mathbf{R}_{\mathrm{j}}^{\mathrm{T}}\mathbf{R}_{\mathrm{i}}\tilde{\mathbf{w}}_{\mathrm{J}}\overline{\mathbf{G}}_{\mathrm{i}} \end{bmatrix} \quad \mathbf{C}_{\mathbf{q}_{\mathrm{Jj}}} = \begin{bmatrix} \mathbf{I} & -\mathbf{R}_{\mathrm{j}}\tilde{\tilde{\mathbf{u}}}_{\mathrm{Jj}}\overline{\mathbf{G}}_{\mathrm{j}} \\ \mathbf{0} & -\hat{\mathbf{u}}_{\mathrm{J}}^{\mathrm{T}}\mathbf{R}_{\mathrm{i}}^{\mathrm{T}}\mathbf{R}_{\mathrm{j}}\tilde{\mathbf{v}}_{\mathrm{J}}\overline{\mathbf{G}}_{\mathrm{j}} \\ \mathbf{0} & -\hat{\mathbf{w}}_{\mathrm{J}}^{\mathrm{T}}\mathbf{R}_{\mathrm{i}}^{\mathrm{T}}\mathbf{R}_{\mathrm{j}}\tilde{\mathbf{v}}_{\mathrm{J}}\overline{\mathbf{G}}_{\mathrm{j}} \end{bmatrix} \tag{40}$$

$$\mathbf{C}_{\mathbf{d}_{\mathrm{J}}} = \mathbf{0}$$

A further time differentiation in (41) leads to the acceleration problem contributions.

$$\dot{\mathbf{C}}_{\mathbf{q}_{\mathrm{Ji}}} = \begin{bmatrix} \mathbf{0} & \tilde{\boldsymbol{\omega}}_{\mathrm{i}}\mathbf{R}_{\mathrm{i}}\tilde{\tilde{\mathbf{u}}}_{\mathrm{Ji}}\overline{\mathbf{G}}_{\mathrm{i}} + \mathbf{R}_{\mathrm{i}}\tilde{\tilde{\mathbf{u}}}_{\mathrm{Ji}}\dot{\overline{\mathbf{G}}}_{\mathrm{i}} \\ \mathbf{0} & \hat{\mathbf{v}}_{\mathrm{J}}^{\mathrm{T}}\mathbf{R}_{\mathrm{j}}^{\mathrm{T}}\left(\tilde{\boldsymbol{\omega}}_{\mathrm{j}} - \tilde{\boldsymbol{\omega}}_{\mathrm{i}}\right)\mathbf{R}_{\mathrm{i}}\tilde{\mathbf{u}}_{\mathrm{J}}\overline{\mathbf{G}}_{\mathrm{i}} - \hat{\mathbf{v}}_{\mathrm{J}}^{\mathrm{T}}\mathbf{R}_{\mathrm{j}}^{\mathrm{T}}\mathbf{R}_{\mathrm{i}}\tilde{\mathbf{u}}_{\mathrm{J}}\dot{\overline{\mathbf{G}}}_{\mathrm{i}} \\ \mathbf{0} & \hat{\mathbf{v}}_{\mathrm{J}}^{\mathrm{T}}\mathbf{R}_{\mathrm{j}}^{\mathrm{T}}\left(\tilde{\boldsymbol{\omega}}_{\mathrm{j}} - \tilde{\boldsymbol{\omega}}_{\mathrm{i}}\right)\mathbf{R}_{\mathrm{i}}\tilde{\mathbf{w}}_{\mathrm{J}}\overline{\mathbf{G}}_{\mathrm{i}} - \hat{\mathbf{v}}_{\mathrm{J}}^{\mathrm{T}}\mathbf{R}_{\mathrm{j}}^{\mathrm{T}}\mathbf{R}_{\mathrm{i}}\tilde{\mathbf{w}}_{\mathrm{J}}\dot{\overline{\mathbf{G}}}_{\mathrm{i}} \end{bmatrix}$$

$$\dot{\mathbf{C}}_{\mathbf{q}_{\mathrm{Jj}}} = \begin{bmatrix} \mathbf{0} & -\tilde{\boldsymbol{\omega}}_{\mathrm{j}}\mathbf{R}_{\mathrm{j}}\tilde{\tilde{\mathbf{u}}}_{\mathrm{Jj}}\overline{\mathbf{G}}_{\mathrm{j}} - \mathbf{R}_{\mathrm{j}}\tilde{\tilde{\mathbf{u}}}_{\mathrm{Jj}}\dot{\overline{\mathbf{G}}}_{\mathrm{j}} \\ \mathbf{0} & -\hat{\mathbf{u}}_{\mathrm{J}}^{\mathrm{T}}\mathbf{R}_{\mathrm{i}}^{\mathrm{T}}\left(\tilde{\boldsymbol{\omega}}_{\mathrm{j}} - \tilde{\boldsymbol{\omega}}_{\mathrm{i}}\right)\mathbf{R}_{\mathrm{j}}\tilde{\mathbf{v}}_{\mathrm{J}}\overline{\mathbf{G}}_{\mathrm{j}} - \hat{\mathbf{u}}_{\mathrm{J}}^{\mathrm{T}}\mathbf{R}_{\mathrm{i}}^{\mathrm{T}}\mathbf{R}_{\mathrm{j}}\tilde{\mathbf{v}}_{\mathrm{J}}\dot{\overline{\mathbf{G}}}_{\mathrm{j}} \\ \mathbf{0} & -\hat{\mathbf{w}}_{\mathrm{J}}^{\mathrm{T}}\mathbf{R}_{\mathrm{i}}^{\mathrm{T}}\left(\tilde{\boldsymbol{\omega}}_{\mathrm{j}} - \tilde{\boldsymbol{\omega}}_{\mathrm{i}}\right)\mathbf{R}_{\mathrm{j}}\tilde{\mathbf{v}}_{\mathrm{J}}\overline{\mathbf{G}}_{\mathrm{j}} - \hat{\mathbf{w}}_{\mathrm{J}}^{\mathrm{T}}\mathbf{R}_{\mathrm{i}}^{\mathrm{T}}\mathbf{R}_{\mathrm{j}}\tilde{\mathbf{v}}_{\mathrm{J}}\dot{\overline{\mathbf{G}}}_{\mathrm{j}} \end{bmatrix} \tag{41}$$

$$\dot{\mathbf{C}}_{\mathbf{d}_{\mathrm{J}}} = \mathbf{0}$$

Let move to the mobility equation time differentiation. Recalling the time derivative of the angle operator, let identify in (42) the relative quaternion derivative with respect to its angle with $\boldsymbol{\theta}_{\Theta_{\mathrm{J}}}$.

$$\dot{\mathbf{D}}_{\mathrm{J}} = 4\boldsymbol{\theta}_{\Theta_{\mathrm{J}}}^{\mathrm{T}}\left(\dot{\mathbf{H}}_{\mathrm{i}}^{\mathrm{T}}\boldsymbol{\theta}_{\mathrm{j}} + \mathbf{H}_{\mathrm{i}}^{\mathrm{T}}\dot{\boldsymbol{\theta}}_{\mathrm{j}}\right) - \dot{\Theta}_{\mathrm{J}} = \mathbf{0} \tag{42}$$

While the linear combination with respect to $\dot{\boldsymbol{\theta}}_{\mathrm{j}}$ is evident, let focus on the first term in order to make explicit the linear combination with respect to $\dot{\boldsymbol{\theta}}_{\mathrm{i}}$ hidden within the $\dot{\mathbf{H}}_{\mathrm{i}}$ matrix: let develop in (43) the related product and rearrange.

$$\dot{\mathbf{H}}_{\mathrm{i}}^{\mathrm{T}}\boldsymbol{\theta}_{\mathrm{j}} = \begin{bmatrix} \dot{\theta}_{\mathrm{Re_i}} & \dot{\boldsymbol{\theta}}_{\mathrm{Im_i}}^{\mathrm{T}} \\ -\dot{\boldsymbol{\theta}}_{\mathrm{Im_i}} & \dot{\theta}_{\mathrm{Re_i}}\mathbf{I} - \tilde{\dot{\boldsymbol{\theta}}}_{\mathrm{Im_i}} \end{bmatrix} \begin{bmatrix} \theta_{\mathrm{Re_j}} \\ \boldsymbol{\theta}_{\mathrm{Im_j}} \end{bmatrix} \tag{43}$$

$$\dot{\mathbf{H}}_{\mathrm{i}}^{\mathrm{T}}\boldsymbol{\theta}_{\mathrm{j}} = \begin{bmatrix} \theta_{\mathrm{Re_j}} & -\boldsymbol{\theta}_{\mathrm{Im_j}}^{\mathrm{T}} \\ \boldsymbol{\theta}_{\mathrm{Im_j}} & \theta_{\mathrm{Re_j}}\mathbf{I} - \widetilde{\boldsymbol{\theta}}_{\mathrm{Im_j}} \end{bmatrix} \begin{bmatrix} \dot{\theta}_{\mathrm{Re_i}} \\ -\dot{\boldsymbol{\theta}}_{\mathrm{Im_i}} \end{bmatrix} = \overline{\mathbf{H}}_{\mathrm{j}}\dot{\overline{\boldsymbol{\theta}}}_{\mathrm{i}}$$

Let recall the quaternion conjugation matrix and let highlight in (44) the linear combinations with respect the Lagrangian and the DoF velocities.

$$\begin{gathered} \dot{\mathbf{D}}_{\mathrm{J}} = 4\boldsymbol{\theta}_{\Theta_{\mathrm{J}}}^{\mathrm{T}}\left(\overline{\mathbf{H}}_{\mathrm{j}}\overline{\mathbf{C}}\dot{\boldsymbol{\theta}}_{\mathrm{i}} + \mathbf{H}_{\mathrm{i}}^{\mathrm{T}}\dot{\boldsymbol{\theta}}_{\mathrm{j}}\right) - \dot{\Theta}_{\mathrm{J}} = \mathbf{0} \\ \begin{bmatrix} \mathbf{0} & 4\boldsymbol{\theta}_{\Theta_{\mathrm{J}}}^{\mathrm{T}}\overline{\mathbf{H}}_{\mathrm{j}}\overline{\mathbf{C}} \end{bmatrix} \begin{bmatrix} \dot{\mathbf{t}}_{\mathrm{i}} \\ \dot{\boldsymbol{\theta}}_{\mathrm{i}} \end{bmatrix} + \begin{bmatrix} \mathbf{0} & 4\boldsymbol{\theta}_{\Theta_{\mathrm{J}}}^{\mathrm{T}}\mathbf{H}_{\mathrm{i}}^{\mathrm{T}} \end{bmatrix} \begin{bmatrix} \dot{\mathbf{t}}_{\mathrm{j}} \\ \dot{\boldsymbol{\theta}}_{\mathrm{j}} \end{bmatrix} + [-1][\dot{\Theta}_{\mathrm{J}}] = \mathbf{0} \\ \mathbf{D}_{\mathbf{q}_{\mathrm{Ji}}} = \begin{bmatrix} \mathbf{0} & 4\boldsymbol{\theta}_{\Theta_{\mathrm{J}}}^{\mathrm{T}}\overline{\mathbf{H}}_{\mathrm{j}}\overline{\mathbf{C}} \end{bmatrix} \quad \mathbf{D}_{\mathbf{q}_{\mathrm{Jj}}} = \begin{bmatrix} \mathbf{0} & 4\boldsymbol{\theta}_{\Theta_{\mathrm{J}}}^{\mathrm{T}}\mathbf{H}_{\mathrm{i}}^{\mathrm{T}} \end{bmatrix} \quad \mathbf{D}_{\mathbf{d}_{\mathrm{J}}} = [-1] \end{gathered} \tag{44}$$

The acceleration problem contributions are found in (45) by a further time differentiation, finalizing the revolute joint equations characterization.

$$\begin{gathered} \dot{\mathbf{D}}_{\mathbf{q}_{\mathrm{Ji}}} = \left[\mathbf{0} \quad 4\left(\dot{\boldsymbol{\theta}}_{\Theta_{\mathrm{J}}}^{\mathrm{T}}\overline{\mathbf{H}}_{\mathrm{j}} + \boldsymbol{\theta}_{\Theta_{\mathrm{J}}}^{\mathrm{T}}\dot{\overline{\mathbf{H}}}_{\mathrm{j}}\right)\overline{\mathbf{C}}\right] \\ \dot{\mathbf{D}}_{\mathbf{q}_{\mathrm{Jj}}} = \left[\mathbf{0} \quad 4\left(\dot{\boldsymbol{\theta}}_{\Theta_{\mathrm{J}}}^{\mathrm{T}}\mathbf{H}_{\mathrm{i}}^{\mathrm{T}} + \boldsymbol{\theta}_{\Theta_{\mathrm{J}}}^{\mathrm{T}}\dot{\mathbf{H}}_{\mathrm{i}}^{\mathrm{T}}\right)\right] \\ \dot{\mathbf{D}}_{\mathbf{d}_{\mathrm{J}}} = [0] \end{gathered} \tag{45}$$

1.3.2. Cam joint

Let move to the cam joint case reported in the Figure 17: in this work it can be modelled as a revolute joint that allows a single DoF, i.e., the relative rotation Θ_{J} around the joint axis $\hat{\mathbf{v}}_{\mathrm{J}}$ between the linked bodies i and j, while, in addition, it permits a relative translation $\mathbf{t}_{\mathrm{J}}$ in a plane (generally orthogonal to $\hat{\mathbf{v}}_{\mathrm{J}}$) identified by two unit vectors $\hat{\mathbf{a}}_{\mathrm{J}}$ and $\hat{\mathbf{b}}_{\mathrm{J}}$ along which the components of the joint location in the parent body frame $\overline{\mathbf{u}}_{\mathrm{Ji}}$ are known functions of the DoF Θ_{J}, i.e., $\mathrm{a_J}(\Theta_{\mathrm{J}})$ and $\mathrm{b_J}(\Theta_{\mathrm{J}})$, (eq. (46)).

$$\overline{\mathbf{u}}_{\mathrm{Ji}}(\Theta_{\mathrm{J}}) = \mathrm{a_J}(\Theta_{\mathrm{J}})\hat{\mathbf{a}}_{\mathrm{J}} + \mathrm{b_J}(\Theta_{\mathrm{J}})\hat{\mathbf{b}}_{\mathrm{J}} = \begin{bmatrix} \hat{\mathbf{a}}_{\mathrm{J}} & \hat{\mathbf{b}}_{\mathrm{J}} \end{bmatrix} \begin{bmatrix} \mathrm{a_J}(\Theta_{\mathrm{J}}) \\ \mathrm{b_J}(\Theta_{\mathrm{J}}) \end{bmatrix} = \mathbf{U}_{\mathrm{J}}\mathbf{t}_{\mathrm{J}}(\Theta_{\mathrm{J}}) \tag{46}$$

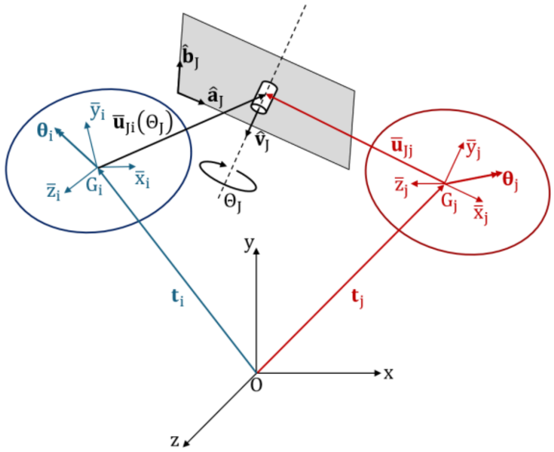

Figure 17 *Cam joint scheme*

While the constraint equations referred to the suppressed rotations and the mobility equation are the same of the revolute joint case (and so their time derivatives), the cam joint constraint equations related to the suppressed translations have a similar form but they are affected by the joint parent-location $\bar{\mathbf{u}}_{Ji}$ dependence on the joint DoF Θ_J (eq. (47)).

$$\mathbf{d}_J = [\Theta_J] \qquad \mathbf{C}_J(\mathbf{q}_i, \mathbf{q}_j, \mathbf{d}_J) = \begin{bmatrix} \mathbf{t}_j + \mathbf{R}_j\bar{\mathbf{u}}_{Jj} - \mathbf{t}_i - \mathbf{R}_i\mathbf{U}_J\mathbf{t}_J(\Theta_J) \\ \hat{\mathbf{v}}_J^T\mathbf{R}_j^T\mathbf{R}_i\hat{\mathbf{u}}_J \\ \hat{\mathbf{v}}_J^T\mathbf{R}_j^T\mathbf{R}_i\hat{\mathbf{w}}_J \end{bmatrix} = \mathbf{0} \tag{47}$$
$$\mathbf{D}_J(\mathbf{q}_i, \mathbf{q}_j, \mathbf{d}_J) = \langle \mathbf{H}_i^T\boldsymbol{\theta}_j \rangle - \Theta_J = \mathbf{0}$$

The time derivative of the cam joint translational constraint equations is given in (48) by the knowledge of the functions $a_J(\Theta_J)$ and $b_J(\Theta_J)$ derivatives with respect to the angle Θ_J, collected in the vector $\mathbf{t}_{J_\Theta}$.

$$\dot{\mathbf{t}}_j - \mathbf{R}_j\tilde{\bar{\mathbf{u}}}_{Jj}\bar{\mathbf{G}}_j\dot{\boldsymbol{\theta}}_j - \dot{\mathbf{t}}_i + \mathbf{R}_i\tilde{\bar{\mathbf{u}}}_{Ji}\bar{\mathbf{G}}_i\dot{\boldsymbol{\theta}}_i - \mathbf{R}_i\mathbf{U}_J\mathbf{t}_{J_\Theta}\dot{\Theta}_J = \mathbf{0}$$
$$\mathbf{C}_{\mathbf{q}_{Ji}} = \begin{bmatrix} -\mathbf{I} & \mathbf{R}_i\tilde{\bar{\mathbf{u}}}_{Ji}\bar{\mathbf{G}}_i \\ \mathbf{0} & -\hat{\mathbf{v}}_J^T\mathbf{R}_j^T\mathbf{R}_i\tilde{\mathbf{u}}_J\bar{\mathbf{G}}_i \\ \mathbf{0} & -\hat{\mathbf{v}}_J^T\mathbf{R}_j^T\mathbf{R}_i\tilde{\mathbf{w}}_J\bar{\mathbf{G}}_i \end{bmatrix} \quad \mathbf{C}_{\mathbf{q}_{Jj}} = \begin{bmatrix} \mathbf{I} & -\mathbf{R}_j\tilde{\bar{\mathbf{u}}}_{Jj}\bar{\mathbf{G}}_j \\ \mathbf{0} & -\hat{\mathbf{u}}_J^T\mathbf{R}_i^T\mathbf{R}_j\tilde{\mathbf{v}}_J\bar{\mathbf{G}}_j \\ \mathbf{0} & -\hat{\mathbf{w}}_J^T\mathbf{R}_i^T\mathbf{R}_j\tilde{\mathbf{v}}_J\bar{\mathbf{G}}_j \end{bmatrix} \tag{48}$$
$$\mathbf{C}_{\mathbf{d}_J} = \left[-\mathbf{R}_i\mathbf{U}_J\mathbf{t}_{J_\Theta}\right]$$

The time derivative of the above matrices is provided in (49), introducing also the second derivative of $\mathbf{t}_J$ with respect to Θ_J, i.e., $\mathbf{t}_{J_{\Theta\Theta}}$.

$$\dot{\mathbf{C}}_{\mathbf{q}_{Ji}} = \begin{bmatrix} \mathbf{0} & \mathbf{R}_i\left(\dot{\tilde{\bar{\mathbf{u}}}}_{Ji} + \tilde{\boldsymbol{\omega}}_i\tilde{\bar{\mathbf{u}}}_{Ji}\right)\bar{\mathbf{G}}_i + \mathbf{R}_i\tilde{\bar{\mathbf{u}}}_{Ji}\dot{\bar{\mathbf{G}}}_i \\ \mathbf{0} & \hat{\mathbf{v}}_J^T\mathbf{R}_j^T(\tilde{\boldsymbol{\omega}}_j - \tilde{\boldsymbol{\omega}}_i)\mathbf{R}_i\tilde{\mathbf{u}}_J\bar{\mathbf{G}}_i - \hat{\mathbf{v}}_J^T\mathbf{R}_j^T\mathbf{R}_i\tilde{\mathbf{u}}_J\dot{\bar{\mathbf{G}}}_i \\ \mathbf{0} & \hat{\mathbf{v}}_J^T\mathbf{R}_j^T(\tilde{\boldsymbol{\omega}}_j - \tilde{\boldsymbol{\omega}}_i)\mathbf{R}_i\tilde{\mathbf{w}}_J\bar{\mathbf{G}}_i - \hat{\mathbf{v}}_J^T\mathbf{R}_j^T\mathbf{R}_i\tilde{\mathbf{w}}_J\dot{\bar{\mathbf{G}}}_i \end{bmatrix} \tag{49}$$

$$\dot{\mathbf{C}}_{\mathbf{q}_{Jj}} = \begin{bmatrix} \mathbf{0} & -\widetilde{\boldsymbol{\omega}}_j \mathbf{R}_j \widetilde{\overline{\mathbf{u}}}_{Jj} \overline{\mathbf{G}}_j - \mathbf{R}_j \widetilde{\overline{\mathbf{u}}}_{Jj} \dot{\overline{\mathbf{G}}}_j \\ \mathbf{0} & -\hat{\mathbf{u}}_J^T \mathbf{R}_i^T (\widetilde{\boldsymbol{\omega}}_j - \widetilde{\boldsymbol{\omega}}_i) \mathbf{R}_j \tilde{\mathbf{v}}_J \overline{\mathbf{G}}_j - \hat{\mathbf{u}}_J^T \mathbf{R}_i^T \mathbf{R}_j \tilde{\mathbf{v}}_J \dot{\overline{\mathbf{G}}}_j \\ \mathbf{0} & -\widehat{\mathbf{w}}_J^T \mathbf{R}_i^T (\widetilde{\boldsymbol{\omega}}_j - \widetilde{\boldsymbol{\omega}}_i) \mathbf{R}_j \tilde{\mathbf{v}}_J \overline{\mathbf{G}}_j - \widehat{\mathbf{w}}_J^T \mathbf{R}_i^T \mathbf{R}_j \tilde{\mathbf{v}}_J \dot{\overline{\mathbf{G}}}_j \end{bmatrix}$$

$$\dot{\mathbf{C}}_{\mathbf{d}_J} = \left[-\widetilde{\boldsymbol{\omega}}_i \mathbf{R}_i \mathbf{U}_J \mathbf{t}_{J_\Theta} - \mathbf{R}_i \mathbf{U}_J \mathbf{t}_{J_{\Theta\Theta}} \dot{\Theta}_J \right]$$

1.3.3. Spherical joint

The spherical joint, reported in the Figure 18, is a 3 DoF joint that allows a free relative orientation between the linked bodies i and j: the relative transformation can be described by 3 successive rotations α_J, β_J and γ_J around 3 axes oriented as the unit vectors, respectively, $\hat{\mathbf{u}}_J$, $\hat{\mathbf{v}}_J$ and $\widehat{\mathbf{w}}_J$ (eq. (50)). Since there is no relative translation, the spherical joint constraint equations (and so their time derivatives) are the same of the revolute joint case at the translation level, while it needs to impose 3 mobility equations: the writing of the mobility equations starts from the evaluation of the child body orientation $\boldsymbol{\theta}_j$ accounting for all the relative rotations (identified by the intermediary quaternions $\boldsymbol{\alpha}$, $\boldsymbol{\beta}$ and $\boldsymbol{\gamma}$) beginning with the parent body orientation $\boldsymbol{\theta}_i$.

$$\begin{aligned} \boldsymbol{\alpha} &= \boldsymbol{\theta}(\hat{\mathbf{u}}_J, \alpha_J) \\ \boldsymbol{\beta} &= \boldsymbol{\theta}(\hat{\mathbf{v}}_J, \beta_J) \quad \rightarrow \quad \boldsymbol{\theta}_j = \mathbf{H}_i \mathbf{H}_\alpha \mathbf{H}_\beta \boldsymbol{\gamma} \\ \boldsymbol{\gamma} &= \boldsymbol{\theta}(\widehat{\mathbf{w}}_J, \gamma_J) \end{aligned} \tag{50}$$

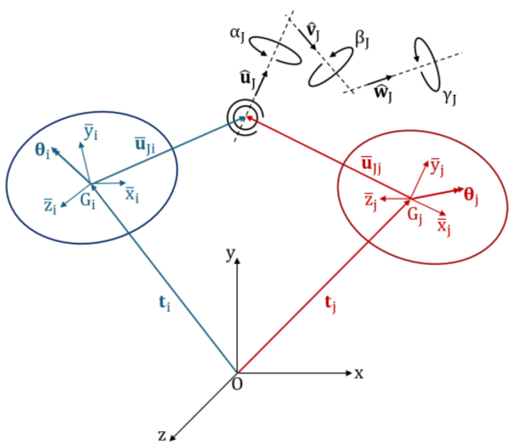

Figure 18 *Spherical joint scheme*

The objective is to exploit the angle operator as for the revolute joint case, so it is necessary to manipulate the relative Hamiltonian matrices to isolate in

(51) the 3 relative quaternions referred to the 3 spherical joint DoF (the auxiliary quaternion $\boldsymbol{\delta}$ is introduced).

$$\boldsymbol{\delta} = \mathbf{H}_\beta \boldsymbol{\gamma} \;\; \rightarrow \;\; \begin{aligned} \boldsymbol{\alpha} &= \overline{\mathbf{H}}_\delta^T \mathbf{H}_i^T \boldsymbol{\theta}_j \\ \boldsymbol{\beta} &= \overline{\mathbf{H}}_\gamma^T \mathbf{H}_\alpha^T \mathbf{H}_i^T \boldsymbol{\theta}_j \\ \boldsymbol{\gamma} &= \mathbf{H}_\beta^T \mathbf{H}_\alpha^T \mathbf{H}_i^T \boldsymbol{\theta}_j \end{aligned} \tag{51}$$

Then, the spherical joint equations are reported in (52).

$$\mathbf{d}_J = \begin{bmatrix} \alpha_J \\ \beta_J \\ \gamma_J \end{bmatrix} \qquad \begin{aligned} \mathbf{C}_J(\mathbf{q}_i, \mathbf{q}_j, \mathbf{d}_J) &= \mathbf{t}_j + \mathbf{R}_j \bar{\mathbf{u}}_{Jj} - \mathbf{t}_i - \mathbf{R}_i \bar{\mathbf{u}}_{Ji} = \mathbf{0} \\ \mathbf{D}_J(\mathbf{q}_i, \mathbf{q}_j, \mathbf{d}_J) &= \begin{bmatrix} \langle \overline{\mathbf{H}}_\delta^T \mathbf{H}_i^T \boldsymbol{\theta}_j \rangle - \alpha_J \\ \langle \overline{\mathbf{H}}_\gamma^T \mathbf{H}_\alpha^T \mathbf{H}_i^T \boldsymbol{\theta}_j \rangle - \beta_J \\ \langle \mathbf{H}_\beta^T \mathbf{H}_\alpha^T \mathbf{H}_i^T \boldsymbol{\theta}_j \rangle - \gamma_J \end{bmatrix} = \mathbf{0} \end{aligned} \tag{52}$$

Let develop the time derivative of the spherical joint mobility equations in (53).

$$\dot{\mathbf{D}}_J = \cdots$$

$$\begin{bmatrix} 4\boldsymbol{\alpha}_{\alpha_J}^T \left(\dot{\overline{\mathbf{H}}}_\delta^T \mathbf{H}_i^T \boldsymbol{\theta}_j + \overline{\mathbf{H}}_\delta^T \dot{\mathbf{H}}_i^T \boldsymbol{\theta}_j + \overline{\mathbf{H}}_\delta^T \mathbf{H}_i^T \dot{\boldsymbol{\theta}}_j \right) - \dot{\alpha}_J \\ 4\boldsymbol{\beta}_{\beta_J}^T \left[\left(\dot{\overline{\mathbf{H}}}_\gamma^T \mathbf{H}_\alpha^T + \overline{\mathbf{H}}_\gamma^T \dot{\mathbf{H}}_\alpha^T \right) \mathbf{H}_i^T \boldsymbol{\theta}_j + \overline{\mathbf{H}}_\gamma^T \mathbf{H}_\alpha^T \left(\dot{\mathbf{H}}_i^T \boldsymbol{\theta}_j + \mathbf{H}_i^T \dot{\boldsymbol{\theta}}_j \right) \right] - \dot{\beta}_J \\ 4\boldsymbol{\gamma}_{\gamma_J}^T \left[\left(\dot{\mathbf{H}}_\beta^T \mathbf{H}_\alpha^T + \mathbf{H}_\beta^T \dot{\mathbf{H}}_\alpha^T \right) \mathbf{H}_i^T \boldsymbol{\theta}_j + \mathbf{H}_\beta^T \mathbf{H}_\alpha^T \left(\dot{\mathbf{H}}_i^T \boldsymbol{\theta}_j + \mathbf{H}_i^T \dot{\boldsymbol{\theta}}_j \right) \right] - \dot{\gamma}_J \end{bmatrix} = \mathbf{0} \tag{53}$$

While it is known how to make explicit the linear combination with respect to $\dot{\boldsymbol{\theta}}_i$ starting from $\dot{\mathbf{H}}_i$, is necessary to extract also the DoF velocities $\dot{\mathbf{d}}_J$ to compose the matrix $\mathbf{D}_{\mathbf{d}_J}$. The Hamiltonian matrix $\mathbf{H}$ is a linear operator applied to a quaternion $\boldsymbol{\theta}$: its time derivative is then the matrix $\mathbf{H}$ applied to the quaternion time derivative $\dot{\boldsymbol{\theta}}$; furthermore, the quaternion time derivative is proportional to the quaternion angle velocity $\dot{\Theta}$ through a linear relation involving the quaternion variation with respect to its angle, i.e., $\boldsymbol{\theta}_\Theta$; as a consequence, the linearity of the Hamiltonian operator allows to write $\dot{\mathbf{H}}$ in (54) as the product between the matrix $\mathbf{H}$ applied to $\boldsymbol{\theta}_\Theta$ and the angle velocity $\dot{\Theta}$, where the former is indicated as the matrix $\mathbf{h}$.

$$\begin{cases} \dot{\mathbf{H}} = \mathbf{H}(\dot{\boldsymbol{\theta}}) \\ \dot{\boldsymbol{\theta}} = \boldsymbol{\theta}_\Theta \dot{\boldsymbol{\Theta}} \end{cases} \rightarrow \quad \dot{\mathbf{H}} = \mathbf{H}(\boldsymbol{\theta}_\Theta \dot{\Theta}) = \mathbf{H}(\boldsymbol{\theta}_\Theta) \dot{\boldsymbol{\Theta}} = \mathbf{h} \dot{\Theta} \tag{54}$$

Particular attention has to be paid to the $\dot{\overline{\mathbf{H}}}_\delta$ term in (55), which leads to the definition of the auxiliary matrices $\bar{\mathbf{h}}_{\delta\beta}$ and $\bar{\mathbf{h}}_{\delta\gamma}$.

$$\begin{cases} \dot{\overline{\mathbf{H}}}_\delta = \overline{\mathbf{H}}(\dot{\boldsymbol{\delta}}) \\ \boldsymbol{\delta} = \mathbf{H}_\beta \boldsymbol{\gamma} \end{cases} \rightarrow \quad \begin{aligned} &\dot{\overline{\mathbf{H}}}_\delta = \overline{\mathbf{H}}(\mathbf{h}_\beta \boldsymbol{\gamma}) \dot{\beta}_J + \overline{\mathbf{H}}\left(\mathbf{H}_\beta \boldsymbol{\gamma}_{\gamma_J}\right) \dot{\gamma}_J \\ &\bar{\mathbf{h}}_{\delta\beta} = \overline{\mathbf{H}}(\mathbf{h}_\beta \boldsymbol{\gamma}) \quad \bar{\mathbf{h}}_{\delta\gamma} = \overline{\mathbf{H}}\left(\mathbf{H}_\beta \boldsymbol{\gamma}_{\gamma_J}\right) \end{aligned} \tag{55}$$

The above properties allow to make evident the spherical joint mobility equations linear dependencies with respect to the DoF velocities $\dot{\mathbf{d}}_J$ and so to constitute in (56) their contribution to the velocity problem.

$$
\begin{gathered}
\mathbf{D}_{\mathbf{q}_{\mathrm{Ji}}} = \begin{bmatrix} \mathbf{0}^{\mathrm{T}} & 4\boldsymbol{\alpha}_{\alpha_{\mathrm{J}}}^{\mathrm{T}}\bar{\mathbf{H}}_{\delta}^{\mathrm{T}}\bar{\mathbf{H}}_{\mathrm{j}}\bar{\mathbf{C}} \\ \mathbf{0}^{\mathrm{T}} & 4\boldsymbol{\beta}_{\beta_{\mathrm{J}}}^{\mathrm{T}}\bar{\mathbf{H}}_{\gamma}^{\mathrm{T}}\mathbf{H}_{\alpha}^{\mathrm{T}}\bar{\mathbf{H}}_{\mathrm{j}}\bar{\mathbf{C}} \\ \mathbf{0}^{\mathrm{T}} & 4\boldsymbol{\gamma}_{\gamma_{\mathrm{J}}}^{\mathrm{T}}\mathbf{H}_{\beta}^{\mathrm{T}}\mathbf{H}_{\alpha}^{\mathrm{T}}\bar{\mathbf{H}}_{\mathrm{j}}\bar{\mathbf{C}} \end{bmatrix} \quad \mathbf{D}_{\mathbf{q}_{\mathrm{Jj}}} = \begin{bmatrix} \mathbf{0}^{\mathrm{T}} & 4\boldsymbol{\alpha}_{\alpha_{\mathrm{J}}}^{\mathrm{T}}\bar{\mathbf{H}}_{\delta}^{\mathrm{T}}\mathbf{H}_{\mathrm{i}}^{\mathrm{T}} \\ \mathbf{0}^{\mathrm{T}} & 4\boldsymbol{\beta}_{\beta_{\mathrm{J}}}^{\mathrm{T}}\bar{\mathbf{H}}_{\gamma}^{\mathrm{T}}\mathbf{H}_{\alpha}^{\mathrm{T}}\mathbf{H}_{\mathrm{i}}^{\mathrm{T}} \\ \mathbf{0}^{\mathrm{T}} & 4\boldsymbol{\gamma}_{\gamma_{\mathrm{J}}}^{\mathrm{T}}\mathbf{H}_{\beta}^{\mathrm{T}}\mathbf{H}_{\alpha}^{\mathrm{T}}\mathbf{H}_{\mathrm{i}}^{\mathrm{T}} \end{bmatrix} \\
\mathbf{D}_{\mathbf{d}_{\mathrm{J}}} = \begin{bmatrix} -1 & 4\boldsymbol{\alpha}_{\alpha_{\mathrm{J}}}^{\mathrm{T}}\bar{\mathbf{h}}_{\delta\beta}^{\mathrm{T}}\mathbf{H}_{\mathrm{i}}^{\mathrm{T}}\boldsymbol{\theta}_{\mathrm{j}} & 4\boldsymbol{\alpha}_{\alpha_{\mathrm{J}}}^{\mathrm{T}}\bar{\mathbf{h}}_{\delta\gamma}^{\mathrm{T}}\mathbf{H}_{\mathrm{i}}^{\mathrm{T}}\boldsymbol{\theta}_{\mathrm{j}} \\ 4\boldsymbol{\beta}_{\beta_{\mathrm{J}}}^{\mathrm{T}}\bar{\mathbf{H}}_{\gamma}^{\mathrm{T}}\mathbf{h}_{\alpha}^{\mathrm{T}}\mathbf{H}_{\mathrm{i}}^{\mathrm{T}}\boldsymbol{\theta}_{\mathrm{j}} & -1 & 4\boldsymbol{\beta}_{\beta_{\mathrm{J}}}^{\mathrm{T}}\bar{\mathbf{h}}_{\gamma}^{\mathrm{T}}\mathbf{H}_{\alpha}^{\mathrm{T}}\mathbf{H}_{\mathrm{i}}^{\mathrm{T}}\boldsymbol{\theta}_{\mathrm{j}} \\ 4\boldsymbol{\gamma}_{\gamma_{\mathrm{J}}}^{\mathrm{T}}\mathbf{H}_{\beta}^{\mathrm{T}}\mathbf{h}_{\alpha}^{\mathrm{T}}\mathbf{H}_{\mathrm{i}}^{\mathrm{T}}\boldsymbol{\theta}_{\mathrm{j}} & 4\boldsymbol{\gamma}_{\gamma_{\mathrm{J}}}^{\mathrm{T}}\mathbf{h}_{\beta}^{\mathrm{T}}\mathbf{H}_{\alpha}^{\mathrm{T}}\mathbf{H}_{\mathrm{i}}^{\mathrm{T}}\boldsymbol{\theta}_{\mathrm{j}} & -1 \end{bmatrix}
\end{gathered}
\tag{56}
$$

Finally, the spherical joint mobility equations contribution to the acceleration problem is given in (57) by the last time differentiation; the product rule applied to the following are left to the reader for the ease of the writing.

$$
\begin{gathered}
\dot{\mathbf{D}}_{\mathbf{q}_{\mathrm{Ji}}} = \begin{bmatrix} \mathbf{0}^{\mathrm{T}} & 4\,\dot{\left(\boldsymbol{\alpha}_{\alpha_{\mathrm{J}}}^{\mathrm{T}}\bar{\mathbf{H}}_{\delta}^{\mathrm{T}}\bar{\mathbf{H}}_{\mathrm{j}}\right)}\bar{\mathbf{C}} \\ \mathbf{0}^{\mathrm{T}} & 4\,\dot{\left(\boldsymbol{\beta}_{\beta_{\mathrm{J}}}^{\mathrm{T}}\bar{\mathbf{H}}_{\gamma}^{\mathrm{T}}\mathbf{H}_{\alpha}^{\mathrm{T}}\bar{\mathbf{H}}_{\mathrm{j}}\right)}\bar{\mathbf{C}} \\ \mathbf{0}^{\mathrm{T}} & 4\,\dot{\left(\boldsymbol{\gamma}_{\gamma_{\mathrm{J}}}^{\mathrm{T}}\mathbf{H}_{\beta}^{\mathrm{T}}\mathbf{H}_{\alpha}^{\mathrm{T}}\bar{\mathbf{H}}_{\mathrm{j}}\right)}\bar{\mathbf{C}} \end{bmatrix} \quad \dot{\mathbf{D}}_{\mathbf{q}_{\mathrm{Jj}}} = \begin{bmatrix} \mathbf{0}^{\mathrm{T}} & 4\,\dot{\left(\boldsymbol{\alpha}_{\alpha_{\mathrm{J}}}^{\mathrm{T}}\bar{\mathbf{H}}_{\delta}^{\mathrm{T}}\mathbf{H}_{\mathrm{i}}^{\mathrm{T}}\right)} \\ \mathbf{0}^{\mathrm{T}} & 4\,\dot{\left(\boldsymbol{\beta}_{\beta_{\mathrm{J}}}^{\mathrm{T}}\bar{\mathbf{H}}_{\gamma}^{\mathrm{T}}\mathbf{H}_{\alpha}^{\mathrm{T}}\mathbf{H}_{\mathrm{i}}^{\mathrm{T}}\right)} \\ \mathbf{0}^{\mathrm{T}} & 4\,\dot{\left(\boldsymbol{\gamma}_{\gamma_{\mathrm{J}}}^{\mathrm{T}}\mathbf{H}_{\beta}^{\mathrm{T}}\mathbf{H}_{\alpha}^{\mathrm{T}}\mathbf{H}_{\mathrm{i}}^{\mathrm{T}}\right)} \end{bmatrix} \\
\dot{\mathbf{D}}_{\mathbf{d}_{\mathrm{J}}} = 4\begin{bmatrix} 0 & \dot{\left(\boldsymbol{\alpha}_{\alpha_{\mathrm{J}}}^{\mathrm{T}}\bar{\mathbf{h}}_{\delta\beta}^{\mathrm{T}}\mathbf{H}_{\mathrm{i}}^{\mathrm{T}}\boldsymbol{\theta}_{\mathrm{j}}\right)} & \dot{\left(\boldsymbol{\alpha}_{\alpha_{\mathrm{J}}}^{\mathrm{T}}\bar{\mathbf{h}}_{\delta\gamma}^{\mathrm{T}}\mathbf{H}_{\mathrm{i}}^{\mathrm{T}}\boldsymbol{\theta}_{\mathrm{j}}\right)} \\ \dot{\left(\boldsymbol{\beta}_{\beta_{\mathrm{J}}}^{\mathrm{T}}\bar{\mathbf{H}}_{\gamma}^{\mathrm{T}}\mathbf{h}_{\alpha}^{\mathrm{T}}\mathbf{H}_{\mathrm{i}}^{\mathrm{T}}\boldsymbol{\theta}_{\mathrm{j}}\right)} & 0 & \dot{\left(\boldsymbol{\beta}_{\beta_{\mathrm{J}}}^{\mathrm{T}}\bar{\mathbf{h}}_{\gamma}^{\mathrm{T}}\mathbf{H}_{\alpha}^{\mathrm{T}}\mathbf{H}_{\mathrm{i}}^{\mathrm{T}}\boldsymbol{\theta}_{\mathrm{j}}\right)} \\ \dot{\left(\boldsymbol{\gamma}_{\gamma_{\mathrm{J}}}^{\mathrm{T}}\mathbf{H}_{\beta}^{\mathrm{T}}\mathbf{h}_{\alpha}^{\mathrm{T}}\mathbf{H}_{\mathrm{i}}^{\mathrm{T}}\boldsymbol{\theta}_{\mathrm{j}}\right)} & \dot{\left(\boldsymbol{\gamma}_{\gamma_{\mathrm{J}}}^{\mathrm{T}}\mathbf{h}_{\beta}^{\mathrm{T}}\mathbf{H}_{\alpha}^{\mathrm{T}}\mathbf{H}_{\mathrm{i}}^{\mathrm{T}}\boldsymbol{\theta}_{\mathrm{j}}\right)} & 0 \end{bmatrix}
\end{gathered}
\tag{57}
$$

1.3.4. Free joint

Lastly, the free joint, reported in the Figure 19, allows the full relative mobility between the linked bodies i and j, so it imposes no constraint equations and 6 mobility equations, of which the 3 rotational ones are the same of the spherical joint case; the relative translation $\mathbf{t}_{\mathrm{J}}$, identified by the DoF a_{J}, b_{J} and c_{J}, occurs along the 3 known unit vectors, respectively, $\hat{\mathbf{a}}_{\mathrm{J}}$, $\hat{\mathbf{b}}_{\mathrm{J}}$ and $\hat{\mathbf{c}}_{\mathrm{J}}$: the parent joint location $\bar{\mathbf{u}}_{\mathrm{Ji}}$ is going to be dependent on the translational DoF $\mathbf{t}_{\mathrm{J}}$ (eq. (58)).

$$
\bar{\mathbf{u}}_{\mathrm{Ji}} = \mathrm{a}_{\mathrm{J}}\hat{\mathbf{a}}_{\mathrm{J}} + \mathrm{b}_{\mathrm{J}}\hat{\mathbf{b}}_{\mathrm{J}} + \mathrm{c}_{\mathrm{J}}\hat{\mathbf{c}}_{\mathrm{J}} = \begin{bmatrix} \hat{\mathbf{a}}_{\mathrm{J}} & \hat{\mathbf{b}}_{\mathrm{J}} & \hat{\mathbf{c}}_{\mathrm{J}} \end{bmatrix} \begin{bmatrix} \mathrm{a}_{\mathrm{J}} \\ \mathrm{b}_{\mathrm{J}} \\ \mathrm{c}_{\mathrm{J}} \end{bmatrix} = \mathbf{U}_{\mathrm{J}}\mathbf{t}_{\mathrm{J}} \tag{58}
$$

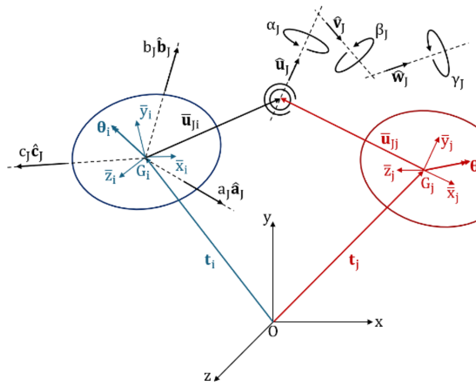

Figure 19 *Free joint scheme*

Then, the free joint mobility equations are written in (59).

$$\mathbf{t}_i + \mathbf{R}_i\mathbf{U}_J\mathbf{t}_J = \mathbf{t}_j + \mathbf{R}_j\bar{\mathbf{u}}_{Jj}$$

$$\mathbf{d}_J = \begin{bmatrix} \mathbf{t}_J \\ \alpha_J \\ \beta_J \\ \gamma_J \end{bmatrix} \quad \mathbf{D}_J(\mathbf{q}_i, \mathbf{q}_j, \mathbf{d}_J) = \begin{bmatrix} \mathbf{U}_J^{-1}\mathbf{R}_i^T(\mathbf{t}_j - \mathbf{t}_i + \mathbf{R}_j\bar{\mathbf{u}}_{Jj}) - \mathbf{t}_J \\ \langle \bar{\mathbf{H}}_\delta^T\mathbf{H}_i^T\boldsymbol{\theta}_j\rangle - \alpha_J \\ \langle \bar{\mathbf{H}}_\gamma^T\mathbf{H}_\alpha^T\mathbf{H}_i^T\boldsymbol{\theta}_j\rangle - \beta_J \\ \langle \mathbf{H}_\beta^T\mathbf{H}_\alpha^T\mathbf{H}_i^T\boldsymbol{\theta}_j\rangle - \gamma_J \end{bmatrix} = \mathbf{0} \tag{59}$$

The time derivative of the mobility equations leads in (60) to their contribution to the velocity problem matrices by introducing an auxiliary vector $\mathbf{u}_i$.

$$\mathbf{u}_i = \mathbf{t}_j - \mathbf{t}_i + \mathbf{R}_j\bar{\mathbf{u}}_{Jj}$$

$$\mathbf{D}_{\mathbf{q}_{Ji}} = \begin{bmatrix} -\mathbf{U}_J^{-1}\mathbf{R}_i^T & \mathbf{U}_J^{-1}\mathbf{R}_i^T\tilde{\mathbf{u}}_i\mathbf{G}_i \\ \mathbf{0}^T & 4\boldsymbol{\alpha}_{\alpha_J}^T\bar{\mathbf{H}}_\delta^T\bar{\mathbf{H}}_j\bar{\mathbf{C}} \\ \mathbf{0}^T & 4\boldsymbol{\beta}_{\beta_J}^T\bar{\mathbf{H}}_\gamma^T\mathbf{H}_\alpha^T\bar{\mathbf{H}}_j\bar{\mathbf{C}} \\ \mathbf{0}^T & 4\boldsymbol{\gamma}_{\gamma_J}^T\mathbf{H}_\beta^T\mathbf{H}_\alpha^T\bar{\mathbf{H}}_j\bar{\mathbf{C}} \end{bmatrix}$$

$$\mathbf{D}_{\mathbf{q}_{Jj}} = \begin{bmatrix} \mathbf{U}_J^{-1}\mathbf{R}_i^T & -\mathbf{U}_J^{-1}\mathbf{R}_i^T\mathbf{R}_j\tilde{\bar{\mathbf{u}}}_{Jj}\bar{\mathbf{G}}_j \\ \mathbf{0}^T & 4\boldsymbol{\alpha}_{\alpha_J}^T\bar{\mathbf{H}}_\delta^T\mathbf{H}_i^T \\ \mathbf{0}^T & 4\boldsymbol{\beta}_{\beta_J}^T\bar{\mathbf{H}}_\gamma^T\mathbf{H}_\alpha^T\mathbf{H}_i^T \\ \mathbf{0}^T & 4\boldsymbol{\gamma}_{\gamma_J}^T\mathbf{H}_\beta^T\mathbf{H}_\alpha^T\mathbf{H}_i^T \end{bmatrix} \tag{60}$$

$$\mathbf{D}_{\mathbf{d}_J} = \begin{bmatrix} -\mathbf{I} & \mathbf{0} & \mathbf{0} & \mathbf{0} \\ \mathbf{0}^T & -1 & 4\boldsymbol{\alpha}_{\alpha_J}^T\bar{\mathbf{h}}_{\delta\beta}^T\mathbf{H}_i^T\boldsymbol{\theta}_j & 4\boldsymbol{\alpha}_{\alpha_J}^T\bar{\mathbf{h}}_{\delta\gamma}^T\mathbf{H}_i^T\boldsymbol{\theta}_j \\ \mathbf{0}^T & 4\boldsymbol{\beta}_{\beta_J}^T\bar{\mathbf{H}}_\gamma^T\mathbf{h}_\alpha^T\mathbf{H}_i^T\boldsymbol{\theta}_j & -1 & 4\boldsymbol{\beta}_{\beta_J}^T\bar{\mathbf{h}}_\gamma^T\mathbf{H}_\alpha^T\mathbf{H}_i^T\boldsymbol{\theta}_j \\ \mathbf{0}^T & 4\boldsymbol{\gamma}_{\gamma_J}^T\mathbf{H}_\beta^T\mathbf{h}_\alpha^T\mathbf{H}_i^T\boldsymbol{\theta}_j & 4\boldsymbol{\gamma}_{\gamma_J}^T\mathbf{h}_\beta^T\mathbf{H}_\alpha^T\mathbf{H}_i^T\boldsymbol{\theta}_j & -1 \end{bmatrix}$$

Finally, the last time differentiation leads in (61) to the free joint mobility equations contribution to the acceleration problem matrices.

$$
\dot{\mathbf{D}}_{\mathbf{q}_{\mathrm{Ji}}} = \begin{bmatrix} \mathbf{U}_{\mathrm{J}}^{-1}\mathbf{R}_{\mathrm{i}}^{\mathrm{T}}\tilde{\boldsymbol{\omega}}_{\mathrm{i}} & \mathbf{U}_{\mathrm{J}}^{-1}\mathbf{R}_{\mathrm{i}}^{\mathrm{T}}\left(\dot{\tilde{\mathbf{u}}}_{\mathrm{i}} - \tilde{\boldsymbol{\omega}}_{\mathrm{i}}\tilde{\mathbf{u}}_{\mathrm{i}}\right)\mathbf{G}_{\mathrm{i}} + \mathbf{U}_{\mathrm{J}}^{-1}\mathbf{R}_{\mathrm{i}}^{\mathrm{T}}\tilde{\mathbf{u}}_{\mathrm{i}}\dot{\mathbf{G}}_{\mathrm{i}} \\ \mathbf{0}^{\mathrm{T}} & 4\left(\boldsymbol{\alpha}_{\alpha_{\mathrm{J}}}^{\mathrm{T}}\dot{\bar{\mathbf{H}}}_{\delta}^{\mathrm{T}}\bar{\mathbf{H}}_{\mathrm{J}}\right)\bar{\mathbf{C}} \\ \mathbf{0}^{\mathrm{T}} & 4\left(\boldsymbol{\beta}_{\beta_{\mathrm{J}}}^{\mathrm{T}}\dot{\bar{\mathbf{H}}}_{\gamma}^{\mathrm{T}}\mathbf{H}_{\alpha}^{\mathrm{T}}\bar{\mathbf{H}}_{\mathrm{J}}\right)\bar{\mathbf{C}} \\ \mathbf{0}^{\mathrm{T}} & 4\left(\boldsymbol{\gamma}_{\gamma_{\mathrm{J}}}^{\mathrm{T}}\dot{\mathbf{H}}_{\beta}^{\mathrm{T}}\mathbf{H}_{\alpha}^{\mathrm{T}}\bar{\mathbf{H}}_{\mathrm{J}}\right)\bar{\mathbf{C}} \end{bmatrix}
$$

$$
\dot{\mathbf{D}}_{\mathbf{q}_{\mathrm{Jj}}} = \begin{bmatrix} -\mathbf{U}_{\mathrm{J}}^{-1}\mathbf{R}_{\mathrm{i}}^{\mathrm{T}}\tilde{\boldsymbol{\omega}}_{\mathrm{i}} & \mathbf{U}_{\mathrm{J}}^{-1}\mathbf{R}_{\mathrm{i}}^{\mathrm{T}}\left(\tilde{\boldsymbol{\omega}}_{\mathrm{i}} - \tilde{\boldsymbol{\omega}}_{\mathrm{j}}\right)\mathbf{R}_{\mathrm{j}}\tilde{\bar{\mathbf{u}}}_{\mathrm{Jj}}\bar{\mathbf{G}}_{\mathrm{j}} - \mathbf{U}_{\mathrm{J}}^{-1}\mathbf{R}_{\mathrm{i}}^{\mathrm{T}}\mathbf{R}_{\mathrm{j}}\tilde{\bar{\mathbf{u}}}_{\mathrm{Jj}}\dot{\bar{\mathbf{G}}}_{\mathrm{j}} \\ \mathbf{0}^{\mathrm{T}} & 4\left(\boldsymbol{\alpha}_{\alpha_{\mathrm{J}}}^{\mathrm{T}}\dot{\bar{\mathbf{H}}}_{\delta}^{\mathrm{T}}\mathbf{H}_{\mathrm{I}}^{\mathrm{T}}\right) \\ \mathbf{0}^{\mathrm{T}} & 4\left(\boldsymbol{\beta}_{\beta_{\mathrm{J}}}^{\mathrm{T}}\dot{\bar{\mathbf{H}}}_{\gamma}^{\mathrm{T}}\mathbf{H}_{\alpha}^{\mathrm{T}}\mathbf{H}_{\mathrm{I}}^{\mathrm{T}}\right) \\ \mathbf{0}^{\mathrm{T}} & 4\left(\boldsymbol{\gamma}_{\gamma_{\mathrm{J}}}^{\mathrm{T}}\dot{\mathbf{H}}_{\beta}^{\mathrm{T}}\mathbf{H}_{\alpha}^{\mathrm{T}}\mathbf{H}_{\mathrm{I}}^{\mathrm{T}}\right) \end{bmatrix} \tag{61}
$$

$$
\dot{\mathbf{D}}_{\mathbf{d}_{\mathrm{J}}} = \cdots
$$

$$
\begin{bmatrix} \mathbf{0} & & \mathbf{0} & \\ & 0 & \left(\boldsymbol{\alpha}_{\alpha_{\mathrm{J}}}^{\mathrm{T}}\dot{\bar{\mathbf{h}}}_{\delta\beta}^{\mathrm{T}}\mathbf{H}_{\mathrm{I}}^{\mathrm{T}}\boldsymbol{\theta}_{\mathrm{J}}\right) & \left(\boldsymbol{\alpha}_{\alpha_{\mathrm{J}}}^{\mathrm{T}}\dot{\bar{\mathbf{h}}}_{\delta\gamma}^{\mathrm{T}}\mathbf{H}_{\mathrm{I}}^{\mathrm{T}}\boldsymbol{\theta}_{\mathrm{J}}\right) \\ \mathbf{0} & \left(\boldsymbol{\beta}_{\beta_{\mathrm{J}}}^{\mathrm{T}}\bar{\mathbf{H}}_{\gamma}^{\mathrm{T}}\dot{\mathbf{h}}_{\alpha}^{\mathrm{T}}\mathbf{H}_{\mathrm{I}}^{\mathrm{T}}\boldsymbol{\theta}_{\mathrm{J}}\right) & 0 & \left(\boldsymbol{\beta}_{\beta_{\mathrm{J}}}^{\mathrm{T}}\bar{\mathbf{h}}_{\gamma}^{\mathrm{T}}\dot{\mathbf{H}}_{\alpha}^{\mathrm{T}}\mathbf{H}_{\mathrm{I}}^{\mathrm{T}}\boldsymbol{\theta}_{\mathrm{J}}\right) \\ & \left(\boldsymbol{\gamma}_{\gamma_{\mathrm{J}}}^{\mathrm{T}}\mathbf{H}_{\beta}^{\mathrm{T}}\dot{\mathbf{h}}_{\alpha}^{\mathrm{T}}\mathbf{H}_{\mathrm{I}}^{\mathrm{T}}\boldsymbol{\theta}_{\mathrm{J}}\right) & \left(\boldsymbol{\gamma}_{\gamma_{\mathrm{J}}}^{\mathrm{T}}\mathbf{h}_{\beta}^{\mathrm{T}}\dot{\mathbf{H}}_{\alpha}^{\mathrm{T}}\mathbf{H}_{\mathrm{I}}^{\mathrm{T}}\boldsymbol{\theta}_{\mathrm{J}}\right) & 0 \end{bmatrix}
$$

At this point, all the constraint and mobility equations for the joints considered in this work have been addressed.

1.3.5. Unit quaternion constraint

Lastly, the body equations keeping unitary the norm of the bodies' quaternions have to be characterized: they can be easily obtained in (62) by literally imposing the associated unitary norm.

$$
\begin{aligned} &\mathrm{B}_{\mathrm{i}}(\mathbf{q}_{\mathrm{i}}) = \boldsymbol{\theta}_{\mathrm{i}}^{\mathrm{T}}\boldsymbol{\theta}_{\mathrm{i}} - 1 = 0 \\ &\dot{\mathrm{B}}_{\mathrm{i}} = 2\boldsymbol{\theta}_{\mathrm{i}}^{\mathrm{T}}\dot{\boldsymbol{\theta}}_{\mathrm{i}} = [\mathbf{0}^{\mathrm{T}} \quad 2\boldsymbol{\theta}_{\mathrm{i}}^{\mathrm{T}}]\begin{bmatrix}\dot{\mathbf{t}}_{\mathrm{i}} \\ \dot{\boldsymbol{\theta}}_{\mathrm{i}}\end{bmatrix} = \mathrm{B}_{\mathbf{q}_{\mathrm{i}}}\dot{\mathbf{q}}_{\mathrm{i}} = 0 \\ &\dot{\mathrm{B}}_{\mathbf{q}_{\mathrm{i}}} = [\mathbf{0}^{\mathrm{T}} \quad 2\dot{\boldsymbol{\theta}}_{\mathrm{i}}^{\mathrm{T}}] \end{aligned} \tag{62}
$$

All the quantities needed to solve the position, the velocity and the acceleration problems were addressed: now it's time to move towards the dynamical problem, where the found Lagrangian coordinates $\mathbf{q}$, velocities $\dot{\mathbf{q}}$ and accelerations $\ddot{\mathbf{q}}$ will determine the driving and the reaction forces.

1.4. Multi-Body system Lagrangian dynamics

As anticipated in the previous, the kinematics problem solution provides the Lagrangian coordinates $\mathbf{q}$, velocities $\dot{\mathbf{q}}$ and accelerations $\ddot{\mathbf{q}}$ due to a given set of DoF (and time derivatives) $\mathbf{d}$, $\dot{\mathbf{d}}$ and $\ddot{\mathbf{d}}$ over the time t, by solving the joint constraint/mobility and the body equations $\mathbf{\Phi}$, $\dot{\mathbf{\Phi}}$ and $\ddot{\mathbf{\Phi}}$.

The bodies Lagrangian coordinates will determine the EoM of the Multi-Body system that in this chapter will be extrapolated with the Lagrangian dynamics approach (Shabana, 2020).

First of all, the kinetic energy T_i of the rigid body i has to be evaluated: it is obtained in (63) through the integration over the body volume Ω_i of the kinetic energy of the infinitesimal volumes dV located in the body frame by the constant vector $\bar{\mathbf{u}}$ and moving with velocity $\dot{\mathbf{r}}_i$ in the global reference frame considering a known density distribution ρ_i (Figure 20).

$$T_i = \frac{1}{2}\int_{\Omega_i} \rho_i \dot{\mathbf{r}}_i^T \dot{\mathbf{r}}_i \, dV \tag{63}$$

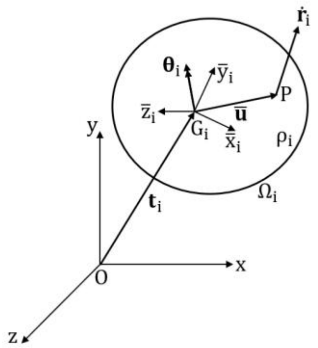

Figure 20 *Rigid body moving volume*

Recalling the linear relation between the point global velocity $\dot{\mathbf{r}}_i$ and the body Lagrangian velocities $\dot{\mathbf{q}}_i$, the kinetic energy can be expressed in (64) as a function of $\mathbf{q}_i$ and $\dot{\mathbf{q}}_i$: in particular it keeps its quadratic form with respect to the Lagrangian velocities that can be taken out from the integral since they do not vary within the body volume.

$$\begin{gathered}\dot{\mathbf{r}}_i(\mathbf{q}_i, \dot{\mathbf{q}}_i) = [\mathbf{I} \quad -\mathbf{R}_i \tilde{\bar{\mathbf{u}}} \bar{\mathbf{G}}_i] \begin{bmatrix} \dot{\mathbf{t}}_i \\ \dot{\boldsymbol{\theta}}_i \end{bmatrix} = \mathbf{J}_i(\mathbf{q}_i)\dot{\mathbf{q}}_i \\ T_i(\mathbf{q}_i, \dot{\mathbf{q}}_i) = \frac{1}{2}\dot{\mathbf{q}}_i^T \left(\int_{\Omega_i} \rho_i \mathbf{J}_i^T \mathbf{J}_i \, dV \right) \dot{\mathbf{q}}_i \end{gathered} \tag{64}$$

Let develop in (65) the product within the volume integral.

$$\mathbf{J}_i^T\mathbf{J}_i = \begin{bmatrix} \mathbf{I} \\ -\overline{\mathbf{G}}_i^T\tilde{\bar{\mathbf{u}}}^T\mathbf{R}_i^T \end{bmatrix}\begin{bmatrix} \mathbf{I} & -\mathbf{R}_i\tilde{\bar{\mathbf{u}}}\overline{\mathbf{G}}_i \end{bmatrix} = \begin{bmatrix} \mathbf{I} & -\mathbf{R}_i\tilde{\bar{\mathbf{u}}}\overline{\mathbf{G}}_i \\ -\overline{\mathbf{G}}_i^T\tilde{\bar{\mathbf{u}}}^T\mathbf{R}_i^T & \overline{\mathbf{G}}_i^T\tilde{\bar{\mathbf{u}}}^T\tilde{\bar{\mathbf{u}}}\overline{\mathbf{G}}_i \end{bmatrix} \tag{65}$$

Let integrate over the body volume in (66) the obtained matrix taking out from the integrals the quantities that do not exhibit variation within the volume.

$$\int_{\Omega_i} \rho_i\mathbf{J}_i^T\mathbf{J}_i\,dV = \begin{bmatrix} \left(\int_{\Omega_i} \rho_i\,dV\right)\mathbf{I} & -\mathbf{R}_i\left(\int_{\Omega_i} \rho_i\tilde{\bar{\mathbf{u}}}\,dV\right)\overline{\mathbf{G}}_i \\ -\overline{\mathbf{G}}_i^T\left(\int_{\Omega_i} \rho_i\tilde{\bar{\mathbf{u}}}\,dV\right)^T\mathbf{R}_i^T & \overline{\mathbf{G}}_i^T\left(\int_{\Omega_i} \rho_i\tilde{\bar{\mathbf{u}}}^T\tilde{\bar{\mathbf{u}}}\,dV\right)\overline{\mathbf{G}}_i \end{bmatrix} \tag{66}$$

In the found matrix, the zeroth, the first and second mass moment of the body can be recognised:

- the first one is the body mass m_i;
- the second one is the product between the body mass and the local mass centre position (so it is null since the latter is the origin of the local reference frame);
- the third one is the body inertia tensor defined in the local reference frame $\bar{\mathbf{I}}_i$.

So, the found matrix is nothing that the 7x7 symmetric body mass matrix $\mathbf{M}_i$ in the Lagrangian space, reported in the eq. (67), that, for the chosen reference frame, shows decoupled translational and rotational contributions to the kinetic energy; it is worth to note that if the body local reference frame aligns with the body principal axes of inertia, the 3x3 symmetric inertia tensor $\bar{\mathbf{I}}_i$ is diagonal.

$$\begin{gathered} \mathbf{M}_i(\mathbf{q}_i) = \begin{bmatrix} m_i\mathbf{I} & \mathbf{0} \\ \mathbf{0} & \overline{\mathbf{G}}_i^T\bar{\mathbf{I}}_i\overline{\mathbf{G}}_i \end{bmatrix} \\ T_i(\mathbf{q}_i,\dot{\mathbf{q}}_i) = \frac{1}{2}\dot{\mathbf{q}}_i^T\mathbf{M}_i(\mathbf{q}_i)\dot{\mathbf{q}}_i = \frac{1}{2}\dot{\mathbf{t}}_i^T(m_i\mathbf{I})\dot{\mathbf{t}}_i + \frac{1}{2}\dot{\boldsymbol{\theta}}_i^T\left(\overline{\mathbf{G}}_i^T\bar{\mathbf{I}}_i\overline{\mathbf{G}}_i\right)\dot{\boldsymbol{\theta}}_i \end{gathered} \tag{67}$$

The kinetic energy in this form is needed in order to derive the Multi-Body EoM from the Lagrange eq. (68), i.e., the energetic equilibrium of the whole mechanical system for a set of Lagrangian virtual displacement $\delta\mathbf{q}_i$ and accounting for generalised applied forces $\mathbf{Q}_i$ which is a 7x1 force vector acting on the Lagrangian coordinates $\mathbf{q}_i$, in particular on the body position $\mathbf{t}_i$ and orientation $\boldsymbol{\theta}_i$, that will be characterised in the next.

$$\sum_{i=1}^{n_B-1}\left(\frac{d}{dt}\frac{\partial T_i}{\partial\dot{\mathbf{q}}_i} - \frac{\partial T_i}{\partial\mathbf{q}_i} - \mathbf{Q}_i^T\right)\delta\mathbf{q}_i = 0 \tag{68}$$

Let develop in (69) the first term derivative in the Lagrange equation in which the inertial terms dealing with the product between mass and acceleration come out.

$$\frac{\mathrm{d}}{\mathrm{dt}}\frac{\partial \mathrm{T_i}}{\partial \dot{\mathbf{q}}_\mathrm{i}} = \frac{\mathrm{d}}{\mathrm{dt}}\frac{\partial}{\partial \dot{\mathbf{q}}_\mathrm{i}}\left(\frac{1}{2}\dot{\mathbf{q}}_\mathrm{i}^\mathrm{T}\mathbf{M}_\mathrm{i}\dot{\mathbf{q}}_\mathrm{i}\right) = \frac{\mathrm{d}}{\mathrm{dt}}\left(\dot{\mathbf{q}}_\mathrm{i}^\mathrm{T}\mathbf{M}_\mathrm{i}\right) = \ddot{\mathbf{q}}_\mathrm{i}^\mathrm{T}\mathbf{M}_\mathrm{i} + \dot{\mathbf{q}}_\mathrm{i}^\mathrm{T}\dot{\mathbf{M}}_\mathrm{i} \tag{69}$$

In order to develop the second term derivative, let rearrange in (70) the rotational kinetic energy to highlight its dependency with respect to the body orientation $\boldsymbol{\theta}_\mathrm{i}$.

$$\begin{gathered}\bar{\boldsymbol{\omega}}_\mathrm{i} = \bar{\mathbf{G}}_\mathrm{i}\dot{\boldsymbol{\theta}}_\mathrm{i} = -\dot{\bar{\mathbf{G}}}_\mathrm{i}\boldsymbol{\theta}_\mathrm{i} \quad \rightarrow \quad \mathrm{T_i} = \frac{1}{2}\mathrm{m_i}\dot{\mathbf{t}}_\mathrm{i}^\mathrm{T}\dot{\mathbf{t}}_\mathrm{i} + \frac{1}{2}\boldsymbol{\theta}_\mathrm{i}^\mathrm{T}\dot{\bar{\mathbf{G}}}_\mathrm{i}^\mathrm{T}\bar{\mathbf{I}}_\mathrm{i}\dot{\bar{\mathbf{G}}}_\mathrm{i}\boldsymbol{\theta}_\mathrm{i} \\ \frac{\partial \mathrm{T_i}}{\partial \mathbf{q}_\mathrm{i}} = \begin{bmatrix}\frac{\partial \mathrm{T_i}}{\partial \mathbf{t}_\mathrm{i}} & \frac{\partial \mathrm{T_i}}{\partial \boldsymbol{\theta}_\mathrm{i}}\end{bmatrix} = \begin{bmatrix}\mathbf{0}^\mathrm{T} & \boldsymbol{\theta}_\mathrm{i}^\mathrm{T}\dot{\bar{\mathbf{G}}}_\mathrm{i}^\mathrm{T}\bar{\mathbf{I}}_\mathrm{i}\dot{\bar{\mathbf{G}}}_\mathrm{i}\end{bmatrix} = \begin{bmatrix}\mathbf{0}^\mathrm{T} & -\bar{\boldsymbol{\omega}}_\mathrm{i}^\mathrm{T}\bar{\mathbf{I}}_\mathrm{i}\dot{\bar{\mathbf{G}}}_\mathrm{i}\end{bmatrix}\end{gathered} \tag{70}$$

Now let execute in (71) the time derivative of the mass matrix $\dot{\mathbf{M}}_\mathrm{i}$ and let develop its product with the Lagrangian velocities $\dot{\mathbf{q}}_\mathrm{i}$.

$$\begin{gathered}\dot{\mathbf{M}}_\mathrm{i} = \begin{bmatrix}\mathbf{0} & \mathbf{0} \\ \mathbf{0} & \dot{\bar{\mathbf{G}}}_\mathrm{i}^\mathrm{T}\bar{\mathbf{I}}_\mathrm{i}\bar{\mathbf{G}}_\mathrm{i} + \bar{\mathbf{G}}_\mathrm{i}^\mathrm{T}\bar{\mathbf{I}}_\mathrm{i}\dot{\bar{\mathbf{G}}}_\mathrm{i}\end{bmatrix} \\ \dot{\mathbf{q}}_\mathrm{i}^\mathrm{T}\dot{\mathbf{M}}_\mathrm{i} = \begin{bmatrix}\mathbf{0}^\mathrm{T} & \dot{\boldsymbol{\theta}}_\mathrm{i}^\mathrm{T}\dot{\bar{\mathbf{G}}}_\mathrm{i}^\mathrm{T}\bar{\mathbf{I}}_\mathrm{i}\bar{\mathbf{G}}_\mathrm{i} + \dot{\boldsymbol{\theta}}_\mathrm{i}^\mathrm{T}\bar{\mathbf{G}}_\mathrm{i}^\mathrm{T}\bar{\mathbf{I}}_\mathrm{i}\dot{\bar{\mathbf{G}}}_\mathrm{i}\end{bmatrix}\end{gathered} \tag{71}$$

Exploiting the quaternion properties in (72), it can be noted that the above product is equal to the negative of the kinetic energy derivative with respect to the Lagrangian coordinates.

$$\begin{matrix}\bar{\boldsymbol{\omega}}_\mathrm{i} = \bar{\mathbf{G}}_\mathrm{i}\dot{\boldsymbol{\theta}}_\mathrm{i} \\ \dot{\bar{\mathbf{G}}}_\mathrm{i}\dot{\boldsymbol{\theta}}_\mathrm{i} = \mathbf{0}\end{matrix} \quad \rightarrow \quad \dot{\mathbf{q}}_\mathrm{i}^\mathrm{T}\dot{\mathbf{M}}_\mathrm{i} = \begin{bmatrix}\mathbf{0}^\mathrm{T} & \bar{\boldsymbol{\omega}}_\mathrm{i}^\mathrm{T}\bar{\mathbf{I}}_\mathrm{i}\dot{\bar{\mathbf{G}}}_\mathrm{i}\end{bmatrix} \tag{72}$$

So, adding them in (73), a new generalised force vector $\mathbf{Q}_{\mathrm{v}_\mathrm{i}}$ is defined: it is called quadratic velocity force vector because it deals with the square of the angular velocity entries and, in fact, it describes the inertial effects due to the centrifugal and Coriolis forces.

$$\begin{gathered}\frac{\partial \mathrm{T_i}}{\partial \mathbf{q}_\mathrm{i}} - \dot{\mathbf{q}}_\mathrm{i}^\mathrm{T}\dot{\mathbf{M}}_\mathrm{i} = \begin{bmatrix}\mathbf{0}^\mathrm{T} & -2\bar{\boldsymbol{\omega}}_\mathrm{i}^\mathrm{T}\bar{\mathbf{I}}_\mathrm{i}\dot{\bar{\mathbf{G}}}_\mathrm{i}\end{bmatrix} = \mathbf{Q}_{\mathrm{v}_\mathrm{i}}^\mathrm{T} \\ \mathbf{Q}_{\mathrm{v}_\mathrm{i}}(\mathbf{q}_\mathrm{i}, \dot{\mathbf{q}}_\mathrm{i}) = \begin{bmatrix}\mathbf{0} \\ -2\dot{\bar{\mathbf{G}}}_\mathrm{i}^\mathrm{T}\bar{\mathbf{I}}_\mathrm{i}\bar{\boldsymbol{\omega}}_\mathrm{i}\end{bmatrix}\end{gathered} \tag{73}$$

Then, the Lagrange equation, reported in (74) after transposition, demonstrates that, for a set of virtual displacements, the work produced by the generalised inertial forces is balanced by the work of the generalised applied ones.

$$\sum_{\mathrm{i}=1}^{\mathrm{n_B}-1} \delta\mathbf{q}_\mathrm{i}^\mathrm{T}\left(\mathbf{M}_\mathrm{i}\ddot{\mathbf{q}}_\mathrm{i} - \mathbf{Q}_{\mathrm{v}_\mathrm{i}} - \mathbf{Q}_\mathrm{i}\right) = 0 \tag{74}$$

The sum for all the bodies can be expressed in a more compact form in (75) by concatenating the Lagrangian coordinates and force vectors in the Multi-Body system space.

$$\begin{gathered}\begin{bmatrix}\cdots & \delta\mathbf{q}_\mathrm{i}^\mathrm{T} & \cdots\end{bmatrix}\left(\begin{bmatrix}\ddots & \cdots & \mathbf{0} \\ \vdots & \mathbf{M}_\mathrm{i} & \vdots \\ \mathbf{0} & \cdots & \ddots\end{bmatrix}\begin{bmatrix}\vdots \\ \ddot{\mathbf{q}}_\mathrm{i} \\ \vdots\end{bmatrix} - \begin{bmatrix}\vdots \\ \mathbf{Q}_{\mathrm{v}_\mathrm{i}} \\ \vdots\end{bmatrix} - \begin{bmatrix}\vdots \\ \mathbf{Q}_\mathrm{i} \\ \vdots\end{bmatrix}\right) = 0 \\ \delta\mathbf{q}^\mathrm{T}(\mathbf{M}\ddot{\mathbf{q}} - \mathbf{Q}_\mathrm{v} - \mathbf{Q}) = 0\end{gathered} \tag{75}$$

The Lagrange energy balance cannot be true regardless the set of virtual displacement $\delta\mathbf{q}$, because the Lagrangian coordinates $\mathbf{q}$ of the Multi-Body system are not independent, so, basically, the solution to the eq. (76) is undeterminable.

$$\mathbf{M}\ddot{\mathbf{q}} - \mathbf{Q}_\mathrm{v} - \mathbf{Q} = \mathbf{0} \tag{76}$$

1.4.1. Embedding technique

One way to disregard from the virtual displacement set $\delta\mathbf{q}$ and to obtain a solvable system of equations is called the embedding technique (Shabana, 2020): the aim is to implement into the energy balance a relation between the system Lagrangian coordinates $\mathbf{q}$ and its DoF $\mathbf{d}$, since the latter are a set of independent coordinates. The searched relation that establishes a communication between $\mathbf{q}$ and $\mathbf{d}$ is given in (77) by the joint equations $\mathbf{\Phi}$ assembled during the kinematical problem, in particular in their velocity and acceleration forms.

$$\mathbf{\Phi}(\mathbf{q},\mathbf{d}) = \mathbf{0} \quad \rightarrow \quad \begin{matrix} \dot{\mathbf{q}} = -{\mathbf{\Phi}_\mathbf{q}}^{-1}\mathbf{\Phi}_\mathbf{d}\dot{\mathbf{d}} \\ \ddot{\mathbf{q}} = -\mathbf{\Phi}_\mathbf{q}^{-1}\left(\dot{\mathbf{\Phi}}_\mathbf{q}\dot{\mathbf{q}} + \dot{\mathbf{\Phi}}_\mathbf{d}\dot{\mathbf{d}} + \mathbf{\Phi}_\mathbf{d}\ddot{\mathbf{d}}\right) \end{matrix} \tag{77}$$

The velocity problem provides a relationship between the Lagrangian velocities $\dot{\mathbf{q}}$ and the DoF velocities $\dot{\mathbf{d}}$ that is equivalent to a variational relation between the Lagrangian virtual displacements $\delta\mathbf{q}$ and the DoF ones $\delta\mathbf{d}$ through the matrix $\mathbf{B}$; furthermore, substituting the velocity problem solution into the acceleration problem, the Lagrangian accelerations $\ddot{\mathbf{q}}$ result to be a linear combination of the DoF velocities $\dot{\mathbf{d}}$ and accelerations $\ddot{\mathbf{d}}$ (eq. (78)).

$$\begin{matrix} \mathbf{B} = -{\mathbf{\Phi}_\mathbf{q}}^{-1}\mathbf{\Phi}_\mathbf{d} \quad \rightarrow \quad \begin{matrix} \dot{\mathbf{q}} = \mathbf{B}\dot{\mathbf{d}} \\ \delta\mathbf{q} = \mathbf{B}\delta\mathbf{d} \end{matrix} \\ \mathbf{A} = -\mathbf{\Phi}_\mathbf{q}^{-1}\left(\dot{\mathbf{\Phi}}_\mathbf{q}\mathbf{B}\dot{\mathbf{d}} + \dot{\mathbf{\Phi}}_\mathbf{d}\right) \quad \rightarrow \quad \ddot{\mathbf{q}} = \mathbf{A}\dot{\mathbf{d}} + \mathbf{B}\ddot{\mathbf{d}} \end{matrix} \tag{78}$$

Let substitute in (79) the found relations into the Lagrange energetic equilibrium.

$$\begin{matrix} \delta\mathbf{d}^\mathrm{T}\mathbf{B}^\mathrm{T}\left[\mathbf{M}\left(\mathbf{A}\dot{\mathbf{d}} + \mathbf{B}\ddot{\mathbf{d}}\right) - \mathbf{Q}_\mathrm{v} - \mathbf{Q}\right] = 0 \\ \delta\mathbf{d}^\mathrm{T}\left[\left(\mathbf{B}^\mathrm{T}\mathbf{M}\mathbf{B}\right)\ddot{\mathbf{d}} - \mathbf{B}^\mathrm{T}\left(\mathbf{Q}_\mathrm{v} - \mathbf{M}\mathbf{A}\dot{\mathbf{d}}\right) - \mathbf{B}^\mathrm{T}\mathbf{Q}\right] = 0 \end{matrix} \tag{79}$$

Once the new mass matrix $\mathbf{M}_\mathrm{d}$, quadratic velocity force vector $\mathbf{Q}_{\mathrm{v}_\mathrm{d}}$ and applied forces $\mathbf{Q}_\mathrm{d}$ are recognised in (80), the resulting energetic equilibrium keeps its validity regardless of the DoF virtual displacement $\delta\mathbf{d}$, so the Multi-Body system EoM in which every term is referred to its DoF $\mathbf{d}$ is obtained.

$$\begin{matrix} \mathbf{M}_\mathrm{d} = \mathbf{B}^\mathrm{T}\mathbf{M}\mathbf{B} \\ \mathbf{Q}_{\mathrm{v}_\mathrm{d}} = \mathbf{B}^\mathrm{T}\left(\mathbf{Q}_\mathrm{v} - \mathbf{M}\mathbf{A}\dot{\mathbf{d}}\right) \\ \mathbf{Q}_\mathrm{d} = \mathbf{B}^\mathrm{T}\mathbf{Q} \end{matrix} \quad \rightarrow \quad \begin{matrix} \delta\mathbf{d}^\mathrm{T}\left(\mathbf{M}_\mathrm{d}\ddot{\mathbf{d}} - \mathbf{Q}_{\mathrm{v}_\mathrm{d}} - \mathbf{Q}_\mathrm{d}\right) = 0 \\ \mathbf{M}_\mathrm{d}\ddot{\mathbf{d}} - \mathbf{Q}_{\mathrm{v}_\mathrm{d}} - \mathbf{Q}_\mathrm{d} = \mathbf{0} \end{matrix} \tag{80}$$

The used embedding technique exploits the constraint equations to reduce the EoM to a minimum number of independent equations (the number of DoF $\mathrm{n_D}$), so it does not give information about the joint reactions (that are needed in this work for the tribological problem) and in general about the internal actions.

1.4.2. Augmented formulation

Another way to disregard from the set of Lagrangian virtual displacements $\delta\mathbf{q}$ by introducing information about the joint reactions is the augmented formulation (Shabana, 2020): the aim is to introduce a new set of unknowns called the Lagrange multipliers $\boldsymbol{\lambda}$ (one multiplier for each equation in $\boldsymbol{\Phi}$) that impose in (81) a null variation of the all constraint equations $\delta\boldsymbol{\Phi}$ in correspondence of the virtual displacements $\delta\mathbf{q}$ (this variation takes into account the derivative of the constraint equations with respect to the Lagrangian coordinates, i.e., the Jacobian $\boldsymbol{\Phi}_\mathbf{q}$).

$$\begin{cases} \boldsymbol{\lambda}^\mathrm{T}\delta\boldsymbol{\Phi} = 0 \\ \delta\boldsymbol{\Phi} = \boldsymbol{\Phi}_\mathbf{q}\delta\mathbf{q} \end{cases} \rightarrow \quad \boldsymbol{\lambda}^\mathrm{T}\boldsymbol{\Phi}_\mathbf{q}\delta\mathbf{q} = 0 \tag{81}$$

The latter scalar quantity can be intended as the work of the internal forces, i.e., the energy spent by the Lagrange multipliers $\boldsymbol{\lambda}$ to impose the constraint equations $\boldsymbol{\Phi}$. Since the internal forces work is zero, it can be added into the Lagrange energetic equilibrium in (82) without altering it.

$$\begin{gathered} \delta\mathbf{q}^\mathrm{T}(\mathbf{M}\ddot{\mathbf{q}} - \mathbf{Q}_\mathrm{v} - \mathbf{Q}) + \boldsymbol{\lambda}^\mathrm{T}\boldsymbol{\Phi}_\mathbf{q}\delta\mathbf{q} = 0 \\ \delta\mathbf{q}^\mathrm{T}\left(\mathbf{M}\ddot{\mathbf{q}} - \mathbf{Q}_\mathrm{v} - \mathbf{Q} + \boldsymbol{\Phi}_\mathbf{q}^\mathrm{T}\boldsymbol{\lambda}\right) = 0 \end{gathered} \tag{82}$$

At this point, even if the Lagrangian coordinates are still not a set of independent parameters, the introduction of the Lagrange multipliers as additional unknowns allows to disregard from the virtual displacements, obtaining in (83) the Multi-Body system EoM referred to its Lagrangian coordinates $\mathbf{q}$ and accounting for the multipliers $\boldsymbol{\lambda}$.

$$\mathbf{M}\ddot{\mathbf{q}} - \mathbf{Q}_\mathrm{v} - \mathbf{Q} + \boldsymbol{\Phi}_\mathbf{q}^\mathrm{T}\boldsymbol{\lambda} = \mathbf{0} \tag{83}$$

Let note in (84) that the Lagrange multipliers $\boldsymbol{\lambda}$ are composed by:

- the ones imposing the constraint equations $\mathbf{C}$, i.e., the joint interfacial forces that keep the joint structure $\boldsymbol{\lambda}_\mathrm{C}$ (constraint multipliers);
- the ones imposing the mobility equations $\mathbf{D}$, i.e., the driving forces acting directly on the DoF $\boldsymbol{\lambda}_\mathrm{D}$ (mobility multipliers);
- the ones imposing the body equations $\mathbf{B}$, i.e., the actions keeping the bodies' quaternions unitary norm $\boldsymbol{\lambda}_\mathrm{B}$ (body multipliers).

$$\mathbf{M}\ddot{\mathbf{q}} - \mathbf{Q}_\mathrm{v} - \mathbf{Q} + \begin{bmatrix} \mathbf{C}_\mathbf{q}^\mathrm{T} & \mathbf{D}_\mathbf{q}^\mathrm{T} & \mathbf{B}_\mathbf{q}^\mathrm{T} \end{bmatrix} \begin{bmatrix} \boldsymbol{\lambda}_\mathrm{C} \\ \boldsymbol{\lambda}_\mathrm{D} \\ \boldsymbol{\lambda}_\mathrm{B} \end{bmatrix} = \mathbf{0} \tag{84}$$

At this point, the last thing to characterise is the generalised applied force vector $\mathbf{Q}$: let start with the external actions.

The external actions are generally defined in the global reference, for example (Figure 21) an external force $\mathbf{F}_\mathrm{e}$ acting on the body i in the point of application P located in the body frame by the vector $\bar{\mathbf{u}}$ and an external torque $\mathbf{T}_e$ acting on the same body (eq. (85)).

$$\mathbf{F}_e = \begin{bmatrix} F_{e_x} \\ F_{e_y} \\ F_{e_z} \end{bmatrix} \quad \mathbf{T}_e = \begin{bmatrix} T_{e_x} \\ T_{e_y} \\ T_{e_z} \end{bmatrix} \tag{85}$$

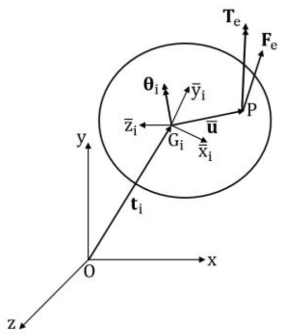

Figure 21 *External action applied to a rigid body*

In order to consider the external actions $\mathbf{F}_e$ and $\mathbf{T}_e$ into the Multi-Body system space, they have to be turned into the generalised force $\mathbf{Q}_{e_i}$, i.e., their effect with respect to a variation of the body Lagrangian coordinates $\mathbf{q}_i$ has to be evaluated: the transformation is given by analysing the virtual work δW_{e_i} in (86) accounting for the virtual displacement of the point P $\delta\mathbf{r}_i$ and the body virtual angular variation $\delta\boldsymbol{\varphi}_i$.

$$\delta W_{e_i} = \delta\mathbf{r}_i^T\mathbf{F}_e + \delta\boldsymbol{\varphi}_i^T\mathbf{T}_e \tag{86}$$

The relation between the virtual displacements and rotations is the same relation between the velocities, so let recall the global velocity vectors as function of the Lagrangian coordinates and velocities in (87).

$$\begin{aligned} \dot{\mathbf{r}}_i &= [\mathbf{I} \quad -\mathbf{R}_i\tilde{\bar{\mathbf{u}}}\bar{\mathbf{G}}_i]\begin{bmatrix} \dot{\mathbf{t}}_i \\ \dot{\boldsymbol{\theta}}_i \end{bmatrix} = \mathbf{J}_i\dot{\mathbf{q}}_i \\ \boldsymbol{\omega}_i &= \mathbf{G}_i\dot{\boldsymbol{\theta}}_i = [\mathbf{0} \quad \mathbf{G}_i]\begin{bmatrix} \dot{\mathbf{t}}_i \\ \dot{\boldsymbol{\theta}}_i \end{bmatrix} = \mathbf{K}_i\dot{\mathbf{q}}_i \end{aligned} \quad \rightarrow \quad \begin{aligned} \delta\mathbf{r}_i &= \mathbf{J}_i\delta\mathbf{q}_i \\ \delta\boldsymbol{\varphi}_i &= \mathbf{K}_i\delta\mathbf{q}_i \end{aligned} \tag{87}$$

Substituting the above in the virtual work, the generalised external force $\mathbf{Q}_{e_i}$ associated to $\mathbf{F}_e$ and $\mathbf{T}_e$ is found in (88): it is a 7x1 vector of which the first 3 affect the body position $\mathbf{t}_i$ while the last 4 affect the body orientation $\boldsymbol{\theta}_i$; the generalised external force vector $\mathbf{Q}_e$ is given by the summation of all the external actions applied to the related bodies.

$$\begin{aligned} \delta W_{e_i} &= \delta\mathbf{q}_i^T\left(\mathbf{J}_i^T\mathbf{F}_e + \mathbf{K}_i^T\mathbf{T}_e\right) = \delta\mathbf{q}_i^T\mathbf{Q}_{e_i} \\ \mathbf{Q}_{e_i} &= \mathbf{J}_i^T\mathbf{F}_e + \mathbf{K}_i^T\mathbf{T}_e \end{aligned} \tag{88}$$

If the external actions $\mathbf{Q}_e$ are the only source of generalised applied forces $\mathbf{Q}$, then the Multi-Body system EoM in the inverse dynamics verse is a linear system supplied by the time evolution of the Lagrangian coordinates (and their time derivatives), coming from the solved kinematical problem, in the unknown Lagrange multipliers $\boldsymbol{\lambda}$ along the time t (eq. (89)): basically, the objective is to evaluate the joint reactions $\boldsymbol{\lambda}_{\mathrm{C}}$ and the net joint driving forces/torques $\boldsymbol{\lambda}_{\mathrm{D}}$ produced by a known kinematics of the Multi-Body system.

$$\begin{array}{lcl} \mathbf{q}(\mathrm{t}) & & \boldsymbol{\lambda}_{\mathrm{C}}(\mathrm{t}) \\ \dot{\mathbf{q}}(\mathrm{t}) & \rightarrow \quad \boldsymbol{\Phi}_{\mathbf{q}}^{\mathrm{T}}\boldsymbol{\lambda} = -(\mathbf{M}\ddot{\mathbf{q}} - \mathbf{Q}_{\mathrm{v}} - \mathbf{Q}_{\mathrm{e}}) \quad \rightarrow & \boldsymbol{\lambda}_{\mathrm{D}}(\mathrm{t}) \\ \ddot{\mathbf{q}}(\mathrm{t}) & & \boldsymbol{\lambda}_{\mathrm{B}}(\mathrm{t}) \end{array} \tag{89}$$

The above role of the Lagrange multipliers is no more valid for a musculoskeletal Multi-Body system because of the two following reasons (Silva and Ambrósio, 2003; Oliveira, 2016):

- the driving actions are not produced by actuators generating forces/torques at the level of each translational/rotational DoF, but they are instead produced by a complex redundant muscular actuation system that generates forces resulting in the above net joint driving forces/torques;
- the muscles are responsible for the production of actuating forces but also of passive actions due to the muscle tissue resistance that are going to contribute to the load of the articulations, i.e., the joints.

So, the above EoM, in the case of a musculoskeletal system, provides the joint driving actions represented by the mobility multipliers $\boldsymbol{\lambda}_{\mathrm{D}}$ but it is not actually able to provide the joint reactions through the constraint multipliers $\boldsymbol{\lambda}_{\mathrm{C}}$: the latter represent the joint reactions only if the generalised applied force vector $\mathbf{Q}$ considers also the generalised muscular forces $\mathbf{Q}_{\mathrm{m}}$ in (90).

$$\mathbf{Q} = \mathbf{Q}_{\mathrm{e}} + \mathbf{Q}_{\mathrm{m}} \quad \rightarrow \quad \mathbf{M}\ddot{\mathbf{q}} - \mathbf{Q}_{\mathrm{v}} - \mathbf{Q}_{\mathrm{e}} - \mathbf{Q}_{\mathrm{m}} + \boldsymbol{\Phi}_{\mathbf{q}}^{\mathrm{T}}\boldsymbol{\lambda} = \mathbf{0} \tag{90}$$

With the above EoM formulation, while the constraint multipliers $\boldsymbol{\lambda}_{\mathrm{C}}$ actually are the joint reactions, the mobility multipliers $\boldsymbol{\lambda}_{\mathrm{D}}$ have the role of residual actuators that are useful during the EoM numerical resolution, because, since the known kinematics given by the time evolution of the DoF $\mathbf{d}$ generally come from experimental measurements that are subjected to sensor errors, they contribute to the validity of the EoM through minimal residual DoF actuations.

In order to solve the obtained Multi-Body system EoM, the muscle generalised force vector $\mathbf{Q}_{\mathrm{m}}$ needs to be characterised.

1.5. Muscular actuation system

The skeletal muscle is a human organ connected to the bones mainly devoted to their motion, but also to their protection and heating (Nordin and Frankel, 2001).

Before describing its actuation mechanism, let focus on its role from a mechanical point of view in the Multi-Body system: it can be considered as a linear or curved actuator attached to the bones that develops relative motion by contraction (Oliveira, 2016).

1.5.1. Linear muscle actuator

Let start with the muscle linear actuator m, shown in the Figure 22, intended as a segment that produces a contraction force f_m between the points A and B attached, respectively, to the bodies i and j; the attachment points A and B are located in the respective reference frames by the vectors $\bar{\mathbf{u}}_A$ and $\bar{\mathbf{u}}_B$, so their global position $\mathbf{r}_A$ and $\mathbf{r}_B$ can be evaluated to determine in (91) the muscle line action identified by the unit vector $\hat{\mathbf{v}}_m$ and the consequent virtual work δW_m done by the muscle to produce the attachment points virtual displacements $\delta\mathbf{r}_A$ and $\delta\mathbf{r}_B$.

$$
\begin{aligned}
&\begin{matrix}\mathbf{r}_A = \mathbf{t}_i + \mathbf{R}_i\bar{\mathbf{u}}_A \\ \mathbf{r}_B = \mathbf{t}_j + \mathbf{R}_j\bar{\mathbf{u}}_B\end{matrix} \quad \rightarrow \quad \hat{\mathbf{v}}_m = \frac{\mathbf{r}_B - \mathbf{r}_A}{\|\mathbf{r}_B - \mathbf{r}_A\|} \\
&\delta W_m = f_m\hat{\mathbf{v}}_m^T\delta\mathbf{r}_A - f_m\hat{\mathbf{v}}_m^T\delta\mathbf{r}_B
\end{aligned}
\tag{91}
$$

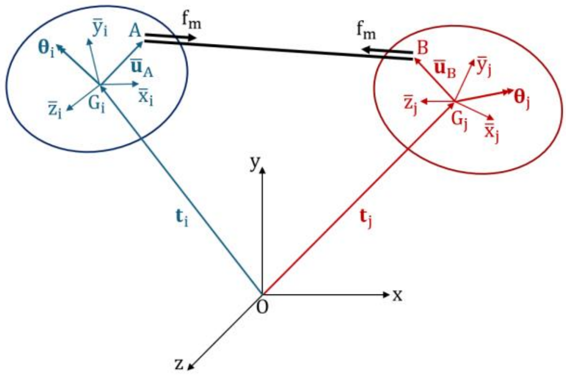

Figure 22 *Linear muscle actuator scheme*

Recalling the variational relationship between the global virtual displacements and the Lagrangian ones, the muscle virtual work δW_m is written in (92) as a function of the muscle force intensity f_m and of the bodies i and j virtual Lagrangian displacements through the definition of the vectors, respectively, $\mathbf{A}_{mi}$ and $\mathbf{A}_{mj}$.

$$
\begin{aligned}
&\delta\mathbf{r}_A = [\mathbf{I} \quad -\mathbf{R}_i\tilde{\bar{\mathbf{u}}}_A\bar{\mathbf{G}}_i]\begin{bmatrix}\delta\mathbf{t}_i \\ \delta\boldsymbol{\theta}_i\end{bmatrix} = \mathbf{J}_{Ai}\delta\mathbf{q}_i \\
&\delta\mathbf{r}_B = [\mathbf{I} \quad -\mathbf{R}_j\tilde{\bar{\mathbf{u}}}_B\bar{\mathbf{G}}_j]\begin{bmatrix}\delta\mathbf{t}_j \\ \delta\boldsymbol{\theta}_j\end{bmatrix} = \mathbf{J}_{Bj}\delta\mathbf{q}_j \\
&\delta W_m = f_m(\hat{\mathbf{v}}_m^T\mathbf{J}_{Ai}\delta\mathbf{q}_i - \hat{\mathbf{v}}_m^T\mathbf{J}_{Bj}\delta\mathbf{q}_j) = f_m(\mathbf{A}_{mi}\delta\mathbf{q}_i + \mathbf{A}_{mj}\delta\mathbf{q}_j)
\end{aligned}
\tag{92}
$$

The above virtual work analysis allows to move from the local body space to the global Multi-Body one: this procedure is followed to evaluate the generalised force produced by muscles that can show a more complex path than a line, for example with reference to the Figure 23, modelled as a series of segments along which the same muscle force f_m is shared. In the eq. (93) the muscle m virtual work acting along the path identified by the 3 points A, B and C belonging to the bodies, respectively, i, j and k while located by the vectors $\bar{\mathbf{u}}_A$, $\bar{\mathbf{u}}_B$ and $\bar{\mathbf{u}}_C$ is evaluated.

$$\begin{array}{l} \mathbf{r}_A = \mathbf{t}_i + \mathbf{R}_i\bar{\mathbf{u}}_A \\ \mathbf{r}_B = \mathbf{t}_j + \mathbf{R}_j\bar{\mathbf{u}}_B \\ \mathbf{r}_C = \mathbf{t}_k + \mathbf{R}_k\bar{\mathbf{u}}_C \end{array} \rightarrow \begin{array}{l} \hat{\mathbf{v}}_{m1} = \dfrac{\mathbf{r}_B - \mathbf{r}_A}{\|\mathbf{r}_B - \mathbf{r}_A\|} \\ \hat{\mathbf{v}}_{m2} = \dfrac{\mathbf{r}_C - \mathbf{r}_B}{\|\mathbf{r}_C - \mathbf{r}_B\|} \end{array}$$
$$\delta W_m = f_m\hat{\mathbf{v}}_{m1}^T\delta\mathbf{r}_A + \left(f_m\hat{\mathbf{v}}_{m2}^T - f_m\hat{\mathbf{v}}_{m1}^T\right)\delta\mathbf{r}_B - f_m\hat{\mathbf{v}}_{m2}^T\delta\mathbf{r}_C \qquad (93)$$

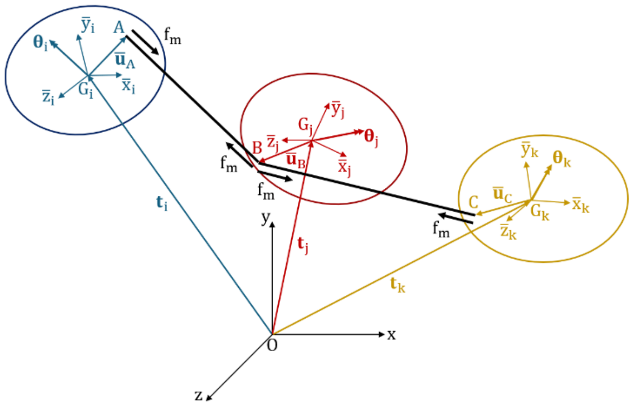

Figure 23 *Linear series muscle actuator scheme*

As for the previous case, let apply in (94) the variational relationships to evaluate the vectors $\mathbf{A}_{mi}$, $\mathbf{A}_{mj}$ and $\mathbf{A}_{mk}$.

$$\delta\mathbf{r}_A = \mathbf{J}_{Ai}\delta\mathbf{q}_i \quad \delta\mathbf{r}_B = \mathbf{J}_{Bj}\delta\mathbf{q}_j \quad \delta\mathbf{r}_C = \mathbf{J}_{Ck}\delta\mathbf{q}_k$$
$$\delta W_m = f_m\left[\hat{\mathbf{v}}_{m1}^T\mathbf{J}_{Ai}\delta\mathbf{q}_i + \left(\hat{\mathbf{v}}_{m2}^T - \hat{\mathbf{v}}_{m1}^T\right)\mathbf{J}_{Bj}\delta\mathbf{q}_j - \hat{\mathbf{v}}_{m2}^T\mathbf{J}_{Ck}\delta\mathbf{q}_k\right] \qquad (94)$$
$$\delta W_m = f_m\left(\mathbf{A}_{mi}\delta\mathbf{q}_i + \mathbf{A}_{mj}\delta\mathbf{q}_j + \mathbf{A}_{mk}\delta\mathbf{q}_k\right)$$

1.5.2. Curved muscle actuator

The last case considered in this work is represented by the curved muscle actuator: some muscles can make contact during their motion with bony surfaces, so they wrap around them providing a curved path along which the muscle force is produced. In order to evaluate the virtual work produced in this particular configuration, the curved muscle path has to be modelled: in this work the geodesic approach is chosen, since it is assumed that the wrapping muscle curve follows the shortest path around the surface (Gao *et* *al.*, 2002; Stavness, Sherman and Delp, 2012; Scholz *et al.*, 2014; Zarifi and Stavness, 2016).

A geodesic curve can be defined as the trajectory of a particle moving on a surface in absence of external forces and friction (Stavness, Sherman and Delp, 2012; Scholz *et al.*, 2014): basically, it is a further constrained mechanical problem but in the forward dynamics verse and along the independent variable identified by the curvilinear coordinate s instead of the time t.

Some concepts needed to describe surfaces and curves in the 3D space are introduced. A surface can be described in (95) with respect to a xyz reference frame through an explicit relation $\mathbf{x}(\mathbf{u})$ based on the two surface independent parameters u and v or through an implicit function $\mathrm{f}(\mathbf{x})$ (both the descriptions are equivalent).

$$\mathbf{x}(\mathbf{u}) = \begin{bmatrix} \mathrm{x}(\mathrm{u},\mathrm{v}) \\ \mathrm{y}(\mathrm{u},\mathrm{v}) \\ \mathrm{z}(\mathrm{u},\mathrm{v}) \end{bmatrix} \quad \leftrightarrow \quad \mathrm{f}(\mathbf{x}) = 0 \tag{95}$$

The 3D coordinates of a curve $\mathbf{c}$ are defined in (96) with respect to the curvilinear coordinate s.

$$\mathbf{c}(\mathrm{s}) = \begin{bmatrix} \mathrm{x}(\mathrm{s}) \\ \mathrm{y}(\mathrm{s}) \\ \mathrm{z}(\mathrm{s}) \end{bmatrix} \tag{96}$$

If the curve $\mathbf{c}$ belongs to the surface $\mathbf{x}$, then the relation in (97) holds.

$$\mathbf{c}(\mathrm{s}) = \mathbf{x}\big(\mathbf{u}(\mathrm{s})\big) \tag{97}$$

Along the surface path (and so along s), each point of the curve is identified by a triad of orthogonal unit vectors:

- the derivative of the point position with respect to the curvilinear coordinate s (indicated by the apostrophe) provides the tangent unit vector $\hat{\mathbf{t}}$ (tangent to both the curve and the surface), which is given in (98) by the combination of the surface parameters velocities $\mathbf{u}'$ along the surface tangential directions identified by its explicit function derivatives with respect to its parameters $\mathbf{x}_\mathrm{u}$ and $\mathbf{x}_\mathrm{v}$;

$$\hat{\mathbf{t}}(\mathrm{s}) = \mathbf{c}'(\mathrm{s}) = \mathbf{x}'\big(\mathbf{u}(\mathrm{s})\big) = \mathbf{x}_\mathbf{u}\mathbf{u}' \qquad \mathbf{x}_\mathbf{u}(\mathbf{u}) = [\mathbf{x}_\mathrm{u}(\mathbf{u}) \quad \mathbf{x}_\mathrm{v}(\mathbf{u})] \tag{98}$$

- the normal unit vector $\hat{\mathbf{n}}$ in (99) which is perpendicular to both the tangential directions $\mathbf{x}_\mathrm{u}$ and $\mathbf{x}_\mathrm{v}$;

$$\hat{\mathbf{n}}(\mathrm{s}) = \frac{\mathbf{x}_\mathrm{u} \times \mathbf{x}_\mathrm{v}}{\|\mathbf{x}_\mathrm{u} \times \mathbf{x}_\mathrm{v}\|} \tag{99}$$

- the binormal unit vector $\hat{\mathbf{b}}$ in (100) which is orthogonal to both the tangent and the normal unit vectors.

$$\hat{\mathbf{b}}(\mathrm{s}) = \hat{\mathbf{t}}(\mathrm{s}) \times \hat{\mathbf{n}}(\mathrm{s}) \tag{100}$$

The above information are needed to solve the mentioned forward dynamics problem in which the geodesic curve $\mathbf{c}(\mathrm{s})$ starts from a surface point $\mathbf{c}_0$ with tangent $\hat{\mathbf{t}}_0$, as reported in the Figure 24.

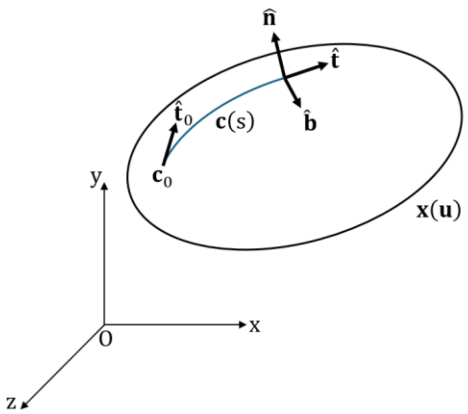

Figure 24 *Geodesic curve on a surface*

In order to address the above constrained mechanical problem with the Lagrangian approach, let define in (101) the kinetic energy T of the unitary mass particle moving along the geodesic and the related Lagrange equation in absence of generalised applied forces for a chosen set of Lagrangian coordinates $\mathbf{q}$.

$$\mathrm{T} = \frac{1}{2}\mathbf{c}'^{\mathrm{T}}\mathbf{c}' \quad \rightarrow \quad \left(\frac{\mathrm{d}}{\mathrm{ds}}\frac{\partial \mathrm{T}}{\partial \mathbf{q}'} - \frac{\partial \mathrm{T}}{\partial \mathbf{q}}\right)\delta\mathbf{q} = 0 \tag{101}$$

Both the augmented formulation and the embedding technique approaches (Shabana, 2020) can be followed: starting with the first one, let choose in (102) the geodesic curve coordinates $\mathbf{c}$ as the Lagrangian coordinates.

$$\left(\frac{\mathrm{d}}{\mathrm{ds}}\frac{\partial \mathrm{T}}{\partial \mathbf{c}'} - \frac{\partial \mathrm{T}}{\partial \mathbf{c}}\right)\delta\mathbf{c} = 0 \tag{102}$$

Let evaluate in (103) the needed kinetic energy derivatives.

$$\begin{matrix} \dfrac{\mathrm{d}}{\mathrm{ds}}\dfrac{\partial \mathrm{T}}{\partial \mathbf{c}'} = \mathbf{c}''^{\mathrm{T}} \\ \dfrac{\partial \mathrm{T}}{\partial \mathbf{c}} = \mathbf{0}^{\mathrm{T}} \end{matrix} \quad \rightarrow \quad \mathbf{c}''^{\mathrm{T}}\delta\mathbf{c} = 0 \tag{103}$$

In order to disregard from the virtual displacements $\delta\mathbf{c}$, let introduce in (104) the constraint equations: the particle has to belong to the surface, meaning that the particle position $\mathbf{c}$ has to satisfy the implicit surface equation f; then, the Lagrange multiplier λ associated to the single constraint introduces the internal work dependent on the constraint Jacobian $\mathrm{f}_{\mathbf{c}}$.

$$\mathrm{f}(\mathbf{c}) = 0 \quad \rightarrow \quad \lambda\,\mathrm{f}_{\mathbf{c}}\delta\mathbf{c} = 0 \tag{104}$$

Let note that the implicit surface function gradient $\mathrm{f}_{\mathbf{c}}$ identifies the surface normal direction, so the Lagrange multiplier λ, once projected through the Jacobian $\mathrm{f}_{\mathbf{c}}$, is nothing that the surface normal force constraining the particle to move without leaving the surface. Once the internal work is introduced into the Lagrange energetic equilibrium, the particle EoM is obtained in (105) (coupled with the surface constraint equation and with the initial conditions on the position $\mathbf{c}_0$ and on its derivative, i.e., the tangent unit vector $\hat{\mathbf{t}}_0$).

$$\left(\mathbf{c}'' + \mathrm{f}_{\mathbf{c}}^{\mathrm{T}}\lambda\right)^{\mathrm{T}}\delta\mathbf{c} = 0 \quad \rightarrow \quad \begin{cases} \mathbf{c}'' + \mathrm{f}_{\mathbf{c}}^{\mathrm{T}}\lambda = \mathbf{0} \\ \mathrm{f}(\mathbf{c}) = 0 \\ \mathbf{c}(0) = \mathbf{c}_0 \\ \mathbf{c}'(0) = \hat{\mathbf{t}}_0 \end{cases} \tag{105}$$

The obtained constrained EoM is a Differential Algebraic Equation (DAE) system in the unknown geodesic coordinates $\mathbf{c}$ and normal force λ: among the several ways to solve a DAE system (which will be discussed in a section of the tribological part of this work), here the simplest explicit way is adopted.

Let develop in (106) the constraint equation first and second derivative.

$$\begin{aligned} &\mathrm{f}'(\mathbf{c},\mathbf{c}') = \mathrm{f}_{\mathbf{c}}\mathbf{c}' = 0 \\ &\mathrm{f}''(\mathbf{c},\mathbf{c}',\mathbf{c}'') = \mathrm{f}_{\mathbf{c}}'\mathbf{c}' + \mathrm{f}_{\mathbf{c}}\mathbf{c}'' = 0 \end{aligned} \tag{106}$$

Provided that the particle initial position $\mathbf{c}_0$ and direction $\hat{\mathbf{t}}_0$ satisfy the constraint equation f and its derivative f′, the DAE is manipulated by replacing the constraint equation with its second derivative, so that a 4x4 linear system in the unknown accelerations $\mathbf{c}''$ and normal force λ is obtained in (107).

$$\begin{aligned} &\mathrm{f}(\mathbf{c}_0) = 0 \quad \mathrm{f}'(\mathbf{c}_0,\hat{\mathbf{t}}_0) = 0 \\ &\begin{cases} \mathbf{c}'' + \mathrm{f}_{\mathbf{c}}^{\mathrm{T}}\lambda = \mathbf{0} \\ \mathrm{f}_{\mathbf{c}}'\mathbf{c}' + \mathrm{f}_{\mathbf{c}}\mathbf{c}'' = 0 \end{cases} \rightarrow \begin{bmatrix} \mathbf{I} & \mathrm{f}_{\mathbf{c}}^{\mathrm{T}} \\ \mathrm{f}_{\mathbf{c}} & 0 \end{bmatrix}\begin{bmatrix} \mathbf{c}'' \\ \lambda \end{bmatrix} = \begin{bmatrix} \mathbf{0} \\ -\mathrm{f}_{\mathbf{c}}'\mathbf{c}' \end{bmatrix} \end{aligned} \tag{107}$$

The above linear system is exploited in the context of the numerical resolution of the EoM with the simple Backward Euler finite difference method: given the values of the coordinates and velocities at the previous step n, $\mathbf{c}_{\mathrm{n}}$ and $\mathbf{c}_{\mathrm{n}}'$, the linear system is solved to evaluate the new states at the next step $\mathrm{n}+1$ for a chosen curvilinear coordinate step size $\Delta\mathrm{s}$ and the value of the normal force λ_{n} (eq. (108)).

$$\begin{bmatrix} \mathbf{I} & \mathrm{f}_{\mathbf{c}}^{\mathrm{T}}(\mathbf{c}_{\mathrm{n}}) \\ \mathrm{f}_{\mathbf{c}}(\mathbf{c}_{\mathrm{n}}) & 0 \end{bmatrix}\begin{bmatrix} \mathbf{c}_{\mathrm{n}}'' \\ \lambda_{\mathrm{n}} \end{bmatrix} = \begin{bmatrix} \mathbf{0} \\ -\mathrm{f}_{\mathbf{c}}'(\mathbf{c}_{\mathrm{n}},\mathbf{c}_{\mathrm{n}}')\mathbf{c}_{\mathrm{n}}' \end{bmatrix} \rightarrow \begin{aligned} \mathbf{c}_{\mathrm{n}+1} &= \mathbf{c}_{\mathrm{n}} + \mathbf{c}_{\mathrm{n}}'\Delta\mathrm{s} \\ \mathbf{c}_{\mathrm{n}+1}' &= \mathbf{c}_{\mathrm{n}}' + \mathbf{c}_{\mathrm{n}}''\Delta\mathrm{s} \end{aligned} \tag{108}$$

In order to ensure the validity of the constraint equation and its derivative in correspondence of the initial conditions, the latter can be evaluated with the following procedure.

Instead of starting from a known position, let choose a starting surface parameters vector $\mathbf{u}_0$ from which $\mathbf{c}_0$ is evaluated in (109) through the explicit surface function $\mathbf{x}(\mathbf{u})$: in this way the implicit surface function is automatically satisfied by definition.

$$\mathbf{u}_0 \;\rightarrow\; \mathbf{c}_0 = \mathbf{x}(\mathbf{u}_0) \;\rightarrow\; \mathrm{f}(\mathbf{c}_0) = 0 \tag{109}$$

The choice of the starting tangent direction $\hat{\mathbf{t}}_0$ depends on the unknown starting surface parameters velocities $\mathbf{u}_0'$: let start with a given general direction $\mathbf{v}_0$ which at the moment is not tangent to the surface. Therefore, the direction $\mathbf{v}_0$ can be written in (110) as a combination of components $\mathbf{u}_0'$ along the surface tangential directions $\mathbf{x}_\mathrm{u}$ and $\mathbf{x}_\mathrm{v}$ with a component α along the surface normal direction $\hat{\mathbf{n}}$.

$$\mathbf{v}_0 = \mathbf{x_u}(\mathbf{u}_0)\mathbf{u}_0' + \alpha\hat{\mathbf{n}} \tag{110}$$

Let project the direction $\mathbf{v}_0$ along the tangential directions in $\mathbf{x_u}$ in (111), recalling that they are both orthogonal to the normal unit vector $\hat{\mathbf{n}}$.

$$\mathbf{x}_\mathbf{u}^\mathrm{T}(\mathbf{u}_0)\mathbf{v}_0 = \mathbf{x}_\mathbf{u}^\mathrm{T}(\mathbf{u}_0)\mathbf{x_u}(\mathbf{u}_0)\mathbf{u}_0' + \alpha\mathbf{x}_\mathbf{u}^\mathrm{T}(\mathbf{u}_0)\hat{\mathbf{n}} = [\mathbf{x}_\mathbf{u}^\mathrm{T}(\mathbf{u}_0)\mathbf{x_u}(\mathbf{u}_0)]\mathbf{u}_0' \tag{111}$$

By denoting the right-hand side 2x2 matrix as $\mathbf{M}_0$, the above linear system can be solved to evaluate in (112) the starting surface velocities parameters $\mathbf{u}_0'$: in this way it is ensured that the searched starting tangent direction $\hat{\mathbf{t}}_0$ can be obtained by linear combination of the found $\mathbf{u}_0'$ (after normalization) and, since $\hat{\mathbf{t}}_0$ is orthogonal to the surface normal direction identified by the constraint Jacobian $\mathrm{f}_\mathbf{c}$, the constraint derivative is satisfied.

$$\begin{gathered}\mathbf{u}_0' = \mathbf{M}_0^{-1}(\mathbf{u}_0)[\mathbf{x}_\mathbf{u}^\mathrm{T}(\mathbf{u}_0)\mathbf{v}_0] \quad \rightarrow \quad \hat{\mathbf{t}}_0 = \frac{\mathbf{x_u}(\mathbf{u}_0)\mathbf{u}_0'}{\|\mathbf{x_u}(\mathbf{u}_0)\mathbf{u}_0'\|} \\ \mathrm{f}'(\mathbf{c}_0, \hat{\mathbf{t}}_0) = \mathrm{f}_\mathbf{c}\hat{\mathbf{t}}_0 = 0\end{gathered} \tag{112}$$

The augmented formulation is now completely addressed and it allows to simulate the geodesic curve $\mathbf{c}(\mathrm{s})$: while it provides the value of the normal force λ along the curve (which is not necessary in the evaluation of the wrapping muscle path), the numerical error due to the discrete marching along the curvilinear coordinate could lead to an appreciable violation of the constraint equation, resulting in a geodesic path that leaves the surface. Furthermore, the procedure that leads to the evaluation of the initial conditions $\mathbf{c}_0$ and $\hat{\mathbf{t}}_0$ starting from the initial surface parameters vector $\mathbf{u}_0$ and a general initial direction $\mathbf{v}_0$ to obtain the velocities $\mathbf{u}_0'$, suggests that the two surface parameters $\mathbf{u}$ can be considered as the DoF of the particle (and indeed they are): as a consequence, the embedding technique, resulting in the particle EoM referred to its DoF, would lead to a more precise geodesic computation, since the surface constraint is directly embedded into the EoM.

Therefore, let rewrite the Lagrange energetic equilibrium in (113) by choosing the surface parameters DoF $\mathbf{u}$ as the Lagrangian coordinates: in this case the equilibrium is satisfied regardless of the Lagrangian virtual displacements $\delta\mathbf{u}$.

$$\frac{\mathrm{d}}{\mathrm{ds}}\frac{\partial \mathrm{T}}{\partial \mathbf{u}'} - \frac{\partial \mathrm{T}}{\partial \mathbf{u}} = \mathbf{0} \tag{113}$$

Let highlight in (114) the particle kinetic energy T dependencies on the surface parameters $\mathbf{u}$ and their velocities $\mathbf{u}'$, retrieving the particle symmetric mass matrix $\mathbf{M}$.

$$\begin{matrix}\mathbf{c} = \mathbf{x}(\mathbf{u}) \\ \mathbf{c}' = \mathbf{x_u}(\mathbf{u})\mathbf{u}'\end{matrix} \quad \rightarrow \quad \begin{matrix}\mathrm{T}(\mathbf{u}, \mathbf{u}') = \frac{1}{2}\mathbf{c}'^\mathrm{T}\mathbf{c}' = \frac{1}{2}\mathbf{u}'^\mathrm{T}\mathbf{M}(\mathbf{u})\mathbf{u}' \\ \mathbf{M}(\mathbf{u}) = \mathbf{x}_\mathbf{u}^\mathrm{T}(\mathbf{u})\mathbf{x_u}(\mathbf{u}) = \begin{bmatrix}\mathbf{x}_\mathrm{u}^\mathrm{T}\mathbf{x}_\mathrm{u} & \mathbf{x}_\mathrm{u}^\mathrm{T}\mathbf{x}_\mathrm{v} \\ \mathbf{x}_\mathrm{u}^\mathrm{T}\mathbf{x}_\mathrm{v} & \mathbf{x}_\mathrm{v}^\mathrm{T}\mathbf{x}_\mathrm{v}\end{bmatrix}\end{matrix} \tag{114}$$

Let evaluate in (115) the kinetic energy derivatives into the Lagrange equation.

$$\frac{d}{ds}\frac{\partial T}{\partial \mathbf{u}'} = \mathbf{u}''^{T}\mathbf{M}(\mathbf{u}) + \mathbf{u}'^{T}\mathbf{M}'(\mathbf{u},\mathbf{u}') \qquad \frac{\partial T}{\partial \mathbf{u}} = \begin{bmatrix} \frac{1}{2}\mathbf{u}'^{T}\mathbf{M}_{u}(\mathbf{u})\mathbf{u}' & \frac{1}{2}\mathbf{u}'^{T}\mathbf{M}_{v}(\mathbf{u})\mathbf{u}' \end{bmatrix} \tag{115}$$

The derivatives of the mass matrix can be evaluated in (116) by further differentiating the tangential directions $\mathbf{x}_u$ and $\mathbf{x}_v$ with respect to the surface parameters.

$$\begin{matrix} \mathbf{M}_u(\mathbf{u}) = 2\mathbf{x}_{\mathbf{u}}^{T}(\mathbf{u})\mathbf{x}_{\mathbf{uu}}(\mathbf{u}) \\ \mathbf{M}_v(\mathbf{u}) = 2\mathbf{x}_{\mathbf{u}}^{T}(\mathbf{u})\mathbf{x}_{\mathbf{uv}}(\mathbf{u}) \end{matrix} \rightarrow \mathbf{M}'(\mathbf{u},\mathbf{u}') = \mathbf{M}_u u' + \mathbf{M}_v v' \tag{116}$$

Let define in (117) the generalised quadratic force vector $\mathbf{Q}_v$ referred to the surface parameters $\mathbf{u}$.

$$\mathbf{Q}_v(\mathbf{u},\mathbf{u}') = \left(\frac{\partial T}{\partial \mathbf{u}} - \mathbf{u}'^{T}\mathbf{M}'(\mathbf{u},\mathbf{u}')\right)^{T} \tag{117}$$

Then, the particle EoM referred to the geodesic DoF is obtained in (118) and coupled with the initial conditions $\mathbf{u}_0$ and $\mathbf{u}'_0$, where the latter are found with the procedure described in the augmented formulation case.

$$\begin{cases} \mathbf{M}(\mathbf{u})\mathbf{u}'' - \mathbf{Q}_v(\mathbf{u},\mathbf{u}') = \mathbf{0} \\ \mathbf{u}(0) = \mathbf{u}_0 \\ \mathbf{u}'(0) = \mathbf{u}'_0 \end{cases} \tag{118}$$

The obtained EoM is now an Ordinary Differential Equation (ODE) system, which is solved with the same Backward Euler finite difference method described previously inverting the 2x2 linear system (linear during the explicit marching): then, the geodesic curve $\mathbf{c}$, and eventually its tangent $\mathbf{c}'$, is evaluated in (119) by plug the surface parameters $\mathbf{u}$ into the surface explicit function $\mathbf{x}(\mathbf{u})$.

$$\mathbf{M}(\mathbf{u}_n)\mathbf{u}''_n = \mathbf{Q}_v(\mathbf{u}_n,\mathbf{u}'_n) \rightarrow \begin{matrix} \mathbf{u}_{n+1} = \mathbf{u}_n + \mathbf{u}'_n\Delta s \\ \mathbf{u}'_{n+1} = \mathbf{u}'_n + \mathbf{u}''_n\Delta s \end{matrix} \qquad \mathbf{c}_n = \mathbf{x}(\mathbf{u}_n) \quad \mathbf{c}'_n = \mathbf{x}_{\mathbf{u}}(\mathbf{u}_n)\mathbf{u}'_n \tag{119}$$

At this point the curved muscle path can be evaluated. Let say that the muscle in consideration has attachment points A and B located in the wrapping surface reference frame by the vectors $\mathbf{x}_A$ and $\mathbf{x}_B$, as shown in the Figure 25; first of all, it has to be verified that the straight line segment going from A to B intercepts the wrapping surface: to do that, the parametric equation of the line AB dependent on the unknown line parameter m is plugged into the implicit surface equation $f(\mathbf{x}) = 0$ to evaluate if it provides solutions (eq. (120)); if so, since quadric surfaces are mostly used to describe the wrapping bony geometries, generally two solutions m_P and m_Q in the range between 0 and 1 are provided, which identify the intersection points coordinates $\mathbf{x}_P$ and $\mathbf{x}_Q$.

$$f\big(\mathbf{x}_A + m(\mathbf{x}_B - \mathbf{x}_A)\big) = 0 \rightarrow m_P, m_Q \tag{120}$$

$$\mathbf{x}_{\mathrm{P}} = \mathbf{x}_{\mathrm{A}} + \mathrm{m}_{\mathrm{P}}(\mathbf{x}_{\mathrm{B}} - \mathbf{x}_{\mathrm{A}}) \quad \mathbf{x}_{\mathrm{Q}} = \mathbf{x}_{\mathrm{A}} + \mathrm{m}_{\mathrm{Q}}(\mathbf{x}_{\mathrm{B}} - \mathbf{x}_{\mathrm{A}})$$

The found intersections $\mathbf{x}_{\mathrm{P}}$ and $\mathbf{x}_{\mathrm{Q}}$ are used in (121) to evaluate the associated surface parameters $\mathbf{u}_{\mathrm{P}}$ and $\mathbf{u}_{\mathrm{Q}}$ by inverting the surface explicit function $\mathbf{x}(\mathbf{u})$, while the directions $\mathbf{v}_{\mathrm{P}}$ and $\mathbf{v}_{\mathrm{Q}}$, i.e., the vectors going, respectively, from A to P and from B to Q, are used to evaluate the surface parameters velocities $\mathbf{u}'_{\mathrm{P}}$ and $\mathbf{u}'_{\mathrm{Q}}$ through the procedure described above.

$$\begin{aligned} &\mathbf{u}_{\mathrm{P}} = \mathbf{x}^{-1}(\mathbf{x}_{\mathrm{P}}) \quad \mathbf{v}_{\mathrm{P}} = \mathbf{x}_{\mathrm{P}} - \mathbf{x}_{\mathrm{A}} \\ &\mathbf{u}_{\mathrm{Q}} = \mathbf{x}^{-1}(\mathbf{x}_{\mathrm{Q}}) \quad \mathbf{v}_{\mathrm{Q}} = \mathbf{x}_{\mathrm{Q}} - \mathbf{x}_{\mathrm{B}} \\ &\mathbf{u}'_{\mathrm{P}} = \mathbf{M}^{-1}(\mathbf{u}_{\mathrm{P}})[\mathbf{x}_{\mathbf{u}}^{\mathrm{T}}(\mathbf{u}_{\mathrm{P}})\mathbf{v}_{\mathrm{P}}] \quad \mathbf{u}'_{\mathrm{Q}} = \mathbf{M}^{-1}(\mathbf{u}_{\mathrm{Q}})[\mathbf{x}_{\mathbf{u}}^{\mathrm{T}}(\mathbf{u}_{\mathrm{Q}})\mathbf{v}_{\mathrm{Q}}] \end{aligned} \tag{121}$$

At this point, the two geodesics $\mathbf{c}_{\mathrm{P}}$ and $\mathbf{c}_{\mathrm{Q}}$ starting from the intersections can be evaluated with the initial conditions, respectively, $\mathbf{u}_{\mathrm{P}}$, $\mathbf{u}'_{\mathrm{P}}$ and $\mathbf{u}_{\mathrm{Q}}$, $\mathbf{u}'_{\mathrm{Q}}$; the searched muscle curved path is obtained when (Stavness, Sherman and Delp, 2012):

- the two split segments AP and BQ are tangent to the surface, i.e., the two directions $\mathbf{v}_{\mathrm{P}}$ and $\mathbf{v}_{\mathrm{Q}}$ are orthogonal to the surface normal unit vectors in P and Q (evaluated by knowing $\mathbf{u}_{\mathrm{P}}$ and $\mathbf{u}_{\mathrm{Q}}$);
- the two geodesics are connected in their closest points P^* and Q^* ensuring collinearity.

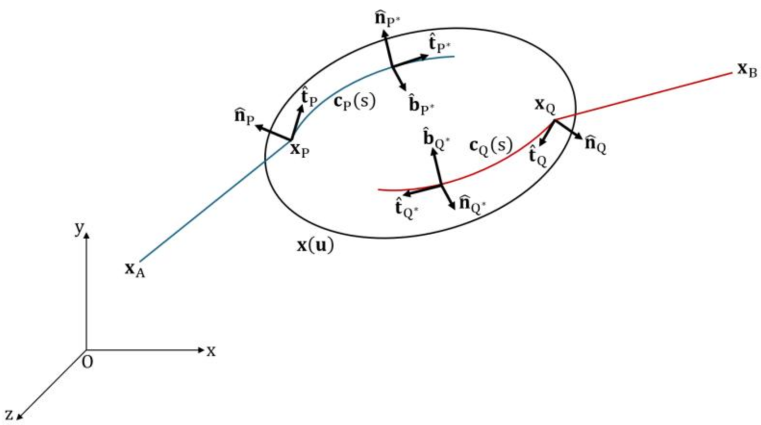

Figure 25 *Geodesics starting from the split muscle segments*

In particular, the 4 surface parameters collected in the vector $\boldsymbol{\xi}$ have to satisfy the following 4 equations in $\mathbf{g}$, where the first 2 impose the tangency of the split straight lines with respect to the surface while the latter 2 impose the collinearity in the joining point based on the local tangent and binormal unit vectors (eq. (122)).

$$\boldsymbol{\xi} = \begin{bmatrix} \mathbf{u}_P \\ \mathbf{u}_Q \end{bmatrix} \rightarrow \mathbf{g}(\boldsymbol{\xi}) = \begin{bmatrix} \mathbf{v}_P^T \hat{\mathbf{n}}_P \\ \mathbf{v}_Q^T \hat{\mathbf{n}}_Q \\ \hat{\mathbf{b}}_{P^*}^T (\mathbf{c}_{P^*} - \mathbf{c}_{Q^*}) \\ \hat{\mathbf{b}}_{P^*}^T \hat{\mathbf{t}}_{Q^*} \end{bmatrix} = \mathbf{0} \tag{122}$$

The above nonlinear system of equations is numerically solved in this work with the Newton method by updating the 4 surface parameters in $\boldsymbol{\xi}$ along the k iteration through a numerical Jacobian accounting for a small perturbation ε (eq. (123)).

$$\begin{gathered} \boldsymbol{\xi}^{(k+1)} = \boldsymbol{\xi}^{(k)} - \mathbf{g}_{\xi}^{-1}(\boldsymbol{\xi}^{(k)}) \mathbf{g}(\boldsymbol{\xi}^{(k)}) \\ [g_\xi]_{ij} = \frac{g_i\left(\xi_j(1+\varepsilon)\right) - g_i(\xi_j)}{\varepsilon \xi_j} \end{gathered} \tag{123}$$

Finally, once the above problem is solved, the geodesics are linked in the collinearity point, as shown in the Figure 26, and the muscle path composed by the straight line AP, the geodesic curve $\mathbf{c}_{PQ}$ and the straight line QB is found.

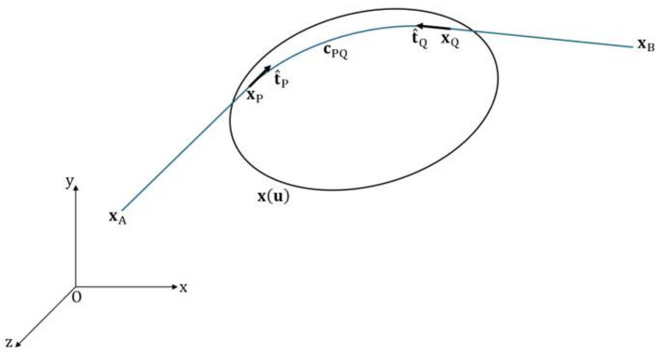

Figure 26 *Geodesic curve wrapping on the surface*

In this work two geometries of the wrapping surfaces are considered (eq. (124)), i.e., cylinders with radius r and height h and ellipsoids with semi-axes s_x, s_y and s_z.

$$\begin{gathered} u \in [0, 2\pi] \quad v \in \left[-\frac{h}{2}, \frac{h}{2}\right] \\ \mathbf{x}(\mathbf{u}) = \begin{bmatrix} r\cos u \\ r\sin u \\ v \end{bmatrix} \qquad f(\mathbf{x}) = x^2 + y^2 - r^2 \end{gathered} \tag{124}$$

$$u \in [0,2\pi] \quad v \in \left[-\frac{\pi}{2},\frac{\pi}{2}\right]$$

$$\mathbf{x}(\mathbf{u}) = \begin{bmatrix} s_x \cos v \cos u \\ s_y \cos v \sin u \\ s_z \sin v \end{bmatrix} \quad \left(\frac{x}{s_x}\right)^2 + \left(\frac{y}{s_y}\right)^2 + \left(\frac{z}{s_z}\right)^2 - 1$$

Furthermore, as shown in the Figure 27, a segment can wrap around multiple surfaces with the same logic (Stavness, Sherman and Delp, 2012; Scholz *et al.*, 2014).

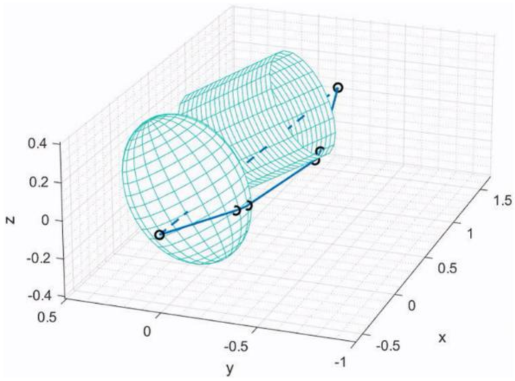

Figure 27 *Multiple wrapping*

Once a muscle curved path is evaluated, its virtual work can be analysed. Let discuss the case of a muscle m connecting the bodies i and k through the attachment point A and B located in their frames by the vectors $\bar{\mathbf{u}}_A$ and $\bar{\mathbf{u}}_B$, while wrapping on the surface w fixed to the body j (Figure 28): with respect to the body j the latter is located by the vector $\bar{\mathbf{u}}_w$ and it is oriented by the unit quaternion $\bar{\boldsymbol{\theta}}_w$ (which can be obtained by a known triplet of Euler angles α_w, β_w and γ_w around the local cartesian axes oriented as the unit vectors $\hat{\mathbf{i}}$, $\hat{\mathbf{j}}$ and $\hat{\mathbf{k}}$); the geodesic curve goes from the point P to the point Q that are located in the j body frame by the unknown vectors $\bar{\mathbf{u}}_P$ and $\bar{\mathbf{u}}_Q$.

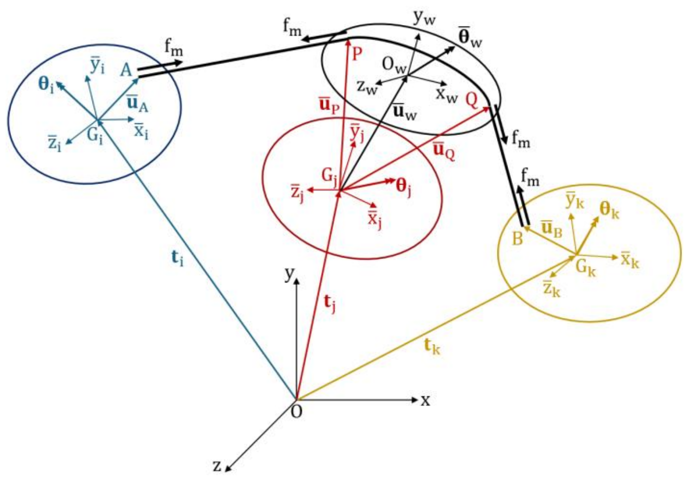

Figure 28 *Curved muscle actuator scheme*

The global position $\mathbf{t}_w$ and orientation $\boldsymbol{\theta}_w$ of the wrapping surface are given in (125) by the Lagrangian coordinates of the body j.

$$\begin{matrix} \boldsymbol{\alpha} = \boldsymbol{\theta}(\hat{\mathbf{i}}, \alpha_w) \\ \boldsymbol{\beta} = \boldsymbol{\theta}(\hat{\mathbf{j}}, \beta_w) \\ \boldsymbol{\gamma} = \boldsymbol{\theta}(\hat{\mathbf{k}}, \gamma_w) \end{matrix} \rightarrow \bar{\boldsymbol{\theta}}_w = \mathbf{H}_\alpha \mathbf{H}_\beta \boldsymbol{\theta}_\gamma \qquad \begin{matrix} \mathbf{t}_w = \mathbf{t}_j + \mathbf{R}_j \bar{\mathbf{u}}_w \\ \boldsymbol{\theta}_w = \mathbf{H}_j \bar{\boldsymbol{\theta}}_w \end{matrix} \tag{125}$$

The global position of the attachment points A and B, $\mathbf{r}_A$ and $\mathbf{r}_B$, can be evaluated in (126) with respect to the wrapping surface reference frame, i.e., $\mathbf{x}_A$ and $\mathbf{x}_B$, for the geodesic computation.

$$\begin{matrix} \mathbf{r}_A = \mathbf{t}_i + \mathbf{R}_i \bar{\mathbf{u}}_A \\ \mathbf{r}_B = \mathbf{t}_k + \mathbf{R}_k \bar{\mathbf{u}}_B \end{matrix} \rightarrow \begin{matrix} \mathbf{x}_A = \mathbf{R}_w^T (\mathbf{r}_A - \mathbf{t}_w) \\ \mathbf{x}_B = \mathbf{R}_w^T (\mathbf{r}_B - \mathbf{t}_w) \end{matrix} \tag{126}$$

Once the intersection surface parameters $\mathbf{u}_P$ and $\mathbf{u}_Q$ are determined from the geodesic computation, the consequent coordinates $\mathbf{x}_P$ and $\mathbf{x}_Q$ are used to evaluate in (127) the wrapping points P and Q position in the j body reference frame, i.e., $\bar{\mathbf{u}}_P$ and $\bar{\mathbf{u}}_Q$.

$$\begin{matrix} \mathbf{t}_j + \mathbf{R}_j \bar{\mathbf{u}}_P = \mathbf{t}_w + \mathbf{R}_w \mathbf{x}_P \\ \mathbf{t}_j + \mathbf{R}_j \bar{\mathbf{u}}_Q = \mathbf{t}_w + \mathbf{R}_w \mathbf{x}_Q \end{matrix} \rightarrow \begin{matrix} \bar{\mathbf{u}}_P = \mathbf{R}_j^T (\mathbf{t}_w + \mathbf{R}_w \mathbf{x}_P - \mathbf{t}_j) \\ \bar{\mathbf{u}}_Q = \mathbf{R}_j^T (\mathbf{t}_w + \mathbf{R}_w \mathbf{x}_Q - \mathbf{t}_j) \end{matrix} \tag{127}$$

Finally, all the needed quantities to evaluate in (128) the curved muscle virtual work are available, considering that the frictionless wrapped curve is not able to share the muscle force f_m along its path but only in correspondence of the wrapping points, so the muscle force is produced only along the split muscle straight segments.

$$\begin{aligned}
&\mathbf{r}_A = \mathbf{t}_i + \mathbf{R}_i\bar{\mathbf{u}}_A \\
&\mathbf{r}_P = \mathbf{t}_j + \mathbf{R}_j\bar{\mathbf{u}}_P \\
&\mathbf{r}_Q = \mathbf{t}_j + \mathbf{R}_j\bar{\mathbf{u}}_Q \\
&\mathbf{r}_B = \mathbf{t}_k + \mathbf{R}_k\bar{\mathbf{u}}_B
\end{aligned}
\quad \rightarrow \quad
\begin{aligned}
\hat{\mathbf{v}}_{m1} &= \frac{\mathbf{r}_P - \mathbf{r}_A}{\|\mathbf{r}_P - \mathbf{r}_A\|} \\
\hat{\mathbf{v}}_{m2} &= \frac{\mathbf{r}_B - \mathbf{r}_Q}{\|\mathbf{r}_B - \mathbf{r}_Q\|}
\end{aligned}
\tag{128}$$

$$\delta W_m = f_m\hat{\mathbf{v}}_{m1}^T\delta\mathbf{r}_A - f_m\hat{\mathbf{v}}_{m1}^T\delta\mathbf{r}_P + f_m\hat{\mathbf{v}}_{m2}^T\delta\mathbf{r}_Q - f_m\hat{\mathbf{v}}_{m2}^T\delta\mathbf{r}_B$$

At this point, the variational relationships are exploited in (129) to determine the vectors $\mathbf{A}_{mi}$, $\mathbf{A}_{mj}$ and $\mathbf{A}_{mk}$.

$$\begin{aligned}
&\delta\mathbf{r}_A = \mathbf{J}_{Ai}\delta\mathbf{q}_i \quad \delta\mathbf{r}_P = \mathbf{J}_{Pj}\delta\mathbf{q}_j \quad \delta\mathbf{r}_Q = \mathbf{J}_{Qj}\delta\mathbf{q}_j \quad \delta\mathbf{r}_B = \mathbf{J}_{Bk}\delta\mathbf{q}_k \\
&\delta W_m = f_m\left[\hat{\mathbf{v}}_{m1}^T\mathbf{J}_{Ai}\delta\mathbf{q}_i + \left(\hat{\mathbf{v}}_{m2}^T\mathbf{J}_{Qj} - \hat{\mathbf{v}}_{m1}^T\mathbf{J}_{Pj}\right)\delta\mathbf{q}_j - \hat{\mathbf{v}}_{m2}^T\mathbf{J}_{Bk}\delta\mathbf{q}_k\right] \\
&\delta W_m = f_m\left(\mathbf{A}_{mi}\delta\mathbf{q}_i + \mathbf{A}_{mj}\delta\mathbf{q}_j + \mathbf{A}_{mk}\delta\mathbf{q}_k\right)
\end{aligned}
\tag{129}$$

All the muscle cases are addressed, so let evaluate in (130) the total muscle work accounting for all the n_M muscles considered in the musculoskeletal system and taking into account the possibility that a muscle m can generally affect at least 2 body virtual displacements.

$$\sum_{m=1}^{n_M}\delta W_m = \sum_{m=1}^{n_M} f_m\left(\mathbf{A}_{mi}\delta\mathbf{q}_i + \mathbf{A}_{mj}\delta\mathbf{q}_j + \mathbf{A}_{mk}\delta\mathbf{q}_k + \cdots\right) \tag{130}$$

In the Multi-Body space, the muscle virtual work producing the Lagrangian displacements $\delta\mathbf{q}$ is related to the muscle force vector $\mathbf{f}$ through the actuation matrix $\mathbf{A}$: then the generalised muscle force vector $\mathbf{Q}_m$ is determined in (131).

$$\begin{aligned}
&[\cdots \quad f_m \quad \cdots]\begin{bmatrix} & & & \vdots & & & \\ \cdots & \mathbf{A}_{mi} & \cdots & \mathbf{A}_{mj} & \cdots & \mathbf{A}_{mk} & \cdots \\ & & & \vdots & & & \end{bmatrix}\begin{bmatrix}\vdots \\ \delta\mathbf{q}_i \\ \vdots \\ \delta\mathbf{q}_j \\ \vdots \\ \delta\mathbf{q}_k \\ \vdots\end{bmatrix} = \cdots \\
&\ldots = \mathbf{f}^T\mathbf{A}\delta\mathbf{q} = \mathbf{Q}_m^T\delta\mathbf{q} \quad \rightarrow \quad \mathbf{Q}_m = \mathbf{A}^T\mathbf{f}
\end{aligned}
\tag{131}$$

Therefore, the musculoskeletal Multi-Body EoM is reported in (132) in the unknown muscle forces $\mathbf{f}$ and Lagrange multipliers $\boldsymbol{\lambda}$.

$$\mathbf{A}^T\mathbf{f} - \boldsymbol{\Phi}_{\mathbf{q}}^T\boldsymbol{\lambda} = \mathbf{M}\ddot{\mathbf{q}} - \mathbf{Q}_v - \mathbf{Q}_e \tag{132}$$

The last things to characterize before being able to solve the Multi-Body EoM are the active and the passive muscle forces contributions.

1.5.3. Hill muscle-tendon model

The skeletal muscle (Nordin and Frankel, 2001; Jovanovic, Vranic and Miljkovic, 2015) is a striated bundle of fascicles that provides relative motion between the linked bones by contraction; the fascicles are composed by several striated fibres formed by the sarcomeres, i.e., the main muscle unit devoted to the voluntary contraction controlled by neural excitation; the fascicles are surrounded by connective tissues that provide the muscle resistance to lengthening and the produced muscle force is transmitted to the bones through the extremities by the tendons, i.e., a very stiff tissue attaching to the bone. Lastly, the muscle fibres can be oriented differently from the action line linking the attachment points in the case of pennated muscles.

So, the muscle-tendon actuator model introduced by Hill (Thelen, 2003; Hada, Yamada and Tsuji, 2007; Chand, 2011; Millard *et al.*, 2013; Jovanovic, Vranic and Miljkovic, 2015; Romero and Alonso, 2016) can be considered as a series between (Figure 29):

- a Series Element (SE), i.e., the tendon modelled as a non-linear spring exerting a dimensionless force f_{SE} dependent on the tendon length l_t;
- a parallel unit, inclined by the pennation angle α_p with respect to the action line AB, composed by the Contractile Element (CE), i.e., the unit devoted to the muscle contraction through the activation level a_m (a number in the range $[0,1]$ controlled by the brain) and two dimensionless force functions f_l and f_v describing the muscle behaviour with respect to its length l_m and its deformation velocity v_m, and by a Parallel Element (PE), i.e., a non-linear spring producing the connective tissues resistance to lengthening dimensionless force f_{PE} depending on the muscle length l_m.

Due to the series arrangement, the force produced by the muscle f_m projected on the muscle line AB through the pennation angle α_p is the same as that transmitted by the tendon f_t, also equal to the force generated by the whole muscle-tendon unit f_{mt}.

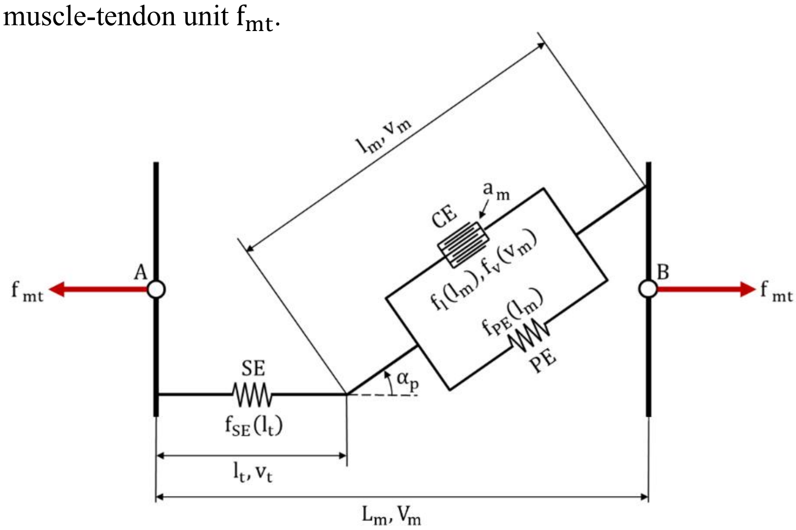

Figure 29 *Hill muscle-tendon model*

The tendon is able to respond only to its lengthening, so when its length l_t is greater than its slack length l_{t0}; the tendon force production is exponential with respect to its deformation ε_t up to a given threshold f_{t0} in correspondence of the given deformation ε_{t0} after which it grows linearly (eq. (133)); the exponential and the linear growths are governed by the parameters k_e and k_l.

$$\varepsilon_t = \frac{l_t - l_{t0}}{l_{t0}} \quad \rightarrow \quad f_{SE}(l_t) = \begin{cases} 0 & \varepsilon_t < 0 \\ f_{t0} \dfrac{e^{k_e \frac{\varepsilon_t}{\varepsilon_{t0}}} - 1}{e^{k_e - 1}} & 0 \leq \varepsilon_t < \varepsilon_{t0} \\ f_{t0} + k_l(\varepsilon_t - \varepsilon_{t0}) & \varepsilon_t \geq \varepsilon_{t0} \end{cases} \tag{133}$$

The muscle CE unit force production in the eq. (134) depends on both its length and deformation velocity:

- the force-length behaviour resembles a gaussian bell with respect to its deformation ε_m with width governed by the parameter γ and reaching its unitary peak in correspondence of the optimal fibre length l_0;
- the force-velocity relationship describes that the muscle produces a growing force with increasing deformation velocity (higher for lengthening with respect to the shortening), while reaching a lengthening asymptote f_{v0} and it is no more able to produce force below the maximum contraction velocity v_0; furthermore, in correspondence of zero velocity the dimensionless force is unitary; the shortening and the lengthening phases are governed by the parameters k_1 and k_2.

$$\varepsilon_m = \frac{l_m - l_0}{l_0} \quad \rightarrow \quad f_l(l_m) = e^{-\frac{\varepsilon_m^2}{\gamma}}$$

$$f_v(v_m) = \begin{cases} 0 & v_m < -v_0 \\ k_1 \dfrac{1 + \frac{v_m}{v_0}}{k_1 - \frac{v_m}{v_0}} & -v_0 \leq v_m < 0 \\ \dfrac{k_2 + f_{v0}\frac{v_m}{v_0}}{k_2 + \frac{v_m}{v_0}} & v_m \geq 0 \end{cases} \tag{134}$$

The passive force contribution due to the muscle resistance to lengthening responds only to positive muscle deformation ε_m: it grows exponentially up to the unitary threshold in correspondence of a given deformation ε_{m0} after which it grows linearly according to the parameter k_p (eq. (135)).

$$f_{PE}(l_m) = \begin{cases} 0 & l_m < l_0 \\ \dfrac{e^{k_p \frac{\varepsilon_m}{\varepsilon_{m0}}} - 1}{e^{k_p} - 1} & l_0 \leq l_m < 1 + \varepsilon_{m0} \\ 1 + \dfrac{k_p}{\varepsilon_{m0}} \dfrac{\varepsilon_m - \varepsilon_{m0}}{1 - e^{-k_p}} & l_m \geq 1 + \varepsilon_{m0} \end{cases} \tag{135}$$

All the dimensionless forces (depicted in the Figure 30) are referred to the maximum isometric force f_0 that is reached in correspondence of the optimal muscle fibres length l_0 and zero deformation velocity.

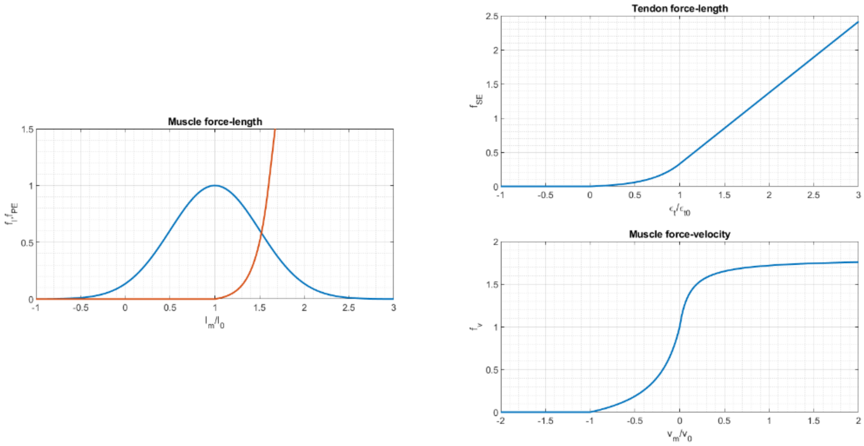

Figure 30 *Muscle-tendon dimensionless force laws*

While the tendon force f_t is already characterised, the muscle force f_m is given by the product between the CE length and velocity relationships scaled by the activation level a_m and projected along the muscle-tendon line action AB through the pennation angle α_p (eq. (136)).

$$\begin{cases} f_t = f_{SE}(l_t) f_0 \\ f_m = \big(a_m f_l(l_m) f_v(v_m) + f_{PE}(l_m)\big) f_0 \cos\alpha_p \end{cases} \tag{136}$$

Therefore, equating the series contributions, the muscle equilibrium is given in the eq. (137).

$$f_{SE}(l_t) = \big(a_m f_l(l_m) f_v(v_m) + f_{PE}(l_m)\big) \cos\alpha_p \tag{137}$$

The muscle-tendon lengths and deformation velocities are unknown at this point: they have to be determined by the knowledge of the muscle attachment or wrapping points. Let refer to the general curved muscle actuator rigidly attached to the i and k bodies while wrapping around the surface fixed to the j body, determined by the kinematics of the points A, P, Q and B reported in the eq. (138).

$$\begin{matrix} \mathbf{r}_A = \mathbf{t}_i + \mathbf{R}_i \bar{\mathbf{u}}_A \\ \mathbf{r}_P = \mathbf{t}_j + \mathbf{R}_j \bar{\mathbf{u}}_P \\ \mathbf{r}_Q = \mathbf{t}_j + \mathbf{R}_j \bar{\mathbf{u}}_Q \\ \mathbf{r}_B = \mathbf{t}_k + \mathbf{R}_k \bar{\mathbf{u}}_B \end{matrix} \rightarrow \begin{matrix} \hat{\mathbf{v}}_{m1} = \dfrac{\mathbf{r}_P - \mathbf{r}_A}{\|\mathbf{r}_P - \mathbf{r}_A\|} \\ \hat{\mathbf{v}}_{m2} = \dfrac{\mathbf{r}_B - \mathbf{r}_Q}{\|\mathbf{r}_B - \mathbf{r}_Q\|} \end{matrix} \tag{138}$$

The related muscle-tendon length L_m can be written in (139) as the sum of the straight segment lengths and the curved one, where the latter is given by the curvilinear integration along the curve γ of the absolute value of the geodesic tangent unit vector $\mathbf{c}'_{PQ}$.

$$L_m = \|\mathbf{r}_P - \mathbf{r}_A\| + \int_\gamma \left\|\mathbf{c}'_{PQ}\right\| ds + \left\|\mathbf{r}_B - \mathbf{r}_Q\right\| \tag{139}$$

The muscle-tendon deformation velocity V_m is given in (140) by the time derivative of its length L_m: considering that the geodesic is fixed to the surface during the wrapping, only the straight segments contribute to the curved actuator deformation velocity.

$$\begin{aligned} &\frac{d}{dt}(\|\mathbf{r}_P - \mathbf{r}_A\|) = \hat{\mathbf{v}}_{m1}^T (\dot{\mathbf{r}}_P - \dot{\mathbf{r}}_A) \quad && \dot{\mathbf{r}}_A = \mathbf{J}_{Ai}\dot{\mathbf{q}}_i \\ & && \dot{\mathbf{r}}_P = \mathbf{J}_{Pj}\dot{\mathbf{q}}_j \\ &\frac{d}{dt}(\|\mathbf{r}_B - \mathbf{r}_Q\|) = \hat{\mathbf{v}}_{m2}^T (\dot{\mathbf{r}}_B - \dot{\mathbf{r}}_Q) && \dot{\mathbf{r}}_Q = \mathbf{J}_{Qj}\dot{\mathbf{q}}_j \\ & && \dot{\mathbf{r}}_B = \mathbf{J}_{Bk}\dot{\mathbf{q}}_k \\ &V_m = \hat{\mathbf{v}}_{m1}^T (\dot{\mathbf{r}}_P - \dot{\mathbf{r}}_A) + \hat{\mathbf{v}}_{m2}^T (\dot{\mathbf{r}}_B - \dot{\mathbf{r}}_Q) \end{aligned} \tag{140}$$

While the muscle-tendon length and deformation velocity L_m and V_m are determined from the kinematics of the muscle attachment/wrapping points, the geometrical quantities related to the single units are unknown. The muscle-tendon length is the sum of the tendon length plus the projection of the muscle one while, according to the Hill hypotheses (Silva and Ambrósio, 2003; Millard *et al.*, 2013; Jovanovic, Vranic and Miljkovic, 2015), the muscle-tendon width can be considered as constant and equal to the width in correspondence of the given optimal fibres length l_0 and pennation angle α_0: this provides an expression in (141) for the muscle length l_m and pennation angle α_p dependent on the tendon length l_t.

$$\begin{cases} l_m \sin\alpha_p = l_0 \sin\alpha_0 \\ L_m = l_t + l_m \cos\alpha_p \end{cases} \rightarrow \quad \begin{aligned} l_m &= \sqrt{(l_0 \sin\alpha_0)^2 + (L_m - l_t)^2} \\ \alpha_p &= \arctan\left(\frac{l_0 \sin\alpha_0}{L_m - l_t}\right) \end{aligned} \tag{141}$$

The first time derivative of the muscle length provides in (142) its deformation velocity v_m, dependent on the tendon deformation velocity v_t and its length l_t through the pennation angle.

$$v_m = (V_m - v_t)\cos\alpha_p \tag{142}$$

For the musculoskeletal kinematics intensities analysed in this work, the tendon dynamics can be neglected and it becomes a simple force transmitter, so its length can be considered as constant and equal to its slack one l_{t0} and, as a consequence, its deformation velocity is null: this provides in (143) a functional relationship between the muscle-tendon quantities L_m and V_m coming from the bodies' kinematics and the muscle length l_m, deformation velocity v_m and pennation angle α_p.

$$\begin{matrix} L_m \\ V_m \end{matrix} \rightarrow \quad \begin{aligned} l_m &= \sqrt{(l_0 \sin\alpha_0)^2 + (L_m - l_{t0})^2} \\ v_m &= V_m \cos\alpha_p \\ \alpha_p &= \arctan\left(\frac{l_0 \sin\alpha_0}{L_m - l_{t0}}\right) \end{aligned} \tag{143}$$

Once the above muscle states are evaluated, its force production can be determined in (144): in particular, the muscle force f_m can be decomposed into an active contribution due to the CE, f_{CE_m}, scaled by the muscular activation a_m and a passive contribution due to the PE, f_{PE_m}.

$$\begin{cases} f_{CE_m} = f_l(l_m) f_v(v_m) f_0 \cos\alpha_p \\ f_{PE_m} = f_{PE}(l_m) f_0 \cos\alpha_p \end{cases} \rightarrow \quad f_m = a_m f_{CE_m} + f_{PE_m} \tag{144}$$

Therefore, the muscle force vector $\mathbf{f}$ in the Multi-Body EoM can be written in (145) as a linear function of the muscle activation vector $\mathbf{a}$ through a diagonal matrix $\mathbf{F}_{CE}$ and the passive force vector $\mathbf{f}_{PE}$.

$$\begin{bmatrix} \vdots \\ f_m \\ \vdots \end{bmatrix} = \begin{bmatrix} \ddots & \cdots & \mathbf{0} \\ \vdots & f_{CE_m} & \vdots \\ \mathbf{0} & \cdots & \ddots \end{bmatrix} \begin{bmatrix} \vdots \\ a_m \\ \vdots \end{bmatrix} + \begin{bmatrix} \vdots \\ f_{PE_m} \\ \vdots \end{bmatrix} \quad \rightarrow \quad \mathbf{f} = \mathbf{F}_{CE}\mathbf{a} + \mathbf{f}_{PE} \tag{145}$$

Noting that the matrix $\mathbf{F}_{CE}$ and the vector $\mathbf{f}_{PE}$ are known from the bodies' kinematics, the muscle generalised force vector $\mathbf{Q}_m$ can be decomposed into the active and the passive contributions, so that the musculoskeletal Multi-Body EoM in (146) becomes a linear system in the unknown muscle activation $\mathbf{a}$ and the Lagrange multipliers $\boldsymbol{\lambda}$, which is the tool answering to the inverse dynamics question: what driving and reactions forces are produced during a known kinematics?

$$\begin{gathered} \mathbf{A}^T(\mathbf{F}_{CE}\mathbf{a} + \mathbf{f}_{PE}) - \boldsymbol{\Phi}_\mathbf{q}^T\boldsymbol{\lambda} = \mathbf{M}\ddot{\mathbf{q}} - \mathbf{Q}_v - \mathbf{Q}_e \\ \begin{bmatrix} \mathbf{A}^T\mathbf{F}_{CE} & -\boldsymbol{\Phi}_\mathbf{q}^T \end{bmatrix} \begin{bmatrix} \mathbf{a} \\ \boldsymbol{\lambda} \end{bmatrix} = \mathbf{M}\ddot{\mathbf{q}} - \mathbf{Q}_v - \mathbf{Q}_e - \mathbf{A}^T\mathbf{f}_{PE} \end{gathered} \tag{146}$$

The length of the EoM unknown vector is the number of muscles plus the number of the constraints, which is generally much longer than the number of equations due to the redundancy of the muscular actuation system: there are far more muscles than DoF to move in the musculoskeletal system. As a consequence, the obtained EoM linear system is underdetermined and its solution needs further considerations.

1.6. Musculoskeletal simulation optimizations

1.6.1. Static Optimization

The Multi-Body system EoM in the unknown muscle activations and Lagrange multipliers requires a method to solve the lower number of equations with respect to the unknowns; for a musculoskeletal system the characterization of the criterion adopted by the brain to choose what muscle to activate and with which intensity to produce the given kinematics, matches the need.

In fact it is assumed that the brain makes the above choice by minimizing the effort, the energy required to generate a movement (Silva and Ambrósio, 2003; Silva, Pereira and Martins, 2011; Quental *et al.*, 2013, 2018; Oliveira, 2016; Quental, Folgado and Ambrosio, 2016): the energetic muscle effort can be related to the sum of the squared muscle activations, so the inverse dynamics problem can be set in (147) as the research of the muscle activations (and the Lagrange multipliers) that minimize the effort while subjected to the constraints, to the inertial and the external actions; then, the minimization problem has to be coupled with the linear equality constraint represented by the EoM and with the linear inequality constraints bounding the muscle activations between 0 and 1. Recalling the role of the residual actuators represented by the mobility Lagrange multipliers $\boldsymbol{\lambda}_\mathrm{D}$, also their effort has to be minimized together with the muscles' one.

$$\begin{cases} \min\limits_{\mathbf{a},\boldsymbol{\lambda}} \mathbf{a}^\mathrm{T}\mathbf{a} + \boldsymbol{\lambda}_\mathrm{D}^\mathrm{T}\boldsymbol{\lambda}_\mathrm{D} \\ \begin{bmatrix} \mathbf{A}^\mathrm{T}\mathbf{F}_\mathrm{CE} & -\boldsymbol{\Phi}_\mathbf{q}^\mathrm{T} \end{bmatrix} \begin{bmatrix} \mathbf{a} \\ \boldsymbol{\lambda} \end{bmatrix} = \mathbf{M}\ddot{\mathbf{q}} - \mathbf{Q}_\mathrm{v} - \mathbf{Q}_\mathrm{e} - \mathbf{A}^\mathrm{T}\mathbf{f}_\mathrm{PE} \\ \mathbf{0} \le \mathbf{a} \le \mathbf{1} \end{cases} \tag{147}$$

The above procedure is called "static optimization" since it is performed at each discrete time instant and it can be solved with any optimizer, which can be supplied also by the gradient and the Hessian of the objective function and of the constraints: in this case the constraints are both linear so their gradient is not needed and their Hessian is null, while the objective function is quadratic so its derivatives are straight-forward to derive.

The unknowns are collected in the vector $\mathbf{x}$, so the activations $\mathbf{a}$ and the mobility Lagrange multipliers $\boldsymbol{\lambda}_\mathrm{D}$ can be extracted from $\mathbf{x}$ by the application of the matrices $\mathbf{I}_\mathrm{a}$ and $\mathbf{I}_\mathrm{D}$ (eq. (148)).

$$\mathbf{x} = \begin{bmatrix} \mathbf{a} \\ \boldsymbol{\lambda} \end{bmatrix} = \begin{bmatrix} \mathbf{a} \\ \boldsymbol{\lambda}_\mathrm{C} \\ \boldsymbol{\lambda}_\mathrm{D} \\ \boldsymbol{\lambda}_\mathrm{B} \end{bmatrix} \quad \begin{matrix} \mathbf{a} = \begin{bmatrix} \mathbf{I} & \mathbf{0} & \mathbf{0} & \mathbf{0} \end{bmatrix} \begin{bmatrix} \mathbf{a} \\ \boldsymbol{\lambda}_\mathrm{C} \\ \boldsymbol{\lambda}_\mathrm{D} \\ \boldsymbol{\lambda}_\mathrm{B} \end{bmatrix} = \mathbf{I}_\mathrm{a}\mathbf{x} \\ \boldsymbol{\lambda}_\mathrm{D} = \begin{bmatrix} \mathbf{0} & \mathbf{0} & \mathbf{I} & \mathbf{0} \end{bmatrix} \begin{bmatrix} \mathbf{a} \\ \boldsymbol{\lambda}_\mathrm{C} \\ \boldsymbol{\lambda}_\mathrm{D} \\ \boldsymbol{\lambda}_\mathrm{B} \end{bmatrix} = \mathbf{I}_\mathrm{D}\mathbf{x} \end{matrix} \tag{148}$$

Let highlight in (149) the quadratic form of the objective function f with respect to the unknowns $\mathbf{x}$, so that its gradient $\mathbf{g}$ and its Hessian $\mathbf{H}$ can be easily evaluated,

$$\begin{aligned} &\mathrm{f}(\mathbf{x}) = \mathbf{a}^\mathrm{T}\mathbf{a} + \boldsymbol{\lambda}_\mathrm{D}^\mathrm{T}\boldsymbol{\lambda}_\mathrm{D} = \mathbf{x}^\mathrm{T}\left(\mathbf{I}_\mathrm{a}^\mathrm{T}\mathbf{I}_\mathrm{a} + \mathbf{I}_\mathrm{D}^\mathrm{T}\mathbf{I}_\mathrm{D}\right)\mathbf{x} \\ &\mathbf{g}(\mathbf{x}) = \mathrm{f}_\mathbf{x}^\mathrm{T}(\mathbf{x}) = 2\left(\mathbf{I}_\mathrm{a}^\mathrm{T}\mathbf{I}_\mathrm{a} + \mathbf{I}_\mathrm{D}^\mathrm{T}\mathbf{I}_\mathrm{D}\right)\mathbf{x} \\ &\mathbf{H} = \mathbf{g}_\mathbf{x} = 2\left(\mathbf{I}_\mathrm{a}^\mathrm{T}\mathbf{I}_\mathrm{a} + \mathbf{I}_\mathrm{D}^\mathrm{T}\mathbf{I}_\mathrm{D}\right) \end{aligned} \tag{149}$$

The EoM linear equality constraint is given by the definition in (150) of the matrix $\mathbf{C}$ and the vector $\mathbf{b}$.

$$\mathbf{C} = \begin{bmatrix} \mathbf{A}^\mathrm{T}\mathbf{F}_\mathrm{CE} & -\boldsymbol{\Phi}_\mathbf{q}^\mathrm{T} \end{bmatrix} \quad \mathbf{b} = \mathbf{M}\ddot{\mathbf{q}} - \mathbf{Q}_\mathrm{v} - \mathbf{Q}_\mathrm{e} - \mathbf{A}^\mathrm{T}\mathbf{f}_\mathrm{PE} \tag{150}$$

The activation bounds linear inequality constraints are given by the definition in (151) of the matrix $\mathbf{G}$ and the vector $\mathbf{n}$.

$$\mathbf{G} = \begin{bmatrix} -\mathbf{I}_\mathrm{a} \\ \mathbf{I}_\mathrm{a} \end{bmatrix} \quad \mathbf{n} = \begin{bmatrix} \mathbf{0} \\ \mathbf{1} \end{bmatrix} \tag{151}$$

Finally, the static optimization problem referred to the inverse dynamics of the musculoskeletal system can be written in general form in (152).

$$\begin{cases} \min\limits_{\mathbf{x}} \mathrm{f}(\mathbf{x}) \\ \mathbf{Cx} = \mathbf{b} \\ \mathbf{Gx} \leq \mathbf{n} \end{cases} \tag{152}$$

The above problem represents the last step to completely characterize the inverse dynamics of the musculoskeletal system and it is able to evaluate the muscle activations $\mathbf{a}$ and the Lagrange multipliers $\boldsymbol{\lambda}$ generated by a known kinematics of the system Lagrangian coordinates $\mathbf{q}$, which is in turn produced by a known time evolution of the system DoF $\mathbf{d}$ and governed by the constraint equations $\boldsymbol{\Phi}$ (eq. (153)).

$$\boldsymbol{\Phi}(\mathbf{q}, \mathbf{d}) = \mathbf{0} \quad \begin{cases} \min\limits_{\mathbf{a},\boldsymbol{\lambda}} \mathbf{a}^{\mathrm{T}}\mathbf{a} + \boldsymbol{\lambda}_{\mathrm{D}}^{\mathrm{T}}\boldsymbol{\lambda}_{\mathrm{D}} \\ \begin{bmatrix} \mathbf{A}^{\mathrm{T}}\mathbf{F}_{\mathrm{CE}} & -\boldsymbol{\Phi}_{\mathbf{q}}^{\mathrm{T}} \end{bmatrix} \begin{bmatrix} \mathbf{a} \\ \boldsymbol{\lambda} \end{bmatrix} = \mathbf{M}\ddot{\mathbf{q}} - \mathbf{Q}_{\mathrm{v}} - \mathbf{Q}_{\mathrm{e}} - \mathbf{A}^{\mathrm{T}}\mathbf{f}_{\mathrm{PE}} \\ \mathbf{0} \leq \mathbf{a} \leq \mathbf{1} \end{cases} \tag{153}$$

1.6.2. Inverse Kinematics

In the context of biomechanics simulations, the optimization is widely used also at the kinematical analysis level; the DoF $\mathbf{d}$ of a Multi-Body system, even during an inverse dynamics analysis, are generally unknown, but the musculoskeletal kinematics can be recorded in Motion Capture laboratories with the application of markers on the person skin, so the time evolution of their trajectories over time is available. The procedure that leads to the evaluation of the system DoF that match the recorded marker positions is called inverse kinematics and it is generally conducted with an optimization routine.

With reference to the Figure 31, let say that the k maker is fixed to the body i and located in its frame by the vector $\bar{\mathbf{u}}_{\mathrm{k}}$: then, its global position $\mathbf{r}_{\mathrm{k}}$ can be written in (154) as a function of the body i Lagrangian coordinates.

$$\mathbf{r}_{\mathrm{k}}(\mathbf{q}_{\mathrm{i}}) = \mathbf{t}_{\mathrm{i}} + \mathbf{R}_{\mathrm{i}}\bar{\mathbf{u}}_{\mathrm{k}} \tag{154}$$

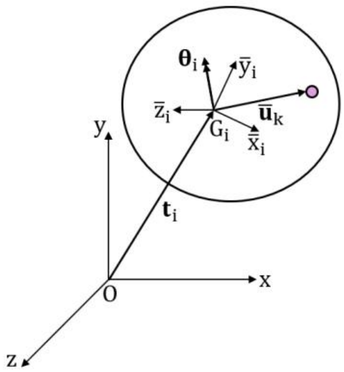

Figure 31 *Marker attached to a rigid body*

The above is extended for a set of n_m markers, introducing the relation (155) between the recorder marker positions $\mathbf{p}$ and the $\mathbf{r}$ ones obtained through the unknown Multi-Body system Lagrangian coordinates $\mathbf{q}$.

$$\begin{bmatrix} \vdots \\ \mathbf{r}_k \\ \vdots \end{bmatrix} = \begin{bmatrix} \vdots \\ \mathbf{t}_i + \mathbf{R}_i \bar{\mathbf{u}}_k \\ \vdots \end{bmatrix} \quad \rightarrow \quad \mathbf{p} = \mathbf{r}(\mathbf{q}) \tag{155}$$

The obtained vector relationship links the $3n_m$ 3D marker positions to the $7(n_B - 1)$ Lagrangian coordinates and no information about the DoF is given at the moment; it is known that the Lagrangian coordinates $\mathbf{q}$ and the DoF $\mathbf{d}$ are related by the constraint equations $\boldsymbol{\Phi}$, which represent the position problem solvable iteratively by the Newton method as described previously: so, if one had the set of DoF $\mathbf{d}$, the marker positions $\mathbf{p}$ could be derived after solving the position problem, as reported in the eq. (156).

$$\mathbf{d} \quad \rightarrow \quad \boldsymbol{\Phi}(\mathbf{q}, \mathbf{d}) = \mathbf{0} \quad \rightarrow \quad \mathbf{p} = \mathbf{r}(\mathbf{q}) \tag{156}$$

The musculoskeletal inverse kinematics is based on the above functional chain: it searches for the set of DoF $\mathbf{d}$ that minimizes the sum of the squared errors $\mathbf{e}$ with respect to the recorder marker positions $\mathbf{p}$ (eq. (157)).

$$\mathbf{e}(\mathbf{d}) = \mathbf{r}\big(\mathbf{q}(\mathbf{d})\big) - \mathbf{p} \quad \rightarrow \quad \min_{\mathbf{d}} \mathbf{e}^T(\mathbf{d})\mathbf{e}(\mathbf{d}) \tag{157}$$

In this case the objective function f is no more quadratic with respect to the minimizing variables, i.e., the DoF $\mathbf{d}$, but its gradient $\mathbf{g}$ can be anyway evaluated by combining the Jacobian $\mathbf{r}_\mathbf{q}$ coming from the variational relationships and the matrix $\mathbf{B}$ relating the virtual Lagrangian displacements to the DoF ones introduced into the embedding technique explanation (eq. (158)).

$$\delta\mathbf{r} = \begin{bmatrix} \vdots \\ \delta\mathbf{r}_k \\ \vdots \end{bmatrix} = \begin{bmatrix} \cdots & \begin{matrix} \vdots \\ [\mathbf{I} \quad -\mathbf{R}_i \tilde{\bar{\mathbf{u}}}_k \bar{\mathbf{G}}_i] \\ \vdots \end{matrix} & \cdots \end{bmatrix} \begin{bmatrix} \vdots \\ \begin{bmatrix} \delta\mathbf{t}_i \\ \delta\boldsymbol{\theta}_i \end{bmatrix} \\ \vdots \end{bmatrix} = \mathbf{r}_\mathbf{q} \delta\mathbf{q} \tag{158}$$

$$\delta\mathbf{q} = \mathbf{B}\delta\mathbf{d}$$

Then, the objective function gradient $\mathbf{g}$ is given in the eq. (159); let note that with this approach the DoF $\mathbf{d}$ and the Lagrangian coordinates $\mathbf{q}$ are simultaneously obtained after the minimization.

$$\begin{matrix} \mathrm{f}(\mathbf{d}) = \mathbf{e}^{\mathrm{T}}(\mathbf{d})\mathbf{e}(\mathbf{d}) \\ \mathrm{f}_{\mathbf{d}} = 2\mathbf{e}^{\mathrm{T}}\mathbf{e}_{\mathbf{d}} = 2\mathbf{e}^{\mathrm{T}}\mathbf{r}_{\mathbf{q}}\mathbf{B} \end{matrix} \rightarrow \quad \mathbf{g} = \mathrm{f}_{\mathbf{d}}^{\mathrm{T}} = 2\mathbf{B}^{\mathrm{T}}\mathbf{r}_{\mathbf{q}}^{\mathrm{T}}\mathbf{e} \tag{159}$$

Finally, once all the introduced and described tools are assembled, a powerful tool that evaluates the muscle activations $\mathbf{a}$ and the Lagrange multipliers $\boldsymbol{\lambda}$ starting from the knowledge of the marker positions $\mathbf{p}$ by solving the inverse kinematics and the inverse dynamics of the Multi-Body musculoskeletal system is developed (eq. (160)).

$$\min_{\mathbf{d}} \mathbf{e}^{\mathrm{T}}(\mathbf{d})\mathbf{e}(\mathbf{d}) \quad \begin{cases} \min\limits_{\mathbf{a},\boldsymbol{\lambda}} \mathbf{a}^{\mathrm{T}}\mathbf{a} + \boldsymbol{\lambda}_{\mathrm{D}}^{\mathrm{T}}\boldsymbol{\lambda}_{\mathrm{D}} \\ \begin{bmatrix} \mathbf{A}^{\mathrm{T}}\mathbf{F}_{\mathrm{CE}} & -\boldsymbol{\Phi}_{\mathbf{q}}^{\mathrm{T}} \end{bmatrix} \begin{bmatrix} \mathbf{a} \\ \boldsymbol{\lambda} \end{bmatrix} = \mathbf{M}\ddot{\mathbf{q}} - \mathbf{Q}_{\mathrm{v}} - \mathbf{Q}_{\mathrm{e}} - \mathbf{A}^{\mathrm{T}}\mathbf{f}_{\mathrm{PE}} \\ \mathbf{0} \leq \mathbf{a} \leq \mathbf{1} \end{cases} \tag{160}$$

1.7. Simulations

In this section the musculoskeletal inverse dynamics simulation results based on the theory developed previously are reported.

The two analysed systems are an upper limb and a lower limb models: the input data are taken from models available on the OpenSim® software, i.e., an open-source software dedicated to the Multi-Body kinematical and dynamical simulations, particularly focused on the biomechanical systems.

The two models shown in the Figure 32 with their bones, muscle red segments and pink markers are:

- the “arm26” musculoskeletal model (Holzbaur, Murray and Delp, 2005) composed by 3 markers, by the humerus and the radius-ulna bodies, by the shoulder and the elbow joints and by 6 muscles being the biceps, the triceps and the brachialis; the system is defined in the torso reference frame (playing the role of the ground) and the joints are able to rotate only in the sagittal (lateral plane), providing the 2 DoF of the mechanism;
- the “gait2392” musculoskeletal model (Yamaguchi and Zajac, 1989; Delp *et al.*, 1990; Anderson and Pandy, 1999, 2001; Arnold *et al.*, 2010) composed by 31 markers,12 bodies, i.e., 3 kinematical open chains being the two legs and the torso converging in the pelvis, by 15 joints providing 23 DoF to the mechanism and by 92 muscles; the system is defined with respect to the ground reference frame from which the ground reaction forces, measured by instrumented platforms during the Motion Capture in terms of components and position of the application point, are applied to the right and the left calcaneus bodies.

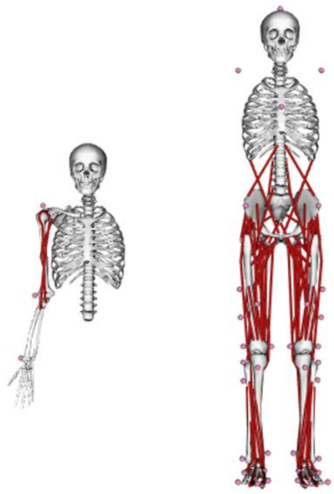

Figure 32 *OpenSim® musculoskeletal models arm26 and gait2392*

The Multi-Body theory developed to perform the inverse dynamics simulation is implemented in this work in a Matlab® code that performs the several phases of the pipeline that starts from the marker trajectories and leads to the muscle activations and the Lagrange multipliers.

The data taken from the OpenSim® models are organized into an excel file that is read by the developed Matlab® script and they are processed; then, the script provides the musculoskeletal system and the output data plots.

Joint angles, joint driving torques, muscle forces and joint reactions regarding the lower limb system simulation will be compared against the OpenSim® software calculations, while the calculated hip joint reactions will be further compared with *in vivo* data discussed in the next.

1.7.1. Upper limb

The excel file referred to the arm26 musculoskeletal system is organized as follows:

- the Body sheet (Figure 33) contains information about the involved bodies' name, mass, inertia tensor and mass centre local position (this latter information is needed since the OpenSim® body frames have the origin in correspondence of the parent joint);

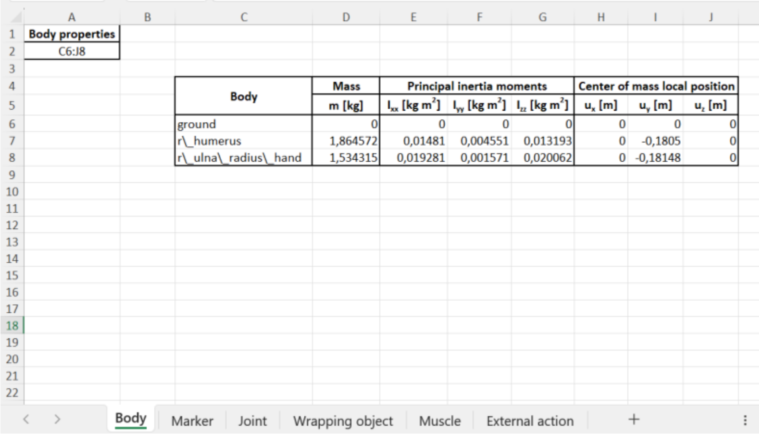

Body	Mass	Principal inertia moments			Center of mass local position		
	m [kg]	I_{xx} [kg m²]	I_{yy} [kg m²]	I_{zz} [kg m²]	u_x [m]	u_y [m]	u_z [m]
ground	0	0	0	0	0	0	0
r_humerus	1,864572	0,01481	0,004551	0,013193	0	-0,1805	0
r_ulna_radius_hand	1,534315	0,019281	0,001571	0,020062	0	-0,18148	0

Figure 33 *Excel input file Body sheet*

- the Marker sheet (Figure 34) contains information about the markers' name, local position with respect to the reference body, the discrete time vector and their trajectories over time;

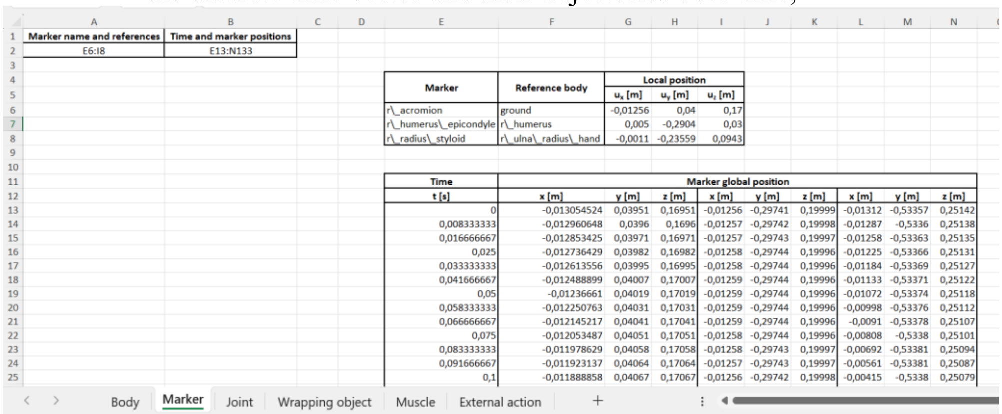

Marker	Reference body	Local position		
		u_x [m]	u_y [m]	u_z [m]
r_acromion	ground	-0,01256	0,04	0,17
r_humerus_epicondyle	r_humerus	0,005	-0,2904	0,03
r_radius_styloid	r_ulna_radius_hand	-0,0011	-0,23559	0,0943

Time	Marker global position								
t [s]	x [m]	y [m]	z [m]	x [m]	y [m]	z [m]	x [m]	y [m]	z [m]
0	-0,013054524	0,03951	0,16951	-0,01256	-0,29741	0,19999	-0,01312	-0,53357	0,25142
0,008333333	-0,012960648	0,0396	0,1696	-0,01257	-0,29742	0,19998	-0,01287	-0,5336	0,25138
0,016666667	-0,012853425	0,03971	0,16971	-0,01257	-0,29743	0,19997	-0,01258	-0,53363	0,25135
0,025	-0,012736429	0,03982	0,16982	-0,01258	-0,29744	0,19996	-0,01225	-0,53366	0,25131
0,033333333	-0,012613556	0,03995	0,16995	-0,01258	-0,29744	0,19996	-0,01184	-0,53369	0,25127
0,041666667	-0,012488899	0,04007	0,17007	-0,01259	-0,29744	0,19996	-0,01133	-0,53371	0,25122
0,05	-0,01236661	0,04019	0,17019	-0,01259	-0,29744	0,19996	-0,01072	-0,53374	0,25118
0,058333333	-0,012250763	0,04031	0,17031	-0,01259	-0,29744	0,19996	-0,00998	-0,53376	0,25112
0,066666667	-0,012145217	0,04041	0,17041	-0,01259	-0,29744	0,19996	-0,0091	-0,53378	0,25107
0,075	-0,012053487	0,04051	0,17051	-0,01258	-0,29744	0,19996	-0,00808	-0,5338	0,25101
0,083333333	-0,011978629	0,04058	0,17058	-0,01258	-0,29743	0,19997	-0,00692	-0,53381	0,25094
0,091666667	-0,011923137	0,04064	0,17064	-0,01257	-0,29743	0,19997	-0,00561	-0,53381	0,25087
0,1	-0,011888858	0,04067	0,17067	-0,01256	-0,29742	0,19998	-0,00415	-0,5338	0,25079

Figure 34 *Excel input file Marker sheet*

- the Joint sheet (Figure 35) contains information about the joints' name, kinematical typology, local position with respect to the parent body, unit vectors along/around which they allow the relative motion, a topology table identifying the parent/child relationship between the bodies though the joints, the DoF name (and a starting trial set for the inverse kinematics) and, eventually, the points to obtain a cam translation law by spline interpolation (the arm26 model has no cam joints);

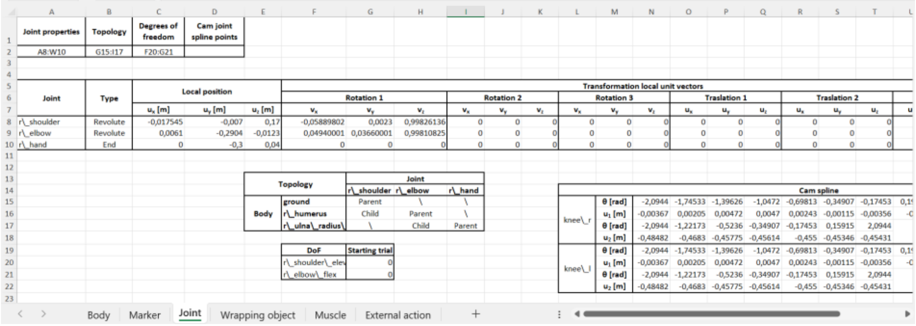

Joint properties	Topology	Degrees of freedom	Cam joint spline points
A8:W10	G15:I17	F20:G21	

Joint	Type	Local position u_x [m]	u_y [m]	u_z [m]	Rotation 1 v_x	v_y	v_z	Rotation 2 v_x	v_y	v_z	Rotation 3 v_x	v_y	v_z	Traslation 1 u_x	u_y	u_z	Traslation 2 u_x	u_y	u_z
r_shoulder	Revolute	-0,017545	-0,007	0,17	-0,05889802	0,0023	0,99826136	0	0	0	0	0	0	0	0	0	0	0	0
r_elbow	Revolute	0,0061	-0,2904	-0,0123	0,04940001	0,03660001	0,99810825	0	0	0	0	0	0	0	0	0	0	0	0
r_hand	End	0	-0,3	0,04	0	0	0	0	0	0	0	0	0	0	0	0	0	0	0

Topology		Joint r_shoulder	r_elbow	r_hand
Body	ground	Parent	\	\
	r_humerus	Child	Parent	\
	r_ulna_radius\	\	Child	Parent

DoF	Starting trial
r_shoulder_elev	0
r_elbow_flex	0

Cam spline								
knee_r	θ [rad]	-2,0944	-1,74533	-1,39626	-1,0472	-0,69813	-0,34907	-0,17453
	u_1 [m]	-0,00367	0,00205	0,00472	0,0047	0,00243	-0,00115	-0,00356
	θ [rad]	-2,0944	-1,22173	-0,5236	-0,34907	-0,17453	0,15915	2,0944
	u_2 [m]	-0,48482	-0,4683	-0,45775	-0,45614	-0,455	-0,45346	-0,45431
knee_l	θ [rad]	-2,0944	-1,74533	-1,39626	-1,0472	-0,69813	-0,34907	-0,17453
	u_1 [m]	-0,00367	0,00205	0,00472	0,0047	0,00243	-0,00115	-0,00356
	θ [rad]	-2,0944	-1,22173	-0,5236	-0,34907	-0,17453	0,15915	2,0944
	u_2 [m]	-0,48482	-0,4683	-0,45775	-0,45614	-0,455	-0,45346	-0,45431

Figure 35 *Excel input file Joint sheet*

- the Wrapping object sheet (Figure 36) contains information about the wrapping surfaces name, geometry, local position and orientation (Euler angles) with respect to the reference body and numerical parameters to simulate the geodesic finite difference marching;

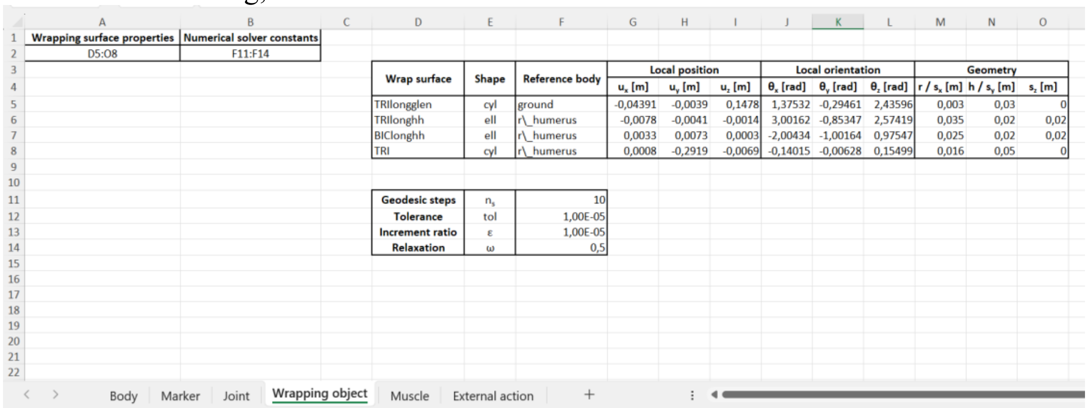

Wrapping surface properties	Numerical solver constants
D5:O8	F11:F14

Wrap surface	Shape	Reference body	Local position u_x [m]	u_y [m]	u_z [m]	Local orientation θ_x [rad]	θ_y [rad]	θ_z [rad]	Geometry r / s_x [m]	h / s_y [m]	s_z [m]
TRIlongglen	cyl	ground	-0,04391	-0,0039	0,1478	1,37532	-0,29461	2,43596	0,003	0,03	0
TRIlonghh	ell	r_humerus	-0,0078	-0,0041	-0,0014	3,00162	-0,85347	2,57419	0,035	0,02	0,02
BIClonghh	ell	r_humerus	0,0033	0,0073	0,0003	-2,00434	-1,00164	0,97547	0,025	0,02	0,02
TRI	cyl	r_humerus	0,0008	-0,2919	-0,0069	-0,14015	-0,00628	0,15499	0,016	0,05	0

Geodesic steps	n_s	10
Tolerance	tol	1,00E-05
Increment ratio	ε	1,00E-05
Relaxation	ω	0,5

Figure 36 *Excel input file Wrapping object sheet*

- the Muscle sheet (Figure 37) contains information about the muscles' name, Hill parameters, attachment points local position with respect to reference bodies and a table identifying which muscle segments is able to curve around the wrapping surfaces;

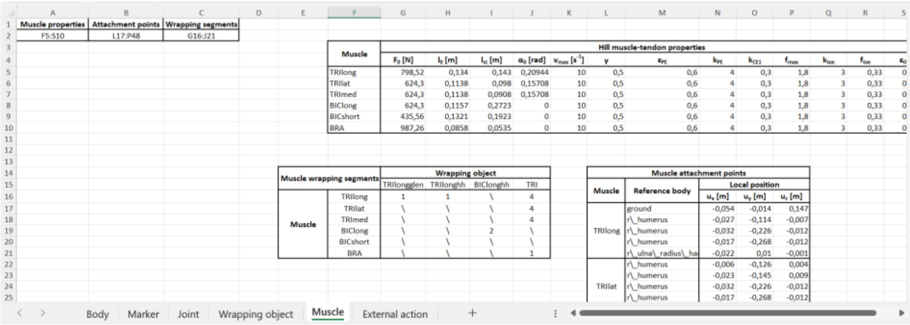

Figure 37 *Excel input file Muscle sheet*

- the External action sheet (Figure 38) contains information about the eventual external forces/torques time evolution, their application point local position with respect to the reference body and the gravity acceleration vector with respect to the ground reference frame (while the external gravity forces are always included in the simulations, the arm26 is not subjected to further external actions).

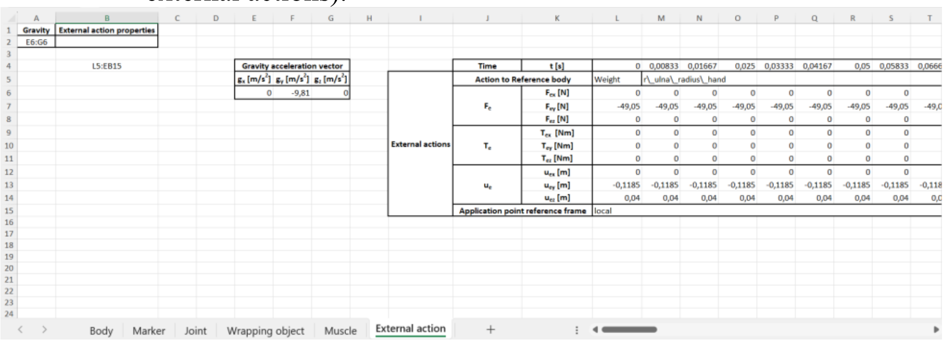

Figure 38 *Excel input file External action sheet*

Starting with the arm26 model simulation, the input marker trajectories are shown in the Figure 39.

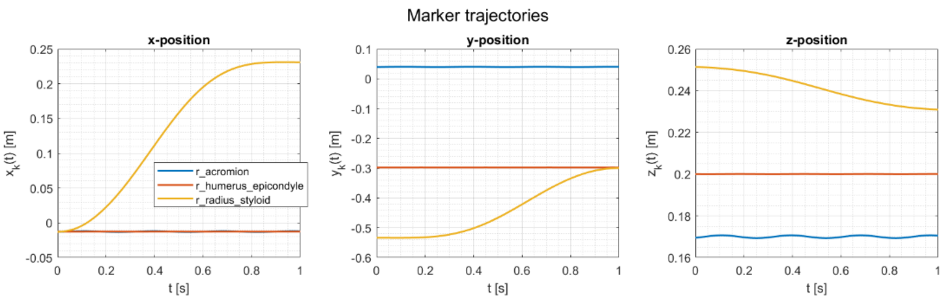

Figure 39 *Marker trajectories for the arm26 model*

The above is represented in the 3D space in the Figure 40 showing that the input kinematics is characterised by a fixed shoulder and by a rotating elbow of about 90° in 1 second: the ground reference frame is shown with the black circle origin and the red-yellow-green xyz axes, while the markers are the pink dots.

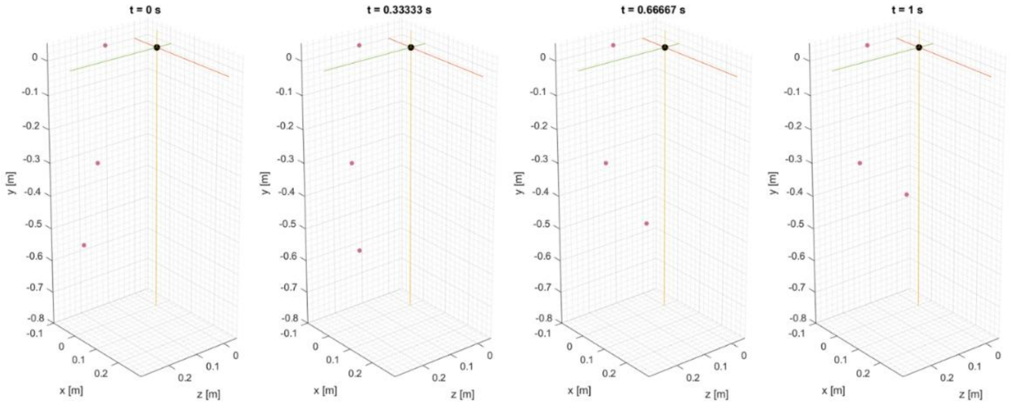

Figure 40 *Markers of the arm26 model*

The inverse kinematics provided the DoF time evolution reported in the Figure 41, i.e., the shoulder and elbow revolute joint angles. It is specified that from here on the labels regarding the DoF will report the measurement units of [m or rad], identifying the [m] measure for the translational DoF or the [rad] for the rotational DoF.

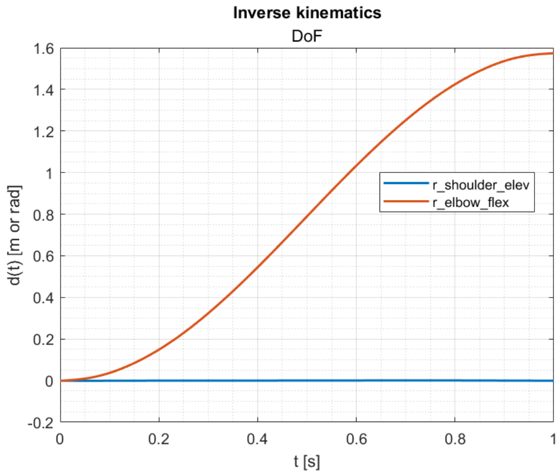

Figure 41 *DoF of the arm26 model*

Recalling that the inverse kinematics elaborates at the same time both the DoF and the system Lagrangian coordinates, the bodies of the musculoskeletal system can be visualised in the Figure 42: they are drawn as black segments, delimited by the joint circles, to which the local reference frames with green mass centre are associated.

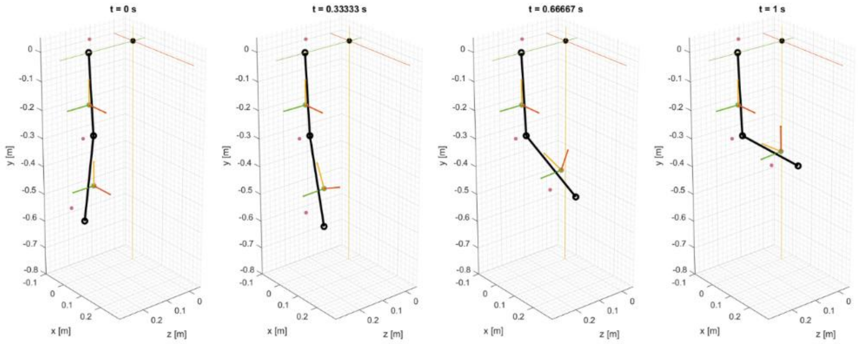

Figure 42 *Bodies of the arm26 model*

At this point, the system Lagrange multipliers in absence of the muscular actuation system are evaluated and depicted in the Figure 43: let recall that they are the responsible for the constraint, mobility and body equations validity, so it could be interesting from the biomechanical point of view to have the net torque at the level of the shoulder and the elbow joints (mobility multipliers) that move the musculoskeletal system according to the provided kinematics. Again, it is specified that from here on the labels regarding the Lagrange multipliers quantities will report the measurement units of [N or Nm], identifying the [N] measure for the multipliers referring to a constraint equation locking a relative translation, i.e., forces, or the [Nm] for the multipliers referring to a constraint equation locking a relative rotation, i.e., torques.

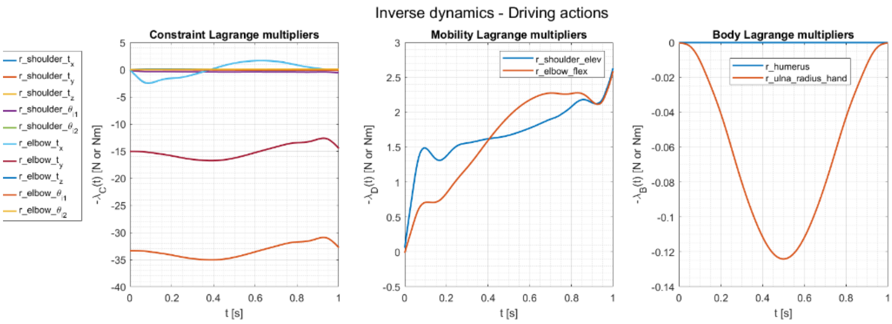

Figure 43 *Lagrange multipliers in absence of muscles for the arm26 model*

In order to introduce the muscular actuation system, the kinematics of the system wrapping surfaces has to be evaluated: they are included in the system plot as cyan surfaces respecting their cylinder/ellipsoid geometries in the Figure 44.

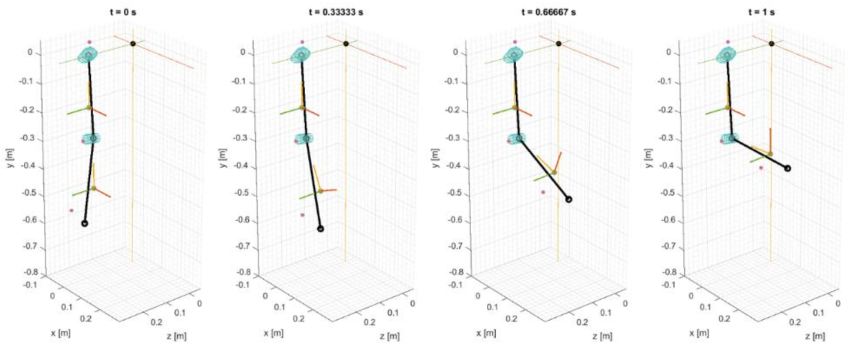

Figure 44 *Wrapping surfaces of the arm26 model*

Then, the muscle path (straight segments and eventual curves) can be evaluated: they are shown in the Figure 45, where the muscles are drawn as blue curves and the zooms about the upper limb wrapping muscles are provided, in particular the long bicep around an ellipsoid fixed to the shoulder, the brachialis around the front part of the cylinder fixed to elbow and the triceps around the back part of the same cylinder.

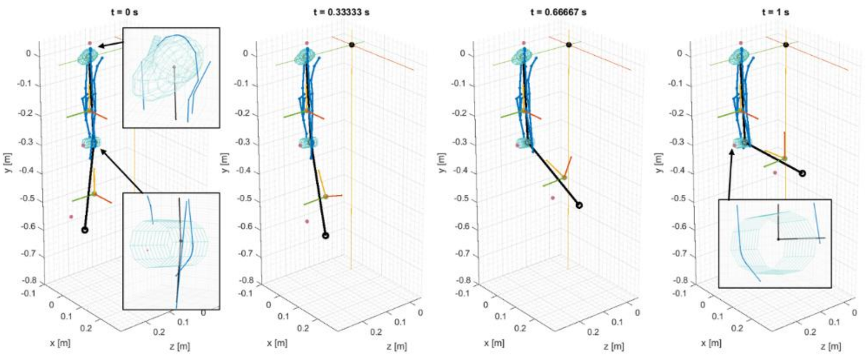

Figure 45 *Muscles of the arm26 model*

At this point, the static optimization provided the muscle activations and the Lagrange multipliers that are produced during the input kinematics: they are shown in the Figure 46, where, in addition to the joint reaction information, one can analyse the role of the muscles during the kinematics, in particular the increasing activation of the long bicep (and the delimited one of the short bicep) to rotate the forearm around the elbow and the activation of the lateral and the medial triceps to brake the rotation in the last part of the movement; it is worth to note that the presence of the residual actions (mobility multipliers) it's useful from the modelling point of view: if the static optimization (that tries to minimize also that residual actions) provides high mobility multipliers, it means that the muscular actuation system is not well modelled, in terms of attachment points location or force production capacity or maybe some muscle is missing, because, due to the EoM constraint, the mobility multipliers will compensate at the DoF level the given muscles' inability to produce the force (and the moments) needed to produce that motion.

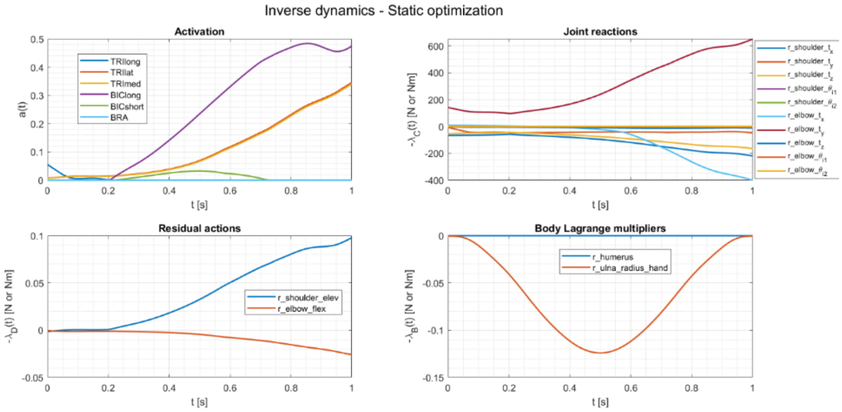

Figure 46 *Muscle activations and Lagrange multipliers for the arm26 model*

Furthermore, the muscle states in terms of force transmitted through the tendon, length and deformation velocity of the muscle fibres and pennation angle can be evaluated: they are shown for the simulated upper limb system in the Figure 47, where it can be appreciated the passive force production of the long tricep (since there was no activation in the previous) and the sudden change in deformation velocity of the triceps and the brachialis muscles due to their wrapping.

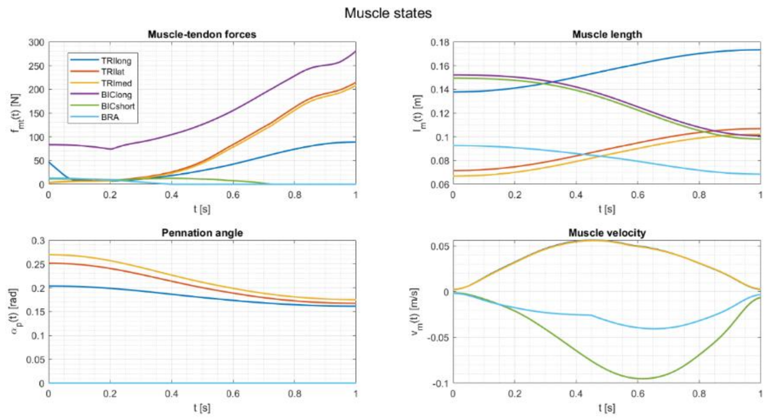

Figure 47 *Muscle states for the arm26 model*

Finally, the simulated upper limb musculoskeletal system is visualised in the Figure 48, where the muscle paths have a colour shade that goes from blue (no activation) to red (full activation).

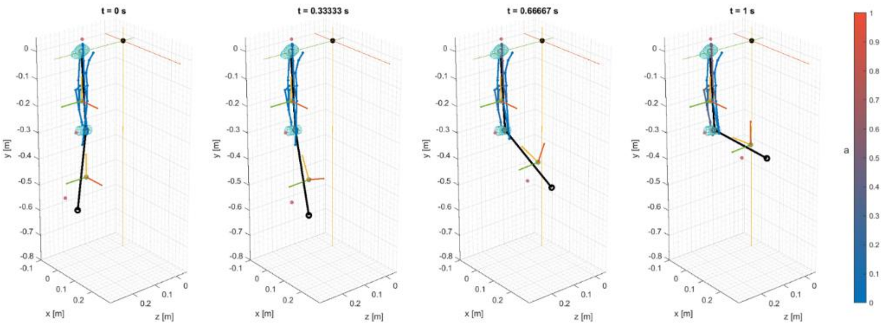

Figure 48 *Solved musculoskeletal system of the arm26 model*

1.7.2. Lower limb

Let move to the lower limb gait2392 musculoskeletal system that will provide the tribological operating conditions in terms of loading and relative motion referred to the hip joint. Since the gait2392 model is characterized by far more data with respect to the arm26 one, only 3 information included in the associated excel input file are shown in the Figure 49, i.e., the joints kinematical typology, the DoF and the topology table.

Joint	Type	Local position			Transformation local unit vectors																	
					Rotation 1			Rotation 2			Rotation 3			Traslation 1			Traslation 2			Traslation 3		
		u_x [m]	u_y [m]	u_z [m]	v_x	v_y	v_z	v_x	v_y	v_z	v_x	v_y	v_z	u_x	u_y	u_z	u_x	u_y	u_z	u_x	u_y	u_z
ground_pelvis	Free	0	0	0	0	0	1	1	0	0	0	1	0	1	0	0	0	1	0	0	0	1
hip_r	Spherical	-0,0707	-0,0661	0,0835	0	0	1	1	0	0	0	1	0	0	0	0	0	0	0	0	0	0
knee_r	Cam	0	0	0	0	0	1	0	0	0	0	0	0	1	0	0	0	1	0	0	0	0
ankle_r	Revolute	0	-0,43	0	-0,105	-0,174	0,97913	0	0	0	0	0	0	0	0	0	0	0	0	0	0	0
subtalar_r	Revolute	-0,0488	-0,042	0,00792	0,78718	0,60475	-0,1209	0	0	0	0	0	0	0	0	0	0	0	0	0	0	0
mtp_r	Revolute	0,1788	-0,002	0,00108	-0,581	0	0,81394	0	0	0	0	0	0	0	0	0	0	0	0	0	0	0
toe_r	End	0,045	0	0	0	0	0	0	0	0	0	0	0	0	0	0	0	0	0	0	0	0
hip_l	Spherical	-0,0707	-0,0661	-0,0835	0	0	1	-1	0	0	0	-1	0	0	0	0	0	0	0	0	0	0
knee_l	Cam	0	0	0	0	0	1	0	0	0	0	0	0	1	0	0	0	1	0	0	0	0
ankle_l	Revolute	0	-0,43	0	0,10501	0,17402	0,97913	0	0	0	0	0	0	0	0	0	0	0	0	0	0	0
subtalar_l	Revolute	-0,0488	-0,042	-0,0079	-0,7872	-0,6047	-0,1209	0	0	0	0	0	0	0	0	0	0	0	0	0	0	0
mtp_l	Revolute	0,1788	-0,002	-0,0011	0,58095	0	0,81394	0	0	0	0	0	0	0	0	0	0	0	0	0	0	0
toe_l	End	0,045	0	0	0	0	0	0	0	0	0	0	0	0	0	0	0	0	0	0	0	0
back	Spherical	-0,1007	0,0815	0	0	0	1	1	0	0	0	1	0	0	0	0	0	0	0	0	0	0
spine	End	0	0,5	0	0	0	0	0	0	0	0	0	0	0	0	0	0	0	0	0	0	0

DoF
pelvis_tilt
pelvis_list
pelvis_rotation
pelvis_tx
pelvis_ty
pelvis_tz
hip_flexion_r
hip_adduction_r
hip_rotation_r
knee_angle_r
ankle_angle_r
subtalar_angle_r
mtp_angle_r
hip_flexion_l
hip_adduction_l
hip_rotation_l
knee_angle_l
ankle_angle_l
subtalar_angle_l
mtp_angle_l
lumbar_extension
lumbar_bending
lumbar_rotation

Topology		Joint														
		round_pelvi	hip_r	knee_r	ankle_r	ubtalar_	mtp_r	toe_r	hip_l	knee_l	ankle_l	ubtalar_	mtp_l	toe_l	back	spine
Body	ground	Parent	\	\	\	\	\	\	\	\	\	\	\	\	\	\
	pelvis	Child	Parent	\	\	\	\	\	Parent	\	\	\	\	\	Parent	\
	femur_r	\	Child	Parent	\	\	\	\	\	\	\	\	\	\	\	\
	tibia_r	\	\	Child	Parent	\	\	\	\	\	\	\	\	\	\	\
	talus_r	\	\	\	Child	Parent	\	\	\	\	\	\	\	\	\	\
	calcn_r	\	\	\	\	Child	Parent	\	\	\	\	\	\	\	\	\
	toes_r	\	\	\	\	\	Child	Parent	\	\	\	\	\	\	\	\
	femur_l	\	\	\	\	\	\	\	Child	Parent	\	\	\	\	\	\
	tibia_l	\	\	\	\	\	\	\	\	Child	Parent	\	\	\	\	\
	talus_l	\	\	\	\	\	\	\	\	\	Child	Parent	\	\	\	\
	calcn_l	\	\	\	\	\	\	\	\	\	\	Child	Parent	\	\	\
	toes_l	\	\	\	\	\	\	\	\	\	\	\	Child	Parent	\	\
	torso	\	\	\	\	\	\	\	\	\	\	\	\	\	Child	Parent

Figure 49 *Joints, DoF and topology of the gait2392 model*

The marker trajectories for the gait2392 model are depicted in the Figure 50.

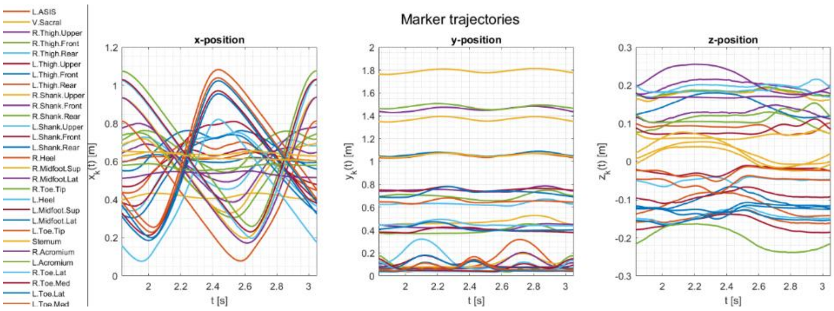

Figure 50 *Marker trajectories for the gait2392 model*

The above kinematic input refers to a gait cycle, i.e., the normal walking starting with the stance phase when the right heel strikes the ground, proceeding to the swing phase when the right foot toes leave the ground and ending in correspondence of the next ground heel strike: it lasts for about one second and the marker trajectories in the 3D space reported in the Figure 51 give a better sketch.

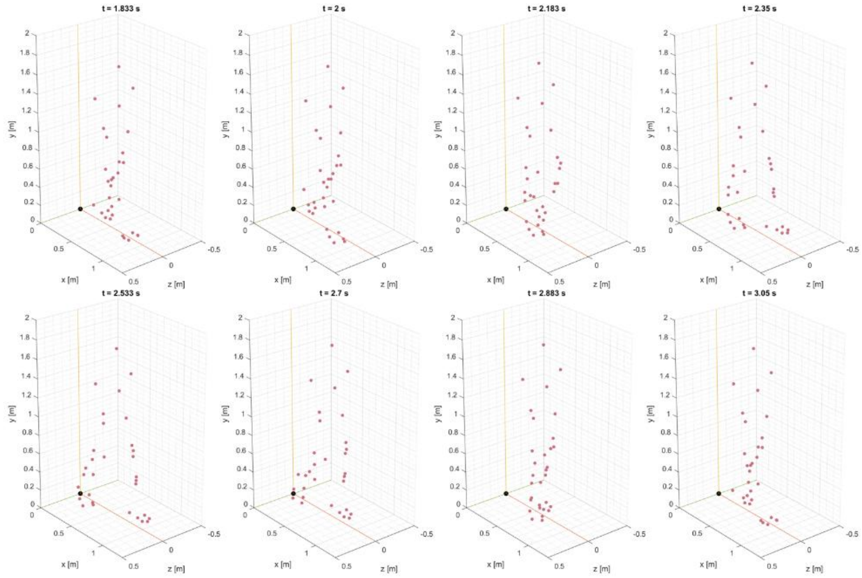

Figure 51 *Markers of the gait2392 model*

The inverse kinematics provided the lower limb DoF during the gait cycle: in the Figure 52 the time evolution of the DoF referred to the right leg main joints is reported, i.e., the 3 hip rotations (flexion/extension, adduction/abduction and internal/external rotation), the knee and the ankle rotations; the same joint angles computed by the OpenSim® routine are reported in the same graph.

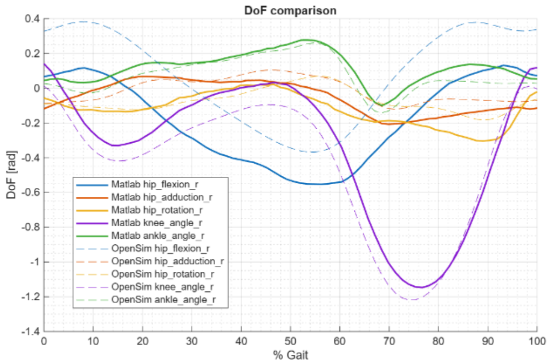

Figure 52 *Right leg DoF of the gait2392 model*

A quantitative comparison between the angles computed by the proposed model and the OpenSim® software is given in the Figure 53 reporting the error metrics of Normalised Root Mean Square Error, NRMSE, and correlation coefficient R.

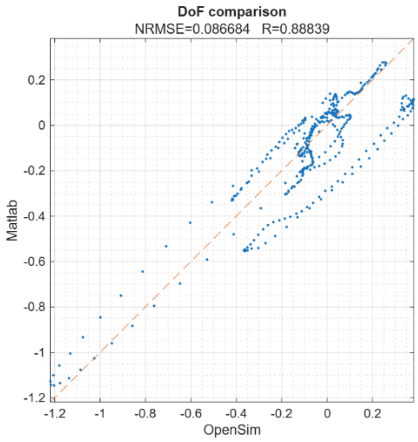

Figure 53 *Right leg DoF error metrics between Matlab® and OpenSim®*

Again, the bodies configuration can be evaluated: in the Figure 54 they are shown together with the ground reaction forces represented by the 2 green arrows rising from the ground when the feet are in their stance phase.

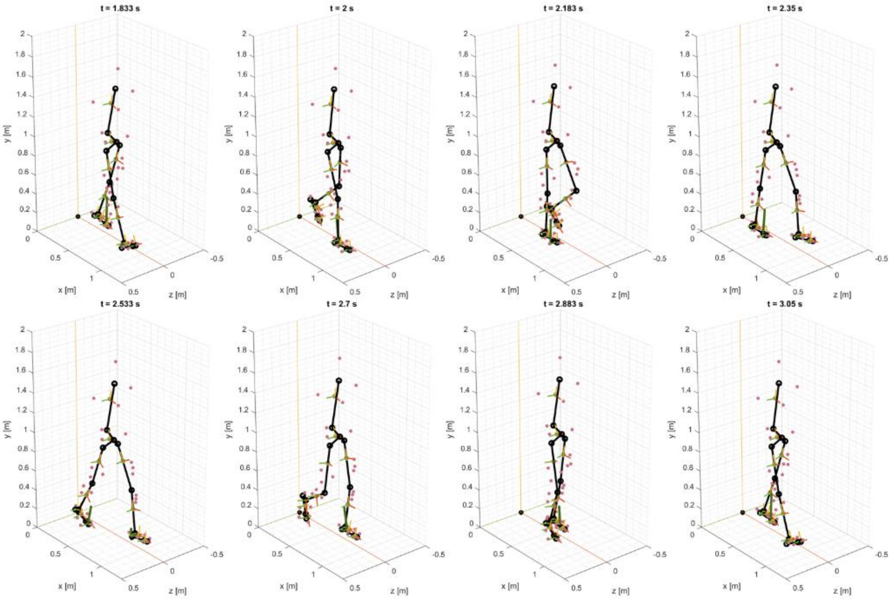

Figure 54 *Bodies and ground reaction forces of the gait2392 model*

The two ground reaction forces applied to the right and the left calcaneus bodies are depicted in the Figure 55 in terms of force/torque components and coordinates of the application point (in this case with respect to the ground).

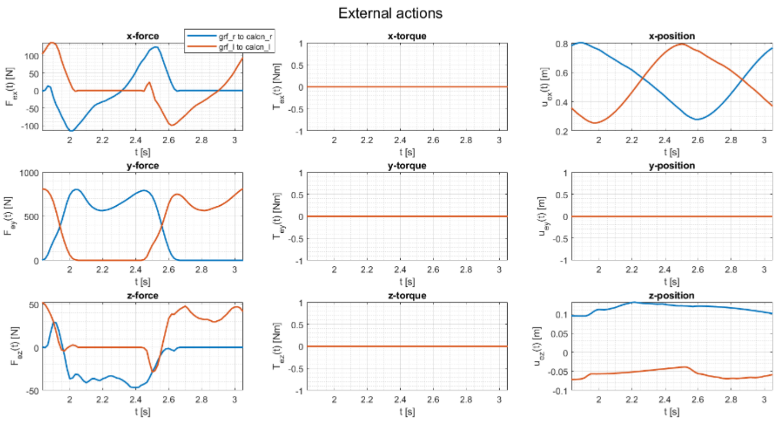

Figure 55 *Ground reaction forces of the gait2392 model*

The above is enough to evaluate the lower limb musculoskeletal system Lagrange multiplier in absence of muscles: in the Figure 56 the Lagrange multipliers referred to the right leg main bodies and joints, i.e., femur/tibia/calcaneus and hip/knee/ankle, are shown; again, it is interesting to evaluate the driving net torques that move the hip, the knee and the ankle DoF during the gait cycle.

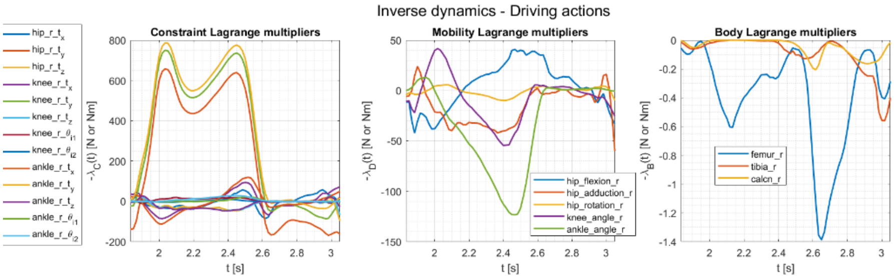

Figure 56 *Right leg Lagrange multipliers in absence of muscles for the gait2392 model*

A further comparison with respect to the OpenSim® benchmark at the level of the joint net torques, i.e., the driving forces represented by the mobility Lagrange multipliers reported in the Figure 56, is given in the Figure 57.

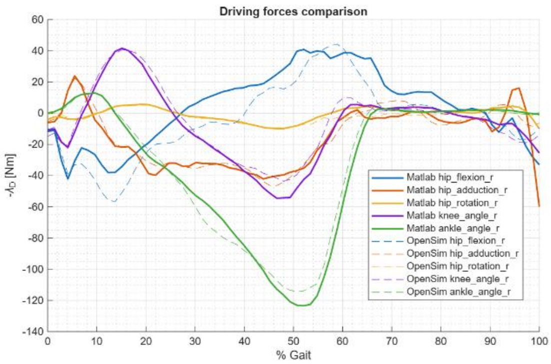

Figure 57 *Right leg net torques of the gait2392 model*

The error metrics referred to the data in the Figure 57 are reported in the Figure 58.

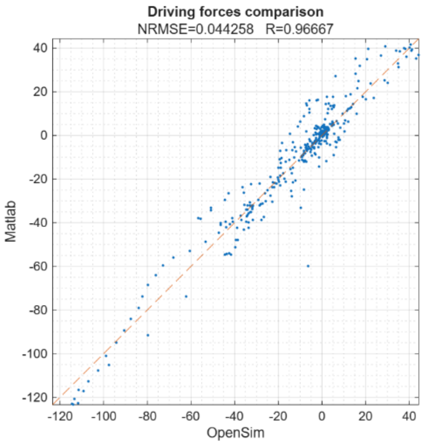

Figure 58 *Right leg joint net torques error metrics between Matlab® and OpenSim®*

Then, the kinematics of the wrapping surfaces included in the gait2392 system is identified and reported in the Figure 59.

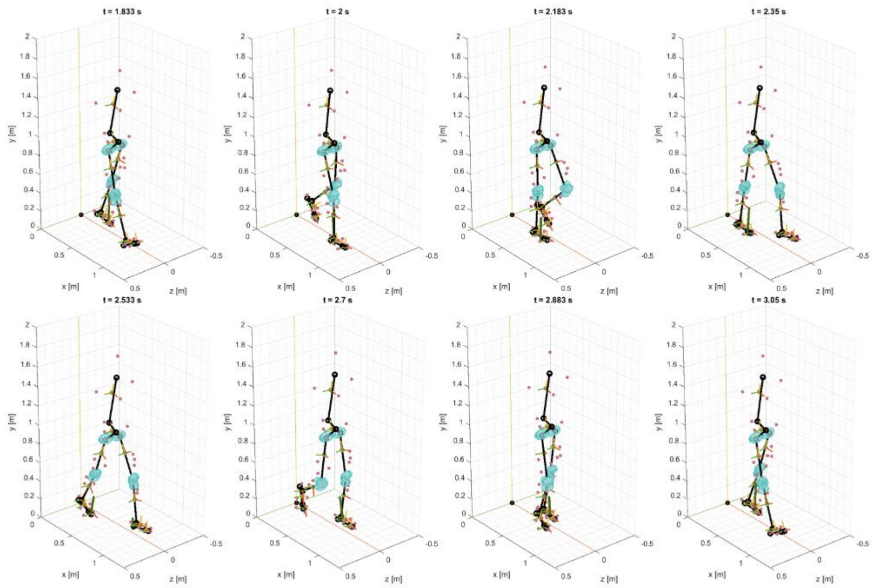

Figure 59 *Wrapping surfaces of the gait2392 model*

Hence, the muscle paths are evaluated and shown in the Figure 60.

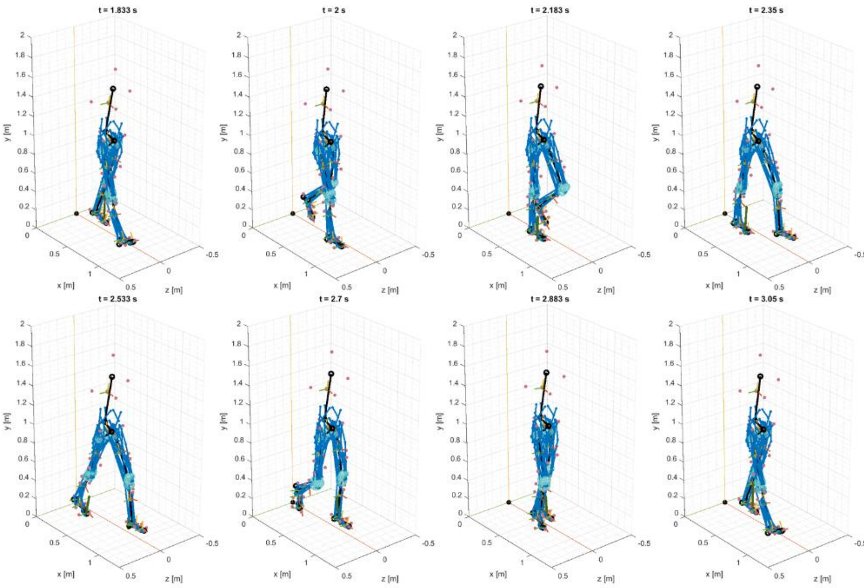

Figure 60 *Muscles of the gait2392 model*

Therefore, the static optimization is conducted and the muscle activations and Lagrange multipliers are evaluated. In the Figure 61 the following is shown:

- activations referred to 4 muscles devoted to the hip abduction/adduction and flexion/extension, i.e., gluteus medius/pectineus and iliacus/gluteus maximus, to 2 muscles devoted to the knee bending/extension, i.e., long biceps femoris/rectus femoris, and to 2 muscles devoted to the ankle plantarflexion/dorsiflexion, i.e., soleus/tibialis anterior;
- constraint and mobility Lagrange multipliers referred to the main right leg joints, i.e., the hip, the knee and the ankle;
- body Lagrange multipliers referred to the main right leg bodies, i.e., the femur, the tibia and the calcaneus.

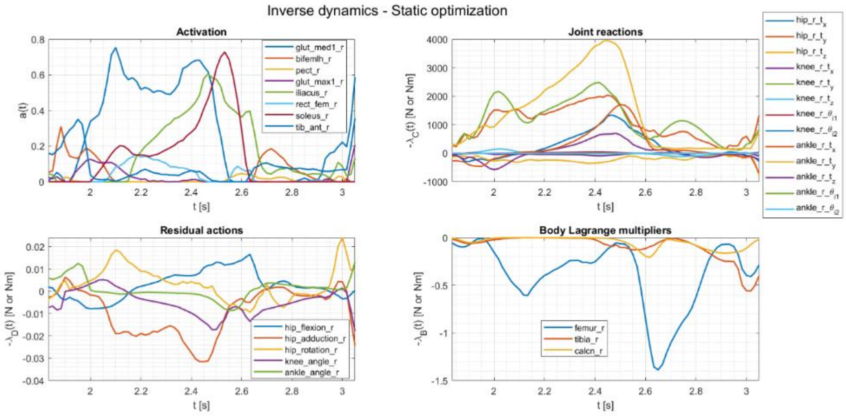

Figure 61 *Right leg muscle activations and Lagrange multipliers for the gait2392 model*

Finally, the states referred to the same muscles are reported in the Figure 62.

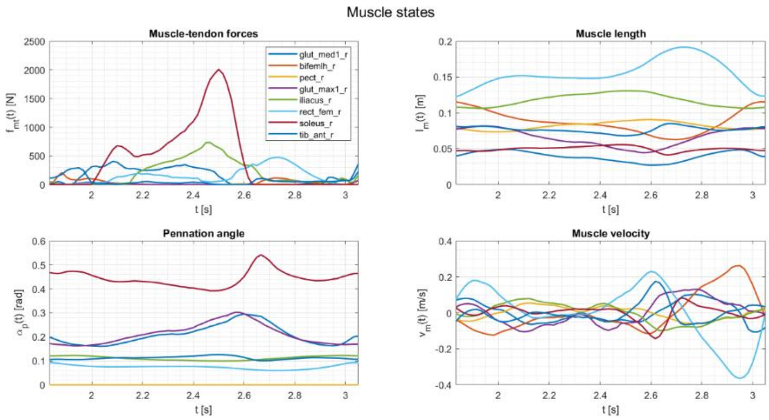

Figure 62 *Right leg muscle states for the gait2392 model*

Before proceeding with the visualization of the solved lower limb musculoskeletal system, two further comparisons with respect to the OpenSim® simulation are given:

- the one associated with the muscle forces generated by the gluteus medius, the iliacus and soleus muscles (time evolution in the Figure 63 and error metrics in the Figure 64);
- the one associated with the hip joint reactions (time evolution in the Figure 65 and error metrics in the Figure 66).

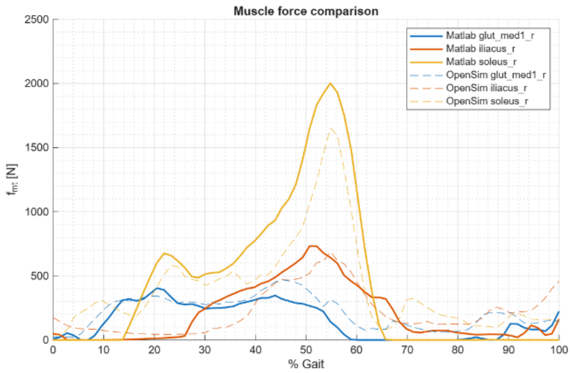

Figure 63 *Right leg muscle forces of the gait2392 model*

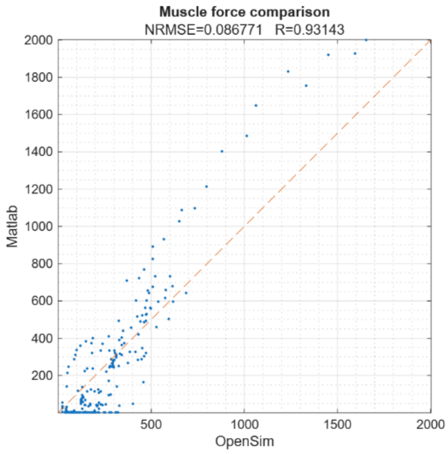

Figure 64 *Right leg muscle forces error metrics between Matlab® and OpenSim®*

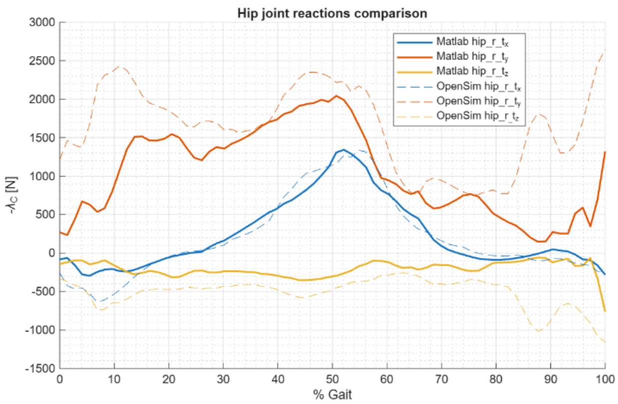

Figure 65 *Hip joint reactions of the gait2392 model*

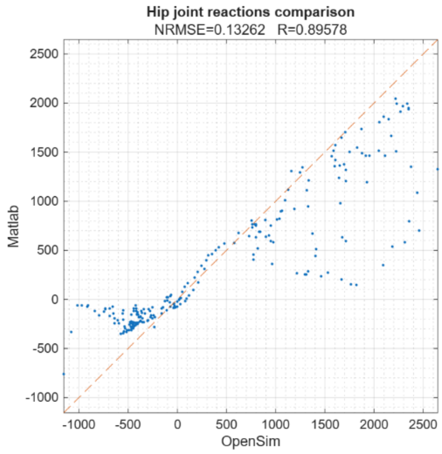

Figure 66 *Hip joint reactions error metrics between Matlab® and OpenSim®*

Lastly, the solved lower limb musculoskeletal system is visualised in the Figure 67, with the muscles coloured based on their activations.

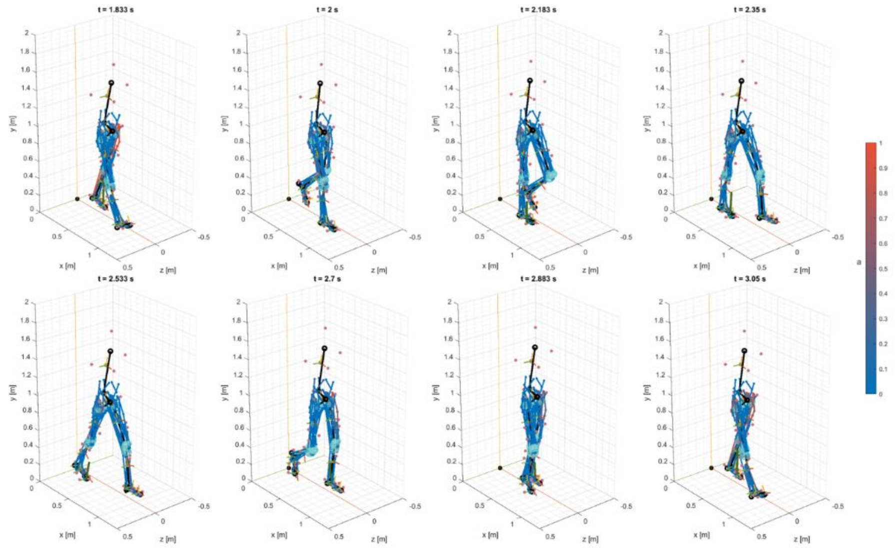

Figure 67 *Solved musculoskeletal system of the gait2392 model*

Among all the outputs that could be of interest from a biomechanical point of view, surely in this work the hip joint loading and relative motion are of great importance for the next tribological part. In order to elaborate them, let focus on the constraint generalised force vector $\mathbf{Q}_\lambda$ in the eq. (161).

$$\mathbf{Q}_\lambda = -\mathbf{\Phi}_\mathbf{q}^\mathrm{T}\boldsymbol{\lambda} \tag{161}$$

Let focus now on the contributions to $\mathbf{Q}_\lambda$ provided by the right hip joint J that links the pelvis parent body i to the right femur child body j from the constraint point of view (we are interested into the constraint and not the mobility of the joint): the related contributions $\mathbf{Q}_{\lambda\mathrm{Ci}}$ and $\mathbf{Q}_{\lambda\mathrm{Cj}}$ are obtained in (162) by projecting the hip constraint multipliers $\boldsymbol{\lambda}_{\mathrm{CJ}}$ in the Multi-Body system space through the respective sub-blocks of the constraint Jacobian $\mathbf{C}_{\mathbf{q}}$.

$$\begin{bmatrix}\mathbf{Q}_{\lambda\mathrm{Ci}}\\ \mathbf{Q}_{\lambda\mathrm{Cj}}\end{bmatrix} = -\begin{bmatrix}\mathbf{C}_{\mathbf{q}\mathrm{Ji}}^{\mathrm{T}}\\ \mathbf{C}_{\mathbf{q}\mathrm{Jj}}^{\mathrm{T}}\end{bmatrix}\boldsymbol{\lambda}_{\mathrm{CJ}} \tag{162}$$

Let refer now to the forces that load the femur body $\mathbf{F}_{\mathrm{CJj}}$ ($\mathbf{T}_{\mathrm{CJj}}$ is a 4x1 vector representing a rotational action affecting the body j quaternion): let rotate them in the femur frame by the means of its rotation matrix $\mathbf{R}_{\mathrm{j}}$ to obtain the hip-in-femur loads $\bar{\mathbf{F}}_{\mathrm{CJj}}$ in (163), which components refer to the Anterior/Posterior, Proximal/Distal and Medial/Lateral direction**.**

$$\mathbf{Q}_{\lambda\mathrm{Cj}} = -\mathbf{C}_{\mathbf{q}\mathrm{Jj}}^{\mathrm{T}}\boldsymbol{\lambda}_{\mathrm{CJ}} = \begin{bmatrix}\mathbf{F}_{\mathrm{CJj}}\\ \mathbf{T}_{\mathrm{CJj}}\end{bmatrix} \rightarrow \quad \bar{\mathbf{F}}_{\mathrm{CJj}} = \mathbf{R}_{\mathrm{j}}^{\mathrm{T}}\mathbf{F}_{\mathrm{CJj}} = \begin{bmatrix}\mathrm{F}_{\mathrm{AP}}\\ \mathrm{F}_{\mathrm{PD}}\\ \mathrm{F}_{\mathrm{ML}}\end{bmatrix} \tag{163}$$

The obtained hip loads in the femur frame $\bar{\mathbf{F}}_{\mathrm{CJj}}$ can be directly compared with the well-known Bergmann loads, i.e., average hip loads during the gait cycle obtained *in vivo* from experiments in which instrumented artificial hip joints were implanted into a wide set of subjects (Bergmann *et al.*, 2016): this provides a reliable benchmark for the biomechanical simulations. The comparison between the hip loads *in silico* (obtained in this work) and *in vivo* (given by Bergmann) for the gait cycle kinematics is provided in the Figure 68 with the related error metrics, demonstrating a good reliability of the developed computational tool.

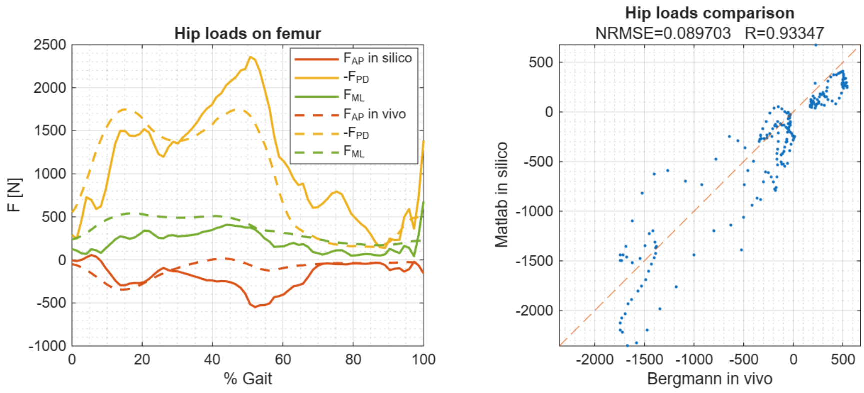

Figure 68 *Hip loads comparison with Bergmann in vivo measurements*

Then, the hip relative motion is identified by the angular velocity vector $\bar{\boldsymbol{\omega}}_{\mathrm{Jj}}$ in the eq. (164), which is obtained with the difference between the femur body j and the pelvis body i global velocities (through the bodies quaternion $\boldsymbol{\theta}_{\mathrm{i}}$, $\boldsymbol{\theta}_{\mathrm{j}}$ and time derivatives $\dot{\boldsymbol{\theta}}_{\mathrm{i}}$, $\dot{\boldsymbol{\theta}}_{\mathrm{j}}$) and then rotated in the femur reference frame.

$$\begin{matrix} \boldsymbol{\omega}_{\mathrm{i}} = \mathbf{G}_{\mathrm{i}}\dot{\boldsymbol{\theta}}_{\mathrm{i}} \\ \boldsymbol{\omega}_{\mathrm{j}} = \mathbf{G}_{\mathrm{j}}\dot{\boldsymbol{\theta}}_{\mathrm{j}} \end{matrix} \quad \rightarrow \quad \overline{\boldsymbol{\omega}}_{\mathrm{Jj}} = \mathbf{R}_{\mathrm{j}}^{\mathrm{T}}\left(\boldsymbol{\omega}_{\mathrm{j}} - \boldsymbol{\omega}_{\mathrm{i}}\right) = \begin{bmatrix} \omega_{\mathrm{AP}} \\ \omega_{\mathrm{PD}} \\ \omega_{\mathrm{ML}} \end{bmatrix} \tag{164}$$

The obtained relative angular velocity is shown in the Figure 69 with the hip loads: the two vectors together are the tribological operating conditions affecting the lubrication/contact regime governing the interaction between the acetabular cup and the femoral head surfaces during the gait cycle.

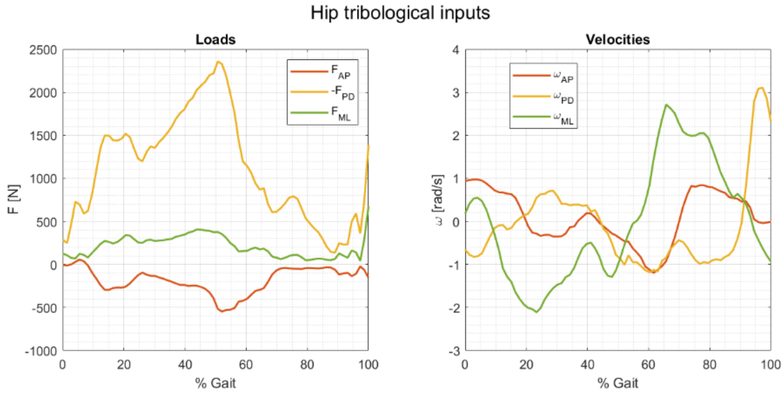

Figure 69 *Gait cycle hip loads and velocities*

The results obtained in the biomechanics part of this work refer to the manuscripts produced by the author (Ruggiero and Sicilia, 2020b, 2021a, 2022a, 2022c, 2024; Sicilia, De Stefano and Ruggiero, 2024).

2. Tribology

In this chapter the techniques adopted by the author to numerically simulate the lubrication/contact regime governing the interaction between the conjugated surfaces composing a tribo-system are discussed. While the numerical strategies to model the main lubrication modes, i.e., HL, EHL and ML, are presented, a particular focus is devoted to the implementation of three deformation models (spring, FEM and BEM) and to the implication of their introduction into the numerical solving of the Reynolds lubrication equation; furthermore, the ML modelling will take into account two strategies to handle the coexistence between fluid and contact pressure within the couple, i.e., the splitting pressure approach for the associated THR simulation and the unified pressure approach for the rectangular tribo-system simulation, while introducing also DCM solvers, roughness generation and surface wear. Then, three simulations are presented:

- the ML of THR with operating conditions coming from the inverse dynamics Multi-Body results, providing an estimation of the implant wear during the gait cycle kinematics;
- the EHL of a ball-in-socket tribo-system which deformation is obtained by a FEM model;
- the ML of a rectangular tribo-system with BEM deformation model considering the unified pressure approach, the roughness and the wear, which is compared also with the results of the associated simulation in DCM regime.

Finally, the last section is devoted to the transient EHL modelling, where the author focused on the coupling of the lubrication, the gap and load balance equations providing a DAE system that is marched over time with several implicit integrators and for different sliding and loading time-varying inputs, giving interesting discussions about the waves characterising the transient phase of line-contact systems.

2.1. Hydrodynamic Lubrication

Let recall that the Reynolds lubrication equation (Reynolds, 1886) in the system (165) is conceived for HL regime, so, since the surfaces are rigid (the gap h is not dependent on the lubricant pressure p, but it comes from the normal shift of the geometrical gap g by the approach δ) and the lubricant fluid is iso-viscous (the viscosity μ is a constant), it is a linear elliptical PDE in the pressure p unknown that has to balance the external applied load N; from a conceptual point of view:

- the geometrical gap g and the surfaces' tangential velocities $\mathbf{U}$ generate positive lubricant pressure p in the zones of the domain Ω characterised by channels converging along the sliding direction through the Couette flow velocity, i.e., the first right-hand-side term;
- the load balance demands lubricant pressure p to match the applied load N and, even if not directly, it acts on the surfaces' rigid approach δ providing pressure by constraining the lubricant to flow across narrow channels and by affecting the squeeze flow velocity, i.e., the second right-hand-side term;
- the interplay between the given sliding effect, i.e., the surfaces' tangential relative motion, and the squeeze effect, i.e., the surfaces' normal relative motion triggered by the given normal load, determines the pressure generation through the Poiseuille flow velocity, i.e., the left-hand-side term dealing with the lubricant pressure gradients.

$$\begin{cases} \boldsymbol{\nabla}\cdot\left(\dfrac{h^3}{12\mu}\boldsymbol{\nabla}p\right) = \boldsymbol{\nabla}\cdot(h\mathbf{U}) + \dfrac{\partial h}{\partial t} \\ h(\mathbf{x},t) = g(\mathbf{x}) - \delta(t) \\ N(t) = \displaystyle\int_{\Omega} p(\mathbf{x},t)\,dA \end{cases} \tag{165}$$

Before addressing the numerical discretization of the Reynolds equation, let introduce some interesting tribological quantities coming from the fluid dynamics of the full-film lubricated system in hydrodynamic regime.

With reference to the Figure 10, given the lower surface velocities vector $\mathbf{U}_1$ and the upper one $\mathbf{U}_2$, the so called entraining velocity $\mathbf{U}$ appearing in the Reynolds equation is given in (166) by the surfaces' velocities arithmetical average, while the sliding velocity vector $\mathbf{V}$ is defined through their difference; let note that the surfaces' velocities are generally time-varying inputs constant everywhere over the domain Ω, but they can exhibit a spatial variation in case of particular tribo-system geometries, e.g., the spherical one that will be addressed in the next.

$$\mathbf{U} = \frac{\mathbf{U}_1 + \mathbf{U}_2}{2} \quad \mathbf{V} = \mathbf{U}_2 - \mathbf{U}_1 \tag{166}$$

Defining with y the normal contact axis that goes from 0 to the gap h in a general position of the contact domain $\mathbf{x}$, the fluid tangential velocity vector $\mathbf{u}$ is given in (167) by the superposition of the Poiseuille contribution (dependent on the lubricant pressure gradient and quadratic with respect to y) and the Couette one (dealing with the sliding velocity and linear with respect to y).

$$\mathbf{u}(\mathbf{x},y,t) = -\frac{1}{2\mu}\boldsymbol{\nabla}p(hy - y^2) + \frac{\mathbf{V}}{h}y + \mathbf{U}_1 \tag{167}$$

The fluid shear stress vector $\boldsymbol{\tau}$ is obtained in (168) according to the Reynolds hypothesis of Newtonian fluid.

$$\boldsymbol{\tau}(\mathbf{x},y,t) = \mu\frac{\partial\mathbf{u}}{\partial y} = -\frac{1}{2}\boldsymbol{\nabla}p(h - 2y) + \mu\frac{\mathbf{V}}{h} \tag{168}$$

In order to define the surfaces shear stresses $\boldsymbol{\tau}_1$ and $\boldsymbol{\tau}_2$ in (169), the (168) has to be evaluated in correspondence of y equal to 0 for the lower surface and equal to h for the upper one.

$$\begin{aligned}\boldsymbol{\tau}_1(\mathbf{x},t) &= \boldsymbol{\tau}(\mathbf{x},0,t) = -\frac{h}{2}\boldsymbol{\nabla}p + \mu\frac{\mathbf{V}}{h}\\ \boldsymbol{\tau}_2(\mathbf{x},t) &= -\boldsymbol{\tau}(\mathbf{x},h,t) = -\frac{h}{2}\boldsymbol{\nabla}p - \mu\frac{\mathbf{V}}{h}\end{aligned} \tag{169}$$

Therefore, the surfaces tangential viscous forces $\mathbf{T}_1$ and $\mathbf{T}_2$ resulting from the tribo-system lubrication are evaluated in (170) by integrating the related shear stress over the domain surface.

$$\mathbf{T}_1(t) = \int_\Omega \boldsymbol{\tau}_1(\mathbf{x},t)\,dA \quad \mathbf{T}_2(t) = \int_\Omega \boldsymbol{\tau}_2(\mathbf{x},t)\,dA \tag{170}$$

Finally, the viscous friction coefficients vectors $\mathbf{f}_1$ and $\mathbf{f}_2$ can be obtained by a Coulomb-like friction law in (171) accounting for the given normal load.

$$\mathbf{f}_1(t) = \frac{|\mathbf{T}_1(t)|}{N(t)} \quad \mathbf{f}_2(t) = \frac{|\mathbf{T}_2(t)|}{N(t)} \tag{171}$$

The described lubrication actors are shown in a cartesian coordinates domain in the Figure 70.

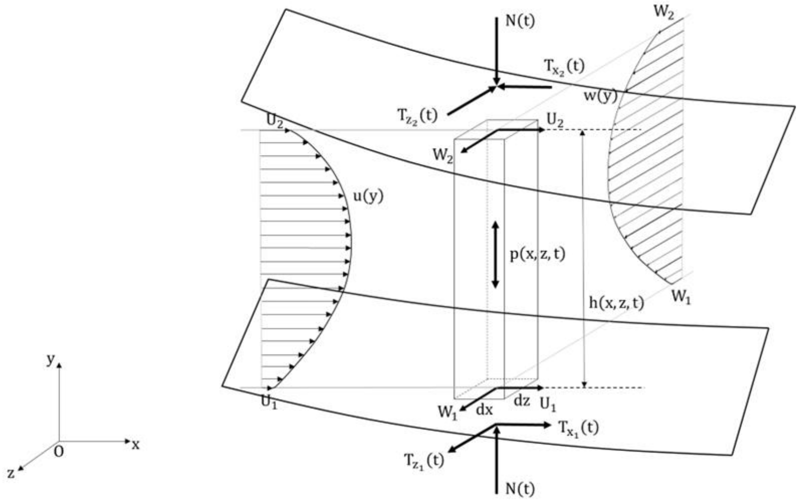

Figure 70 *Lubrication configuration of a cartesian coordinates system*

The HL lubrication eqs. (165) in cartesian coordinates are reported in (172).

$$\begin{cases} \dfrac{\partial}{\partial x}\left(\dfrac{h^3}{12\mu}\dfrac{\partial p}{\partial x}\right)+\dfrac{\partial}{\partial z}\left(\dfrac{h^3}{12\mu}\dfrac{\partial p}{\partial z}\right)=\dfrac{\partial(hU)}{\partial x}+\dfrac{\partial(hW)}{\partial z}+\dfrac{\partial h}{\partial t} \\ h(x,z,t)=g(x,z)-\delta(t) \\ N(t)=\displaystyle\iint_{\Omega} p(x,z,t)\,dxdz \end{cases} \tag{172}$$

2.1.1. Finite Difference discretization

With the aim to numerically solve the HL problem for a given approach δ with the Finite Difference Method (FDM), let refer to the Reynolds equation in (173) coupled with the Dirichlet boundary conditions of zero pressure on the domain bounds $\partial\Omega$.

$$\begin{cases} \dfrac{\partial}{\partial x}\left(\dfrac{h^3}{12\mu}\dfrac{\partial p}{\partial x}\right)+\dfrac{\partial}{\partial z}\left(\dfrac{h^3}{12\mu}\dfrac{\partial p}{\partial z}\right)=\dfrac{\partial(hU)}{\partial x}+\dfrac{\partial(hW)}{\partial z}+\dfrac{\partial h}{\partial t} \\ p_{\partial\Omega}=0 \end{cases} \tag{173}$$

First of all, the domain Ω has to be discretised into a finite number of points (x_i, z_j) identified by the spatial indices i and j (positive integers): with reference to the Figure 71 and to the eq. (174), choosing N points along the x direction and M points along the z one, the grid will be characterised by Δx and Δz uniform spacings.

$$\begin{matrix} i=1,2,\dots,N & \Delta x=\dfrac{x_N-x_1}{N-1} & x_i=x_1+(i-1)\Delta x \\ j=1,2,\dots,M & \Delta z=\dfrac{z_M-z_1}{M-1} & z_j=z_1+(j-1)\Delta z \end{matrix} \tag{174}$$

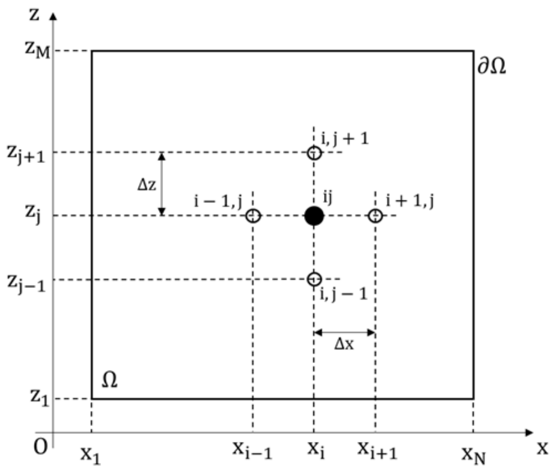

Figure 71 *Discrete cartesian domain grid*

Then, the objective is to write the Reynolds equation in correspondence of each (i, j) grid point by approximating the derivatives with the finite differences and by assuming the field quantities like the pressure $p(x, z)$ to have the value p_{ij} in that point (Hamrock, Schmid and Jacobson, 2004; LeVeque, 2007).

Due to the elliptical nature of the Reynolds PDE in HL regime, spatial central differences are considered: let start with the discretization of the Poiseuille and the Couette terms along the x direction grouping the known quantities into ε and u, adopting the differencing logic reported in the eq. (175) referred to the Figure 72.

$$\varepsilon = \frac{h^3}{12\mu} \quad u = hU$$

$$\left[\frac{\partial}{\partial x}\left(\varepsilon\frac{\partial p}{\partial x}\right)\right]_{ij} = \frac{\frac{\varepsilon_{ij} + \varepsilon_{i+1,j}}{2}\frac{p_{i+1,j} - p_{ij}}{\Delta x} - \frac{\varepsilon_{i-1,j} + \varepsilon_{ij}}{2}\frac{p_{ij} - p_{i-1,j}}{\Delta x}}{\Delta x} \tag{175}$$

$$\left[\frac{\partial u}{\partial x}\right]_{ij} = \frac{u_{i+1,j} - u_{i-1,j}}{2\Delta x}$$

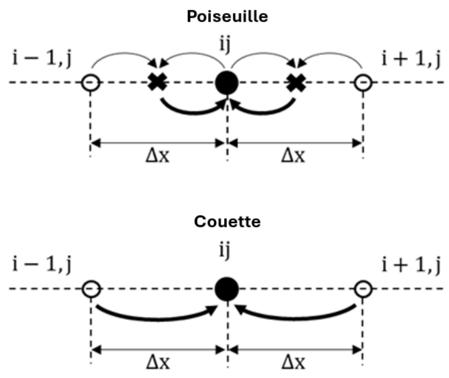

Figure 72 *Poiseuille and Couette differencing logic*

Evidencing the dependence of the equation in the (i,j) point on the neighborhood points $(\mathrm{i}-1,\mathrm{j})$ and $(\mathrm{i}+1,\mathrm{j})$, the forward/backward finite difference and the mean [3,1] vectors, i.e., $\mathbf{d}_{x^\pm}$ and $\mathbf{m}_\pm$, are defined in (176): they are intended as operators applied to the stencil vector $\mathbf{y}_x$, i.e., the values of the generic field y_{ij} involved in the differentiation, that allow to highlight the coefficients multiplying the unknowns.

$$\begin{aligned}
&\mathbf{y}_x = [y_{i-1,j} \quad y_{ij} \quad y_{i+1,j}]^T \\
&\mathbf{m}_- = \frac{[1 \quad 1 \quad 0]^T}{2} \quad \mathbf{d}_{x^-} = \frac{[-1 \quad 1 \quad 0]^T}{\Delta x} \\
&\mathbf{m}_+ = \frac{[0 \quad 1 \quad 1]^T}{2} \quad \mathbf{d}_{x^+} = \frac{[0 \quad -1 \quad 1]^T}{\Delta x} \\
&\left[\frac{\partial}{\partial x}\left(\varepsilon\frac{\partial p}{\partial x}\right)\right]_{ij} = \frac{(\mathbf{m}_+^T \boldsymbol{\varepsilon}_x)(\mathbf{d}_{x^+}^T \mathbf{p}_x) - (\mathbf{m}_-^T \boldsymbol{\varepsilon}_x)(\mathbf{d}_{x^-}^T \mathbf{p}_x)}{\Delta x}
\end{aligned} \tag{176}$$

In fact, after algebraic manipulation, the (176) assumes the more compact form reported in (177) where the [3,3] matrix $\mathbf{D}_{2x}$ is defined: in a single operation, the application of $\mathbf{D}_{2x}$ executes the operations written in (175) referred to the Poiseuille term.

$$\left[\frac{\partial}{\partial x}\left(\varepsilon\frac{\partial p}{\partial x}\right)\right]_{ij} = \boldsymbol{\varepsilon}_x^T \left(\frac{\mathbf{m}_+\mathbf{d}_{x^+}^T - \mathbf{m}_-\mathbf{d}_{x^-}^T}{\Delta x}\right)\mathbf{p}_x = \boldsymbol{\varepsilon}_x^T \mathbf{D}_{2x}\mathbf{p}_x \tag{177}$$

Of course, the same can be done in (178) for the Poiseuille term along the z direction exploiting the same mean vectors already used in (176) while defining the z stencil vector $\mathbf{y}_z$ and the associated forward/backward finite difference vectors $\mathbf{d}_{z^\pm}$.

$$\begin{aligned}
&\mathbf{y}_z = [y_{i,j-1} \quad y_{ij} \quad y_{i,j+1}]^T \\
&\mathbf{d}_{z^-} = \frac{[-1 \quad 1 \quad 0]^T}{\Delta z} \quad \mathbf{d}_{z^+} = \frac{[0 \quad -1 \quad 1]^T}{\Delta z} \\
&\left[\frac{\partial}{\partial z}\left(\varepsilon\frac{\partial p}{\partial z}\right)\right]_{ij} = \boldsymbol{\varepsilon}_z^T \left(\frac{\mathbf{m}_+\mathbf{d}_{z^+}^T - \mathbf{m}_-\mathbf{d}_{z^-}^T}{\Delta z}\right)\mathbf{p}_z = \boldsymbol{\varepsilon}_z^T \mathbf{D}_{2z}\mathbf{p}_z
\end{aligned} \tag{178}$$

The same logic is adopted for the Couette terms by defining the central finite difference vectors $\mathbf{d}_{x^c}$ and $\mathbf{d}_{z^c}$ in (179), where the w quantity is nothing the group hW.

$$\begin{aligned} \mathbf{d}_{x^c} &= \frac{[-1 \quad 0 \quad 1]^T}{2\Delta x} \\ \mathbf{d}_{z^c} &= \frac{[-1 \quad 0 \quad 1]^T}{2\Delta z} \end{aligned} \quad \rightarrow \quad \begin{aligned} \left[\frac{\partial u}{\partial x}\right]_{ij} &= \frac{u_{i+1,j} - u_{i-1,j}}{2\Delta x} = \mathbf{d}_{x^c}^T \mathbf{u}_x \\ \left[\frac{\partial w}{\partial z}\right]_{ij} &= \frac{w_{i,j+1} - w_{i,j-1}}{2\Delta z} = \mathbf{d}_{z^c}^T \mathbf{w}_z \end{aligned} \tag{179}$$

Lastly, the squeeze term is discretised in (180) by the means of a temporal backward finite difference, considering a known gap field at the time $t - \Delta t$, i.e., h_{ij}^-.

$$\left[\frac{\partial h}{\partial t}\right]_{ij} = \frac{h_{ij} - h_{ij}^-}{\Delta t} \tag{180}$$

Also in this case, the time stencil vector $\mathbf{h}_t$ and the time backward finite difference vector operator $\mathbf{d}_t$ are defined in (181).

$$\begin{aligned} \mathbf{h}_t &= [h_{ij}^- \quad h_{ij}]^T \\ \mathbf{d}_t &= \frac{[-1 \quad 1]^T}{\Delta t} \end{aligned} \quad \rightarrow \quad \left[\frac{\partial h}{\partial t}\right]_{ij} = \mathbf{d}_t^T \mathbf{h}_t \tag{181}$$

Then, the discretised form of the Reynolds equation is given in (182).

$$\boldsymbol{\varepsilon}_x^T \mathbf{D}_{2x} \mathbf{p}_x + \boldsymbol{\varepsilon}_z^T \mathbf{D}_{2z} \mathbf{p}_z = \mathbf{d}_{x^c}^T \mathbf{u}_x + \mathbf{d}_{z^c}^T \mathbf{w}_z + \mathbf{d}_t^T \mathbf{h}_t \tag{182}$$

While the right-hand side term is known, due to HL regime, the left-hand side term is dependent on the pressure unknown values in correspondence of 5 grid points, i.e., the current (i, j) point and the neighborhood ones along both the directions x and z $(i \pm 1, j)$ and $(i, j \pm 1)$: in order to highlight that dependency, let define in (183) the so called cross stencil [5,1] vector of a field y_{ij}, i.e., $\mathbf{y}_I$ (referring to the Figure 64 for the cross resembling), and two identity matrices able to collect the x-stencil vector and the z-stencil one components from $\mathbf{y}_I$, respectively $\mathbf{I}_x$ and $\mathbf{I}_z$; the subscript I stands for a 2D spatial index univocally corresponding to the (i, j) grid point obtained by scanning for each i line all the j points, i.e., along the so called lexicographical ordering.

$$\begin{gathered} I = (i-1)M + j \quad \rightarrow \quad \mathbf{y}_I = [y_{i-1,j} \quad y_{i,j-1} \quad y_{ij} \quad y_{i,j+1} \quad y_{i+1,j}]^T \\ \mathbf{y}_x = \begin{bmatrix} y_{i-1,j} \\ y_{ij} \\ y_{i+1,j} \end{bmatrix} = \begin{bmatrix} 1 & 0 & 0 & 0 & 0 \\ 0 & 0 & 1 & 0 & 0 \\ 0 & 0 & 0 & 0 & 1 \end{bmatrix} \begin{bmatrix} y_{i-1,j} \\ y_{i,j-1} \\ y_{ij} \\ y_{i,j+1} \\ y_{i+1,j} \end{bmatrix} = \mathbf{I}_x \mathbf{y}_I \\ \mathbf{y}_z = \begin{bmatrix} y_{i,j-1} \\ y_{ij} \\ y_{i,j+1} \end{bmatrix} = \begin{bmatrix} 0 & 1 & 0 & 0 & 0 \\ 0 & 0 & 1 & 0 & 0 \\ 0 & 0 & 0 & 1 & 0 \end{bmatrix} \begin{bmatrix} y_{i-1,j} \\ y_{i,j-1} \\ y_{ij} \\ y_{i,j+1} \\ y_{i+1,j} \end{bmatrix} = \mathbf{I}_z \mathbf{y}_I \end{gathered} \tag{183}$$

Applying the above, the [5,5] matrix operator $\mathbf{D}_2$ and the [5,1] vectors $\mathbf{D}_x$ and $\mathbf{D}_z$ are defined, providing a more compact form to the discretised Reynolds equation in (184).

$$\begin{array}{l}\mathbf{D}_2 = \mathbf{I}_x^T \mathbf{D}_{2x} \mathbf{I}_x + \mathbf{I}_z^T \mathbf{D}_{2z} \mathbf{I}_z \\ \mathbf{D}_x = \mathbf{I}_x^T \mathbf{d}_{x^c} \quad \mathbf{D}_z = \mathbf{I}_z^T \mathbf{d}_{z^c}\end{array} \rightarrow \boldsymbol{\varepsilon}_I^T \mathbf{D}_2 \mathbf{p}_I = \mathbf{D}_x^T \mathbf{u}_I + \mathbf{D}_z^T \mathbf{w}_I + \mathbf{d}_t^T \mathbf{h}_t \tag{184}$$

In addition the right-hand side term, also the ε field is given in the HL regime, so the [5,1] vector $\mathbf{a}_I$ multiplying the pressure stencil vector and the scalar quantity b_I are defined in (185); at the same time, it is noted that the discretised Reynolds equation can be written for all the internal (i,j) grid points, since it needs previous and successive information with respect to the current location, while its discretization on the boundary grid points is easily given by the imposition of null pressure: so the well-posed linear system referred to the HL Reynolds equation can be assembled.

$$\begin{array}{l}\mathbf{a}_I = \mathbf{D}_2^T \boldsymbol{\varepsilon}_I \quad b_I = \mathbf{D}_x^T \mathbf{u}_I + \mathbf{D}_z^T \mathbf{w}_I + \mathbf{d}_t^T \mathbf{h}_t \\ \begin{cases} \mathbf{a}_I^T \mathbf{p}_I = b_I & 2 \le i \le N-1 \quad 2 \le j \le M-1 \\ p_{1j} = p_{Nj} = 0 & 1 \le j \le M \\ p_{i1} = p_{iM} = 0 & 2 \le i \le N-1 \end{cases}\end{array} \tag{185}$$

Reflecting the linear nature of (173), the problem (185) is a linear system reported in matrix form in (186) following the lexicographical order; the associated matrix **A** is a penta-diagonal matrix which the structure is reported in the Figure 73: the vector $\mathbf{a}_I$ is composed by the first two terms L_{x_I} and L_{z_I} referring to the previous points along x and z belonging to the lower triangular part of **A**, the central term D_I referring to the (i,j) point belonging to the main diagonal of **A** and the last two terms U_{z_I} and U_{x_I} referring to the next points along z and x belonging to the upper triangular part of **A**; let note that in correspondence of the I grid point belonging to the domain boundaries the vector $\mathbf{a}_I$ reduces to a scalar equal to 1 placed in the main diagonal of **A**, while the associated scalar b_I is equal to zero.

$$\mathbf{a}_I = [L_{x_I} \quad L_{z_I} \quad D_I \quad U_{z_I} \quad U_{x_I}]^T \rightarrow \mathbf{A}\mathbf{p} = \mathbf{b} \tag{186}$$

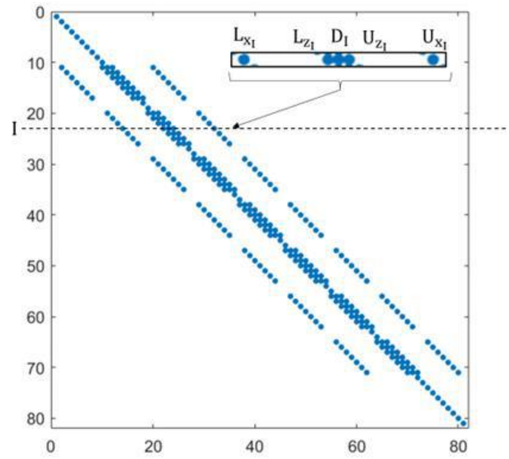

Figure 73 *Penta-diagonal matrix referred to the HL Reynolds linear system*

The linear system in (186) can be easily inverted to find the pressure vector $\mathbf{p}$, but this does not take into account the lubricant pressure cavitation constraint (Hamrock, Schmid and Jacobson, 2004): the eventuality of a positive Couette flow, i.e., the surfaces sliding along a diverging channel, and/or of a positive squeeze velocity, i.e., the surfaces moving away from each other, leads to the lubricant depressurization that, if goes below the cavitation pressure (generally assumed to be zero), shows an abrupt meatus film rupture due to the formation of cavitating bubbles. So, from a numerical point of view, the system (186) has to be solved with an iterative method that allows to truncate the negative lubricant pressure values along the iterations: the golden standard iterative methods to solve linear systems are the Jacobi and the Gauss-Seidel methods (LeVeque, 2007).

Solving the internal grid point equation for the current point pressure value p_{ij}, the Jacobi method consists in iterating the p_{ij} exploiting its local relation with respect to the pressure on the surrounding grid points: introducing the k iteration index, the $k+1$ Jacobi update is given in (187).

$$p_{ij}^{k+1} = \frac{b_I - L_{x_I} p_{i-1,j}^{k} - L_{z_I} p_{i,j-1}^{k} - U_{z_I} p_{i,j+1}^{k} - U_{x_I} p_{i+1,j}^{k}}{D_I} \tag{187}$$

The Gauss-Seidel method uses the same Jacobi approach, but, in order to enhance the iteration convergence, it suggests to use the spatially previous pressures $p_{i-1,j}$ and $p_{i,j-1}$ just updated according to the lexicographical ordering (eq. (188)).

$$p_{ij}^{k+1} = \frac{b_I - L_{x_I} p_{i-1,j}^{k+1} - L_{z_I} p_{i,j-1}^{k+1} - U_{z_I} p_{i,j+1}^{k} - U_{x_I} p_{i+1,j}^{k}}{D_I} \tag{188}$$

While the Gauss-Seidel method is effective with respect to the Jacobi one in terms of convergence rate, the Jacobi approach results in a much faster computation since it can be vectorized due to the update depending entirely on the previous iteration: the Gauss-Seidel method cannot be vectorized because, by its definition, it cannot be performed without a "for" cycle. A way to reduce even more the iterations number is to apply the Successive Over Relaxation (SOR) method reported in (189), i.e., a relaxation of the Gauss-Seidel solution p_{GS} that can be slowed down or accelerated by the means of a relaxation factor ω managing the amount of the update provided to the next iteration (deceleration for $0 < \omega < 1$ and acceleration for $1 < \omega < 2$); an optimal value for the relaxation factor can be determined as a function of the grid spacing. The SOR method, as the Gauss-Seidel one, cannot be vectorized.

$$\begin{aligned} p_{GS} &= \frac{b_I - L_{x_I} p_{i-1,j}^{k+1} - L_{z_I} p_{i,j-1}^{k+1} - U_{z_I} p_{i,j+1}^{k} - U_{x_I} p_{i+1,j}^{k}}{D_I} \\ p_{ij}^{k+1} &= p_{ij}^{k} + \omega\left(p_{GS} - p_{ij}^{k}\right) \end{aligned} \tag{189}$$

The described methods belong to a class of iterative solvers called Fixed Point Iteration, because the $k + 1$ update is a function $\mathbf{f}$ (Jacobi, Gauss-Seidel or SOR) solely of the previous iteration k.

Then, the iterative approach allows to saturate the pressure to positive values by truncating the negative ones along the iterations. If in some zones of the domain the cavitation occurs, the Reynolds equation residual, i.e., $\mathbf{b} - \mathbf{Ap}$, cannot happen to be zero, because the cavitation bubbles "flows" are not taken into account in (173): therefore, the residual decaying below a chosen tolerance tol has to be defined as a quantity related to the pressure change between two consecutive iterations. The resulting iterative cycle is reported in (190).

$$\begin{aligned} &\text{while } \sum_I \left|p_I^{k+1} - p_I^{k}\right| > \text{tol} \\ &\qquad \mathbf{p}^* = \mathbf{f}\left(\mathbf{p}^k\right) \;\rightarrow\; \mathbf{p}^{k+1} = \max\{0, \mathbf{p}^*\} \\ &\qquad k \rightarrow k + 1 \\ &\text{end} \end{aligned} \tag{190}$$

An example of lubricant pressure p field numerical solution simulated in Matlab® environment is reported in the Figure 74, where a bilinear top surface approaches from a height $h_0(t - \Delta t)$ to $h_0(t)$ a moving flat plane with velocities 2U and 2W.

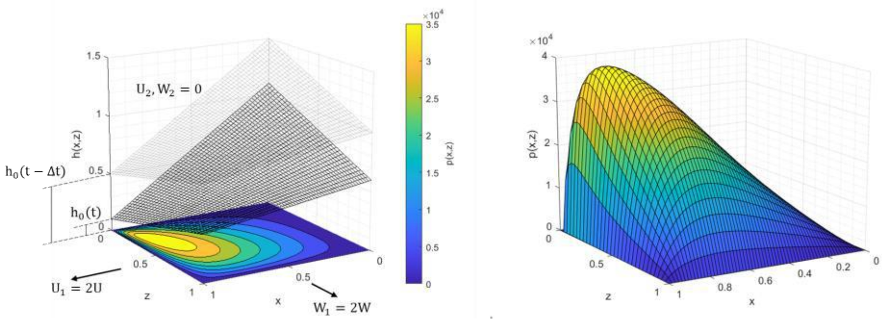

Figure 74 *Numerical HL Reynolds solution for a bilinear gap considering both sliding and squeeze*

If one compares the computational performance of the chosen numerical methods (Jacobi, Gauss-Seidel, SOR) in terms of residual trend along the iterations, the results reported in the Figure 75 will be obtained (here also the computational time is reported in the legend); let note the verification of the methods' characteristics explained above: while the Gauss-Seidel and the SOR methods show the fastest convergence, the Jacobi method (vectorized) is the fastest in terms of computational time.

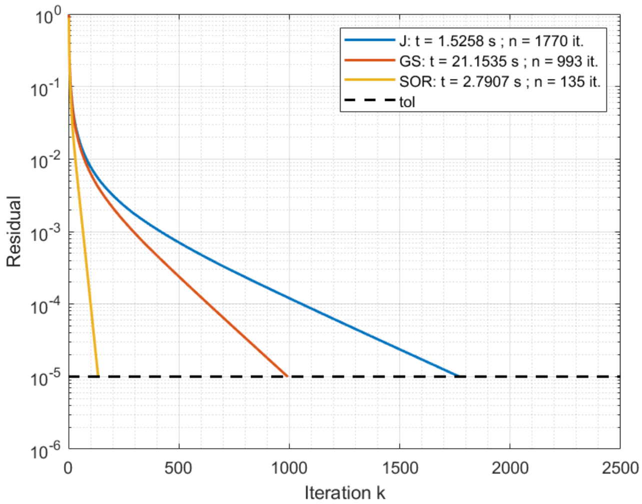

Figure 75 *Iterative methods comparison*

The solution logic provided above is a tool working for a known approach δ (that in the previous case imposed the surfaces' distance h_0) and in fact it does not take into account the load applied to the system.

The most common way to solve the lubrication problem for a given load N and an unknown approach δ is to assemble a nested loop: it consists into assuming the approach, solving iteratively the Reynolds equation for the pressure field p, integrating it over the domain surface to obtain the resulting load and then updating the new approach by a quantity related to the load balance equation error. Introducing the iteration index n for the approach outer iterative cycle (the inner one is the Reynolds equation solver), the explained logic is reported in (191), in which the δ^n update is given by a quantity proportional to the load balance error through the relaxation factor α, considering that if the latter is negative, it means that the too low pressure p^n provides an insufficient load, so it has to be increased by increasing the approach (and vice versa).

$$
\begin{aligned}
&\text{while } \left|\sum_{i,j} p_{ij}^n \Delta x \Delta z - N\right| > \text{tol}\\
&\qquad \mathbf{h}^n = \mathbf{g} - \delta^n\\
&\qquad \mathbf{p}^n = \mathbf{A}^{-1}\mathbf{b}\\
&\qquad \delta^{n+1} = \delta^n + \alpha\left(\sum_{i,j} p_{ij}^n \Delta x \Delta z - N\right)\\
&\qquad n \rightarrow n+1\\
&\text{end}
\end{aligned}
\tag{191}
$$

While the pressure integration in (191) is given by a simple sum for each grid cell contribution, a more accurate surface integration can be achieved by the 2D trapezoidal rule reported in (192).

$$
\iint_{\Omega} p \, dxdz \cong \sum_{i=2}^{N}\sum_{j=2}^{M} \frac{p_{i-1,j-1} + p_{i-1,j} + p_{i,j-1} + p_{ij}}{4} \Delta x \Delta z \tag{192}
$$

Furthermore, others approach update criteria can be chosen with respect to the free-derivative presented in (191), like the Newton one reported in (193), where the load balance equation L is solved by the means of a numerical Jacobian obtained with a chosen approach perturbation ε, since the load balance equation does not directly depend on the approach δ, but it is known that the latter determines the gap h field and so it affects the resulting lubricant pressure p.

$$
\begin{aligned}
&L(\delta) = \sum_{i,j} p_{ij}(\delta)\Delta x \Delta z - N = 0\\
&\frac{dL}{d\delta}(\delta) = \frac{L\big(\delta(1+\varepsilon)\big) - L(\delta)}{\varepsilon\delta}
\end{aligned}
\quad \rightarrow \quad \delta^{n+1} = \delta^n - \frac{L(\delta^n)}{\frac{dL}{d\delta}(\delta^n)} \tag{193}
$$

Let now move to the case of a tribo-system with spherical geometry, as for the THR case, in order to apply the same FDM discretization developed above.

2.1.2. Spherical tribo-system

The spherical tribo-system is modelled as the ball-in-socket joint depicted in the Figure 76 where the ball and the socket, i.e., the THR femoral head and acetabular cup, are, respectively, a sphere with radius r and a hollow hemisphere with inner radius R and thickness H; the reference frame Oxyz is fixed to the socket and has the origin in its centre O, while the xz plane is tangent to its edges and the y axis points towards its inside; the ball is free to move within the socket: its centre C is located by the eccentricity vector $\mathbf{e}$ and it rotates with respect to the socket with the angular velocity vector $\boldsymbol{\omega}$ (Fisher and Dowson, 1991; Mattei *et al.*, 2011).

From the Reynolds equation point of view, the 2D lubricated domain is identified by the spherical angles θ and φ locating a point P belonging to the inner socket surface: θ is the angle between the OP line and the z axis, while φ is the angle between the OP line projection on the xy plane and the x axis. The spherical transformation that rotates the Oxyz reference frame, in this order, by the angle φ around the z axis and by the angle θ around the new y axis is described by the rotation matrix (obtained with the Euler angles approach) reported in the eq. (194) which columns are the local reference frame unit vectors, i.e., the tangential unit vectors $\hat{\mathbf{t}}_\theta$ and $\hat{\mathbf{t}}_\varphi$ and the radial unit vector $\hat{\mathbf{r}}$.

$$\mathbf{R}_z(\varphi)\mathbf{R}_y(\theta) = \begin{bmatrix} \cos\theta\cos\varphi & -\sin\varphi & \sin\theta\cos\varphi \\ \cos\theta\sin\varphi & \cos\varphi & \sin\theta\sin\varphi \\ -\sin\theta & 0 & \cos\theta \end{bmatrix} = \cdots$$
$$\ldots = \begin{bmatrix} \hat{\mathbf{t}}_\theta & \hat{\mathbf{t}}_\varphi & \hat{\mathbf{r}} \end{bmatrix} \quad (194)$$

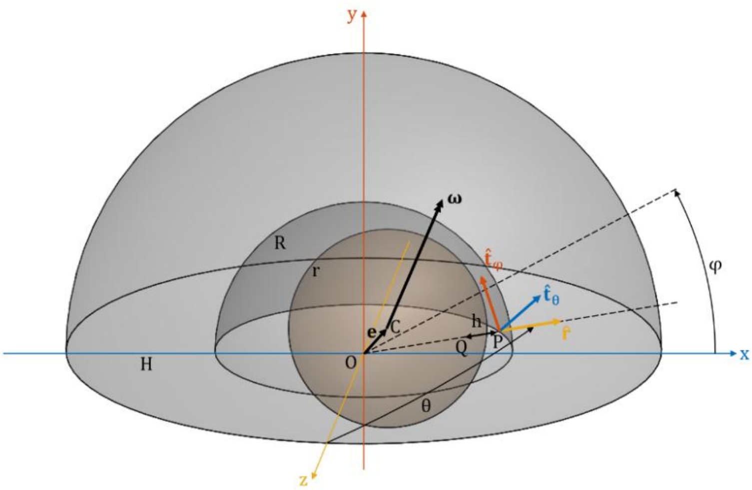

Figure 76 *Spherical tribo-system sketch*

According to the chosen spherical transformation, the Reynolds equation in spherical coordinates is given in (195) coupled with the boundary conditions.

$$\begin{cases} \sin\theta \dfrac{\partial}{\partial\theta}\left(\sin\theta \dfrac{h^3}{12\mu}\dfrac{\partial p}{\partial\theta}\right) + \dfrac{\partial}{\partial\varphi}\left(\dfrac{h^3}{12\mu}\dfrac{\partial p}{\partial\varphi}\right) = \cdots \\ \ldots = R\sin\theta\left[\dfrac{\partial(\sin\theta\, hU_\theta)}{\partial\theta} + \dfrac{\partial(hU_\varphi)}{\partial\varphi} + R\sin\theta\dfrac{\partial h}{\partial t}\right] \\ p(0,\varphi,t) = p(\pi,\varphi,t) = p(\theta,0,t) = p(\theta,\pi,t) = 0 \end{cases} \tag{195}$$

For a given couple of spherical angles (θ, φ) the position vector of the point P on the socket and the point Q on the ball are evaluated in (196), while the point C is located by the eccentricity vector.

$$(P - O) = R\hat{\mathbf{r}} \quad (C - O) = \mathbf{e} \quad (Q - O) \cong (\mathbf{e}^T\hat{\mathbf{r}} + r)\hat{\mathbf{r}} \tag{196}$$

The distance between the points P and Q provides the gap h in (197) where the radial clearance c is defined as the difference between the socket and the ball radii: it is worth to note that the radial clearance c plays the role of the geometrical approach, i.e., the uniform gap in case of concentric ball, while the approach is the result of the ball eccentricity $\mathbf{e}$ projection along the radial direction.

$$\begin{aligned} &(P - Q) = (P - O) - (Q - O) = (R - r - \mathbf{e}^T\hat{\mathbf{r}})\hat{\mathbf{r}} \\ &h = \|P - Q\| = c - \mathbf{e}^T\hat{\mathbf{r}} \end{aligned} \tag{197}$$

The surfaces' velocities at the generic position (θ, φ) is given by the points P and Q velocity vectors reported in (198), recalling that the socket is fixed with respect to the reference frame.

$$\mathbf{v}_P = \mathbf{0} \quad \mathbf{v}_Q = \mathbf{v}_C + \boldsymbol{\omega} \times (Q - C) \tag{198}$$

Regarding the Q point velocity in (199), it is composed by a translational contribution given by the eccentricity time derivative and by a rotational contribution given by the angular velocity vector (Flores, Ambrosio and Claro, 2004; Tian *et al.*, 2009; Askari *et al.*, 2014a, 2014b).

$$\begin{aligned} &\mathbf{v}_C = \dot{\mathbf{e}} \quad (Q - C) = (Q - O) - (C - O) = (\mathbf{e}^T\hat{\mathbf{r}} + r)\hat{\mathbf{r}} - \mathbf{e} \\ &\mathbf{v}_Q = \dot{\mathbf{e}} + \boldsymbol{\omega} \times [(\mathbf{e}^T\hat{\mathbf{r}} + r)\hat{\mathbf{r}} - \mathbf{e}] \end{aligned} \tag{199}$$

Then, recalling that the entraining motion is given by the arithmetical average between the surfaces and considering the fixed socket, the entraining velocities U_θ and U_φ reported in the Reynolds eq. (195) are evaluated in (200) by projecting the Q point velocity vector along the respective tangential directions.

$$\begin{bmatrix} U_\theta \\ U_\varphi \end{bmatrix} = \frac{1}{2}\begin{bmatrix} \hat{\mathbf{t}}_\theta^T \\ \hat{\mathbf{t}}_\varphi^T \end{bmatrix}\{\dot{\mathbf{e}} + \boldsymbol{\omega} \times [(\mathbf{e}^T\hat{\mathbf{r}} + r)\hat{\mathbf{r}} - \mathbf{e}]\} \tag{200}$$

In the spherical case, the load on the socket is given by a 3D vector $\mathbf{N}$ obtained in (201) by integrating the lubricant pressure p oriented with the radial unit vector $\hat{\mathbf{r}}$ over the cup surface (a 3D approach causes a 3D load).

$$\mathbf{N} = \iint_\Omega p\hat{\mathbf{r}} R^2 \sin\theta \, d\theta d\varphi \tag{201}$$

The frictional quantities can be evaluated with the shear stress vector $\boldsymbol{\tau}$ in spherical coordinates in (202) acting on the socket surface and dealing with the sliding velocity vector $\mathbf{V}$.

$$\boldsymbol{\tau} = -\frac{h}{2}\boldsymbol{\nabla}p - \mu\frac{\mathbf{V}}{h} = \begin{bmatrix} -\dfrac{h}{2R}\dfrac{\partial p}{\partial \theta} + 2\mu\dfrac{U_\theta}{h} \\ -\dfrac{h}{2R\sin\theta}\dfrac{\partial p}{\partial \varphi} + 2\mu\dfrac{U_\varphi}{h} \end{bmatrix} = \begin{bmatrix} \tau_\theta \\ \tau_\varphi \end{bmatrix} \tag{202}$$

Then, the shear stress vector $\boldsymbol{\tau}$ is responsible for the viscous friction torque vector $\mathbf{T}$ given in (203).

$$\mathbf{T} = \iint_\Omega R\hat{\mathbf{r}} \times \begin{bmatrix} \hat{\mathbf{t}}_\theta & \hat{\mathbf{t}}_\varphi \end{bmatrix} \begin{bmatrix} \tau_\theta \\ \tau_\varphi \end{bmatrix} R^2 \sin\theta \, d\theta d\varphi \tag{203}$$

Finally, the set of equations governing the HL regime of a ball-in-socket tribo-system is resumed in (204), where the main difference with respect to the cartesian case in (172) is given by the 3D load balance equation to evaluate the unknown eccentricity vector $\mathbf{e}$.

$$\begin{cases} \sin\theta\dfrac{\partial}{\partial\theta}\left(\sin\theta\dfrac{h^3}{12\mu}\dfrac{\partial p}{\partial\theta}\right) + \dfrac{\partial}{\partial\varphi}\left(\dfrac{h^3}{12\mu}\dfrac{\partial p}{\partial\varphi}\right) = \cdots \\ \ldots = R\sin\theta\left[\dfrac{\partial(\sin\theta\, hU_\theta)}{\partial\theta} + \dfrac{\partial\left(hU_\varphi\right)}{\partial\varphi} + R\sin\theta\dfrac{\partial h}{\partial t}\right] \\ h(\theta,\varphi,t) = c - \mathbf{e}^T(t)\hat{\mathbf{r}}(\theta,\varphi) \\ \mathbf{N}(t) = \displaystyle\iint_\Omega p(\theta,\varphi,t)\hat{\mathbf{r}}(\theta,\varphi)\, R^2\sin\theta\, d\theta d\varphi \end{cases} \tag{204}$$

The FDM numerical discretization of the spherical Reynolds equation in (204) follows the same logic of the cartesian case, applying the due modifications because of the variable coefficients inside the derivatives (Jin and Dowson, 1999; Ramjee, 2008). Let define in (205) the 2D spherical grid with the usual grid indices i and j and the angular spacings $\Delta\theta$ and $\Delta\varphi$. Even if a uniform grid characterised by constant $\Delta\theta$ and $\Delta\varphi$ spacings leads to finite areas with different extension in a spherical geometry, it represents a common use in the context of ball-in-socket or THR simulation when using the FDM to discretise the Reynolds equation (Jin and Dowson, 1999): if a uniform areas grid is necessary, other discretization approaches have to be used like the FEM by choosing a particular area element shape and by assembling the weak form of the Reynolds equation based on the chosen shape functions (Habchi, 2018).

$$\begin{aligned} &i = 1,2,\ldots,N \quad \Delta\theta = \frac{\pi}{N-1} \quad \theta_i = (i-1)\Delta\theta \\ &j = 1,2,\ldots,M \quad \Delta\varphi = \frac{\pi}{M-1} \quad \varphi_j = (j-1)\Delta\varphi \end{aligned} \tag{205}$$

Let start with the θ Poiseuille term in (206) which will take into account the usual mean vector operator $\mathbf{m}_\pm$, the new forward/backward finite difference operator $\mathbf{d}_{\theta^\pm}$ applied to the θ-stencil field variable vector $\mathbf{y}_\theta$ and the auxiliary vector $\mathbf{s}_\theta$.

$$\begin{gathered}
\mathbf{y}_\theta = [y_{i-1,j} \quad y_{ij} \quad y_{i+1,j}]^T \quad \mathbf{s}_\theta = [\sin\theta_{i-1} \quad \sin\theta_i \quad \sin\theta_{i+1}]^T \\
\mathbf{d}_{\theta^-} = \frac{[-1 \quad 1 \quad 0]^T}{\Delta\theta} \quad \mathbf{d}_{\theta^+} = \frac{[0 \quad -1 \quad 1]^T}{\Delta\theta} \\
\left[\sin\theta \frac{\partial}{\partial\theta}\left(\sin\theta\, \varepsilon \frac{\partial p}{\partial\theta}\right)\right]_{ij} = \cdots \\
= \sin\theta_i \frac{(\mathbf{m}_+^T\mathbf{s}_\theta)(\mathbf{m}_+^T\boldsymbol{\varepsilon}_\theta)(\mathbf{d}_{\theta^+}^T\mathbf{p}_\theta) - (\mathbf{m}_-^T\mathbf{s}_\theta)(\mathbf{m}_-^T\boldsymbol{\varepsilon}_\theta)(\mathbf{d}_{\theta^-}^T\mathbf{p}_\theta)}{\Delta\theta}
\end{gathered} \tag{206}$$

After algebraic manipulation, the [3,3] matrix operator $\mathbf{D}_{2\theta}$ is defined in (207).

$$\begin{gathered}
\left[\sin\theta \frac{\partial}{\partial\theta}\left(\sin\theta\, \varepsilon \frac{\partial p}{\partial\theta}\right)\right]_{ij} = \cdots \\
= \boldsymbol{\varepsilon}_\theta^T \left(\sin\theta_i \frac{(\mathbf{m}_+^T\mathbf{s}_\theta)\mathbf{m}_+\mathbf{d}_{\theta^+}^T - (\mathbf{m}_-^T\mathbf{s}_\theta)\mathbf{m}_-\mathbf{d}_{\theta^-}^T}{\Delta\theta}\right)\mathbf{p}_\theta = \boldsymbol{\varepsilon}_\theta^T\mathbf{D}_{2\theta}\mathbf{p}_\theta
\end{gathered} \tag{207}$$

Much easier is the φ Poiseuille term in (208) accounting for the φ-stencil field variable vector $\mathbf{y}_\varphi$ and the new forward/backward finite difference operator $\mathbf{d}_{\varphi^\pm}$ leading to the [3,3] matrix operator $\mathbf{D}_{2\varphi}$.

$$\begin{gathered}
\mathbf{y}_\varphi = [y_{i,j-1} \quad y_{ij} \quad y_{i,j+1}]^T \\
\mathbf{d}_{\varphi^-} = \frac{[-1 \quad 1 \quad 0]^T}{\Delta\varphi} \quad \mathbf{d}_{\varphi^+} = \frac{[0 \quad -1 \quad 1]^T}{\Delta\varphi} \\
\left[\frac{\partial}{\partial\varphi}\left(\varepsilon \frac{\partial p}{\partial\varphi}\right)\right]_{ij} = \boldsymbol{\varepsilon}_\varphi^T \left(\frac{\mathbf{m}_+\mathbf{d}_{\varphi^+}^T - \mathbf{m}_-\mathbf{d}_{\varphi^-}^T}{\Delta\varphi}\right)\mathbf{p}_\varphi = \boldsymbol{\varepsilon}_\varphi^T\mathbf{D}_{2\varphi}\mathbf{p}_\varphi
\end{gathered} \tag{208}$$

The Couette terms in (209) account for the new central finite difference operator $\mathbf{d}_{\theta,\varphi^c}$ applied to the new grouped quantities u and w.

$$\begin{gathered}
u = \sin\theta\, hU_\theta \quad w = hU_\varphi \\
\begin{matrix} \mathbf{d}_{\theta^c} = \dfrac{[-1 \quad 0 \quad 1]^T}{2\Delta\theta} \\ \mathbf{d}_{\varphi^c} = \dfrac{[-1 \quad 0 \quad 1]^T}{2\Delta\varphi} \end{matrix} \rightarrow \begin{matrix} \left[\dfrac{\partial u}{\partial\theta}\right]_{ij} = \mathbf{d}_{\theta^c}^T\mathbf{u}_\theta \\ \left[\dfrac{\partial w}{\partial\varphi}\right]_{ij} = \mathbf{d}_{\varphi^c}^T\mathbf{w}_\varphi \end{matrix}
\end{gathered} \tag{209}$$

Lastly, the squeeze term is written in (210) with the usual backward temporal finite difference vector $\mathbf{d}_t$ applied to the time stencil $\mathbf{h}_t$.

$$\left[\frac{\partial h}{\partial t}\right]_{ij} = \mathbf{d}_t^T\mathbf{h}_t \tag{210}$$

Then, the discretised form of the spherical Reynolds equation is given in (211) with the same functional form of (182).

$$\begin{gathered}
\boldsymbol{\varepsilon}_\theta^T\mathbf{D}_{2\theta}\mathbf{p}_\theta + \boldsymbol{\varepsilon}_\varphi^T\mathbf{D}_{2\varphi}\mathbf{p}_\varphi = \cdots \\
= R\sin\theta_i \left(\mathbf{d}_{\theta^c}^T\mathbf{u}_\theta + \mathbf{d}_{\varphi^c}^T\mathbf{w}_\varphi + R\sin\theta_i\, \mathbf{d}_t^T\mathbf{h}_t\right)
\end{gathered} \tag{211}$$

Again, with the application of the identity matrices $\mathbf{I}_\theta$ and $\mathbf{I}_\varphi$ collecting the $\theta\varphi$ stencil vector from the cross one and of the lexicographical index I, the definition of the [5,5] matrix operator $\mathbf{D}_2$, the [5,1] vectors $\mathbf{D}_\theta$ and $\mathbf{D}_\varphi$ and the auxiliary $\mathbf{D}_t$ vector makes explicit in (212) the local equation dependence on the cross neighborhoods.

$$\begin{gathered}
\mathbf{D}_2 = \mathbf{I}_\theta^T \mathbf{D}_{2\theta} \mathbf{I}_\theta + \mathbf{I}_\varphi^T \mathbf{D}_{2\varphi} \mathbf{I}_\varphi \\
\mathbf{D}_\theta = R \sin\theta_i \, \mathbf{I}_\theta^T \mathbf{d}_{\theta^c} \quad \mathbf{D}_\varphi = R \sin\theta_i \, \mathbf{I}_\varphi^T \mathbf{d}_{\varphi^c} \quad \mathbf{D}_t = R^2 \sin^2\theta_i \, \mathbf{d}_t \\
\boldsymbol{\varepsilon}_I^T \mathbf{D}_2 \mathbf{p}_I = \mathbf{D}_\theta^T \mathbf{u}_I + \mathbf{D}_\varphi^T \mathbf{w}_I + \mathbf{D}_t^T \mathbf{h}_t
\end{gathered} \tag{212}$$

Finally, the spherical HL Reynolds equation is numerically described by the usual linear penta-diagonal system reported in (213); then, it can be solved with the iterative methods presented previously: it is worth to note that the spherical geometry is always characterised by diverging channels so the cavitation constraint cannot be avoided.

$$\begin{gathered}
\mathbf{a}_I = \mathbf{D}_2^T \boldsymbol{\varepsilon}_I \quad b_I = \mathbf{D}_\theta^T \mathbf{u}_I + \mathbf{D}_\varphi^T \mathbf{w}_I + \mathbf{D}_t^T \mathbf{h}_t \\
\begin{cases}
\mathbf{a}_I^T \mathbf{p}_I = b_I & 2 \le i \le N-1 \quad 2 \le j \le M-1 \\
p_{1j} = p_{Nj} = 0 & 1 \le j \le M \\
p_{i1} = p_{iM} = 0 & 2 \le i \le N-1
\end{cases} \quad \rightarrow \quad \mathbf{Ap} = \mathbf{b}
\end{gathered} \tag{213}$$

As for the previous case, the solution of (213) is given by a knowing set of eccentricities $\mathbf{e}$, so, for a given load vector $\mathbf{N}$ the nested loop approach can be adopted; first of all, the simple sum and the trapezoidal vector integration are given in (214) through the definition of the auxiliary vector field $\mathbf{P}$.

$$\begin{gathered}
\mathbf{P}_{ij} = p_{ij} \hat{\mathbf{r}}_{ij} R^2 \sin\theta_i \\
\iint_\Omega p \hat{\mathbf{r}} R^2 \sin\theta \, d\theta d\varphi \cong \begin{cases}
\displaystyle\sum_{i,j} \mathbf{P}_{ij} \Delta\theta\Delta\varphi \\
\displaystyle\sum_{i,j} \frac{\mathbf{P}_{i-1,j-1} + \mathbf{P}_{i-1,j} + \mathbf{P}_{i,j-1} + \mathbf{P}_{ij}}{4} \Delta\theta\Delta\varphi
\end{cases}
\end{gathered} \tag{214}$$

The free derivative outer loop update iterating on the trial eccentricity vector $\mathbf{e}^n$ is given in (215).

$$\mathbf{e}^{n+1} = \mathbf{e}^n + \alpha \left(\sum_{i,j} \mathbf{P}_{ij}^n \Delta\theta\Delta\varphi - \mathbf{N} \right) \tag{215}$$

Finally, the Newton method applied to 3D load balance equation $\mathbf{L}$ iterating on the eccentricity vector $\mathbf{e}$ through the ε-perturbed numerical Jacobian $\mathbf{L}_\mathbf{e}$ is reported in (216).

$$\begin{gathered}
\mathbf{L}(\mathbf{e}) = \sum_{i,j} \mathbf{P}_{ij}(\mathbf{e}) \Delta\theta\Delta\varphi - \mathbf{N} = \mathbf{0} \\
[\mathbf{L}_\mathbf{e}]_{ij} = \frac{\partial L_i}{\partial e_j}(\mathbf{e}) = \frac{L_i\left(e_j(1+\varepsilon)\right) - L_i(e_j)}{\varepsilon e_j} \\
\mathbf{e}^{n+1} = \mathbf{e}^n - [\mathbf{L}_\mathbf{e}(\mathbf{e}^n)]^{-1} \mathbf{L}(\mathbf{e}^n)
\end{gathered} \tag{216}$$

When the analysed ball-in-socket tribo-system is the THR the gait hip loads and velocities operating conditions are not the ones reported in the Figure 62: since the eqs. (204) refer to the acetabular cup reference frame, the hip constraint multipliers $\boldsymbol{\lambda}_{\mathrm{CJ}}$ have to be projected in the pelvis body i reference frame though the related constraint Jacobian $\mathbf{C}_{\mathbf{qJi}}$ to obtain the joint reactions supported by the pelvis $\overline{\mathbf{F}}_{\mathrm{CJi}}$ in (217).

$$\mathbf{Q}_{\lambda\mathrm{Ci}} = -\mathbf{C}_{\mathbf{qJi}}^{\mathrm{T}}\boldsymbol{\lambda}_{\mathrm{CJ}} = \begin{bmatrix} \mathbf{F}_{\mathrm{CJi}} \\ \mathbf{T}_{\mathrm{CJi}} \end{bmatrix} \quad \rightarrow \quad \overline{\mathbf{F}}_{\mathrm{CJi}} = \mathbf{R}_{\mathrm{i}}^{\mathrm{T}}\mathbf{F}_{\mathrm{CJi}} \tag{217}$$

The same thing is done in (218) for the femur angular velocity vector with respect to the pelvis that has to be projected in the pelvis reference frame through its rotation matrix $\mathbf{R}_{\mathrm{i}}$ to obtain $\overline{\boldsymbol{\omega}}_{\mathrm{Ji}}$.

$$\begin{matrix} \boldsymbol{\omega}_{\mathrm{i}} = \mathbf{G}_{\mathrm{i}}\dot{\boldsymbol{\theta}}_{\mathrm{i}} \\ \boldsymbol{\omega}_{\mathrm{j}} = \mathbf{G}_{\mathrm{j}}\dot{\boldsymbol{\theta}}_{\mathrm{j}} \end{matrix} \quad \rightarrow \quad \overline{\boldsymbol{\omega}}_{\mathrm{Ji}} = \mathbf{R}_{\mathrm{i}}^{\mathrm{T}}\left(\boldsymbol{\omega}_{\mathrm{j}} - \boldsymbol{\omega}_{\mathrm{i}}\right) \tag{218}$$

In order to refer to the acetabular cup 0xyz frame, one last rotation has to be considered: generally, the THR acetabular cup is implanted by following the physiological inclination angle α_{c}, that in the Multi-Body system pelvis reference frame is given by a rotation around the pelvis Anterior/Posterior axis as shown in the Figure 77 and described by the Euler angle rotation matrix $\mathbf{R}_{\mathrm{c}}$ in (219).

$$\mathbf{R}_{\mathrm{c}} = \mathbf{R}_{\mathrm{x}}(-\alpha_{\mathrm{c}}) \tag{219}$$

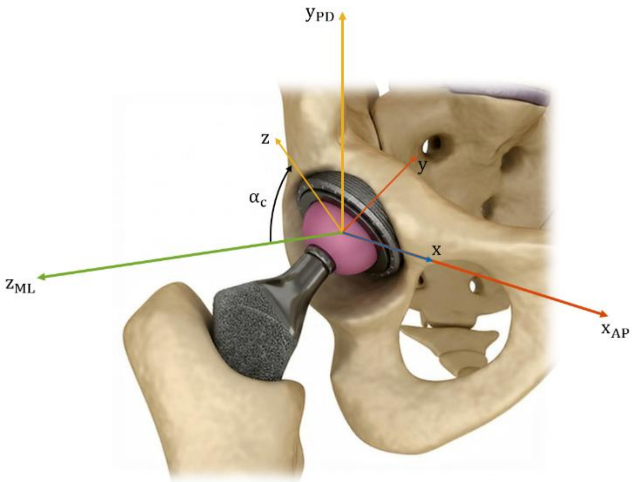

Figure 77 *Acetabular cup reference frame with respect to the pelvis*

Therefore, the gait hip loads $\mathbf{N}$ and velocities $\boldsymbol{\omega}$ input are reported in the eq. (220) and in the Figure 78 with reference to the acetabular cup reference frame, which corresponds to the lubricated ball-in-socket frame adopted for the numerical discretization.

$$\mathbf{N} = \mathbf{R}_{\mathrm{c}}^{\mathrm{T}}\overline{\mathbf{F}}_{\mathrm{CJi}} \quad \boldsymbol{\omega} = \mathbf{R}_{\mathrm{c}}^{\mathrm{T}}\overline{\boldsymbol{\omega}}_{\mathrm{Ji}} \tag{220}$$

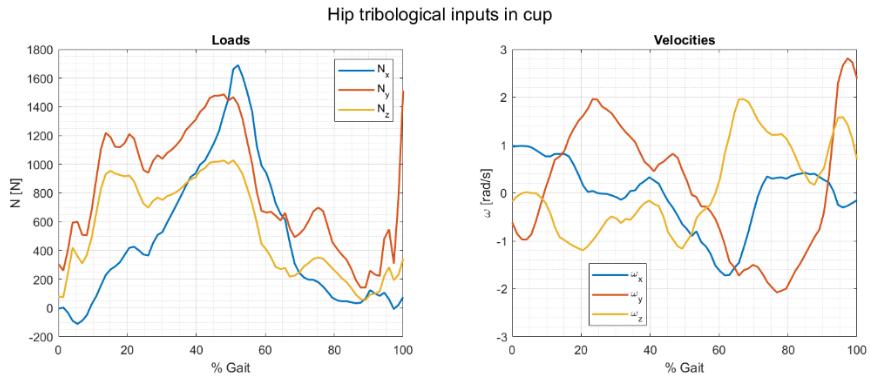

Figure 78 *Gait cycle hip loads and velocities in the acetabular cup frame*

Unfortunately, the THR does not work in HL regime even during a simple kinematics like the gait (Ramjee, 2008; Mattei *et al.*, 2011): the intensity of the hip loads does not allow a full separation of the conjugated surfaces, so the lubrication problem governing equations have to be adapted in order to take into account the EHL and the ML regimes. As a consequence, the successive efforts are devoted to the development of deformation models of the bodies composing the tribo-system, to the searching for a computational logic able to consider the eventuality of a direct contact between the surfaces and to the handling of the consequent numerical burden due to the arising non-linearities.

2.2. Elasto-Hydrodynamic Lubrication and deformation

Getting started with the EHL mode, the first adaptation deals with the consideration of the surfaces' deformation u introduced in the gap equation as a function of the lubricant pressure p reported in the set of eqs. (221) (Greenwood, 2020): the high loads produce enough pressure to deform the surfaces based on their mechanical response.

$$\begin{cases} \sin\theta \dfrac{\partial}{\partial\theta}\left(\sin\theta \dfrac{h^3}{12\mu}\dfrac{\partial p}{\partial\theta}\right) + \dfrac{\partial}{\partial\varphi}\left(\dfrac{h^3}{12\mu}\dfrac{\partial p}{\partial\varphi}\right) = \cdots \\ \ldots = R\sin\theta\left[\dfrac{\partial(\sin\theta\, hU_\theta)}{\partial\theta} + \dfrac{\partial\left(hU_\varphi\right)}{\partial\varphi} + R\sin\theta\dfrac{\partial h}{\partial t}\right] \\ h(\theta,\varphi,t) = u(p) + c - \mathbf{e}^T(t)\hat{\mathbf{r}}(\theta,\varphi) \\ \mathbf{N}(t) = \displaystyle\iint_\Omega p(\theta,\varphi,t)\hat{\mathbf{r}}(\theta,\varphi)\, R^2 \sin\theta\, d\theta d\varphi \end{cases} \tag{221}$$

Generally, the high pressure reached in the lubricant provides a further phenomenon: the sensitivity of the lubricant rheological properties of density ρ and viscosity μ with respect to its pressure p (Greenwood, 2020). While the

Reynolds assumptions refer to an iso-viscous and incompressible fluid (Reynolds, 1886), the so-called piezo-viscous and compressible fluid case can be easily addressed by introducing in the equation the pressure-varying rheological properties because, since they depend solely on the pressure, they do not exhibit variation across the lubricant meatus and this keeps the Reynolds equation functional structure. The two main relationships describing a compressible and piezo-viscous lubricant fluid are the Dowson-Higginson model (Dowson and Higginson, 1966) and the Barus viscosity model (van Leeuwen, 2009) reported in (222), which provide, respectively, a non-linear asymptotical increasing density with the pressure and an exponential growing viscosity with the pressure based on their nominal values ρ_0 and μ_0 and on the constants c, γ and α.

$$\rho(p) = \rho_0 \frac{c + \gamma p}{c + p} \quad \mu(p) = \mu_0 e^{\alpha p} \tag{222}$$

The Barus viscosity piezo-viscous model can provide troubles during a numerical computation because of the exponential indefinite viscosity growth: an easy way to address the issue, without artificially clipping the viscosity, is the Modulus adaptation (Bair, 2022) reported in (223) that imposes an asymptotical limit introducing a further coefficient β.

$$\mu(p) = \mu_0 e^{\frac{\alpha p}{1+\beta p}} \tag{223}$$

The implementation of the deformation, the density and the viscosity pressure-functions in the new EHL lubrication problem system given in (224), brings a high level of non-linearity to the Reynolds equation that now requires different iterative methods with respect to the HL regime to be numerically solved: a further important difference is given by the evidence that the EHL Reynolds PDE loses its elliptical nature, gaining a parabolic behaviour because now the pressure p unknown is hidden in both the squeeze term time derivative and the Couette flow convective term, realising an unsteady advection/diffusion equation.

$$\begin{cases} \sin\theta \dfrac{\partial}{\partial\theta}\left(\sin\theta \dfrac{\rho h^3}{12\mu}\dfrac{\partial p}{\partial\theta}\right) + \dfrac{\partial}{\partial\varphi}\left(\dfrac{\rho h^3}{12\mu}\dfrac{\partial p}{\partial\varphi}\right) = \cdots \\ \ldots = R\sin\theta\left[\dfrac{\partial(\sin\theta\,\rho h U_\theta)}{\partial\theta} + \dfrac{\partial\left(\rho h U_\varphi\right)}{\partial\varphi} + R\sin\theta\dfrac{\partial(\rho h)}{\partial t}\right] \\ h(\theta,\varphi,t) = u(p) + c - \mathbf{e}^T(t)\hat{\mathbf{r}}(\theta,\varphi) \\ \mathbf{N}(t) = \iint\limits_{\Omega} p(\theta,\varphi,t)\hat{\mathbf{r}}(\theta,\varphi)\, R^2 \sin\theta\, d\theta d\varphi \end{cases} \tag{224}$$

In order to completely characterize the eqs. (224), the deformation model $u(p)$ has to be developed. In this work the spring, a FEM and the Boundary Element Method (BEM) models are adopted: all the choices refer to elastic deformations, coherently with the EHL regime.

2.2.1. Spring deformation model

The simplest approach is the spring model (Jalali-Vahid and Jin, 2001; Jalali-Vahid *et al.*, 2001a, 2001b; Jalali-Vahid, Jin and Dowson, 2003) assuming that the deformation in a domain point is given only by the local pressure through a constant proportionality compliance coefficient k_c: the spring approach is justified by the assumption that only the much softer surface deforms, while the hardest is assumed to be rigid; then, this model is feasible for Hard-on-Soft implants where the softer part is the acetabular cup generally made of polymeric materials, and, in fact, the compliance factor k_c is given in (225) by the cup mechanical and geometrical properties, i.e., its Young Modulus E, its Poisson ratio ν, its radius R and its thickness H.

$$k_c = \frac{R}{E}\frac{\left(1+\frac{H}{R}\right)^3 - 1}{\frac{1}{1-2\nu}+\frac{2}{1+\nu}\left(1+\frac{H}{R}\right)^3} \quad \rightarrow \quad u(p) = k_c p \tag{225}$$

So, the spherical EHL gap equation with the spring deformation model is reported in (226).

$$h(\theta,\varphi,t) = k_c p(\theta,\varphi,t) + c - \mathbf{e}^T(t)\hat{\mathbf{r}}(\theta,\varphi) \tag{226}$$

Referring to the FDM discretization presented for the spherical HL case, the gap field can be evaluated according to the (i,j) indicial form reported in (227).

$$h_{ij} = k_c p_{ij} + c - \mathbf{e}^T\hat{\mathbf{r}}_{ij} \tag{227}$$

With the aim of preserving the discretised Reynolds equation structure presented for the HL case, a few modifications have to be made (eq. (228)):

- the quantities ε, u and w are updated, while the new quantity v is defined;
- due to the PDE parabolic new behaviour, and in particular to the hyperbolic one of the convective terms, the central differences applied to the Couette flows $\mathbf{d}_{\theta,\varphi^c}$ have to be replaced with the forward/backward differences $\mathbf{d}_{\theta^\pm}/\mathbf{d}_{\varphi^\pm}$ according to the sign of the entraining velocities U_θ and U_φ, adopting the so-called upwind scheme (LeVeque, 2007) in order to enhance numerical stability.

$$\begin{gathered}\varepsilon = \frac{\rho h^3}{12\mu} \quad u = \sin\theta\,\rho h U_\theta \quad w = \rho h U_\varphi \quad v = \rho h \\ \mathbf{D}_\theta = R\sin\theta_i\,\mathbf{I}_\theta^T\mathbf{d}_\theta \quad \mathbf{d}_\theta = \begin{cases}\mathbf{d}_{\theta^-} & U_\theta > 0\\ \mathbf{d}_{\theta^+} & U_\theta < 0\end{cases} \\ \mathbf{D}_\varphi = R\sin\theta_i\,\mathbf{I}_\varphi^T\mathbf{d}_\varphi \quad \mathbf{d}_\varphi = \begin{cases}\mathbf{d}_{\varphi^-} & U_\varphi > 0\\ \mathbf{d}_{\varphi^+} & U_\varphi < 0\end{cases}\end{gathered} \tag{228}$$

Therefore, the FDM discretised form of the spherical EHL Reynolds equation is given in (229).

$$\sin\theta\frac{\partial}{\partial\theta}\left(\sin\theta\,\varepsilon\frac{\partial p}{\partial\theta}\right)+\frac{\partial}{\partial\varphi}\left(\varepsilon\frac{\partial p}{\partial\varphi}\right)=\cdots$$
$$\ldots=R\sin\theta\left(\frac{\partial u}{\partial\theta}+\frac{\partial w}{\partial\varphi}+R\sin\theta\frac{\partial v}{\partial t}\right) \tag{229}$$
$$\boldsymbol{\varepsilon}_I^T\mathbf{D}_2\mathbf{p}_I=\mathbf{D}_\theta^T\mathbf{u}_I+\mathbf{D}_\varphi^T\mathbf{w}_I+\mathbf{D}_t^T\mathbf{v}_t$$

The non-linearity of the equation in (229) is provided by the vectors $\boldsymbol{\varepsilon}_I$, $\mathbf{u}_I$, $\mathbf{w}_I$ and $\mathbf{v}_t$ which depend on the lubricant pressure through the gap and the rheological pressure-sensitive properties: so, the discretised Reynolds equation system, coupled with its boundary conditions in (230), is now a set of non-linear equations.

$$h_I=k_c p_I+c-\mathbf{e}^T\hat{\mathbf{r}}_I\quad \rho_I=\rho_0\frac{c+\gamma p_I}{c+p_I}\quad \mu_I=\mu_0 e^{\frac{\alpha p_I}{1+\beta p_I}}$$
$$\begin{cases}\boldsymbol{\varepsilon}_I^T\mathbf{D}_2\mathbf{p}_I=\mathbf{D}_\theta^T\mathbf{u}_I+\mathbf{D}_\varphi^T\mathbf{w}_I+\mathbf{D}_t^T\mathbf{v}_t & 2\le i,j\le N,M-1\\ p_{1j}=p_{Nj}=0 & 1\le j\le M\\ p_{i1}=p_{iM}=0 & 2\le i\le N-1\end{cases} \tag{230}$$

The non-linear eqs. (230) residual vector **F** is defined in (231): let note that due to the local pressure-sensitive rheological models and, above all, to the spring local proportional model, the residual in a grid point I depends on the pressure cross stencil vector $\mathbf{p}_I$.

$$F_I(\mathbf{p}_I)=\begin{cases}\boldsymbol{\varepsilon}_I^T\mathbf{D}_2\mathbf{p}_I-\mathbf{D}_\theta^T\mathbf{u}_I-\mathbf{D}_\varphi^T\mathbf{w}_I-\mathbf{D}_t^T\mathbf{v}_t & 2\le i,j\le N,M-1\\ p_{1j},p_{Nj} & 1\le j\le M\\ p_{i1},p_{iM} & 2\le i\le N-1\end{cases} \tag{231}$$
$$\mathbf{F}(\mathbf{p})=\mathbf{0}$$

The dependency on the cross stencil suggests the usage of the Newton iterative method to solve the non-linear system, since the system Jacobian will be a penta-diagonal matrix with the same structure presented in the Figure 66, so with a sparsity that makes its inversion fast. The three fundamental pressure derivatives (gap, density and viscosity) are given in (232) by the compliance coefficient and by the chosen rheological analytical models.

$$\frac{\partial h_I}{\partial p_I}=k_c\quad \frac{\partial\rho_I}{\partial p_I}=\rho_0 c\frac{\gamma-1}{(c+p_I)^2}\quad \frac{\partial\mu_I}{\partial p_I}=\mu_0\frac{\alpha}{(1+\beta p_I)^2}e^{\frac{\alpha p_I}{1+\beta p_I}} \tag{232}$$

The derivatives in (232) are all the needing to evaluate the derivatives of the other quantities involved into the Reynolds equation, which are reported in their local form in (233).

$$\begin{aligned}&\frac{\partial\varepsilon_I}{\partial p_I}=\frac{\partial\rho_I}{\partial p_I}\frac{h_I^3}{12\mu_I}+\frac{\rho_I h_I^2}{4\mu_I}\frac{\partial h_I}{\partial p_I}-\frac{\rho_I h_I^3}{12\mu_I^2}\frac{\partial\mu_I}{\partial p_I}\\ &\frac{\partial u_I}{\partial p_I}=\sin\theta_i\frac{\partial\rho_I}{\partial p_I}h_I U_{\theta I}+\sin\theta_i\,\rho_I\frac{\partial h_I}{\partial p_I}U_{\theta I}\\ &\frac{\partial w_I}{\partial p_I}=\frac{\partial\rho_I}{\partial p_I}h_I U_{\varphi I}+\rho_I\frac{\partial h_I}{\partial p_I}U_{\varphi I}\\ &\frac{\partial v_I}{\partial p_I}=\frac{\partial\rho_I}{\partial p_I}h_I+\rho_I\frac{\partial h_I}{\partial p_I}\end{aligned} \tag{233}$$

Then, the derivative of the local residual $\mathrm{F_I}$ with respect to the pressure stencil vector $\mathbf{p}_\mathrm{I}$ is given in (234): it is a [1,5] row vector in which the vector derivatives, thanks to the local deformation model, are nothing that [5,5] diagonal matrices (except for the squeeze term derivative which is given by a [2,5] matrix); the local residual derivative in correspondence of the Dirichlet boundary conditions is equal to one, so the whole Jacobian $\mathbf{F_p}$ has the same sparse structure of the matrix $\mathbf{A}$ in the HL case.

$$\frac{\partial \mathrm{F_I}}{\partial \mathbf{p}_\mathrm{I}}(\mathbf{p}_\mathrm{I}) = \begin{cases} \boldsymbol{\varepsilon}_\mathrm{I}^\mathrm{T}\mathbf{D}_2 + \mathbf{p}_\mathrm{I}^\mathrm{T}\mathbf{D}_2^\mathrm{T}\dfrac{\partial \boldsymbol{\varepsilon}_\mathrm{I}}{\partial \mathbf{p}_\mathrm{I}} + \cdots & \\ \dots - \mathbf{D}_\theta^\mathrm{T}\dfrac{\partial \mathbf{u}_\mathrm{I}}{\partial \mathbf{p}_\mathrm{I}} - \mathbf{D}_\varphi^\mathrm{T}\dfrac{\partial \mathbf{w}_\mathrm{I}}{\partial \mathbf{p}_\mathrm{I}} - \mathbf{D}_\mathrm{t}^\mathrm{T}\dfrac{\partial \mathbf{v}_\mathrm{t}}{\partial \mathbf{p}_\mathrm{I}} & 2 \le \mathrm{i,j} \le \mathrm{N,M}-1 \\ 1 & \begin{matrix} 1 \le \mathrm{j} \le \mathrm{M} \\ 2 \le \mathrm{i} \le \mathrm{N}-1 \end{matrix} \end{cases} \tag{234}$$

$$\mathbf{F_p}(\mathbf{p}) = \frac{\partial \mathbf{F}}{\partial \mathbf{p}}(\mathbf{p})$$

Finally, the obtained Jacobian $\mathbf{F_p}$ of the discretised EHL Reynolds equation set can be used to iterate the lubricant pressure vector $\mathbf{p}$ according to the Newton cycle reported in (235) relaxed by the coefficient ω; as for the HL case, along the iterations the negative pressure have to be truncated in order to impose the cavitation constraint.

$$\begin{aligned} &\text{while } \sum_\mathrm{I} \left|\mathrm{p_I^{k+1}} - \mathrm{p_I^k}\right| > \mathrm{tol} \\ &\quad \mathbf{p}^* = \mathbf{p}^\mathrm{k} - \omega\left[\mathbf{F_p}(\mathbf{p}^\mathrm{k})\right]^{-1}\mathbf{F}(\mathbf{p}^\mathrm{k}) \;\rightarrow\; \mathbf{p}^{\mathrm{k}+1} = \max\{0, \mathbf{p}^*\} \\ &\quad \mathrm{k} \rightarrow \mathrm{k}+1 \\ &\text{end} \end{aligned} \tag{235}$$

The developed strategy with the spring deformation model will be adapted to the THR ML regime in the successive section and its results will be provided.

2.2.2. Finite Element deformation model

The main limitation of the spring deformation model is that the application is limited to Hard-on-Soft THRs: in order to consider implant materials with comparable mechanical responses, a ball-in-socket elastic deformation FEM model developed in Matlab® environment is presented.

The aim is to discretise the bulk of the ball and of the socket into a several deformable finite elements (Felippa, 2004): in this work the linear tetrahedral finite element is chosen. With reference to the Figure 79, a tetrahedron is a solid composed by 4 triangular faces obtained by the connections between its 4 nodes I, J, K and H; with respect to the Oxyz reference frame, the nodes displacements are identified by the vectors $\mathbf{u}_\mathrm{I}$, $\mathbf{u}_\mathrm{J}$, $\mathbf{u}_\mathrm{K}$ and $\mathbf{u}_\mathrm{H}$, resulting in a 12 DoF structure, while the tetrahedron internal point displacement vector $\mathbf{u}$

depends on the point 3D position $\mathbf{x}$; the linear tetrahedron element associates a linear space function to the displacement field $\mathbf{u}$ dependent by the unknown 12 coefficients $a_{x,y,z}$, $b_{x,y,z}$, $c_{x,y,z}$ and $d_{x,y,z}$ reported in (236).

$$\mathbf{u}(\mathbf{x}) = \begin{cases} u(x,z,y) = a_x + b_x x + c_x y + d_x z \\ v(x,z,y) = a_y + b_y x + c_y y + d_y z \\ w(x,z,y) = a_z + b_z x + c_z y + d_z z \end{cases} \tag{236}$$

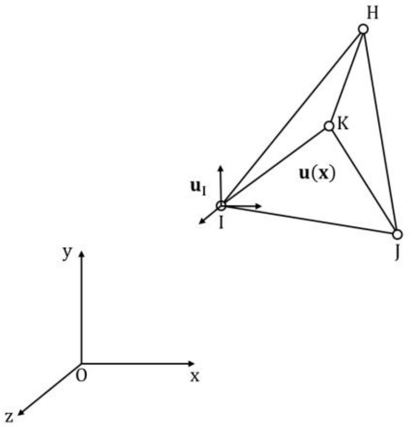

Figure 79 *Linear tetrahedron finite element sketch*

Let write the (236) in matrix form in (237) by introducing the [3,4] coefficient matrix $\mathbf{A}$ and the linear space function [4,1] vector $\boldsymbol{\varphi}$.

$$\begin{bmatrix} u(x,z,y) \\ v(x,z,y) \\ w(x,z,y) \end{bmatrix} = \begin{bmatrix} a_x & b_x & c_x & d_x \\ a_y & b_y & c_y & d_y \\ a_z & b_z & c_z & d_z \end{bmatrix} \begin{bmatrix} 1 \\ x \\ y \\ z \end{bmatrix} \quad \rightarrow \quad \mathbf{u}(\mathbf{x}) = \mathbf{A}\boldsymbol{\varphi}(\mathbf{x}) \tag{237}$$

In order to characterize the displacement field coefficients in $\mathbf{A}$, it can be related in (238) to the nodal displacements by knowing their 3D nodes coordinates $\mathbf{x}_I$, $\mathbf{x}_J$, $\mathbf{x}_K$ and $\mathbf{x}_H$.

$$\begin{cases} \mathbf{u}(\mathbf{x}_I) = \mathbf{A}\boldsymbol{\varphi}(\mathbf{x}_I) = \mathbf{u}_I \\ \mathbf{u}(\mathbf{x}_J) = \mathbf{A}\boldsymbol{\varphi}(\mathbf{x}_J) = \mathbf{u}_J \\ \mathbf{u}(\mathbf{x}_K) = \mathbf{A}\boldsymbol{\varphi}(\mathbf{x}_K) = \mathbf{u}_K \\ \mathbf{u}(\mathbf{x}_H) = \mathbf{A}\boldsymbol{\varphi}(\mathbf{x}_H) = \mathbf{u}_H \end{cases} \tag{238}$$

The matrix form of (238) obtained defining the [4,4] nodal coordinates matrix $\boldsymbol{\Phi}$ and collecting the nodal displacements in the [3,4] matrix $\mathbf{U}$, allows to evaluate the coefficients in $\mathbf{A}$ by inverting the matrix $\boldsymbol{\Phi}$ dependent on the nodal coordinates.

$$\begin{aligned} &\mathbf{A}\left[\boldsymbol{\varphi}(\mathbf{x}_I) \quad \boldsymbol{\varphi}(\mathbf{x}_J) \quad \boldsymbol{\varphi}(\mathbf{x}_K) \quad \boldsymbol{\varphi}(\mathbf{x}_H)\right] = [\mathbf{u}_I \quad \mathbf{u}_J \quad \mathbf{u}_K \quad \mathbf{u}_H] \\ &\mathbf{A}\boldsymbol{\Phi} = \mathbf{U} \quad \rightarrow \quad \mathbf{A} = \mathbf{U}\boldsymbol{\Phi}^{-1} \end{aligned} \tag{239}$$

Then, the displacement field can be written as the product between the [3,4] nodal displacement matrix $\mathbf{U}$ and the so-called shape function [4,1] vector $\mathbf{n}$ defined in (240).

$$\mathbf{u}(\mathbf{x}) = \mathbf{U}\left(\mathbf{\Phi}^{-1}\boldsymbol{\varphi}(\mathbf{x})\right) = \mathbf{Un}(\mathbf{x}) \tag{240}$$

The (240) is rearranged in (241) in order to get a linear relation between the [3,1] displacement field vector **u** and the [12,1] nodal displacement vector **q** through the shape function [3,12] matrix **N**.

$$\begin{gathered}\mathbf{u}(\mathbf{x}) = \mathbf{Un}(\mathbf{x}) = [\mathbf{u}_\mathrm{I} \quad \mathbf{u}_\mathrm{J} \quad \mathbf{u}_\mathrm{K} \quad \mathbf{u}_\mathrm{H}]\begin{bmatrix}\mathrm{n_I}\\ \mathrm{n_J}\\ \mathrm{n_K}\\ \mathrm{n_H}\end{bmatrix}\\ \mathbf{u}(\mathbf{x}) = [\mathrm{n_I}\mathbf{I} \quad \mathrm{n_J}\mathbf{I} \quad \mathrm{n_K}\mathbf{I} \quad \mathrm{n_H}\mathbf{I}]\begin{bmatrix}\mathbf{u}_\mathrm{I}\\ \mathbf{u}_\mathrm{J}\\ \mathbf{u}_\mathrm{K}\\ \mathbf{u}_\mathrm{H}\end{bmatrix} = \mathbf{N}(\mathbf{x})\mathbf{q}\end{gathered} \tag{241}$$

According to the small displacement assumption, the deformation tensor $\boldsymbol{\varepsilon}$ is given by the displacement gradients reported in (242).

$$\boldsymbol{\varepsilon} = \frac{1}{2}\left(\frac{\partial \mathbf{u}}{\partial \mathbf{x}} + \frac{\partial \mathbf{u}}{\partial \mathbf{x}}^{\mathrm{T}}\right) \tag{242}$$

Let report the displacement field in its first form in (240) to obtain its gradient, evaluating the gradient of the space function vector $\boldsymbol{\varphi}$ in (243).

$$\begin{gathered}\mathbf{u}(\mathbf{x}) = \mathbf{U\Phi}^{-1}\boldsymbol{\varphi}(\mathbf{x})\\ \frac{\partial \mathbf{u}}{\partial \mathbf{x}} = \mathbf{U\Phi}^{-1}\frac{\partial \boldsymbol{\varphi}}{\partial \mathbf{x}} \qquad \frac{\partial \boldsymbol{\varphi}}{\partial \mathbf{x}} = \begin{bmatrix}0 & 0 & 0\\ 1 & 0 & 0\\ 0 & 1 & 0\\ 0 & 0 & 1\end{bmatrix}\end{gathered} \tag{243}$$

The product between the nodal coordinates matrix $\mathbf{\Phi}$ inverse and the space function $\boldsymbol{\varphi}$ gradient is nothing that the last 3 columns of the former matrix that, for the ease of reading, is indicated with **D**; then, making explicit the entries of the displacement field **u** gradient, of the nodal displacement matrix **U** and of the last just described product, the (243) is turned into (244).

$$\begin{bmatrix}\mathrm{u_x} & \mathrm{u_y} & \mathrm{u_z}\\ \mathrm{v_x} & \mathrm{v_y} & \mathrm{v_z}\\ \mathrm{w_x} & \mathrm{w_y} & \mathrm{w_z}\end{bmatrix} = \begin{bmatrix}\mathrm{u_I} & \mathrm{u_J} & \mathrm{u_K} & \mathrm{u_H}\\ \mathrm{v_I} & \mathrm{v_J} & \mathrm{v_K} & \mathrm{v_H}\\ \mathrm{w_I} & \mathrm{w_J} & \mathrm{w_K} & \mathrm{w_H}\end{bmatrix}\begin{bmatrix}\mathrm{D_{12}} & \mathrm{D_{13}} & \mathrm{D_{14}}\\ \mathrm{D_{22}} & \mathrm{D_{23}} & \mathrm{D_{24}}\\ \mathrm{D_{32}} & \mathrm{D_{33}} & \mathrm{D_{34}}\\ \mathrm{D_{42}} & \mathrm{D_{43}} & \mathrm{D_{44}}\end{bmatrix} \tag{244}$$

The matrix relation (224) allows to highlight the linear dependence between the 6 independent deformations, i.e., the 3 normal strains ε_x, ε_y, ε_z and the 3 shear strains γ_{xy}, γ_{yz}, γ_{xz}, and the nodal displacement vector through the [6,12] deformability matrix in (245).

$$\begin{bmatrix}\varepsilon_\mathrm{x}\\ \varepsilon_\mathrm{y}\\ \varepsilon_\mathrm{z}\\ \gamma_\mathrm{xy}\\ \gamma_\mathrm{yz}\\ \gamma_\mathrm{xz}\end{bmatrix} = \begin{bmatrix}\mathrm{u_x}\\ \mathrm{v_y}\\ \mathrm{w_z}\\ \mathrm{u_y} + \mathrm{v_x}\\ \mathrm{v_z} + \mathrm{w_y}\\ \mathrm{u_z} + \mathrm{w_x}\end{bmatrix} = \cdots \tag{245}$$

$$
= \begin{bmatrix} D_{12} & 0 & 0 & D_{22} & 0 & 0 & D_{32} & 0 & 0 & D_{42} & 0 & 0 \\ 0 & D_{13} & 0 & 0 & D_{23} & 0 & 0 & D_{33} & 0 & 0 & D_{43} & 0 \\ 0 & 0 & D_{14} & 0 & 0 & D_{24} & 0 & 0 & D_{34} & 0 & 0 & D_{44} \\ D_{13} & D_{12} & 0 & D_{23} & D_{22} & 0 & D_{33} & D_{32} & 0 & D_{43} & D_{42} & 0 \\ 0 & D_{14} & D_{13} & 0 & D_{24} & D_{23} & 0 & D_{34} & D_{33} & 0 & D_{44} & D_{43} \\ D_{14} & 0 & D_{12} & D_{24} & 0 & D_{22} & D_{34} & 0 & D_{32} & D_{44} & 0 & D_{42} \end{bmatrix} \begin{bmatrix} u_I \\ v_I \\ w_I \\ u_J \\ v_J \\ w_J \\ u_K \\ v_K \\ w_K \\ u_H \\ v_H \\ w_H \end{bmatrix}
$$

The (245) is written in matrix form in (246), indicating the deformability matrix with **B**.

$$\boldsymbol{\varepsilon} = \mathbf{Bq} \tag{246}$$

The linear constitutive relation for isotropic elastic materials between the stress vector $\boldsymbol{\sigma}$ (the 3 normal stresses σ_x, σ_y, σ_z and the 3 shear stresses τ_{xy}, τ_{yz}, τ_{xz}) and the strain vector $\boldsymbol{\varepsilon}$ is given by the symmetric [6,6] elasticity matrix $\mathbf{C}$ reported in (247) dependent on the Lamé constants λ and μ (functions of the material Young modulus E and Poisson ratio ν) (Felippa, 2004); let note that due to the linear relation between the strain $\boldsymbol{\varepsilon}$ and the nodal displacement $\mathbf{q}$ vectors, also the stress vector $\boldsymbol{\sigma}$ is a linear combination of $\mathbf{q}$.

$$
\lambda = \frac{\nu E}{(1+\nu)(1-2\nu)} \quad \mu = \frac{E}{2(1+\nu)}
$$
$$
\begin{bmatrix} \sigma_x \\ \sigma_y \\ \sigma_z \\ \tau_{xy} \\ \tau_{yz} \\ \tau_{xz} \end{bmatrix} = \begin{bmatrix} 2\mu+\lambda & \lambda & \lambda & 0 & 0 & 0 \\ \lambda & 2\mu+\lambda & \lambda & 0 & 0 & 0 \\ \lambda & \lambda & 2\mu+\lambda & 0 & 0 & 0 \\ 0 & 0 & 0 & \lambda & 0 & 0 \\ 0 & 0 & 0 & 0 & \lambda & 0 \\ 0 & 0 & 0 & 0 & 0 & \lambda \end{bmatrix} \begin{bmatrix} \varepsilon_x \\ \varepsilon_y \\ \varepsilon_z \\ \gamma_{xy} \\ \gamma_{yz} \\ \gamma_{xz} \end{bmatrix} \tag{247}
$$
$$
\boldsymbol{\sigma} = \mathbf{C}\boldsymbol{\varepsilon} = \mathbf{CBq}
$$

With reference to the Figure 80, the tetrahedron element energetic equilibrium for a set of virtual displacements is given in (248), i.e., the weak form of the dynamical equilibrium neglecting inertial effects (Felippa, 2004); it takes into account:

- the internal elastic energy within the tetrahedron volume Ω due the stress $\boldsymbol{\sigma}$ and to the virtual strain $\delta\boldsymbol{\varepsilon}$;
- the work done by the nodal forces **f** producing a virtual nodal displacement vector $\delta\mathbf{q}$;
- the work done by an external pressure p acting on an exposed tetrahedron face Ω_p, if any, with outward normal $\hat{\mathbf{n}}$ producing an internal virtual displacement $\delta\mathbf{u}$.

$$\int_{\Omega} \boldsymbol{\sigma}^{\mathrm{T}} \delta\boldsymbol{\varepsilon}\, \mathrm{dV} = \mathbf{f}^{\mathrm{T}} \delta\mathbf{q} - \int_{\Omega_{\mathrm{p}}} \mathrm{p}\hat{\mathbf{n}}^{\mathrm{T}} \delta\mathbf{u}\, \mathrm{dA} \tag{248}$$

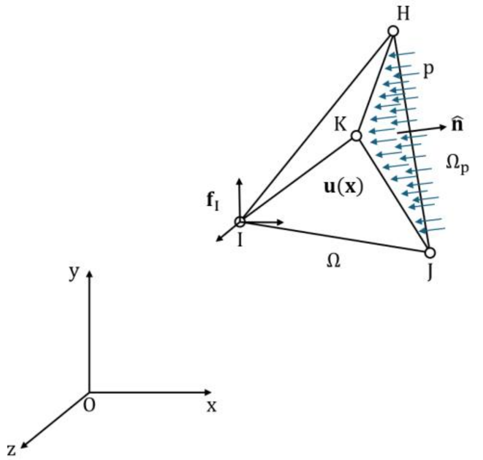

Figure 80 *Linear tetrahedron finite element dynamical configuration*

Substituting in (248) the stresses/nodal displacements linear relation and the variational form of the strains/nodal displacements linear relation, the tetrahedron symmetric [12,12] stiffness matrix $\mathbf{K}$ is obtained in (249): let note that both the deformability $\mathbf{B}$ and elasticity $\mathbf{C}$ matrix do not exhibit variation within the linear tetrahedron volume (the same for the nodal displacements), so they can be taken out from the integral leaving only the tetrahedron volume which can be calculated by exploiting the determinant of the nodal coordinates matrix $\boldsymbol{\Phi}$.

$$\begin{gathered} \boldsymbol{\sigma} = \mathbf{CBq} \quad \delta\boldsymbol{\varepsilon} = \mathbf{B}\delta\mathbf{q} \quad \int_{\Omega} \mathrm{dV} = \frac{1}{6}\|\boldsymbol{\Phi}\| \\ \int_{\Omega} \boldsymbol{\sigma}^{\mathrm{T}} \delta\boldsymbol{\varepsilon}\, \mathrm{dV} = \mathbf{q}^{\mathrm{T}} \left(\int_{\Omega} \mathbf{B}^{\mathrm{T}}\mathbf{CB}\, \mathrm{dV} \right) \delta\mathbf{q} = \mathbf{q}^{\mathrm{T}}\mathbf{K}\delta\mathbf{q} \\ \mathbf{K} = \mathbf{B}^{\mathrm{T}}\mathbf{CB}\frac{1}{6}\|\boldsymbol{\Phi}\| \end{gathered} \tag{249}$$

Moving to the pressure energetic contribution, it is assumed that the pressure acting on the exposed tetrahedron face (the one delimited by the nodes J, K and H in the Figure 73) is homogeneous and equal to the arithmetical average of the respective nodal pressures $\mathrm{p_J}$, $\mathrm{p_K}$ and $\mathrm{p_H}$, which are collected into the pressure face vector $\mathbf{p}_\mathrm{f}$ to which is applied the mean vector operator $\mathbf{m}$ in (250).

$$\mathbf{p}_\mathrm{f} = [\mathrm{p_J} \quad \mathrm{p_K} \quad \mathrm{p_H}]^\mathrm{T}$$
$$\mathbf{m} = \frac{[1 \quad 1 \quad 1]^\mathrm{T}}{3} \quad \rightarrow \quad \mathrm{p} = \frac{\mathrm{p_J} + \mathrm{p_K} + \mathrm{p_H}}{3} = \mathbf{m}^\mathrm{T}\mathbf{p}_\mathrm{f} \tag{250}$$

The exposed outward surface normal is evaluated by firstly calculating in (251) a normal vector $\mathbf{n}_\mathrm{p}$ given by the face nodal coordinates $\mathbf{x}_\mathrm{J}$, $\mathbf{x}_\mathrm{K}$ and $\mathbf{x}_\mathrm{H}$.

$$\mathbf{n}_\mathrm{p} = (\mathbf{x}_\mathrm{J} - \mathbf{x}_\mathrm{K}) \times (\mathbf{x}_\mathrm{J} - \mathbf{x}_\mathrm{H}) \tag{251}$$

Then, defining the face centre coordinates $\mathbf{x}_\mathrm{C}$, the outward normal $\hat{\mathbf{n}}$ is obtained in (252).

$$\mathbf{x}_\mathrm{C} = \frac{\mathbf{x}_\mathrm{J} + \mathbf{x}_\mathrm{K} + \mathbf{x}_\mathrm{H}}{3} \quad \rightarrow \quad \hat{\mathbf{n}} = \mathrm{sign}\left[(\mathbf{x}_\mathrm{C} - \mathbf{x}_\mathrm{I})^\mathrm{T}\mathbf{n}_\mathrm{p}\right]\frac{\mathbf{n}_\mathrm{p}}{\|\mathbf{n}_\mathrm{p}\|} \tag{252}$$

So, the pressure and the normal unit vector can be taken out from the integral, leaving in (253) the virtual displacement $\delta\mathbf{u}$ inside it, which can be related to the virtual nodal displacements $\delta\mathbf{q}$ through the shape function matrix **N**.

$$\delta\mathbf{u} = \mathbf{N}(\mathbf{x})\delta\mathbf{q}$$
$$-\int_{\Omega_\mathrm{p}} \mathrm{p}\hat{\mathbf{n}}^\mathrm{T}\delta\mathbf{u}\,\mathrm{dA} = -(\mathbf{m}^\mathrm{T}\mathbf{p}_\mathrm{f})\hat{\mathbf{n}}^\mathrm{T}\left(\int_{\Omega_\mathrm{p}} \mathbf{N}(\mathbf{x})\,\mathrm{dA}\right)\delta\mathbf{q} \tag{253}$$

The surface integral in (253) can be evaluated by recalling that the shape function matrix **N** comes from the shape function vector **n** in (240): so, the latter integral is evaluated in (254), where the surface integral of the space function $\boldsymbol{\varphi}$ is given by the face centre nodal coordinates $\mathbf{x}_\mathrm{C}$ and the face area related to the norm of the normal vector $\mathbf{n}_\mathrm{p}$.

$$\mathbf{n}(\mathbf{x}) = \boldsymbol{\Phi}^{-1}\boldsymbol{\varphi}(\mathbf{x}) \qquad \int_{\Omega_\mathrm{p}} \mathrm{dA} = \frac{1}{2}\|\mathbf{n}_\mathrm{p}\|$$
$$\int_{\Omega_\mathrm{p}} \mathbf{n}(\mathbf{x})\,\mathrm{dA} = \boldsymbol{\Phi}^{-1}\boldsymbol{\varphi}(\mathbf{x}_\mathrm{C})\frac{1}{2}\|\mathbf{n}_\mathrm{p}\| \tag{254}$$

Therefore, indicating with the [4,1] vector **h** the surface integral result of the shape function vector **n** in (254), the integral of the shape function matrix **N** is given in (255) denoting it as the [3,12] matrix **H**, obtained with the **h** vector components.

$$\mathbf{h} = \int_{\Omega_\mathrm{p}} \mathbf{n}(\mathbf{x})\,\mathrm{dA} = \boldsymbol{\Phi}^{-1}\boldsymbol{\varphi}(\mathbf{x}_\mathrm{C})\frac{1}{2}\|\mathbf{n}_\mathrm{p}\| = \begin{bmatrix} \mathrm{h_I} \\ \mathrm{h_J} \\ \mathrm{h_K} \\ \mathrm{h_H} \end{bmatrix}$$
$$\mathbf{H} = \int_{\Omega_\mathrm{p}} \mathbf{N}(\mathbf{x})\,\mathrm{dA} = [\mathrm{h_I}\mathbf{I} \quad \mathrm{h_J}\mathbf{I} \quad \mathrm{h_K}\mathbf{I} \quad \mathrm{h_H}\mathbf{I}] \tag{255}$$

Finally, the pressure energetic contribution is reported in (256) with the definition of the nodal pressure force vector $\mathbf{f}_p$, which is a linear combination of the nodal pressure vector $\mathbf{p}_f$ through the defined matrix $\mathbf{J}_p$.

$$\begin{aligned} &-\int_{\Omega_p} p\hat{\mathbf{n}}^T \delta\mathbf{u}\, dA = \left[-\left(\mathbf{m}^T\mathbf{p}_f\right)\hat{\mathbf{n}}^T\mathbf{H}\right]\delta\mathbf{q} = \mathbf{f}_p^T\delta\mathbf{q} \\ &\mathbf{f}_p = \left(-\mathbf{H}^T\hat{\mathbf{n}}\mathbf{m}^T\right)\mathbf{p}_f = \mathbf{J}_p\mathbf{p}_f \end{aligned} \tag{256}$$

The above internal elastic and pressure energetic contributions are determined for a single tetrahedron, but the energetic equilibrium (248) has to refer to the global structure discretised in a finite number n_E of tetrahedral elements. The structure is identified by its nodes: let refer for example to the coordinates of the i node belonging to the socket $\mathbf{x}_{si}$ or the ball $\mathbf{x}_{bi}$ bodies calculated with the spherical coordinates ρ,θ and φ in (257) accounting for the socket inner radius R and thickness H and for the ball radius r.

$$\begin{aligned} &\mathbf{x}_{si} = \begin{bmatrix} \rho_i \sin\theta_i \cos\varphi_i \\ \rho_i \sin\theta_i \sin\varphi_i \\ \rho_i \cos\theta_i \end{bmatrix} \quad \begin{matrix} 0 \le \theta \le \pi \\ 0 \le \varphi \le \pi \\ R \le \rho \le R + H \end{matrix} \\ &\mathbf{x}_{bi} = \begin{bmatrix} \rho_i \sin\theta_i \cos\varphi_i \\ \rho_i \sin\theta_i \sin\varphi_i \\ \rho_i \cos\theta_i \end{bmatrix} \quad \begin{matrix} 0 \le \theta \le \pi \\ 0 \le \varphi \le 2\pi \\ 0 \le \rho \le r \end{matrix} \end{aligned} \tag{257}$$

Once the structure nodal coordinates are identified, a regular tetrahedral mesh (Jacobson, 2024) can be performed assigning to each resulting j element the i indices of its I, J, K and H nodes: so, the (248) energetic equilibrium provides the structure dynamical equilibrium in (258) accounting for the j element stiffness matrix $\mathbf{K}_j$, nodal displacements $\mathbf{q}_j$, nodal forces $\mathbf{f}_j$ and nodal pressure forces $\mathbf{f}_{pj}$.

$$\sum_{j=1}^{n_E} \mathbf{K}_j\mathbf{q}_j - \mathbf{f}_j - \mathbf{f}_{pj} = \mathbf{0} \tag{258}$$

The structure dynamical equilibrium is given in matrix form in (259) following the order coming from the concatenation of all the structure nodes given by their positions in (257).

$$\begin{aligned} &\sum_{j=1}^{n_E}\left(\begin{bmatrix} & \vdots & \vdots & \vdots & \vdots & \\ & \mathbf{K}_{IIj} & \mathbf{K}_{IJj} & \mathbf{K}_{IKj} & \mathbf{K}_{IHj} & \\ & \vdots & \vdots & \vdots & \vdots & \\ & \mathbf{K}_{JIj} & \mathbf{K}_{JJj} & \mathbf{K}_{JKj} & \mathbf{K}_{JHj} & \\ \cdots & \vdots & \cdots\ \vdots & \cdots\ \vdots & \cdots\ \vdots & \cdots \\ & \mathbf{K}_{KIj} & \mathbf{K}_{KJj} & \mathbf{K}_{KKj} & \mathbf{K}_{KHj} & \\ & \vdots & \vdots & \vdots & \vdots & \\ & \mathbf{K}_{HIj} & \mathbf{K}_{HJj} & \mathbf{K}_{HKj} & \mathbf{K}_{HHj} & \\ & \vdots & \vdots & \vdots & \vdots & \end{bmatrix}\begin{bmatrix} \vdots \\ \mathbf{u}_{Ij} \\ \vdots \\ \mathbf{u}_{Jj} \\ \vdots \\ \mathbf{u}_{Kj} \\ \vdots \\ \mathbf{u}_{Hj} \\ \vdots \end{bmatrix} - \begin{bmatrix} \vdots \\ \mathbf{f}_{Ij} \\ \vdots \\ \mathbf{f}_{Jj} \\ \vdots \\ \mathbf{f}_{Kj} \\ \vdots \\ \mathbf{f}_{Hj} \\ \vdots \end{bmatrix} - \begin{bmatrix} \vdots \\ \mathbf{f}_{pIj} \\ \vdots \\ \mathbf{f}_{pJj} \\ \vdots \\ \mathbf{f}_{pKj} \\ \vdots \\ \mathbf{f}_{pHj} \\ \vdots \end{bmatrix}\right) \\ &\ldots = \mathbf{0} \quad \rightarrow \quad \mathbf{Kq} = \mathbf{f} + \mathbf{f}_p \end{aligned} \tag{259}$$

The unknowns in the obtained linear system in (259) are not the entire set of nodal displacements $\mathbf{q}$: generally, in a FEM discretised structure some nodes are characterised by imposed displacements, while some nodes are subjected to known nodal forces; moreover, the nodal forces that constrain the element to be connected are not known. So, the (259) system is rearranged in (260) by ordering the nodal displacement vector $\mathbf{q}$ as composed by the free unknown displacements $\mathbf{q}_\mathrm{f}$ to which the free nodal forces $\mathbf{f}_\mathrm{f}$ are associated and then by the known constrained displacements $\mathbf{q}_\mathrm{c}$ to which the constrained nodal forces $\mathbf{f}_\mathrm{c}$ are associated.

$$\begin{bmatrix}\mathbf{K}_\mathrm{ff} & \mathbf{K}_\mathrm{fc}\\ \mathbf{K}_\mathrm{cf} & \mathbf{K}_\mathrm{cc}\end{bmatrix}\begin{bmatrix}\mathbf{q}_\mathrm{f}\\ \mathbf{q}_\mathrm{c}\end{bmatrix}=\begin{bmatrix}\mathbf{f}_\mathrm{f}\\ \mathbf{f}_\mathrm{c}\end{bmatrix}+\begin{bmatrix}\mathbf{f}_\mathrm{pf}\\ \mathbf{f}_\mathrm{pc}\end{bmatrix} \tag{260}$$

From the (260) the free displacements $\mathbf{q}_\mathrm{f}$ and the constraint forces $\mathbf{f}_\mathrm{c}$ can be evaluated, but in this work EHL context only the free displacements are needed; the constrained displacements and pressure loaded nodes are different for the ball and the socket structures:

- the socket fixed nodes are the ones belonging to its external surface ($\mathbf{q}_\mathrm{c}=\mathbf{0}$), while the pressure-loaded nodes are the ones belonging to the inner surface and there are no other imposed nodal forces (so $\mathbf{f}_\mathrm{f}=\mathbf{0}$);
- the ball fixed nodes are the ones belonging to its inferior part below a given y height ($\mathbf{q}_\mathrm{c}=\mathbf{0}$), while the pressure-loaded nodes are the ones belonging to the external surface and there are no other imposed nodal forces (so $\mathbf{f}_\mathrm{f}=\mathbf{0}$).

The two structures meshes are reported in the Figure 81 together with the red/green/blue xyz reference frame, where the pressure-loaded nodes are identified by little red radial arrows, while the fixed nodes are identified by black triangles markers.

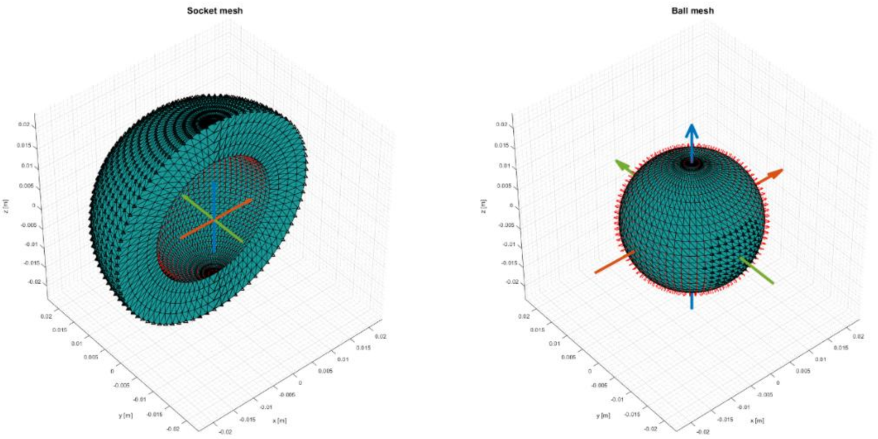

Figure 81 *Ball and socket FEM meshes*

So, the free displacement vector $\mathbf{q}_{\mathrm{f}}$ can be calculated for both the structures with the same formula reported in (261) by considering that the only nodal force source is given by the pressure-dependent ones $\mathbf{f}_{\mathrm{pf}}$.

$$\mathbf{q}_{\mathrm{f}} = \mathbf{K}_{\mathrm{ff}}^{-1}\mathbf{f}_{\mathrm{pf}} \tag{261}$$

Referring to the nodal coordinates in (257), the nodes in correspondence of the inner socket surface, i.e., at $\rho_{\mathrm{i}} = \mathrm{R}$, are the same of the 2D spherical grid defined for the FDM Reynolds equation discretization, so, knowing from (256) that the elemental pressure forces are linearly related to the nodal pressure acting on a tetrahedron face, there will be a linear relation between $\mathbf{f}_{\mathrm{pf}}$ and the pressure vector $\mathbf{p}$ referred to the lexicographical order through the matrix $\mathbf{J}_{\mathrm{p}}$ (eq. (262)); the same can be done for the ball body defining a pressure vector referred to a 2D grid attached to its external surface, i.e., at $\rho_{\mathrm{i}} = \mathrm{r}$.

$$\mathbf{f}_{\mathrm{pf}} = \mathbf{J}_{\mathrm{p}}\mathbf{p} \tag{262}$$

Furthermore, the Reynolds equation deformation vector $\mathbf{u}$, always referred to the spherical grid, can be evaluated as a linear combination of the free displacements $\mathbf{q}_{\mathrm{f}}$ through the matrix $\mathbf{J}_{\mathrm{u}}$ in (263), since the deformation u_{I} on a 2D spherical grid point (i,j) associated with the lexicographical index I can be obtained by the projection of the related structure node i displacement $\mathbf{q}_{\mathrm{i}}$ along the radial direction identified by the radial unit vector $\hat{\mathbf{r}}_{\mathrm{I}}$ in correspondence of that position; again, the same can be done for the ball body by defining a radial deformation vector referred to its 2D external surface grid.

$$\mathrm{u}_{\mathrm{I}} = \hat{\mathbf{r}}_{\mathrm{I}}^{\mathrm{T}}\mathbf{q}_{\mathrm{i}} \quad \rightarrow \quad \mathbf{u} = \mathbf{J}_{\mathrm{u}}\mathbf{q}_{\mathrm{f}} \tag{263}$$

Therefore, applying the (262) and the (263) to the (261), a linear relation between the deformation vectors and the lubricant pressure vectors is obtained through the definition of a dense compliance matrix $\mathbf{C}$ in (264): this is valid for both the inner socket surface grid and the external ball surface grid (subscripts s for the socket and b for the ball).

$$\begin{gathered}\mathbf{u} = \mathbf{J}_{\mathrm{u}}\mathbf{q}_{\mathrm{f}} = \left(\mathbf{J}_{\mathrm{u}}\mathbf{K}_{\mathrm{ff}}^{-1}\mathbf{J}_{\mathrm{p}}\right)\mathbf{p} = \mathbf{C}\mathbf{p} \\ \mathbf{u}_{\mathrm{s}} = \mathbf{C}_{\mathrm{s}}\mathbf{p}_{\mathrm{s}} \quad \mathbf{u}_{\mathrm{b}} = \mathbf{C}_{\mathrm{b}}\mathbf{p}_{\mathrm{b}}\end{gathered} \tag{264}$$

The deformation u considered in the gap equation of the EHL problem system is actually the total deformation given by both the socket and the ball radial displacements, but generally the socket inner surface grid and the ball external one could be different, so, at this level, the deformations $\mathbf{u}_{\mathrm{s}}$ and $\mathbf{u}_{\mathrm{b}}$ cannot be added together: in order to do that, in this work a cubic interpolation approach to move between the two grids is defined.

With reference to the Figure 82, let say that the f variable field defined in the starting 2D grid $\theta\varphi$ has to be interpolated on the arrival grid: the value of f in the point $\theta^*\varphi^*$ can be evaluated by a cubic interpolation characterised by the unknown [12,1] coefficients vector **a** and by the cubic function vector **c** in (265).

$$\mathbf{c}(\theta,\varphi) = [1\ \ \theta\ \ \theta^2\ \ \theta^3\ \ \varphi\ \ \varphi^2\ \ \varphi^3\ \ \theta\varphi\ \ \theta^2\varphi\ \ \theta\varphi^2\ \ \theta^3\varphi\ \ \theta\varphi^3]^{\mathrm{T}} \tag{265}$$

$$f(\theta,\varphi) = \mathbf{a}^{T}\mathbf{c}(\theta,\varphi)$$

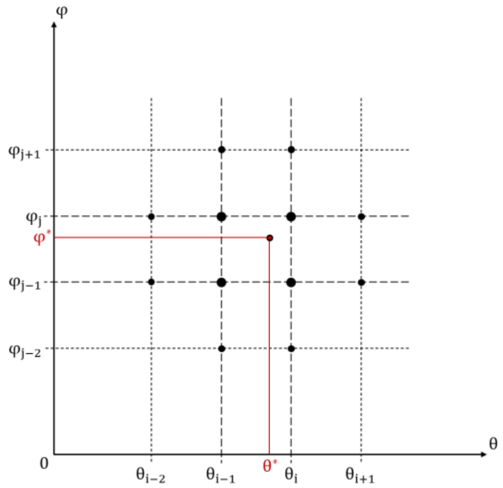

Figure 82 *Grid points for cubic interpolation*

The coefficients vector **a** in (265) can be evaluated by imposing that the cubic interpolation has to return the analysed point $\theta^{*}\varphi^{*}$ surroundings values, i.e., $f_{i-1,j-1}$, $f_{i-1,j}$, $f_{i,j-1}$ and f_{ij}, and also their derivatives along the 2 directions obtained with central finite differences considering the analytic derivatives of the cubic function vector **c**, i.e., $\mathbf{c}_{\theta}$ and $\mathbf{c}_{\varphi}$: the obtained system of equations provides a linear relationship in (266) between the coefficients vector **a** and the $\mathbf{f}^{*}$ vector containing the 12 values of the field f in correspondence of the surrounding points highlighted in the Figure 75 through the cubic interpolation [12,12] matrix **Φ** and a [12,12] matrix **D** that extracts the field values and its derivatives.

$$\begin{aligned} \mathbf{c}_{\theta}(\theta,\varphi) &= [0\ \ 1\ \ 2\theta\ \ 3\theta^{2}\ \ 0\ \ 0\ \ 0\ \ \varphi\ \ 2\theta\varphi\ \ \varphi^{2}\ \ 3\theta^{2}\varphi\ \ \varphi^{3}]^{T} \\ \mathbf{c}_{\varphi}(\theta,\varphi) &= [0\ \ 0\ \ 0\ \ 0\ \ 1\ \ 2\varphi\ \ 3\varphi^{2}\ \ \theta\ \ \theta^{2}\ \ 2\theta\varphi\ \ \theta^{3}\ \ 3\theta\varphi^{2}]^{T} \end{aligned} \qquad (266)$$

$$\left\{\begin{array}{l}
\mathbf{c}^{\mathrm{T}}(\theta_{i-1},\varphi_{j-1})\mathbf{a}=f_{i-1,j-1}\\
\mathbf{c}^{\mathrm{T}}(\theta_{i-1},\varphi_{j})\mathbf{a}=f_{i-1,j}\\
\mathbf{c}^{\mathrm{T}}(\theta_{i},\varphi_{j-1})\mathbf{a}=f_{i,j-1}\\
\mathbf{c}^{\mathrm{T}}(\theta_{i},\varphi_{j})\mathbf{a}=f_{ij}\\
\mathbf{c}_{\theta}^{\mathrm{T}}(\theta_{i-1},\varphi_{j-1})\mathbf{a}=\dfrac{f_{i,j-1}-f_{i-2,j-1}}{2\Delta\theta}\\
\mathbf{c}_{\theta}^{\mathrm{T}}(\theta_{i-1},\varphi_{j})\mathbf{a}=\dfrac{f_{ij}-f_{i-2,j}}{2\Delta\theta}\\
\mathbf{c}_{\theta}^{\mathrm{T}}(\theta_{i},\varphi_{j-1})\mathbf{a}=\dfrac{f_{i+1,j-1}-f_{i-1,j-1}}{2\Delta\theta}\\
\mathbf{c}_{\theta}^{\mathrm{T}}(\theta_{i},\varphi_{j})\mathbf{a}=\dfrac{f_{i+1,j}-f_{i-1,j}}{2\Delta\theta}\\
\mathbf{c}_{\varphi}^{\mathrm{T}}(\theta_{i-1},\varphi_{j-1})\mathbf{a}=\dfrac{f_{i-1,j}-f_{i-1,j-2}}{2\Delta\varphi}\\
\mathbf{c}_{\varphi}^{\mathrm{T}}(\theta_{i-1},\varphi_{j})\mathbf{a}=\dfrac{f_{i-1,j+1}-f_{i-1,j-1}}{2\Delta\varphi}\\
\mathbf{c}_{\varphi}^{\mathrm{T}}(\theta_{i},\varphi_{j-1})\mathbf{a}=\dfrac{f_{ij}-f_{i,j-2}}{2\Delta\varphi}\\
\mathbf{c}_{\varphi}^{\mathrm{T}}(\theta_{i},\varphi_{j})\mathbf{a}=\dfrac{f_{i,j+1}-f_{i,j-1}}{2\Delta\varphi}
\end{array}\right. \quad\rightarrow\quad \mathbf{\Phi a}=\mathbf{Df}^{*}$$

Then, the linear system in (266) can be inverted to evaluate the coefficients vector $\mathbf{a}$ needed to evaluate the searched f value in the arrival grid point $\theta^{*}\varphi^{*}$ as a linear combination of the vector $\mathbf{f}^{*}$ through the [12,1] vector $\mathbf{J}^{*}$: the latter relation can be exploited to define in (267) a cubic interpolation matrix $\mathbf{J}_{bs}$ that interpolates the f field defined on the ball grid $\mathbf{f}_{b}$ into the socket grid to obtain the associated $\mathbf{f}_{s}$ and vice versa.

$$\begin{array}{l}
f(\theta^{*},\varphi^{*})=\mathbf{c}(\theta^{*},\varphi^{*})^{\mathrm{T}}\mathbf{a}=\left(\mathbf{c}(\theta^{*},\varphi^{*})^{\mathrm{T}}\mathbf{\Phi}^{-1}\mathbf{D}\right)\mathbf{f}^{*}={\mathbf{J}^{*}}^{\mathrm{T}}\mathbf{f}^{*}\\
\mathbf{f}_{s}=\mathbf{J}_{bs}\mathbf{f}_{b}\quad \mathbf{f}_{b}=\mathbf{J}_{sb}\mathbf{f}_{s}
\end{array} \tag{267}$$

Finally, recalling the compliance matrices in (264) referred to the socket and the ball FEM structures and underlining that the socket inner surface 2D grid actually is the Reynolds equation FDM grid, the total deformation vector $\mathbf{u}$ is linked to the lubricant pressure vector $\mathbf{p}$ through the final compliance matrix $\mathbf{C}$ in (268), obtaining a deformation model based on accurate FEM discretization of the THR bulks that is feasible also for comparable materials composing the implant: it is worth to note that, due the dense compliance matrix $\mathbf{C}$, the deformation on a grid point I, u_{I}, is given by the effects of the pressure p_{J} on all the grid points J, losing the local properties related to the spring deformation model.

$$\begin{cases} \mathbf{u}_\mathrm{s} = \mathbf{C}_\mathrm{s}\mathbf{p}_\mathrm{s} \\ \mathbf{u}_\mathrm{b} = \mathbf{C}_\mathrm{b}\mathbf{p}_\mathrm{b} \\ \mathbf{p} = \mathbf{p}_\mathrm{s} \\ \mathbf{p}_\mathrm{b} = \mathbf{J}_\mathrm{sb}\mathbf{p}_\mathrm{s} \\ \mathbf{u} = \mathbf{u}_\mathrm{s} + \mathbf{J}_\mathrm{bs}\mathbf{u}_\mathrm{b} \end{cases} \rightarrow \quad \begin{gathered} \mathbf{u} = (\mathbf{C}_\mathrm{s} + \mathbf{J}_\mathrm{bs}\mathbf{C}_\mathrm{b}\mathbf{J}_\mathrm{sb})\mathbf{p} = \mathbf{C}\mathbf{p} \\ \mathrm{u}_\mathrm{I} = \sum_\mathrm{J} \mathrm{C}_\mathrm{IJ}\mathrm{p}_\mathrm{J} \end{gathered} \tag{268}$$

Therefore, the discretised gap equation with the developed FEM deformation model is given in (269).

$$\mathrm{h}_\mathrm{I} = \sum_\mathrm{J} \mathrm{C}_\mathrm{IJ}\mathrm{p}_\mathrm{J} + \mathrm{c} - \mathbf{e}^\mathrm{T}\hat{\mathbf{r}}_\mathrm{I} \tag{269}$$

Due to the global dependence of the gap on the whole lubricant pressure vector $\mathbf{p}$, the discretised Reynolds equation local residual F_I reported in (270) also depends on all the pressure grid values, losing the cross-stencil dependency and, as a consequence, the penta-diagonal matrix structure of its Jacobian.

$$\mathrm{F}_\mathrm{I}(\mathbf{p}) = \begin{cases} \boldsymbol{\varepsilon}_\mathrm{I}^\mathrm{T}\mathbf{D}_2\mathbf{p}_\mathrm{I} - \mathbf{D}_\theta^\mathrm{T}\mathbf{u}_\mathrm{I} - \mathbf{D}_\varphi^\mathrm{T}\mathbf{w}_\mathrm{I} - \mathbf{D}_\mathrm{t}^\mathrm{T}\mathbf{v}_\mathrm{t} & 2 \le \mathrm{i}, \mathrm{j} \le \mathrm{N}, \mathrm{M} - 1 \\ \mathrm{p}_{1\mathrm{j}}, \mathrm{p}_{\mathrm{Nj}} & 1 \le \mathrm{j} \le \mathrm{M} \\ \mathrm{p}_{\mathrm{i}1}, \mathrm{p}_{\mathrm{iM}} & 2 \le \mathrm{i} \le \mathrm{N} - 1 \end{cases} \tag{270}$$

$$\mathbf{F}(\mathbf{p}) = \mathbf{0}$$

The above means that the Newton iterative method is no more convenient, because a dense Jacobian has to assembled and inverted at each iteration; in order to overcome the issue another Fixed Point Iteration strategy is adopted: the non-linear system in (270) has the same structure of the HL case, but the vector $\mathbf{a}_\mathrm{I}$ and the right-hand side term b_I, defined previously, are now dependent on the lubricant pressure vector $\mathbf{p}$ through the FEM deformation model, so the Reynolds equation residual can be written in (271) with the same structure of the HL case but characterised by pressure-dependent penta-diagonal matrix $\mathbf{A}$ and right-hand-side vector $\mathbf{b}$.

$$\mathbf{a}_\mathrm{I}(\mathbf{p}) = \mathbf{D}_2^\mathrm{T}\boldsymbol{\varepsilon}_\mathrm{I}(\mathbf{p}) \quad \mathrm{b}_\mathrm{I}(\mathbf{p}) = \mathbf{D}_\theta^\mathrm{T}\mathbf{u}_\mathrm{I}(\mathbf{p}) + \mathbf{D}_\varphi^\mathrm{T}\mathbf{w}_\mathrm{I}(\mathbf{p}) + \mathbf{D}_\mathrm{t}^\mathrm{T}\mathbf{v}_\mathrm{t}(\mathbf{p})$$

$$\mathrm{F}_\mathrm{I}(\mathbf{p}) = \begin{cases} \mathbf{a}_\mathrm{I}^\mathrm{T}(\mathbf{p})\mathbf{p}_\mathrm{I} - \mathrm{b}_\mathrm{I}(\mathbf{p}) & 2 \le \mathrm{i}, \mathrm{j} \le \mathrm{N}, \mathrm{M} - 1 \\ \mathrm{p}_{1\mathrm{j}}, \mathrm{p}_{\mathrm{Nj}} & 1 \le \mathrm{j} \le \mathrm{M} \\ \mathrm{p}_{\mathrm{i}1}, \mathrm{p}_{\mathrm{iM}} & 2 \le \mathrm{i} \le \mathrm{N} - 1 \end{cases} \tag{271}$$

$$\mathbf{F}(\mathbf{p}) = \mathbf{A}(\mathbf{p})\mathbf{p} - \mathbf{b}(\mathbf{p}) = \mathbf{0}$$

The residual in (271) point of view allows to keep the sparse diagonally-banded matrix $\mathbf{A}$ easy assembling and inversion, so the iteration update logic is reported in (272) within the loop together with the cavitation constraint pressure truncation; let note that the presented strategy is a free-derivative solution.

$$\text{while} \sum_{I} \left|p_I^{k+1} - p_I^k\right| > \text{tol}$$

$$\mathbf{p}^* = \mathbf{p}^k + \omega\left(\left[\mathbf{A}(\mathbf{p}^k)\right]^{-1}\mathbf{b}(\mathbf{p}^k) - \mathbf{p}^k\right) \tag{272}$$

$$\mathbf{p}^{k+1} = \max\{0, \mathbf{p}^*\}$$

$$k \rightarrow k + 1$$

$$\text{end}$$

2.2.3. Boundary Element deformation model

Let introduce the last deformation model studied in this work, i.e., the BEM one which is addressed referring to the case of a rectangular domain described by the xz cartesian coordinates.

The fundamental assumption is represented by the tribo-system bodies extension, in particular they have to be physically described as elastic half-spaces, meaning that they can be considered as semi-infinite bodies with respect to the conjugated interface which is, subsequently, far enough from the bodies' boundaries.

The structural problem represented by an elastic half-space subjected to concentrated loads was addressed by Boussinesq (Johnson, 1987; Li and Berger, 2001; Popov, Hefl and Willert, 2019), who solved analytically the solid mechanics equilibrium equations under the given assumptions. Among the solutions he found, Boussinesq provided the surface normal deformation field u of a 3D elastic half-space with Young modulus E and Poisson ratio ν extending in the xz plane and in the y depth direction due to a concentrated normal load W_0 acting on the surface point (x_0, z_0) (eq. (273)).

$$u(x, z) = \frac{1 - \nu^2}{\pi E} \frac{W_0}{\sqrt{(x - x_0)^2 + (z - z_0)^2}} \tag{273}$$

The Boussinesq solution (273) is characterised by a singularity in the load point of application and then the deformation vanishes far from it.

If one surface dimension, e.g., the z one, is much bigger than the other, then the resulting 2D half-space deformation develops mostly in the x direction, so, neglecting the far edges effects, it can be considered to be equal at each z according to the eq. (274), in which this time the load W_0 is per unit length and the coordinate d_0 is considered as the distance from the load application point in correspondence of zero deformation.

$$u(x) = -2\frac{1 - \nu^2}{\pi E} W_0 \ln\left|\frac{x - x_0}{d_0}\right| \tag{274}$$

If the same load acts on two conjugated surfaces (lower E_l, ν_l and upper E_u, ν_u) communicating over the shared interface, the total normal deformation u can be evaluated in (275), reported for both the 3D and 2D half-spaces (which the tribo-systems are denoted respectively with point-contact and line-contact), as the sum of the individual ones leading to the definition of the equivalent Young modulus E^*.

$$\frac{1}{E^*} = \frac{1-\nu_1^2}{E_1} + \frac{1-\nu_2^2}{E_2}$$

$$u(x,z) = \frac{1}{\pi E^*} \frac{W_0}{\sqrt{(x-x_0)^2 + (z-z_0)^2}} \tag{275}$$

$$u(x) = -\frac{2}{\pi E^*} W_0 \ln\left|\frac{x-x_0}{d_0}\right|$$

In both cases a K function depending on the distance between the analysed position and the load point of application can be defined in (276): it represents the deformation due to an unitary load managing the deformation amount based on the distance with respect to the load position.

$$\begin{aligned} K(x) &= -\frac{2}{\pi E^*} \ln\left|\frac{x}{d_0}\right| \quad \rightarrow \quad u(x) = K(x-x_0)W_0 \\ K(x,z) &= \frac{1}{\pi E^*} \frac{1}{\sqrt{x^2+z^2}} \quad \rightarrow \quad u(x,z) = K(x-x_0, z-z_0)W_0 \end{aligned} \tag{276}$$

Since a linear relation between the deformation and the load holds, the case of more than one acting loads can be accomplished with the superposition, e.g., the 3D half-space subjected to two loads W_0 and W_1 acting respectively on the points (x_0, z_0) and (x_1, z_1) returns the deformation given in (277).

$$u(x,z) = K(x-x_0, z-z_0)W_0 + K(x-x_1, z-z_1)W_1 \tag{277}$$

The superposition is generalised to the case of N loads W_i applied in the points (x_i, z_i) in the eq. (278).

$$u(x,z) = \sum_{i=0}^{N-1} K(x-x_i, z-z_i)W_i \tag{278}$$

Thanks to the superposition principle, the case of a distributed load can be addressed in the eq. (279): if the load is considered to be generated by a pressure field $p(x,z)$ acting on the surface elements with area dxdz, the Boussinesq solution can be extended to a continuous loading configuration.

$$u(x,z) = \iint_{-\infty\,-\infty}^{+\infty\,+\infty} K(x-\xi, z-\eta)p(\xi,\eta)\, d\xi d\eta \tag{279}$$

Of course, the integral can be restricted to the analysed interface domain Ω (both in 2 and in 3 dimensions), turning the half-space deformation problem into a continuous convolution integral where the input pressure field p is convoluted by the means of the so-called Kernel function K to obtain the output deformation field u (eq. (280)).

$$u(x) = \int_{\Omega} K(x-\xi)p(\xi)\, d\xi \tag{280}$$

$$u(x,z) = \iint_{\Omega} K(x-\xi, z-\eta)p(\xi,\eta)\, d\xi d\eta$$

Due to the half space assumption, the numerical evaluation of the convolution integrals in (280) can be obtained by the BEM: since only the surface deformation due to the surface pressure has to be evaluated, only the interface has to be discretised (Figure 83), i.e., the boundaries of the contacting bulks, contrarily to the FEM alternative which requires to mesh the bodies' volume entirely with a grave computational burden as a consequence.

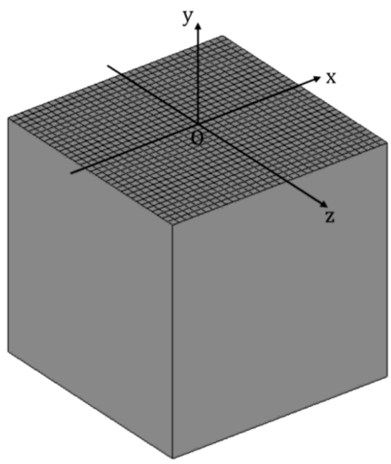

Figure 83 *Half-space BEM discretization*

Proceeding with the elastic half-space deformation problem simulated through the BEM, only the 2D tribo-system formulation will be provided, while the point-contact case will be obtained by generalization of the line-contact one.

Firstly, the line domain x of length L is discretised by the means of the grid reported in (281) composed by N nodes realising $N-1$ equal line elements with length Δx.

$$i = 0, \dots, N-1 \qquad \Delta x = \frac{L}{N-1} \qquad x_i = i\Delta x \tag{281}$$

With reference to the Figure 84, the pressure acting on the i grid point, i.e., $p_i = p(x_i)$, is considered to be homogeneously distributed over the Δx long line element centred in the node: hence, the deformation u_i in correspondence of the i grid point is given in (282) through the Boussinesq convolution summing the effects of the pressure acting on all the boundary elements centred in the grid points j (Love, 1929; Wang *et al.*, 2003; Pohrt and Li, 2014).

$$u_i = \sum_{j=0}^{N-1} \left(\int_{x_j-\Delta x/2}^{x_j+\Delta x/2} K(x_i - \xi)\, d\xi \right) p_j \tag{282}$$

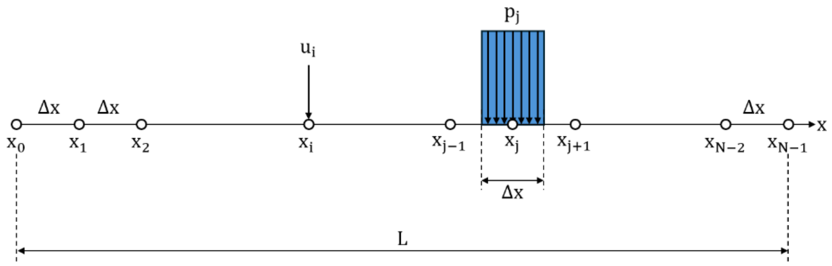

Figure 84 *BEM grid configuration*

Recalling the 1D Kernel in (276), the integral term result in (282) is a quantity depending on the x_i and the x_j position and it is analytically evaluated in (283): it represents the influence coefficient K_{ij}, i.e., the deformation at the point x_i generated by an unitary pressure acting on x_j.

$$K_{ij} = -\frac{2}{\pi E^*} \begin{bmatrix} \left(x_i - x_j + \frac{\Delta x}{2}\right)\left(\ln\left|x_i - x_j + \frac{\Delta x}{2}\right| - 1\right) + \cdots \\ \ldots - \left(x_i - x_j - \frac{\Delta x}{2}\right)\left(\ln\left|x_i - x_j - \frac{\Delta x}{2}\right| - 1\right) + \cdots \\ -\Delta x(\ln|d_0| + 1) \end{bmatrix} \tag{283}$$

Then, the discrete form of the continuous convolution in (280) is given by the matrix-vector multiplication reported in (284), where the deformation vector **u** is obtained by the product between the compliance matrix **K** and the pressure vector **p**: the discretised half-space deformation problem provides the same result of the FEM approach, where the deformation evaluation deals with the application of a dense compliance matrix to an input pressure vector.

$$u_i = \sum_{j=0}^{N-1} K_{ij} p_j \quad \rightarrow \quad \mathbf{u} = \mathbf{K}\mathbf{p} \tag{284}$$

Even if the BEM problem is much smaller than the FEM one due to the possibility to discretize only the interface domain, it could require a high grid resolution based on the tribological application, so the matrix-vector product could be computationally heavy (which in this case requires a computing complexity of order $O(N^2)$) and this is even more true for the FEM approach dealing with the compliance matrix **C** reported in (268).

The first advantage of the BEM approach with respect to the FEM one stays in the assembling of the compliance matrix **K**: it can be easily obtained realising that the analytical form of the entry K_{ij} in (283) does not depend on the individual positions x_i and x_j, but it actually depends on their distance, revealing that **K** is a Toeplitz matrix, i.e., its diagonals are composed by equal values; therefore, the K_{ij} matrix can be obtained by the definition of its first row or column vector only (indicated with K_i). The example for $N = 4$ reported in the eq. (285) demonstrates that the Toeplitz structure of the compliance matrix is also symmetric, reflecting the influence coefficients dependency on the distance between the deformation and the pressure points, so its entries K_{ij} are given by a rearrangement of the vector K_i, in particular by $K_{|i-j|}$.

$$K_i = \begin{bmatrix} K_0 \\ K_1 \\ K_2 \\ K_3 \end{bmatrix} \rightarrow \; K_{ij} = K_{|i-j|}$$
$$\begin{bmatrix} u_0 \\ u_1 \\ u_2 \\ u_3 \end{bmatrix} = \begin{bmatrix} K_0 & K_1 & K_2 & K_3 \\ K_1 & K_0 & K_1 & K_2 \\ K_2 & K_1 & K_0 & K_1 \\ K_3 & K_2 & K_1 & K_0 \end{bmatrix} \begin{bmatrix} p_0 \\ p_1 \\ p_2 \\ p_3 \end{bmatrix} \tag{285}$$

The deformation calculation in (285) can be accelerated by crossing the properties of the found discrete convolution with the Fourier Transform.

Let recall in (286) the Discrete Fourier Transform (DFT) U_k of a N-points discrete periodic signal u_j and the associated Inverse DFT (IDFT): it is a tool able to analyse the signal frequency spectrum, i.e., it's useful to catch the harmonics (frequency and amplitude) that dominate its behaviour (Cooley, Lewis and Welch, 1969).

$$U_k = \mathrm{DFT}(u_j) = \sum_{j=0}^{N-1} u_j e^{-ik\frac{2\pi}{N}j}$$
$$u_j = \mathrm{IDFT}(U_k) = \frac{1}{N} \sum_{k=0}^{N-1} U_k e^{ik\frac{2\pi}{N}j} \tag{286}$$

The summations in (286) also require a computing complexity of order $O(N^2)$, but the DFT symmetry property due to the periodicity of the signal u_j and of its spectrum U_k can be exploited to accelerate the computation: a technique aiming to accelerate the computation of the DFT is known as Fast Fourier Transform (FFT).

The FFT technique due to Cooley-Tukey (Cooley and Tukey, 1965) recognises a recursive pattern along which the two halves of the signal spectrum, i.e., U_k and $U_{k+N/2}$, can be assembled by applying the DFT to the signal u_j even components u_{2n} and the odd ones u_{2n+1}, i.e., with the even spectrum E_k and the odd one O_k defined in (287).

$$E_k = \sum_{n=0}^{N/2-1} u_{2n} e^{-ik\frac{2\pi}{N/2}n} = \mathrm{DFT}(u_{2n}) \tag{287}$$

$$O_k = \sum_{n=0}^{N/2-1} u_{2n+1} e^{-ik\frac{2\pi}{N/2}n} = \mathrm{DFT}(u_{2n+1})$$

$$\begin{bmatrix} U_k \\ U_{k+N/2} \end{bmatrix} = \begin{bmatrix} E_k + e^{-ik\frac{2\pi}{N}} O_k \\ E_k - e^{-ik\frac{2\pi}{N}} O_k \end{bmatrix}$$

The recursion stays in the possibility to apply the same composition during the evaluation of the split spectra E_k and O_k which can be halved again until the signal to elaborate is composed by only one value ($N = 1$) for which the first component of the spectrum U_1 is initialized (eq. (288)).

$$\begin{gathered} U_k = \mathrm{FFT}(u_j) = \begin{bmatrix} E_k + e^{-ik\frac{2\pi}{N}} O_k \\ E_k - e^{-ik\frac{2\pi}{N}} O_k \end{bmatrix} \qquad \begin{matrix} E_k = \mathrm{FFT}(u_{2n}) \\ O_k = \mathrm{FFT}(u_{2n+1}) \end{matrix} \\ U_1 = \sum_{j=0}^{0} u_j e^{-i1\frac{2\pi}{1}j} = u_1 \end{gathered} \tag{288}$$

The Cooley-Tukey FFT approach effectively reduces the computing complexity order from $O(N^2)$ to $O(N \log N)$.

The Inverse FFT (IFFT) can be evaluated by applying the same Cooley-Tukey logic or by noting in (289) that the signal conjugate $\bar{u}_j$ of (286) deals with the direct transform of the spectrum conjugate $\overline{U}_k$.

$$\begin{gathered} \bar{u}_j = \frac{1}{N} \sum_{k=0}^{N-1} \overline{U}_k e^{-ik\frac{2\pi}{N}j} = \frac{1}{N} \mathrm{FFT}(\overline{U}_k) \\ u_j = \mathrm{IFFT}(U_k) = \frac{1}{N} \overline{\mathrm{FFT}(\overline{U}_k)} \end{gathered} \tag{289}$$

The FFT gain in computational speed can be exploited in the context of the discrete convolutions: a continuous convolution problem in (290) convoluting the input function $f(t)$ through the Kernel $h(t)$ to obtain the output function $g(t)$, after discretization over a N points grid, provides the discretised output vector g_n through the product between a generic Toeplitz matrix h_{n-m} and the input discretised vector f_n.

$$g(t) = \int_{\Omega} h(t-\eta) f(\eta)\, d\eta \quad \rightarrow \quad g_n = \sum_{m=0}^{N-1} h_{n-m} f_m \tag{290}$$

Applying the DFT to the vector form of the kernel h_{n-m} and to the input function f_m, obtaining respectively their spectra H_k and F_k, their piecewise product is given in (291).

$$H_k = \sum_{n-m=0}^{N-1} h_{n-m} e^{-ik\frac{2\pi}{N}(n-m)} \quad F_k = \sum_{m=0}^{N-1} f_m e^{-ik\frac{2\pi}{N}m} \tag{291}$$

$$H_k F_k = \sum_{n=m}^{N-1+m} \left(\sum_{m=0}^{N-1} h_{n-m} f_m \right) e^{-ik\frac{2\pi}{N}n}$$

Let recognise in (292) that the term in the brackets is actually the discretised convolution g_n.

$$H_k F_k = \sum_{n=m}^{N-1+m} g_n e^{-ik\frac{2\pi}{N}n} \tag{292}$$

The piecewise product between the Kernel and the input function spectra in (292) is not the DFT of the output function, because the summation n index is shifted by m, but it could be if the kernel h_{n-m} was periodic: in that case the summation index can be shifted by $-m$, welcoming the good news that the matrix-vector product in the signal domain (290) is, in the spectral domain, the piecewise product between vectors reported in (293).

$$H_k F_k = \sum_{n=0}^{N-1} g_n e^{-ik\frac{2\pi}{N}n} = G_k \tag{293}$$

The above property represents a further computational gain accelerating the discretised convolution evaluation reported in matrix form in (294) where **h** is the vector form of the periodic Kernel h_{n-m}.

$$g_n = \sum_{m=0}^{N-1} h_{n-m} f_m \quad \to \quad \mathbf{g} = \mathrm{IFFT}\big(\mathrm{FFT}(\mathbf{h}) \circ \mathrm{FFT}(\mathbf{f})\big) \tag{294}$$

Let analyse the structure of the periodic kernel matrix h_{nm} considering that its periodicity can be obtained by circulating its vector form h_n through the N-modulo operation, i.e., the remainder of the rounded down quotient obtained by the division of the input number by N: as reported in (295) for $N = 4$, the periodic kernel matrix h_{nm} turns out to be a circulant Toeplitz matrix, i.e., each row is obtained by shifting one place to the right the previous one, so the associate discrete convolution is said to be circular.

$$\langle x \rangle_N = x - \left\lfloor \frac{x}{N} \right\rfloor N$$

$$h_n = \begin{bmatrix} h_0 \\ h_1 \\ h_2 \\ h_3 \end{bmatrix} \to \quad h_{nm} = h_{\langle n-m \rangle_N} = \begin{bmatrix} h_0 & h_3 & h_2 & h_1 \\ h_1 & h_0 & h_3 & h_2 \\ h_2 & h_1 & h_0 & h_3 \\ h_3 & h_2 & h_1 & h_0 \end{bmatrix} \tag{295}$$

Unfortunately, as reported in (285), despite the Boussinesq Kernel matrix $K_{|i-j|}$ has a symmetric Toeplitz structure, it is not circulant, so its associated discrete convolution cannot exploit the Fourier transform to accelerate the deformation computation: a technique to obtain an equivalent deformation result by turning the discrete Boussinesq convolution into a circular one is given by doubling the line domain extension, extending the kernel and zero-padding the pressure outside the original domain following the logic reported in the eq. (296) (Ju and Farris, 1996; Liu, Wang and Liu, 2000; Liu and Wang, 2002).

$$\begin{bmatrix} u_{-2} \\ u_{-1} \\ u_0 \\ u_1 \\ u_2 \\ u_3 \\ u_4 \\ u_5 \end{bmatrix} = \begin{bmatrix} K_0 & K_1 & K_2 & K_3 & 0 & K_3 & K_2 & K_1 \\ K_1 & K_0 & K_1 & K_2 & K_3 & 0 & K_3 & K_2 \\ K_2 & K_1 & K_0 & K_1 & K_2 & K_3 & 0 & K_3 \\ K_3 & K_2 & K_1 & K_0 & K_1 & K_2 & K_3 & 0 \\ 0 & K_3 & K_2 & K_1 & K_0 & K_1 & K_2 & K_3 \\ K_3 & 0 & K_3 & K_2 & K_1 & K_0 & K_1 & K_2 \\ K_2 & K_3 & 0 & K_3 & K_2 & K_1 & K_0 & K_1 \\ K_1 & K_2 & K_3 & 0 & K_3 & K_2 & K_1 & K_0 \end{bmatrix} \begin{bmatrix} 0 \\ 0 \\ p_0 \\ p_1 \\ p_2 \\ p_3 \\ 0 \\ 0 \end{bmatrix} \tag{296}$$

The extended Boussinesq periodic Kernel matrix in (296) is now a symmetric circulant Toeplitz matrix, then the associated circular discrete convolution can exploit the presented spectral domain advantages. Resuming, in order to address the so-called Circular Convolution – Fast Fourier Transform (CC-FFT) tool to solve the half-space deformation problem by the BEM, its steps involving the extended Kernel vector $\mathbf{K}_e$ (obtained by the rearrangement of the original Boussinesq Kernel matrix first column K_i reported in (285)), the extended zero-padded pressure vector $\mathbf{p}_e$ and the extended deformation vector $\mathbf{u}_e$ are reported in (297); let note that only the central part of $\mathbf{u}_e$ is needed to evaluate the output deformation vector $\mathbf{u}$ in (284) referred to the analysed line domain.

$$\mathbf{K}_e = \begin{bmatrix} \begin{bmatrix} K_0 \\ \vdots \\ K_{N-1} \end{bmatrix} \\ 0 \\ \begin{bmatrix} K_{N-1} \\ \vdots \\ K_1 \end{bmatrix} \end{bmatrix} \quad \mathbf{p}_e = \begin{bmatrix} \begin{bmatrix} 0 \\ \vdots \\ 0 \end{bmatrix} \\ \begin{bmatrix} \vdots \\ p_i \\ \vdots \end{bmatrix} \\ \begin{bmatrix} 0 \\ \vdots \\ 0 \end{bmatrix} \end{bmatrix}$$

$$\mathbf{u}_e = \mathrm{IFFT}\big(\mathrm{FFT}(\mathbf{K}_e) \circ \mathrm{FFT}(\mathbf{p}_e)\big) = \begin{bmatrix} \begin{bmatrix} u_{-N/2} \\ \vdots \\ u_{-1} \end{bmatrix} \\ \begin{bmatrix} \vdots \\ u_i \\ \vdots \end{bmatrix} \\ \begin{bmatrix} u_N \\ \vdots \\ u_{3N/2-1} \end{bmatrix} \end{bmatrix} \tag{297}$$

The same logic is adopted for 3D elastic half-spaces accounting for 2D FFT. The 2D rectangular grid with sides L_x and L_z is reported in the eq. (298) defining the 2 spatial indices i and j providing uniform spacings Δx and Δz.

$$
\begin{array}{lll}
i = 0, \dots, N-1 & \Delta x = \dfrac{L_x}{N-1} & x_i = i\Delta x \\
j = 0, \dots, M-1 & \Delta z = \dfrac{L_z}{M-1} & z_j = j\Delta z
\end{array} \tag{298}
$$

The 2D convolution in (280) is discretised with the BEM assuming that the pressure acting on the (i, j) grid point, i.e., $p_{ij} = p(x_i, z_j)$, is homogeneously distributed over the surface element with area $\Delta x \Delta z$ centred in the node: hence, the deformation u_{ij} in correspondence of the (i, j) grid point is given in (299) through the Boussinesq convolution summing the effects of the pressure acting on all the boundary elements centred in the grid points (k, h).

$$
u_{ij} = \sum_{i=0}^{N-1} \sum_{j=0}^{M-1} \left(\iint_{x_k-\Delta x/2}^{x_k+\Delta x/2} \,{}_{z_h-\Delta z/2}^{z_h+\Delta z/2} K(x_i - \xi, z_j - \eta)\, d\xi d\eta \right) p_{kh} \tag{299}
$$

The analytical result of the integral in (299) is evaluated in (300) providing a 4-indices compliance matrix K_{ijkh} (Johnson, 1987; Li and Berger, 2001; Pohrt and Li, 2014) function of the defined auxiliary distances δx_{ik}, Δx_{ik}, δz_{jh} and Δz_{jh}.

$$
\begin{array}{ll}
\delta x_{ik} = x_k - x_i - \Delta x/2 & \Delta x_{ik} = x_k - x_i + \Delta x/2 \\
\delta z_{jh} = z_h - z_j - \Delta z/2 & \Delta z_{jh} = z_h - z_j + \Delta z/2
\end{array}
$$

$$
K_{ijkh} = \frac{1}{\pi E^*} \left[\begin{array}{c}
\delta x_{ik} \ln\left(\dfrac{\delta z_{jh} + \sqrt{\delta z_{jh}^2 + \delta x_{ik}^2}}{\Delta z_{jh} + \sqrt{\Delta z_{jh}^2 + \delta x_{ik}^2}} \right) + \cdots \\
\dots + \Delta x_{ik} \ln\left(\dfrac{\Delta z_{jh} + \sqrt{\Delta z_{jh}^2 + \Delta x_{ik}^2}}{\delta z_{jh} + \sqrt{\delta z_{jh}^2 + \Delta x_{ik}^2}} \right) + \cdots \\
\dots + \delta z_{jh} \ln\left(\dfrac{\delta x_{ik} + \sqrt{\delta x_{ik}^2 + \delta z_{jh}^2}}{\Delta x_{ik} + \sqrt{\Delta x_{ik}^2 + \delta z_{jh}^2}} \right) + \cdots \\
\dots + \Delta z_{jh} \ln\left(\dfrac{\Delta x_{ik} + \sqrt{\Delta x_{ik}^2 + \Delta z_{jh}^2}}{\delta x_{ik} + \sqrt{\delta x_{ik}^2 + \Delta z_{jh}^2}} \right)
\end{array} \right] \tag{300}
$$

Referring to the lexicographical order of the rectangular Reynolds equation grid (I index for the (i, j) point and J index for the (k, h) one), the BEM approach provides the linear relation between the deformation and the pressure vectors through the compliance matrix K_{IJ} in (301) with the same structure of the FEM deformation model.

$$u_{ij} = \sum_{i=0}^{N-1}\sum_{j=0}^{M-1} K_{ijkh}p_{kh} \;\rightarrow\; \begin{matrix} I = iM + j \\ J = kM + h \end{matrix} \;\rightarrow\; u_I = \sum_J K_{IJ}p_J \qquad (301)$$

In order to compute the deformation with the CC-FFT tool, the 2D Kernel K_{ij} is obtained from the 4-indices compliance matrix K_{ijkh} in correspondence of $k = h = 0$, then its extended version for the 2D circular convolution is given in (302).

$$\mathbf{K}_e = \cdots$$
$$= \begin{bmatrix} \begin{bmatrix} K_{00} & \cdots & K_{0,M-1} \\ \vdots & \ddots & \vdots \\ K_{N-1,0} & \cdots & K_{N-1,M-1} \end{bmatrix} & \begin{bmatrix} \vdots \\ 0 \\ \vdots \end{bmatrix} & \begin{bmatrix} K_{0,M-1} & \cdots & K_{01} \\ \vdots & \ddots & \vdots \\ K_{N-1,M-1} & \cdots & K_{N-1,1} \end{bmatrix} \\ [\cdots \;\; 0 \;\; \cdots] & 0 & [\cdots \;\; 0 \;\; \cdots] \\ \begin{bmatrix} K_{N-1,0} & \cdots & K_{N-1,M-1} \\ \vdots & \ddots & \vdots \\ K_{10} & \cdots & K_{1,M-1} \end{bmatrix} & \begin{bmatrix} \vdots \\ 0 \\ \vdots \end{bmatrix} & \begin{bmatrix} K_{N-1,M-1} & \cdots & K_{N-1,1} \\ \vdots & \ddots & \vdots \\ K_{1,M-1} & \cdots & K_{11} \end{bmatrix} \end{bmatrix} \qquad (302)$$

Then, the pressure field p_{ij} is extended and zero-padded outside the analysed domain, obtaining the extended pressure field $\mathbf{p}_e$ in (303).

$$\mathbf{p}_e = \begin{bmatrix} \begin{bmatrix} 0 & \cdots & 0 \\ \vdots & \ddots & \vdots \\ 0 & \cdots & 0 \end{bmatrix} & \begin{bmatrix} 0 & \cdots & 0 \\ \vdots & \ddots & \vdots \\ 0 & \cdots & 0 \end{bmatrix} & \begin{bmatrix} 0 & \cdots & 0 \\ \vdots & \ddots & \vdots \\ 0 & \cdots & 0 \end{bmatrix} \\ \begin{bmatrix} 0 & \cdots & 0 \\ \vdots & \ddots & \vdots \\ 0 & \cdots & 0 \end{bmatrix} & \begin{bmatrix} & \vdots & \\ \cdots & p_{ij} & \cdots \\ & \vdots & \end{bmatrix} & \begin{bmatrix} 0 & \cdots & 0 \\ \vdots & \ddots & \vdots \\ 0 & \cdots & 0 \end{bmatrix} \\ \begin{bmatrix} 0 & \cdots & 0 \\ \vdots & \ddots & \vdots \\ 0 & \cdots & 0 \end{bmatrix} & \begin{bmatrix} 0 & \cdots & 0 \\ \vdots & \ddots & \vdots \\ 0 & \cdots & 0 \end{bmatrix} & \begin{bmatrix} 0 & \cdots & 0 \\ \vdots & \ddots & \vdots \\ 0 & \cdots & 0 \end{bmatrix} \end{bmatrix} \qquad (303)$$

Finally, the extended pressure field $\mathbf{u}_e$ is given in (304) by the piecewise product between the bidimensional FFTs of the Kernel and pressure extended matrices, from which the output deformation field u_{ij} is extracted from the central block.

$$\mathbf{u}_e = \mathrm{IFFT}\big(\mathrm{FFT}(\mathbf{K}_e) \circ \mathrm{FFT}(\mathbf{p}_e)\big) = \cdots$$
$$= \begin{bmatrix} [\dots] & [\dots] & [\dots] \\ [\dots] & \begin{bmatrix} & \vdots & \\ \cdots & u_{ij} & \cdots \\ & \vdots & \end{bmatrix} & [\dots] \\ [\dots] & [\dots] & [\dots] \end{bmatrix} \qquad (304)$$

Then, the FDM discretization of the rectangular EHL Reynolds equation with the half-space deformation model (implemented in the gap equation) is given in (305) together with the due modifications to include the pressure-varying rheological properties: it presents the same non-linear functionality structure of the FEM case in (269,270) and also a dense Jacobian (due to the dense compliance matrix **K**) that makes the iterative Newton method too expensive.

$$\varepsilon = \frac{\rho h^3}{12\mu} \quad u = \rho hU \quad w = \rho hW \quad v = \rho h$$
$$h_I = \sum_J K_{IJ} p_J + g_I - \delta$$
$$F_I(\mathbf{p}) = \begin{cases} \boldsymbol{\varepsilon}_I^T \mathbf{D}_2 \mathbf{p}_I - \mathbf{D}_x^T \mathbf{u}_I - \mathbf{D}_z^T \mathbf{w}_I - \mathbf{d}_t^T \mathbf{v}_t & 2 \le i, j \le N, M-1 \\ p_{1j}, p_{Nj} & 1 \le j \le M \\ p_{i1}, p_{iM} & 2 \le i \le N-1 \end{cases} \tag{305}$$
$$\mathbf{F}(\mathbf{p}) = \mathbf{0}$$

The (305) system can be iteratively solved with the same free-derivative method described in (272), but here a local derivative method is proposed: the non-linear Jacobi strategy reported in (306) with the relaxation ω allows to update the local unknown pressure p_I by a local Newton update taking into account the local derivative of the equation F_I, as if the pressure on the other grid points was fixed to the previous iteration.

$$p_I^{k+1} = p_I^k - \omega \frac{F_I(\mathbf{p}^k)}{\frac{\partial F_I}{\partial p_I}(\mathbf{p}^k)} \tag{306}$$

The derivative of the F_I with respect to the local pressure p_I is reported in (307) (accounting for the known derivatives in (232,233) in rectangular form) and it is nothing other than the local entry of the main diagonal of what would be the system dense Jacobian $\mathbf{F_p}$: let note that due to half-space Kernel Toeplitz structure, the local derivative of the gap with respect to the local pressure is the constant influence coefficient K_{00} over all the 2D grid.

$$\frac{\partial h_I}{\partial p_I} = K_{II} = K_{00}$$
$$\frac{\partial F_I}{\partial p_I}(\mathbf{p}) = \begin{cases} \boldsymbol{\varepsilon}_I^T \mathbf{D}_2 \frac{\partial \mathbf{p}_I}{\partial p_I} + \mathbf{p}_I^T \mathbf{D}_2^T \frac{\partial \boldsymbol{\varepsilon}_I}{\partial p_I} + \cdots \\ \ldots - \mathbf{D}_x^T \frac{\partial \mathbf{u}_I}{\partial p_I} - \mathbf{D}_z^T \frac{\partial \mathbf{w}_I}{\partial p_I} - \mathbf{d}_t^T \frac{\partial \mathbf{v}_t}{\partial p_I} & 2 \le i, j \le N, M-1 \\ 1 & \begin{matrix} 1 \le j \le M \\ 2 \le i \le N-1 \end{matrix} \end{cases} \tag{307}$$

The computational gain of the non-linear Jacobi method (as for the linear one) is represented by the possibility to vectorize it, so, indicating with $\mathbf{f_p}$ the vector collecting the local derivatives of the equation F_I, i.e., the main diagonal of the Jacobian $\mathbf{F_p}$, the iterative cycle solving the Reynolds equation in the described configuration is given in (308) together with the cavitation constraint implementation.

$$
\begin{aligned}
&\text{while } \sum_{\mathrm{I}} \left|p_{\mathrm{I}}^{k+1} - p_{\mathrm{I}}^{k}\right| > \mathrm{tol} \\
&\qquad \mathbf{p}^{*} = \mathbf{p}^{k} - \omega\, \mathbf{F}\left(\mathbf{p}^{k}\right) \oslash \mathbf{f}_{\mathbf{p}}\left(\mathbf{p}^{k}\right) \;\rightarrow\; \mathbf{p}^{k+1} = \max\{0, \mathbf{p}^{*}\} \\
&\qquad k \rightarrow k+1 \\
&\text{end}
\end{aligned}
\tag{308}
$$

2.3. Mixed Lubrication

The ML regime, as described previously, is a lubrication mode occurring when the too high load or the too low sliding velocity do not generate enough fluid pressure to sustain a full separation of the tribo-system conjugated surfaces, so in some zones of the interface the surfaces directly touch and there the contact pressure rises.

Before discussing the numerical techniques developed in this work to address the ML simulations, let introduce basic concepts in the framework of the DCM simulations with the objective to transfer the obtained information in the context of the ML regime simulative context, with reference to stationary frictionless dry tribo-systems interacting only along the normal contact direction (the contact interaction produces only the normal stress, i.e., the contact pressure, generating only normal deformation).

Furthermore, it is necessary to introduce the following DCM solvers, because they will be used in the context of the successive ML simulations regarding rectangular tribo-systems in order to:

- supply a first pressure guess starting the associated iterative cycles;
- compare the ML simulation results with respect to the associated DCM configuration for the same operating conditions, in terms of contact area, load, wear and so on.

2.3.1. Dry Contact Mechanics

In the following, the variational principle strategy is presented and addressed with the half-space BEM deformation model described previously; the line-contact tribo-system will be characterised, while the point-contact one will be extrapolated by generalization of the former.

In absence of lubricant and in the described above configuration, the governing eqs. (309) describing the 1D DCM problem are:

- the normal deformation u equation accounting for the 1D Boussinesq Kernel;
- the gap h equation accounting for the normal deformation u, the geometrical gap g and the rigid approach δ;
- the 1D load balance equation, where N is the applied load per unit length.

The input of the problem are the mechanical properties of the involved profiles (equivalent Young modulus E^*), the geometrical gap g and the applied load N, while the output are the gap field h, the contact pressure field p and the approach δ.

$$\begin{cases} u(x) = -\dfrac{2}{\pi E^*}\displaystyle\int_\Omega \ln\left|\dfrac{x-\xi}{d_0}\right| p(\xi)\, d\xi \\ h(x) = u(x) + g(x) - \delta \\ N = \displaystyle\int_\Omega p(x)\, dx \end{cases} \tag{309}$$

The problem in (309) was already solved analytically by Hertz (Hertz, 1882) for simple geometrical configurations: with particular reference to a line-contact tribo-system composed by a cylinder of radius R against a flat, Hertz provided, in addition to the contact pressure ellipsoidal shape in the contact zone, the contact half-width a_H (the contact area is intended as the domain zone in which the contact occurs and so the pressure is positive), the approach δ_H and the maximum contact pressure p_H reported in (310).

$$a_H = \sqrt{\frac{4NR}{\pi E^*}} \quad \delta_H = \frac{a_H^2}{R} \quad p_H = \frac{2N}{\pi a_H} \tag{310}$$

In order to simulate the same configuration, the equations in (309) are scaled with respect to the Hertz analytical results, defining with the respective capital letters the following dimensionless quantities in (311).

$$\begin{aligned} &X = \frac{x}{a_H} \quad P = \frac{p}{p_H} \quad H = \frac{h}{\delta_H} \quad U = \frac{u}{\delta_H} \\ &G = \frac{h}{\delta_H} \quad \Delta = \frac{\delta}{\delta_H} \quad D_0 = \frac{d_0}{a_H} \end{aligned} \tag{311}$$

Implementing the (311), the problem (309) is rewritten in (312).

$$\begin{cases} U(X) = -\dfrac{1}{\pi}\displaystyle\int_\Omega \ln\left|\dfrac{X-\Xi}{D_0}\right| P(\Xi)\, d\Xi \\ H(X) = U(X) + G(X) - \Delta \\ \dfrac{\pi}{2} = \displaystyle\int_\Omega P(X)\, dX \end{cases} \tag{312}$$

The DCM problem addressed with the variational principle is based on the theoretical concept that two surfaces approaching each other make contact reaching a condition of energetic equilibrium. Then, let analyse the energetic configuration of the system (Kalker, 1977; Tian and Bhushan, 1996):

- the rigid body displacement Δ produces the surfaces' interpenetration $\Delta - G$ which is compensated by the deformation generated the contact pressure P, so the associated external work W is given in (313);

$$W = \int_{\Omega} (\Delta - G) P \, dX \tag{313}$$

- the response of the contacting materials is the development of the internal elastic energy E in (314) dealing with the deformation U produced by the pressure P.

$$E = \frac{1}{2} \int_{\Omega} PU \, dX \tag{314}$$

So, the total contact energy V is given in (315).

$$V = E - W = \frac{1}{2} \int_{\Omega} PU \, dX - \int_{\Omega} (\Delta - G) P \, dX \tag{315}$$

Recognising the pressure integral in (315) to be the known input load, the total energy is rewritten in (316).

$$\begin{gathered} \int_{\Omega} (\Delta - G) P \, dX = \frac{\pi}{2} \Delta - \int_{\Omega} GP \, dX \\ V = \frac{1}{2} \int_{\Omega} PU \, dX + \int_{\Omega} GP \, dX - \frac{\pi}{2} \Delta \end{gathered} \tag{316}$$

Let develop in (317) the discrete integrals (summations) on the line grid domain previously presented in (281).

$$V = \frac{1}{2} \sum_{i=0}^{N-1} P_i U_i \, \Delta X + \sum_{i=0}^{N-1} G_i P_i \, \Delta X - \frac{\pi}{2} \Delta \tag{317}$$

Then, the energy per unit length v is given in (318) by substituting the half-space 1D BEM deformation coming from the discrete convolution in (284) (here K_{ij} is the dimensionless 1D Boussinesq Kernel matrix).

$$\begin{gathered} U_i = \sum_{j=0}^{N-1} K_{ij} P_j \\ v = \frac{1}{2} \sum_{i=0}^{N-1} \sum_{j=0}^{N-1} P_i K_{ij} P_j + \sum_{i=0}^{N-1} G_i P_i - \frac{\pi}{2\Delta X} \Delta \end{gathered} \tag{318}$$

In matrix form, the total energy per unit length referred to an elastic contact system is a quadratic form with respect to the contact pressure vector **P** reported in (319).

$$v = \frac{1}{2} \mathbf{P}^T \mathbf{K} \mathbf{P} + \mathbf{G}^T \mathbf{P} - \frac{\pi}{2\Delta X} \Delta \tag{319}$$

According to the variational principle, the contact configuration is reached when the total energy is minimum: the associated minimization problem has to be coupled with the Linear Complementarity Conditions (LCCs) reported in (320), i.e., a constraint imposing positive contact pressure in the contact zones (zero gap) and zero contact pressure in the open gap zones (positive gap).

$$\begin{aligned} &\mathrm{P_i} > 0 \;\; \rightarrow \;\; \mathrm{H_i} = 0 \\ &\mathrm{P_i} = 0 \;\; \rightarrow \;\; \mathrm{H_i} > 0 \end{aligned} \tag{320}$$

The discretization of the load balance eq. (312) is given in (321) by considering the 1D trapezoidal integration leading to the definition of the 1D integration operator vector $\mathbf{t}_\mathrm{X}$.

$$\begin{aligned} &\mathbf{t}_\mathrm{X} = \Delta\mathrm{X}\begin{bmatrix}\frac{1}{2} & 1 & \cdots & 1 & \frac{1}{2}\end{bmatrix}^\mathrm{T} \\ &\frac{\pi}{2} = \sum_{\mathrm{i}=1}^{\mathrm{N}-1} \frac{\mathrm{P_{i-1}} + \mathrm{P_i}}{2}\Delta\mathrm{X} = \mathbf{t}_\mathrm{X}^\mathrm{T}\mathbf{P} \end{aligned} \tag{321}$$

Therefore, the minimum problem associated to the elastic DCM system is given in (322) coupled with the equivalent form of the LCCs and to the load balance equation constraint: the objective is to find the pressure field $\mathbf{P}$ and the rigid approach Δ providing a minimal energetic configuration due to the applied load.

$$\begin{cases} \min\limits_{\mathbf{P},\Delta} \frac{1}{2}\mathbf{P}^\mathrm{T}\mathbf{K}\mathbf{P} + \mathbf{G}^\mathrm{T}\mathbf{P} - \frac{\pi}{2\Delta\mathrm{X}}\Delta \\ \mathbf{P} \geq \mathbf{0} \quad \mathbf{H} \geq \mathbf{0} \quad \mathbf{P} \circ \mathbf{H} = \mathbf{0} \\ \mathbf{t}_\mathrm{X}^\mathrm{T}\mathbf{P} = \frac{\pi}{2} \end{cases} \tag{322}$$

A technique that effectively solves the problem in (322) is the Gradient Descent Method (GDM) (Stanley and Kato, 1997; Polonsky and Keer, 1999) with additional modifications along the iterations to impose the constraints. The algorithm starts with a trial pressure vector $\mathbf{P}^\mathrm{k}$ with which the gradient of the energy v with respect to the pressure (indicated with $\mathbf{H}_0$, since it represents the gap in correspondence of null approach) is evaluated (eq. (323)).

$$\left(\frac{\partial \mathrm{v}}{\partial \mathbf{P}}\right)^\mathrm{T} = \mathbf{H}_0 = \mathbf{K}\mathbf{P}^\mathrm{k} + \mathbf{G} \tag{323}$$

Then, the associated approach Δ^k is evaluated in (324) by considering that it is equal to the mean level of the gap $\mathbf{H}_0$ in the contact zone Ω_c (extended by the length $\mathrm{L_c}$), i.e., where the pressure is positive: this ensure that the consequent gap $\mathbf{H}^\mathrm{k}$ is zero in Ω_c satisfying the LCCs.

$$\begin{aligned} &\Omega_\mathrm{c} = \left\{\forall \mathrm{i} \in \Omega \,:\, \mathrm{P_i^k} > 0\right\} \quad \mathrm{L_c} = \int_{\Omega_\mathrm{c}} \mathrm{dX} \\ &\Delta^\mathrm{k} = \frac{1}{\mathrm{L_c}}\int_{\Omega_\mathrm{c}} \mathrm{H_0}\,\mathrm{dX} \;\; \rightarrow \;\; \mathbf{H}^\mathrm{k} = \mathbf{H}_0 - \Delta^\mathrm{k} \end{aligned} \tag{324}$$

At this point, the residual that has to decay can be defined as the maximum of the absolute value of the gap $\mathbf{H}^\mathrm{k}$ in the contact zone, i.e., the contact points have to lie in the closed gap zones. So, the iterative loop runs until the condition in (325) is true within a chosen tolerance tol.

$$\max\left|\mathbf{H}_{\Omega_c}^{k}\right| > \mathrm{tol} \tag{325}$$

Along the iterations, the pressure update $\mathbf{P}_0$ is given by the means of the gradient descent direction $\mathbf{d}^k$ and the step size ω defined in (326) according to the GDM.

$$\mathbf{d}^k = -\mathbf{H}_0 \quad \omega = \frac{\mathbf{d}^{k^T}\mathbf{d}^k}{\mathbf{d}^{k^T}\mathbf{K}\mathbf{d}^k}$$
$$\mathbf{P}_0 = \mathbf{P}^k + \omega\mathbf{d}^k \tag{326}$$

The update $\mathbf{P}_0$ is not ready yet to move to the next iteration because it is not ensured its positivity and not even the load balance: so, the nested loop in (327) is implemented that shifts the pressure vector $\mathbf{P}_0$ by a quantity α related to the load balance error in the contact zone (let note that Ω_c changes while shifting $\mathbf{P}_0$) until α becomes acceptably lower than the chosen tolerance.

$$\alpha = \frac{1}{L_c}\left(\frac{\pi}{2} - \int_{\Omega_c} P_0 \, dX\right) \quad \mathbf{P}_0 \rightarrow \mathbf{P}_0 + \alpha \tag{327}$$

Finally, the pressure vector negative values are truncated in (328) ensuring the LCCs and the updated pressure vector is evaluated to supply the successive iterations running the eqs. (323-327) loop; the computational speed of the proposed approach is given by the absence of iterative matrix assemblies and inversions and by the CC-FFT tool used every time the product between the compliance matrix **K** and a vector is needed.

$$\mathbf{P}^{k+1} = \max\{0, \mathbf{P}_0\} \quad k \rightarrow k+1 \tag{328}$$

An example simulation result is reported in the Figure 85 in which the red upper cylinder is pushed against the lower flat by the means of the input load resulting in the depicted deformed configuration with the black arrows indicating the contact pressure field in the contact zone; furthermore, for the chosen set of parameters, the percentage of contact area A_c with respect to the domain length is reported.

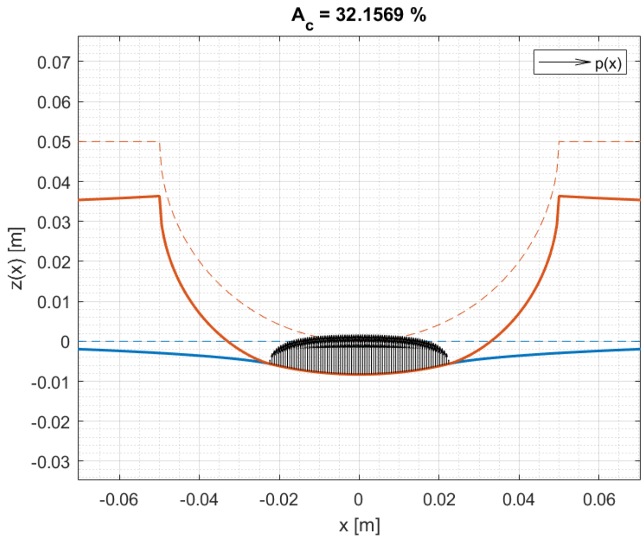

Figure 85 *1D DCM simulation contacting profiles*

The Figure 85 is associated with the Figure 86: here the pressure and gap fields are reported along the domain; it is worth to note the validity of the imposed LCCs and the unitary pressure peak and contact half-width revealing the reliability with respect to the Hertzian analytical solution.

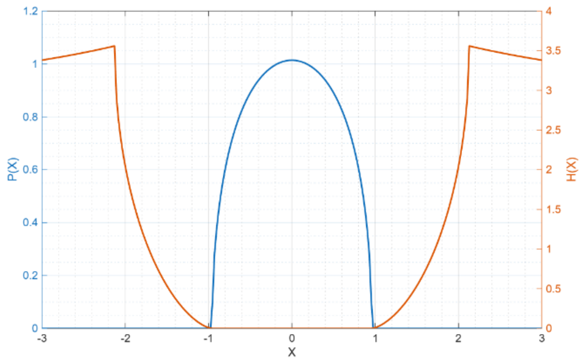

Figure 86 *1D DCM simulation pressure vs gap fields*

The analogous simulations for the point-contact system can be conducted by using the 2D version of the governing equations reported in (329) accounting for the 2D Boussinesq Kernel.

$$\begin{cases} u(x,y) = \dfrac{1}{\pi E^*} \displaystyle\int_\Omega \dfrac{1}{\sqrt{(x-\xi)^2 + (y-\eta)^2}} p(\xi,\eta)\, d\xi d\eta \\ h(x,y) = u(x,y) + g(x,y) - \delta \\ N = \displaystyle\int_\Omega p(x,y)\, dxdy \end{cases} \tag{329}$$

The (329) are scaled with respect to the analytical Hertz solution in (330) referred to a sphere of radius R pushed against a flat by the means of the applied load N, represented by the contact half-width a_H, the approach δ_H and the contact pressure peak p_H.

$$a_H = \sqrt[3]{\frac{3NR}{4E^*}} \quad \delta_H = \frac{a_H^2}{R} \quad p_H = \frac{3N}{2\pi a_H^2} \tag{330}$$

The same scaling logic leads to the dimensionless equations given in (331).

$$\begin{cases} U(X,Y) = \dfrac{2}{\pi^2} \displaystyle\int_\Omega \dfrac{1}{\sqrt{(X-\Xi)^2 + (Y-\Theta)^2}} P(\Xi,\Theta)\, d\Xi d\Theta \\ H(X,Y) = U(X,Y) + G(X,Y) - \Delta \\ \dfrac{2\pi}{3} = \displaystyle\int_\Omega P(X,Y)\, dXdY \end{cases} \tag{331}$$

At this point the 2D discretization is already given in (298), so the 2D Boussinesq Kernel matrix **K**, the 2D CC-FFT tool and the definition of the 2D trapezoidal integration vector operator $\mathbf{t}_2$ are applied to lexicographical ordered quantities (gap **H**, contact pressure **P** and approach Δ) to solve the analogous minimization problem in (332) with the same GDM described above (with the due modifications for the surface integrals along the iterations).

$$\begin{cases} \min\limits_{\mathbf{P},\Delta} \dfrac{1}{2}\mathbf{P}^T\mathbf{K}\mathbf{P} + \mathbf{G}^T\mathbf{P} - \dfrac{2\pi}{3\Delta X \Delta Y}\Delta \\ \mathbf{P} \geq \mathbf{0} \quad \mathbf{H} \geq \mathbf{0} \quad \mathbf{P} \circ \mathbf{H} = \mathbf{0} \\ \mathbf{t}_2^T\mathbf{P} = \dfrac{2\pi}{3} \end{cases} \tag{332}$$

The simulation results for the point-contact system case are reported in the Figure 87 depicting the related deformed configuration for a given set of input parameters and highlighting the contact area percentage A_c.

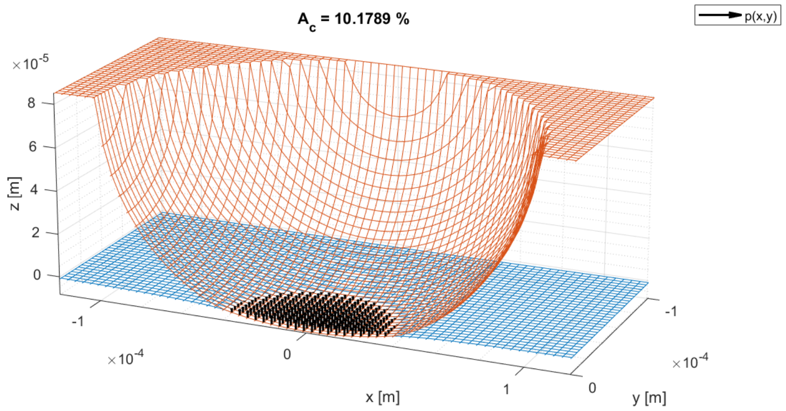

Figure 87 *2D DCM simulation contacting surfaces*

The pressure and gap fields associated with the Figure 87 are reported in the Figure 88, in which the same considerations with respect to the line-contact case about the Hertz analytical reference parameters can be made.

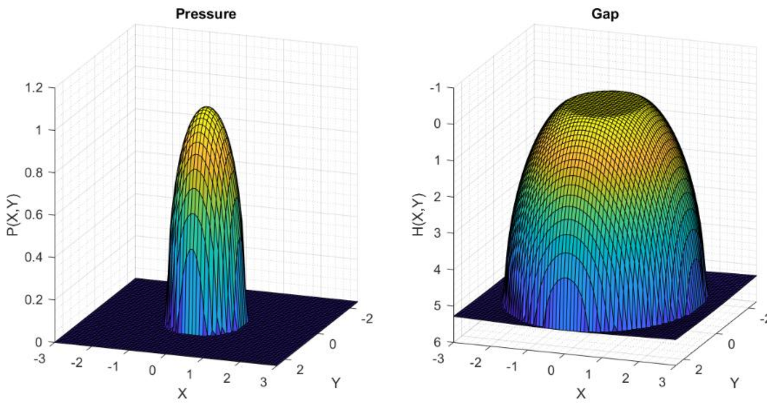

Figure 88 *2D DCM simulation pressure vs gap fields*

In both the dry and wet contact mechanics problems an interesting role is played by the involved surfaces' roughness, intended as the normal deviation of a real surface structure with respect to its ideal (smooth) shape: it would be useful to have a rough surface computational generator, so that a roughness a contribution can be implemented into the gap equation as a deviation with respect to the geometrical (smooth) undeformed gap; in this work the roughness is modelled as a fractal surface.

2.3.2. Fractal roughness

A fractal is a mathematical/geometrical entity showing the same detailed structure at any arbitrary scale, like the fractal tree or the Fibonacci's golden section depicted in the Figure 89, in which, respectively, each tree branch generates two further branches and each square side is given by the sum of the two previous squares' side.

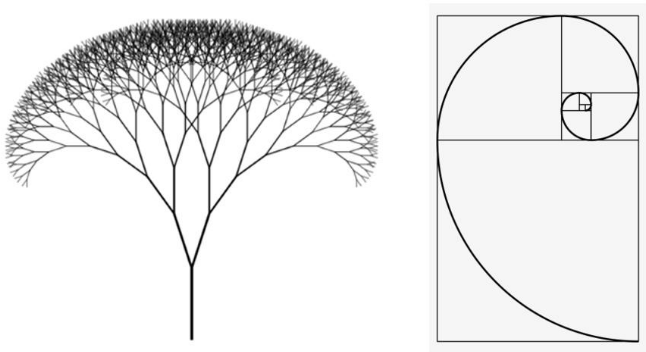

Figure 89 *Fractal tree and Fibonacci's golden section*

A rough surface can be modelled following the fractal principle by characterising its stochastic nature; let introduce a stochastic process called Brownian motion $B(t)$ (Takenaka, 1988), i.e., a continuous function of the time t characterised by null initial value and by a fundamental characteristic: its values in correspondence of two different time instants, t and η, are correlated through the Gaussian normal probability distribution function f with zero mean μ and variance σ^2 equal to the time range $t-\eta$ (eq. (333)), so $\mathcal{N}$ is a normally distributed random number extracted from a set with probability f.

$$\begin{gathered} f(x)=\frac{1}{\sigma\sqrt{2\pi}}e^{-\frac{1}{2}\left(\frac{x-\mu}{\sigma}\right)^2} \quad \rightarrow \quad \mathcal{N}(\mu,\sigma^2) \\ B(0)=0 \quad B(t)-B(\eta)=\mathcal{N}(0,t-\eta) \end{gathered} \tag{333}$$

The above means that the Brownian process $B(t)$ evolving over time is characterised by values more correlated if closer in time and vice versa, while its variation does not follow a preferred direction, in particular it is not dependent on the actual time instant but only on the time range with respect to another instant. Due to its described nature, the Brownian motion can be only simulated by defining its increments (Yang and Zhao, 2016): recalling the relation between a normal distribution and the standard one, i.e., with zero mean and unitary variance, and defining a discrete time grid t_n with N points and uniform spacing Δt, the discrete Brownian motion B_n can be simulated by the incremental recursion given in (334) starting from a null initial value B_0. In the Figure 90, the simulation of several Brownian motions is depicted and the normal distribution f in correspondence of the highlighted time instant (black dotted line) is shown overlapped to the associated histogram.

$$\begin{aligned} &\mathcal{N}(\mu, \sigma^2) = \mu + \sigma\, \mathcal{N}(0,1) \\ &n = 0, \dots, N-1 \quad \Delta t = \frac{T}{N-1} \quad t_n = n\Delta t \\ &B_0 = 0 \;\rightarrow\; B_n = B_{n-1} + \sqrt{\Delta t}\, \mathcal{N}(0,1) \end{aligned} \tag{334}$$

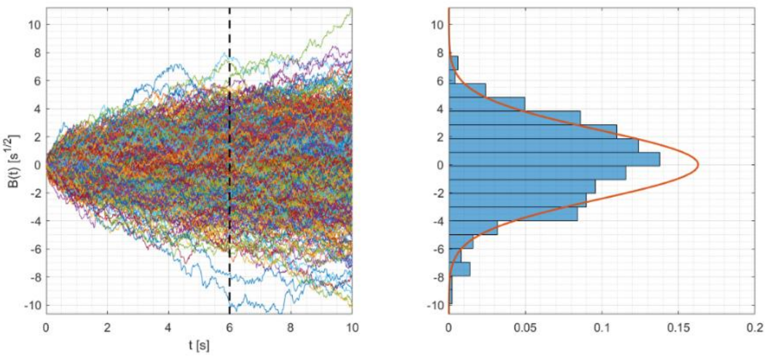

Figure 90 *Brownian motion simulation*

The independent nature of the increments of the Brownian motion in (334) is a characteristic reported at any arbitrary time scale: the same principle is transferred to a fractal surface.

Talking about a 1D configuration, a fractal profile along the line domain x is given by the height $r(x)$: as reported in the eq. (335), two heights in correspondence of different positions x and ξ are correlated through the Gaussian normal probability function $\mathcal{N}$ with zero mean μ and variance σ^2 proportional to the distance $x - \xi$ raised to a power $2H$, where H is the Hurst exponent strictly related to the fractal dimension (Cheraghalizadeh *et al.*, 2024).

$$r(x) - r(\xi) = \mathcal{N}\left(0, k(x-\xi)^{2H}\right) \quad 0 < H < 1 \tag{335}$$

With reference to (333), let note that a fractal surface with $k = 1$ and $H = 1/2$ is actually a Brownian surface: the proportionality factor k is devoted to the macro-dimension of the profile roughness, while the Hurst exponent H is a measure of the "chaos" (greater H provide smoother surfaces and vice versa). The (335) is rewritten in (336) in terms of the fractal profile standard deviation.

$$r(x) - r(\xi) = \sqrt{k}(x-\xi)^{H}\, \mathcal{N}(0,1) \tag{336}$$

In order to simulate a fractal profile on a discretised grid reflecting the property reported in (336), the Random Mid-Point (RMP) algorithm is introduced (Wang *et al.*, 2010): it builds the height profile starting from the grid extremities and then by filling recursively the mid-point of each grid level. In particular, starting from the knowledge of the height of the grid boundaries (by the means of a normally distributed random number generator with zero mean and standard deviation equal to $\sqrt{k}L^H$ since their distance is L), the mid-point height is generated by adding to the mean height (arithmetical average between the height of the boundaries) a noise generated by a normally distributed random number with zero mean and standard deviation equal to $\sqrt{k}(L/2)^H$, which is associated to the distance between the mid-point and the boundaries; then the two resulting half grids are filled with the same concept by finding new mid-point heights until all the grid points are covered. With reference to the Figure 91 the (k) grid level is characterised by the mid-point height $r\left(x_m^{(k)}\right)$ evaluated in the eq. (337) by the knowledge of the boundaries $x_A^{(k)}$ and $x_B^{(k)}$ heights $r_A^{(k)}$ and $r_B^{(k)}$.

$$x_m^{(k)} = \frac{x_A^{(k)} + x_B^{(k)}}{2} \qquad r_m^{(k)} = \frac{r_A^{(k)} + r_B^{(k)}}{2}$$
$$\Delta r_m^{(k)} = \sqrt{k}\left(\frac{x_B^{(k)} - x_A^{(k)}}{2}\right)^H \mathcal{N}(0,1) \quad \rightarrow \quad r\left(x_m^{(k)}\right) = r_m^{(k)} + \Delta r_m^{(k)} \tag{337}$$

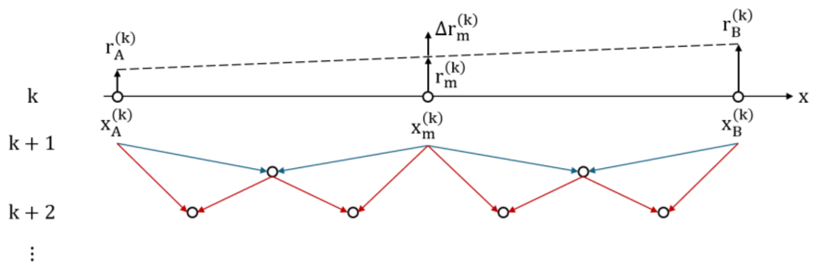

Figure 91 *1D Random Mid-Point algorithm scheme*

An example of generated fractal profiles obtained by varying the Hurst exponent H is shown in the Figure 92.

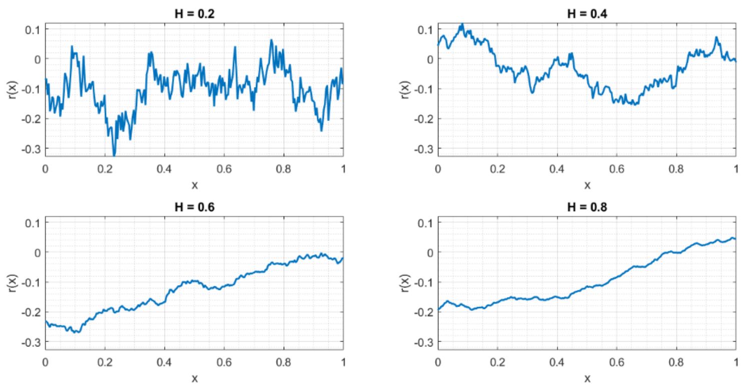

Figure 92 *Fractal profiles*

The RMP algorithm can be adapted in 2 dimensions to generate a fractal surface $r(x,z)$ characterized by the property (336) adapted for the 2D case in (338).

$$r(x,z) - r(\xi,\eta) = \sqrt{k}\left(\sqrt{(x-\xi)^2 + (y-\eta)^2}\right)^H \mathcal{N}(0,1) \tag{338}$$

With reference to the Figure 93 and to the eqs. (339), the 2D RMP is composed by two steps:

- the Square step in which, starting from the (k) 2D grid level known corner heights $r_{AA}^{(k)}$, $r_{BA}^{(k)}$, $r_{BB}^{(k)}$ and $r_{AB}^{(k)}$ in correspondence of the positions delimited by the boundaries $x_A^{(k)}$, $x_B^{(k)}$, $z_A^{(k)}$ and $z_B^{(k)}$, the height of the resulting square midpoint $r_{mm}^{(k)}$ is given by the RMP logic accounting for the Square distance $d_S^{(k)}$ in the normally distributed number standard deviation;
- the Diamond step in which the height of the previous square sides midpoints $r_{Am}^{(k)}$, $r_{mA}^{(k)}$, $r_{Bm}^{(k)}$ and $r_{mB}^{(k)}$ are given by the RMP logic averaging the heights of the 3 related surroundings and perturbing them with the usual normally distributed number with standard deviation accounting for the Diamond distance $d_D^{(k)}$.

$$d_S^{(k)} = \frac{1}{2}\sqrt{\left(x_B^{(k)} - x_A^{(k)}\right)^2 + \left(z_B^{(k)} - z_A^{(k)}\right)^2} \quad d_D^{(k)} = \frac{1}{\sqrt{2}} d_S^{(k)}$$

$$r_{mm}^{(k)} = \frac{r_{AA}^{(k)} + r_{BA}^{(k)} + r_{BB}^{(k)} + r_{AB}^{(k)}}{4} + \sqrt{k}\left(d_S^{(k)}\right)^H \mathcal{N}(0,1)$$

$$\begin{cases} r_{mA}^{(k)} = \dfrac{r_{AA}^{(k)} + r_{BA}^{(k)} + r_{mm}^{(k)}}{3} + \sqrt{k}\left(d_D^{(k)}\right)^H \mathcal{N}(0,1) \\ r_{mB}^{(k)} = \dfrac{r_{AB}^{(k)} + r_{BB}^{(k)} + r_{mm}^{(k)}}{3} + \sqrt{k}\left(d_D^{(k)}\right)^H \mathcal{N}(0,1) \\ r_{Am}^{(k)} = \dfrac{r_{AA}^{(k)} + r_{AB}^{(k)} + r_{mm}^{(k)}}{3} + \sqrt{k}\left(d_D^{(k)}\right)^H \mathcal{N}(0,1) \\ r_{Bm}^{(k)} = \dfrac{r_{BA}^{(k)} + r_{BB}^{(k)} + r_{mm}^{(k)}}{3} + \sqrt{k}\left(d_D^{(k)}\right)^H \mathcal{N}(0,1) \end{cases} \tag{339}$$

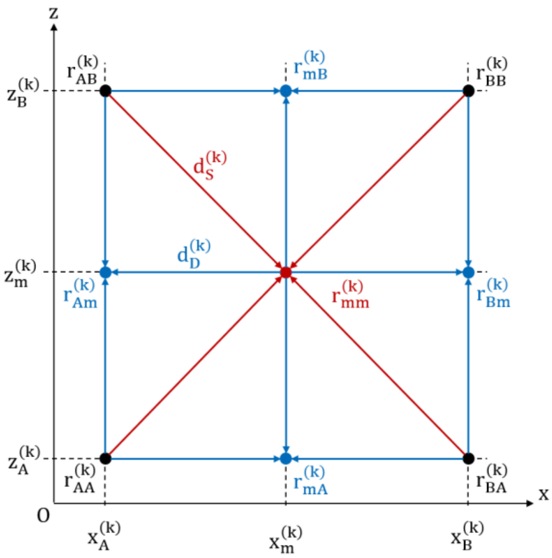

Figure 93 *2D Random Mid-Point algorithm scheme*

An example of generated fractal profiles obtained by varying the Hurst exponent H is shown in the Figure 94.

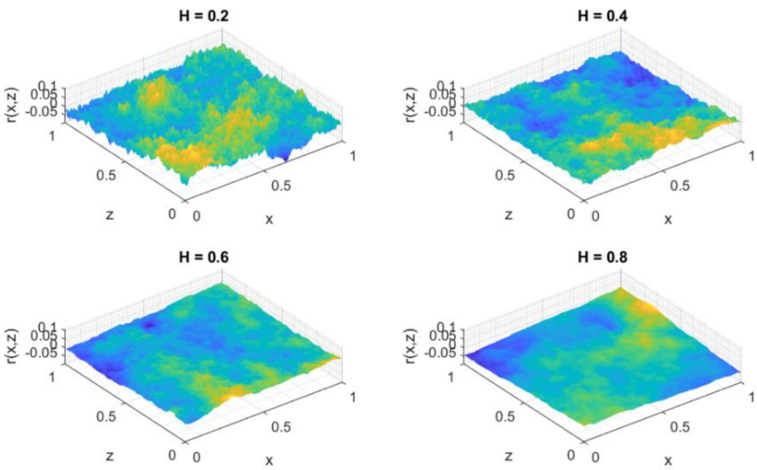

Figure 94 *Fractal surfaces*

As stated above, the DCM solver can be supplied by a geometrical gap g taking into account rough profiles/surfaces: in the Figure 95 and in the Figure 96 the deformed configurations regarding tribo-systems composed by, respectively, a fractal rough profile against a flat (1D line-contact system) and a fractal rough surface against a flat (2D point-contact system) simulated with the variational principle approach through the GDM are shown: it is worth noting that, even if the upper rough surfaces are pushed against the lower flat by the applied load, the real contact area percentage turns out to be significantly smaller with respect to the nominal one, i.e., the length/area of the domain.

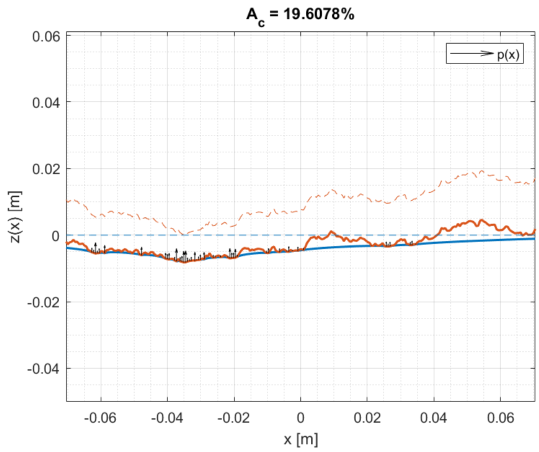

Figure 95 *1D DCM simulation rough profile vs flat*

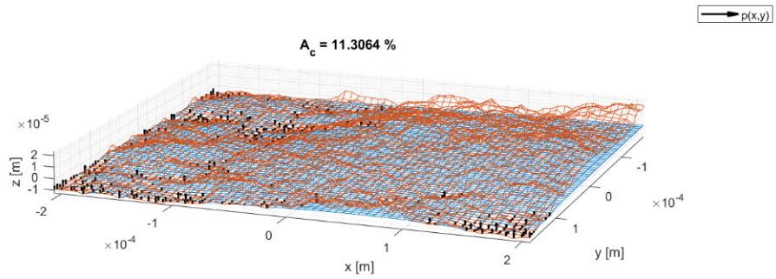

Figure 96 *2D DCM simulation rough surface vs flat*

2.3.3. Numerical strategies coupling lubrication and contact

The main difficulty when trying to adapt the dry contact complementarities to a mixed lubricated tribo-system (Patel *et al.*, 2022) is that, while in DCM regime the pressure and the gap are actually complementary, the ML mode pressure exists anywhere in the domain: the positive pressure in the open gap zones is the lubricant fluid pressure, while the positive pressure in the closed gap zones is the contact pressure.

From above, two big computational/conceptual issues arise (Zhu and Hu, 1999; Hu *et al.*, 2001; Zhu, 2007; Zhang *et al.*, 2016, 2019):

- the pressure generation mechanisms related to the solid contact and to the fluid lubrication are devoted to different phenomena, i.e., the solid materials avoiding interpenetration and the fluid constrained to flow by sliding and squeeze effects, but both the pressures contribute to the same surfaces' deformation and to sustain the same applied load; then, the computation has to link the different governing equations on the same domain;
- the solid contact happens when the surfaces' gap is zero and the Reynolds lubrication equation is singular in correspondence of null gap, since the flow is defined for positive gap; then, there will be numerical singularities in the domain transition zones from fluid to contact areas that have to be handled by the ML solver.

Furthermore, the occurring of direct solid-to-solid contact during a time-evolving surface interaction produces wear, i.e., the loss of material from the surfaces that pushed against each other are subjected to sliding, which over time progressively modifies the surfaces' gap (Ludema, 1996): the wear modelling is necessary to estimate *in silico* the tribo-system degradation during its functioning and, among all the wear mechanisms depending on a multitude of factors (Meng and Ludema, 1995), it can be easily implemented in the gap equation through the Archard wear model (Archard, 1953; Archard and Hirst, 1956).

Even if the original Archard model refer to a global material volume loss due to a given applied load and to a realised sliding distance, it is adapted in a local spatial/temporal form in order to be implemented in the solver that takes into account both the space and time evolution of the tribological event. So, the Archard wear model reported in (340) states that the local wear rate, i.e., the variation over the time t of the wear penetration depth w intended as the normal dimension of the worn volume over the conjugated interface, is proportional to the product between the local pressure p and the local sliding velocity vector $\mathbf{V}$ norm through the wear factor $\mathrm{k_w}$ (a constant depending on the materials composing the tribological pair).

$$\frac{\partial \mathrm{w}}{\partial \mathrm{t}} = \mathrm{k_w p} \|\mathbf{V}\| \tag{340}$$

From the (340) follows that the local wear depth w is given by the cumulative time integral of the wear rate, so, in correspondence of the analysed time instant, the wear field is given in (341).

$$\mathrm{w}(\mathbf{x}, \mathrm{t}) = \int_0^{\mathrm{t}} \mathrm{k_w p} \|\mathbf{V}\| \, d\tau \tag{341}$$

For all the ML models developed in this work accounting for wear, it is assumed a constant wear factor depending on the coupling materials found in literature, so it does not take into account effects like frictional work and multidirectional sliding typical of the polymers: despite this assumption, the aim is the implementation of the wear generation as a progressive loss of materials from the coupled surfaces during their loading/sliding interaction, so further deepening on a variable wear factor will be matter of future perspectives; furthermore, the wear will be considered only in the resulting contact zones, keeping the validity of the Archard wear law even in a lubricated contact configuration.

The wear depth that progressively modifies the gap field until a particular instant can be implemented into the gap eq. (342) as a field quantity that is updated along the time evolution.

$$h(\mathbf{x},t) = u(p) + g(\mathbf{x}) + w(\mathbf{x},t) - \delta(t) \qquad (342)$$

Hence, once the ML solver has simulated the whole analysed time period referred to the tribo-system functioning, the wear volume V time evolution associated to that operating conditions can be evaluated in (343) through the surface integration of the wear depth w.

$$V(t) = \int_{\Omega} w(\mathbf{x},t)\, dA \qquad (343)$$

In this work two approaches were followed to model the ML regime adapting the already addressed governing equation:

- the first approach distinguishes the fluid lubrication and the solid contact by dividing the pressure into fluid pressure p and contact pressure p_c; it has been used in the context of the spherical THR tribo-system characterised by the spring deformation model;
- the second approach keeps a unified pressure field p that in the lubricated zones is fluid pressure while in the contact zones is contact pressure; it has been used in the context of rectangular tribo-systems characterised by the half-space deformation model.

2.3.3.1. Splitting pressure approach

Starting with the first approach, a contact deformation u_c is implemented into the spherical gap eq. (344).

$$h(\theta,\varphi,t) = k_c p(\theta,\varphi,t) + u_c + c + w(\theta,\varphi,t) - \mathbf{e}^T(t)\hat{\mathbf{r}}(\theta,\varphi) \qquad (344)$$

Along the iterations of the method chosen to solve the problem, the trial fluid pressure p is used to elaborate the gap h in absence of contact pressure p_c: the contact deformation u_c rises if the trial fluid pressure p is not high enough to avoid the surfaces' interpenetration, so it is calculated in (345) as the compensation of the eventual negative gap h; in order to avoid the previously described Reynolds equation singularity, the contact deformation u_c compensate the negative gap up to a chosen limit Δ_b, intended as a boundary layer below which the surface contact is direct.

$$u_c = \max\{0, \Delta_b - (k_c p + c + w - \mathbf{e}^T\hat{\mathbf{r}})\} \qquad (345)$$

Then the evaluated contact deformation u_c is added to the gap h and the spring deformation model is inverted as in (346) to evaluate the contact pressure p_c in the contact zones (positive contact deformation): let note the validity of the LCC imposing a positive contact pressure in the closed gap zones.

$$p_c = \frac{u_c}{k_c} \tag{346}$$

So, the Newton iterative loop in (235) runs updating the fluid pressure p and evaluates the contact pressure p_c as a consequence of the former: once it has converged, the contact pressure p_c is going to contribute to the load vector **N** calculation in (347) needed to supply the outer loop iterating on the spherical joint eccentricities.

$$\mathbf{N} = \iint_{\Omega} (p + p_c)\hat{\mathbf{r}}\, R^2 \sin\theta \, d\theta d\varphi \tag{347}$$

Finally, when also the outer loop iterating on the eccentricities has reached the convergence, the resulting discretised contact pressure p_c field is used in (348) to evaluate the discretised wear penetration depth w by adding to the previous one (w_{ij}^-) the variation for the time step Δt governed by the wear rate accounting for the sliding velocity vector norm given by the components of the entraining velocities U_θ and U_φ.

$$w_{ij} = w_{ij}^- + k_w p_{c_{ij}} 2\sqrt{U_{\theta_{ij}}^2 + U_{\varphi_{ij}}^2}\Delta t \tag{348}$$

2.3.3.2. Unified pressure approach

The second approach is, according to the author, more methodical since it consists into imposing a different equation in correspondence of the grid contact points: with reference to the rectangular Reynolds equation local residual F_I in (305), in order to respect the LCCs validity in the contact zones without separating the contact pressure contribution from the fluid one or altering the gap equation, the ML problem can be addressed by imposing the Reynolds equation in the positive gap zones and the null gap equation elsewhere, defining a new residual G_I in (349).

$$G_I(\mathbf{p}) = \begin{cases} F_I(\mathbf{p}) & h_I > 0 \\ h_I(\mathbf{p}) & h_I \leq 0 \end{cases} \tag{349}$$

The (349) suffers from discontinuities due to the Reynolds equation singularity in correspondence of null gap, so, in order to provide a more gentle passage across the lubricated/contact zones, a smooth transition function of the gap θ is defined in (350): it is conceived as a continuous and differential sigmoid which is zero for negative gap and grows to become unitary across the gap range between zero and the boundary limit Δ_b.

$$\theta(h) = \begin{cases} 0 & h \leq 0 \\ \frac{1}{2}\left(1 - \cos\left(\frac{\pi h}{\Delta_b}\right)\right) & 0 < h \leq \Delta_b \\ 1 & h > \Delta_b \end{cases} \tag{350}$$

The transition function θ allows to smoothly move across the lubricated zones in which the Reynolds residual F_I is valid, i.e., $\theta = 1$, and the contact zones where the gap h is imposed to be zero, i.e., $\theta = 0$: the new ML problem residual G_I is defined in (351).

$$\theta_I = \theta(h_I) \quad \rightarrow \quad G_I(\mathbf{p}) = \theta_I F_I(\mathbf{p}) + (1 - \theta_I) h_I(\mathbf{p}) = 0 \tag{351}$$

The new set of equations $\mathbf{G}$ is solved with the same non-linear Jacobi method, so the local derivative of the transition function θ with respect to the gap h is needed in the chain rule and it is reported in (352).

$$\frac{d\theta_I}{dh_I}(h_I) = \begin{cases} 0 & h_I \leq 0 \\ \dfrac{\pi}{2\Delta_b}\sin\left(\dfrac{\pi h_I}{\Delta_b}\right) & 0 < h_I \leq \Delta_b \\ 0 & h_I > \Delta_b \end{cases} \tag{352}$$

With this second approach, while the load is simply given by the unified pressure field p, the wear occurs only in the contact zones, so the wear rate is reported in (353) accounting for the transition function θ identifying where the surfaces are contacting.

$$\frac{\partial w}{\partial t} = k_w(1 - \theta)p\|\mathbf{V}\| \tag{353}$$

2.4. Simulations

In this section the results obtained by the developed tribological solvers are shown; in particular, three configurations based on the author's works were simulated:

- the ML of the THR for the 3D loads and angular velocities coming from the Multi-Body outputs referred to the lower limb musculoskeletal system during the gait cycle; the deformation model for the implant is the spring one and the ML approach is based on the contact deformation splitting the fluid/contact pressure distributions (author's reference works (Ruggiero and Sicilia, 2020a, 2022c, 2024; Ruggiero, Sicilia and Affatato, 2020));
- the EHL of a ball-in-socket joint for a given set of eccentricities and angular velocities, considering the FEM deformation model (author's reference works (Ruggiero and Sicilia, 2021b, 2022b));
- the ML of a rectangular rough tribo-system for given approach and sliding motions addressed with the half-space BEM deformation model, considering the ML strategy based on the unified pressure field managed by the smooth transition function (author's reference work (Sicilia and Ruggiero, 2025)).

At the actual state of this work, the only possibility to estimate the wear of a THR is given by the ML model relying on the splitting pressure approach and on the spring deformation model, which approach is better from a conceptual point of view with respect to a pure EHL simulation or a pure DCM one, since the THR is a lubricated system undergoing in contact due to the high loads acting on the coupled surfaces: the two successive developed models, i.e., pure spherical EHL supported by a FEM deformation model and ML simulation of rectangular tribo-systems with BEM deformation, were created to make a more accurate deformation calculation, to test the unified pressure approach during the occurring of a contact phase and to implement the fractal roughness generator, with the aim to apply the developed tools in the future to a spherical geometry, so that a more detailed and reliable THR ML simulator could be obtained.

2.4.1. THR Mixed Lubrication with Multi-Body inputs

Starting with the first one, let recall in (354) the governing equations accounting for the spherical Reynolds lubrication equation, the gap equation considering the contact deformation and the wear penetration depth and the THR 3D load balance; furthermore, the contact deformation evaluation logic and the Archard wear law are included.

$$\begin{cases} \sin\theta \dfrac{\partial}{\partial\theta}\left(\sin\theta \dfrac{\rho h^3}{12\mu}\dfrac{\partial p}{\partial\theta}\right) + \dfrac{\partial}{\partial\varphi}\left(\dfrac{\rho h^3}{12\mu}\dfrac{\partial p}{\partial\varphi}\right) = \cdots \\ \ldots = R\sin\theta\left[\dfrac{\partial(\sin\theta\,\rho h U_\theta)}{\partial\theta} + \dfrac{\partial\left(\rho h U_\varphi\right)}{\partial\varphi} + R\sin\theta\dfrac{\partial(\rho h)}{\partial t}\right] \\ h(\theta,\varphi,t) = k_c p(\theta,\varphi,t) + u_c + c + w(\theta,\varphi,t) - \mathbf{e}^T(t)\hat{\mathbf{r}}(\theta,\varphi) \\ \mathbf{N}(t) = \iint\limits_{\Omega} \left(p(\theta,\varphi,t) + p_c(\theta,\varphi,t)\right)\hat{\mathbf{r}}(\theta,\varphi)\, R^2 \sin\theta \, d\theta d\varphi \end{cases} \tag{354}$$

$$u_c = \max\left\{0, \Delta_b - \left(k_c p + c + w - \mathbf{e}^T\hat{\mathbf{r}}\right)\right\} \;\rightarrow\; p_c = \frac{u_c}{k_c}$$

$$w(\theta,\varphi,t) = \int_0^t k_w p_c 2\sqrt{U_\theta^2 + U_\varphi^2}\, d\tau$$

The solver structure (355) is based on the nested loop composed by the outer one iterating on the THR eccentricities **e** imposing the load balance **L** through the numerical Newton method described in (216) and by the inner one iterating on the fluid pressure **p** solving the Reynolds equation with the analytical Newton method described in (235).

$$
\begin{aligned}
&\text{while } \|\mathbf{L}(\mathbf{e}^n)\| > \text{tol} \\
&\qquad \text{while } \sum_I \left|p_I^{k+1} - p_I^k\right| > \text{tol} \\
&\qquad\qquad \mathbf{p}^* = \mathbf{p}^k - \omega\left[\mathbf{F}_\mathbf{p}(\mathbf{p}^k)\right]^{-1}\mathbf{F}(\mathbf{p}^k) \\
&\qquad\qquad \mathbf{p}^{k+1} = \max\{0, \mathbf{p}^*\} \\
&\qquad\qquad k \to k+1 \\
&\qquad \text{end} \\
&\qquad \mathbf{L}(\mathbf{e}^n) = \sum_{i,j} \mathbf{P}_{ij}(\mathbf{e}^n)\Delta\theta\Delta\varphi - \mathbf{N} \\
&\qquad \mathbf{e}^{n+1} = \mathbf{e}^n - [\mathbf{L}_\mathbf{e}(\mathbf{e}^n)]^{-1}\mathbf{L}(\mathbf{e}^n) \\
&\qquad n \to n+1 \\
&\text{end}
\end{aligned}
\tag{355}
$$

The input THR loads and angular velocities are the ones elaborated by the Multi-Body model in the case of the lower limb musculoskeletal system moving during the gait cycle and previously reported in the Figure 71, while the THR parameters refer to a Hard-on-Soft THR implant made of UHMWPE acetabular cup against a much harder femoral head (in accordance with the spring deformation model) and the lubricant properties are in line with the synovial fluid ones: the Table 1 collects all the input data together with the parameters for the numerical computation (Dowson and Higginson, 1966; Dumbleton, 1981; Fisher and Dowson, 1991; Nordin and Frankel, 2001; van Leeuwen, 2009; Mattei *et al.*, 2011; Aherwar, Singh and Patnaik, 2015; Zivic *et al.*, 2017; Merola and Affatato, 2019).

Table 2 *THR input data for the ML simulation*

Data	
Femoral head radius r	14 mm
Radial clearance c	100 μm
Acetabular cup thickness H	9.5 mm
Acetabular cup Young modulus E	1 GPa
Acetabular cup Poisson ratio ν	0.4
Barus exponent α	$19.8\ \mathrm{GPa}^{-1}$
Lubricant nominal viscosity μ_0	1 mPa s
Dowson-Higginson coefficient c	$5.9 \cdot 10^8$ Pa
Dowson-Higginson coefficient γ	1.34
Lubricant nominal density ρ_0	$850\ \mathrm{kg\ m^{-3}}$
Boundary limit Δ_b	30 nm
Wear factor k_w	$10^{-7}\ \mathrm{mm^3 N^{-1} m^{-1}}$
2D mesh points	100 × 100
Time vector length	70
Dimensionless pressure tolerance	10^{-5}

Dimensionless load tolerance	10^{-3}
Relaxation ω	0.2
Load balance Jacobian perturbation ε	10^{-4}

The THR eccentricity vector **e** time evolution result is shown in the Figure 97 in its dimensionless form with respect to the implant radial clearance c: it can be seen that the eccentricity y-component pushes the femoral head against the acetabular cup surface, so it is expected the direct contact especially during the gait stance phase; the eccentricity vector substantially follows the load vector trend, since, at least during the gait cycle kinematics, the sliding motion imposed by the angular velocities is less intense with respect to the high loads coming from the hip joint reactions.

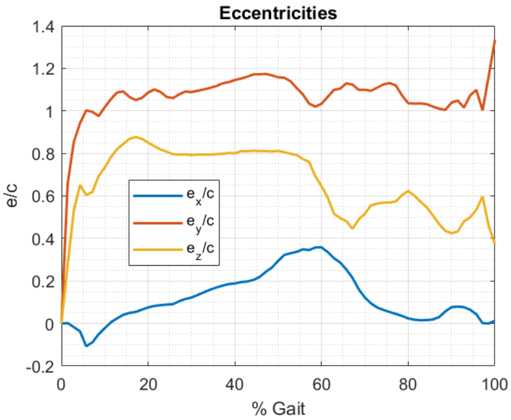

Figure 97 *THR eccentricities during the gait*

In order to verify the expectations about the contact occurring based on a preliminary analysis looking at the eccentricities, let analyse the time evolution of the maximum pressure p_{max} (sum of the fluid and the contact contribution) and the minimum gap h_{min} realised over the interface: looking at the Figure 98, it can be seen that, the initial stage of the gait stance phase is in full-film regime but the minimum gap quickly decreases and reaches the boundary limit Δ_b around the 30% of the gait cycle, from which the surfaces' contact is established somewhere over the domain until the end of the gait cycle, hence confirming that, even during a simple musculoskeletal kinematics like the gait, the hip works in a ML regime due substantially to the hip loading intensity; as a consequence, the maximum pressure trend is very similar to the load y-component.

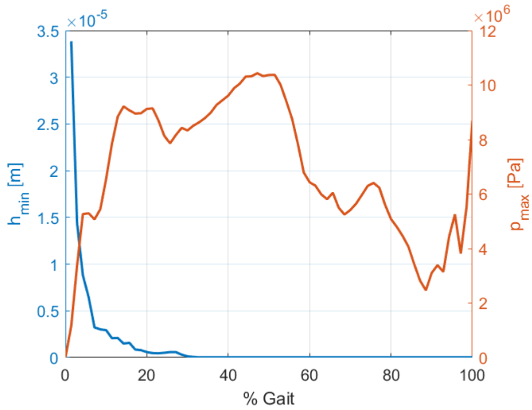

Figure 98 *THR minimum gap and maximum pressure during the gait*

Let now verify the contact area location over the cup surface depicted in the Figure 99 showing the transition from the full-film to a mixed regime around the 30% of the gait cycle: it can be seen that the pressure bell, that from fluid pressure turns into contact one, points towards what would be the Proximal/Distal pelvis direction in accordance to the hip loads in the Figure 61.

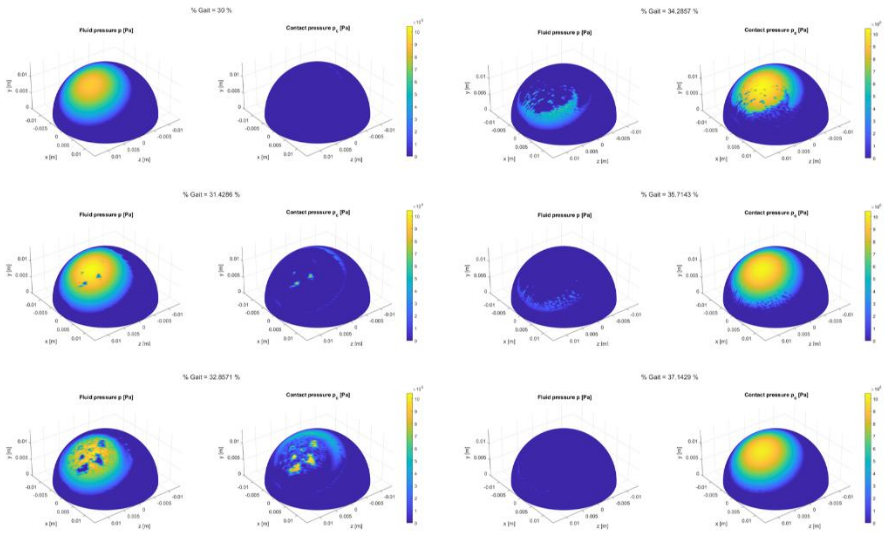

Figure 99 *THR fluid to contact pressure transition during the gait*

Then, the pressure and gap fields are shown in the Figure 100 in correspondence of two time instants, i.e., one referred to a full film regime and one to a mixed regime: in both the instants, the highly deformed zone can be appreciated; the main difference between the regimes stays in the abrupt transition from the open gap zones to contact ones in the mixed configuration in which the gap is imposed to be equal to the boundary limit Δ_b, while in the full-film instant, the gap is smoothly deformed in the region of minimum film thickness.

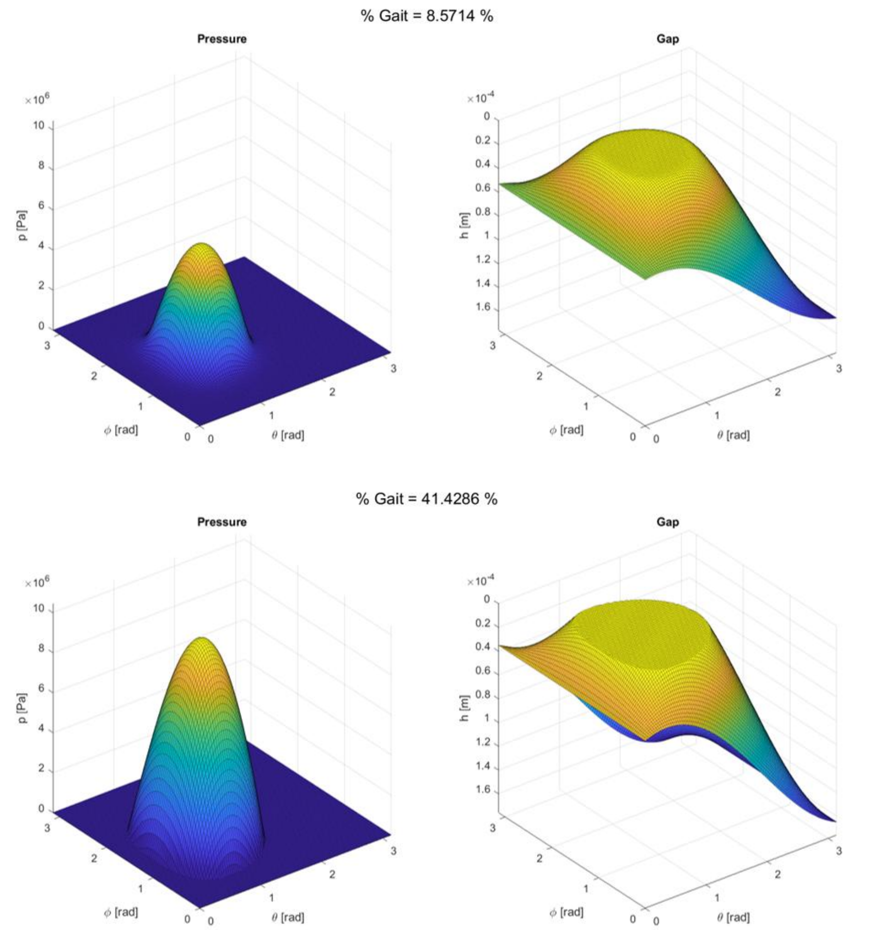

Figure 100 *THR pressure and gap fields in full-film and mixed regimes*

From the applicative point of view, the most important output is the worn material, so the wear penetration depth in correspondence of the end of the gait cycle is shown in the Figure 101: it gives information about what zone of the implant is majorly stressed by the wear.

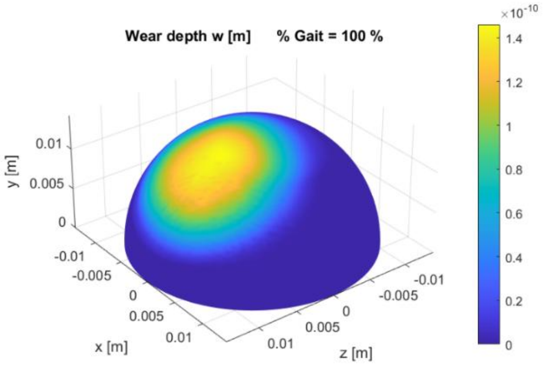

Figure 101 *THR wear depth at the end of the gait cycle*

Even more interesting is the time evolution of the wear volume along the gait cycle shown in the Figure 102: it can be seen that it starts growing with the contact event and keeps growing due to the combination of the contact pressure and the sliding velocities, slowing down towards the end of the gait cycle where the gait swing phase provides less pressure at the interface. Even if the succession of several gait cycles over the implant functioning life continuously degrades the conjugated femoral head and acetabular cup surfaces, the wear volume evolution along the single gait cycle provides a simple estimation of the implant volume loss during a year (considering that an average of a million gait cycle are executed in that period): it is extracted from the last value of the shown wear volume V and it is simply multiplied by cycles done in the year; the results of the presented model provided a annual wear rate of about $32{,}7\ \mathrm{mm}^3$ per year, which is in line with some *in vitro* testing found in the literature (Mattei *et al.*, 2011; Mattei, Di Puccio and Ciulli, 2013; Di Puccio and Mattei, 2015; Ruggiero, Sicilia and Affatato, 2020). Of course, this estimation is simple but it does not take into account the so-called long term wear effects which are referred to the implant functioning over millions of gait cycles, e.g., creep effects, cumulated degradation, and so on: in order to have a more precise estimation, the developed ML code has to be run with the same time resolution over a too much longer time period and so it would require a lot of computational time that cannot actually be handled by this author computational availability. The accuracy of the single gait cycle simulation keeps its validity and the possibility to have a starting estimation of the implant duration: in the future, numerical modelling and techniques strategies able to handle longer time period will be studied and implemented by this author, so that a valid *in silico* competitor to the reliable *in vitro* simulators could be achieved.

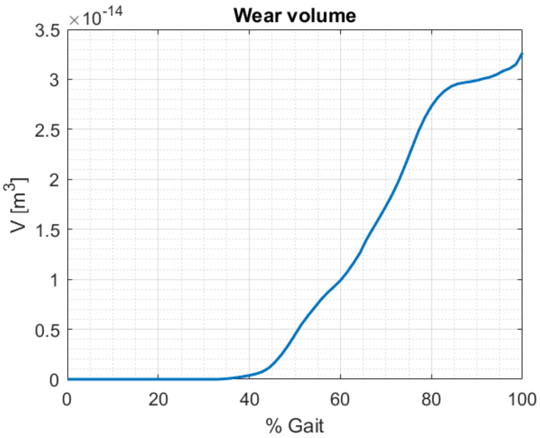

Figure 102 *THR wear volume during the gait*

At this level, the coupling between the Multi-Body model and the ML solver, even if the second one is characterised by a simple deformation model, turns out to be effective in terms of achieving a computational tool estimating the THR implant wear starting from the musculoskeletal kinematics (which is the global aim of the current work resumed in the Figure 103); at the current state, a potential user of the developed computational pipeline has to supply the musculoskeletal properties resumed in the described excel input file to identify the subject mechanical system and the geometrical and rheological input parameters related to the implanted Hard-on-Soft THR: with this inputs, he would be able to obtain mechanical/tribological simulation results associated to the investigated implant load/motion operating conditions and to the surfaces' interaction in terms of fluid/contact pressure, wear and so on.

This developed algorithm could be useful in the context of the artificial joints *in silico* wear estimation with the possibility to be adopted in the context of custom-manufactured implants.

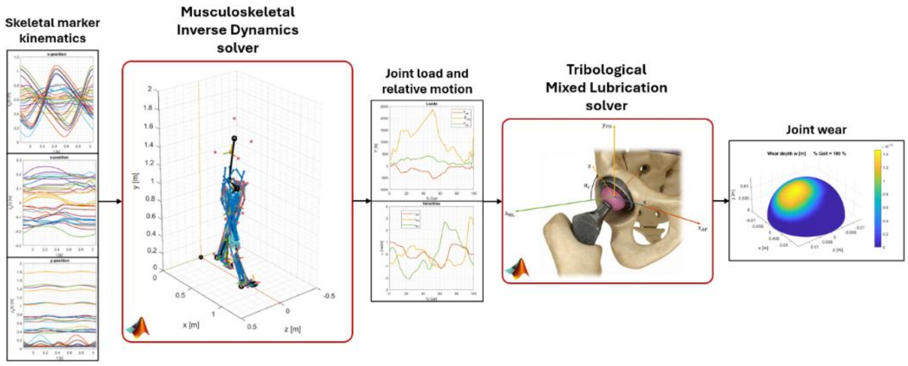

Figure 103 *Models linking from the musculoskeletal kinematics to the joint wear*

The developed routine could be also useful in the context of sensitivity analyses based on the THR response to a variation of input parameters like geometry, rheology, etc.: some of these aspects could be found in the author published chapter (Ruggiero and Sicilia, 2024), while other discussions will be made in future studies.

The remaining part of this work will be devoted to the implementation of the more accurate deformation models previously presented that, with the view of a future perspective, could be applied in the context of the developed hip wear *in silico* simulator.

2.4.2. Spherical Elasto-Hydrodynamic Lubrication and FEM deformation

Let proceed with the spherical EHL simulator with the FEM deformation model; in this case, the developed algorithm is tested for a given ball-in-socket relative motion defined by the input time-varying eccentricities and angular velocities, so the only governing equation is the discretised Reynolds residual $\mathbf{F}$ reported in (356) together with the gap h equation accounting for the FEM compliance matrix $\mathbf{C}$.

$$
\begin{aligned}
&\mathrm{h_I} = \sum_{\mathrm{J}} \mathrm{C_{IJ} p_J} + \mathrm{c} - \mathbf{e}^{\mathrm{T}} \hat{\mathbf{r}}_{\mathrm{I}} \\
&\mathbf{a}_{\mathrm{I}}(\mathbf{p}) = \mathbf{D}_2^{\mathrm{T}} \boldsymbol{\varepsilon}_{\mathrm{I}}(\mathbf{p}) \quad \mathrm{b_I}(\mathbf{p}) = \mathbf{D}_\theta^{\mathrm{T}} \mathbf{u}_{\mathrm{I}}(\mathbf{p}) + \mathbf{D}_\varphi^{\mathrm{T}} \mathbf{w}_{\mathrm{I}}(\mathbf{p}) + \mathbf{D}_{\mathrm{t}}^{\mathrm{T}} \mathbf{v}_{\mathrm{t}}(\mathbf{p}) \\
&\mathrm{F_I}(\mathbf{p}) = \begin{cases} \mathbf{a}_{\mathrm{I}}^{\mathrm{T}}(\mathbf{p}) \mathbf{p}_{\mathrm{I}} - \mathrm{b_I}(\mathbf{p}) & 2 \le \mathrm{i} \le \mathrm{N}-1 \quad 2 \le \mathrm{j} \le \mathrm{M}-1 \\ \mathrm{p_{1j}, p_{Nj}} & 1 \le \mathrm{j} \le \mathrm{M} \\ \mathrm{p_{i1}, p_{iM}} & 2 \le \mathrm{i} \le \mathrm{N}-1 \end{cases}
\end{aligned}
\tag{356}
$$

The solver iterative logic is the free-derivative one reported in the eq. (272), while the input data given in the Table 2 and the input time evolutions of the eccentricity vector $\mathbf{e}$ and of the angular velocity vector $\boldsymbol{\omega}$ are depicted in the Figure 104: they refer to the testing tribo-pair made of a ceramic ball into a UHMWPE socket, which the ball is hardly pushed against the socket through the y-component of the eccentricity and it rotates only around the z axis, according to the simple shown kinematics in order to provide information about the involved tribological fields shape once the steady-state is reached.

Table 3 *Ball-in-socket input data for the EHL simulation*

Data	
Ball radius r	14 mm
Radial clearance c	100 μm
Socket thickness H	9.5 mm
Socket Young modulus E_s	1 GPa
Socket Poisson ratio ν_s	0.4

Ball Young modulus E_b	250 GPa
Ball Poisson ratio ν_b	0.2
Barus exponent α	$19.8\ \mathrm{GPa}^{-1}$
Lubricant nominal viscosity μ_0	1 Pa s
Dowson-Higginson coefficient c	$5.9 \cdot 10^8$ Pa
Dowson-Higginson coefficient γ	1.34
Lubricant nominal density ρ_0	$850\ \mathrm{kg\ m}^{-3}$
2D mesh points	100×100
Time vector length	40
Dimensionless pressure tolerance	10^{-5}
Relaxation ω	0.1
Socket tetrahedral element number n_E	8005
Ball tetrahedral element number n_E	13937

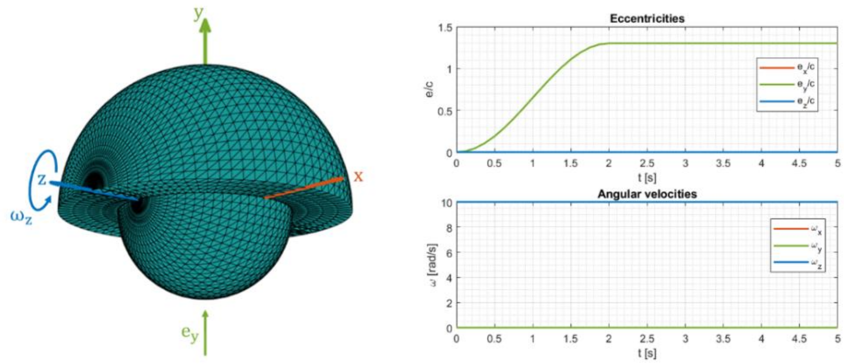

Figure 104 *Ball-in-socket relative motion for the EHL simulation*

The resulting lubricant pressure and gap shapes at the end of the analysed time period are shown in the Figure 105: it can be seen that, due to the ω_z angular motion, the lubricant is dragged along the φ direction, so both the fields resulted to be symmetrical along θ; the combined action of the angular motion and the eccentricity e_y provided the asymmetrical shapes along φ characteristic of the EHL regime, i.e., with the pressure bump and the minimum film thickness in correspondence of the meatus outlet of the highly deformed zone (Dowson and Higginson, 1966; Greenwood, 2020) (the pressure spike is not clearly visible for the chosen operating conditions, due to the low but physiologically reasonable angular velocity).

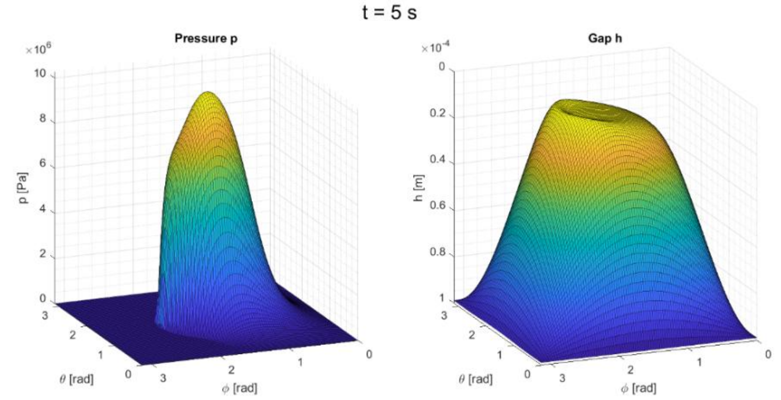

Figure 105 *Pressure and gap fields of the EHL simulation*

Two further interesting shapes are the ones belonging to the socket shear stresses τ_θ and τ_φ fields reported in the Figure 106: the symmetrical behaviour of the lubricant pressure p along θ produces an anti-symmetrical shape of the τ_θ stress, while the τ_φ stress field feels the effects of the ω_z angular motion and of the piezo-viscous lubricant rheology showing a clear spike in correspondence of the meatus outlet.

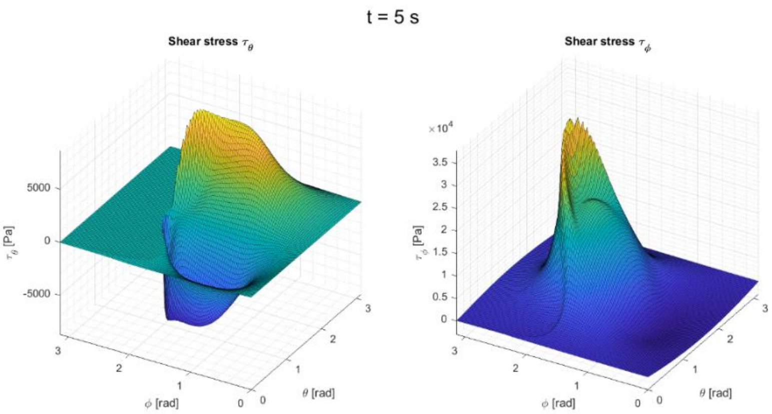

Figure 106 *Shear stress fields of the EHL simulation*

The surface integration of the pressure p and of the shear stresses τ_θ and τ_φ leads to the time evolution of the load vector **N** and of the viscous friction torque vector **T** depicted in the Figure 107: the simulated operating conditions provided a great amount of load along y and a less intense one along x, while, as expected, the friction torque was generated only around the z axis in response to the imposed angular motion; it can be seen from the time evolutions that the steady-state was reached.

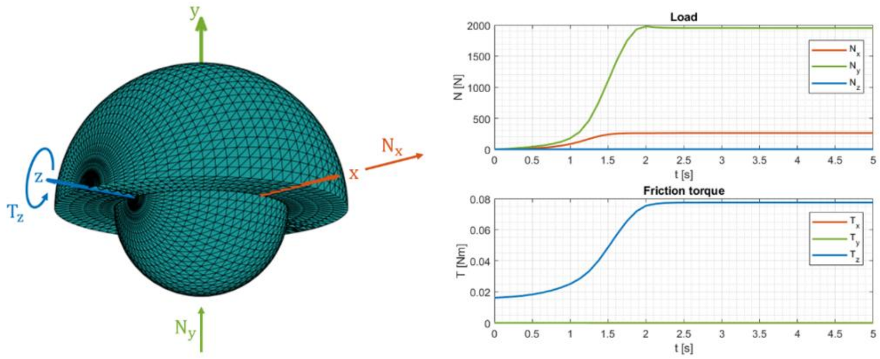

Figure 107 *Load and friction torque of the EHL simulation*

The reliability of the simulator can be verified by comparing the minimum film thickness h_{min} realised over the interface along the time t with the stationary one obtained analytically by the Hamrock-Dowson empirical formula (Hamrock and Dowson, 1976; Lubrecht, Venner and Colin, 2009) in (357) accounting for:

- the material dimensionless group dealing with the lubricant Barus exponent α and the bulks' equivalent Young modulus E^* (given by the ball and the socket Young moduli E_b, E_s and Poisson ratios ν_b, ν_s);
- the speed dimensionless group dealing with the lubricant nominal viscosity μ_0, the sliding velocity U_x (given by the ending angular velocity ω_z and the socket radius R), the modulus E^* and the equivalent curvature radius R_x along the sliding direction (given by the ball and socket radii r and R);
- the load dimensionless group dealing with the normal load w (in this case assumed to be the ending N_y component of the load vector), the modulus E^* and the radius R_x;
- the ellipticity factor dealing with the radius R_x and the equivalent curvature radius in the plane orthogonal to the sliding direction R_y (equal to R_x in the spherical case).

The comparison reported in the Figure 108 confirms that the minimum film thickness, after a transient phase starting from the radial clearance c value, decreases as the load increases, reaching a stationary phase in which it tends to the Hamrock-Dowson empirical value.

$$\begin{gathered}\frac{1}{R_x}=\frac{1}{R_y}=\frac{1}{r}-\frac{1}{R} \quad \frac{1}{E^*}=\frac{1-\nu_b^2}{E_b}+\frac{1-\nu_s^2}{E_s} \quad U_x=\omega_z R \quad w=N_y \\ k=1.0339\left(\frac{R_y}{R_x}\right)^{0.64}\end{gathered} \tag{357}$$

$$\frac{h_{min}}{R_x} = 3.63(2\alpha E^*)^{0.49}\left(\frac{\mu_0 U_x}{2E^* R_x}\right)^{0.68}\left(\frac{w}{2E^* R_x^2}\right)^{-0.073}\left(1 - e^{-0.68k}\right)$$

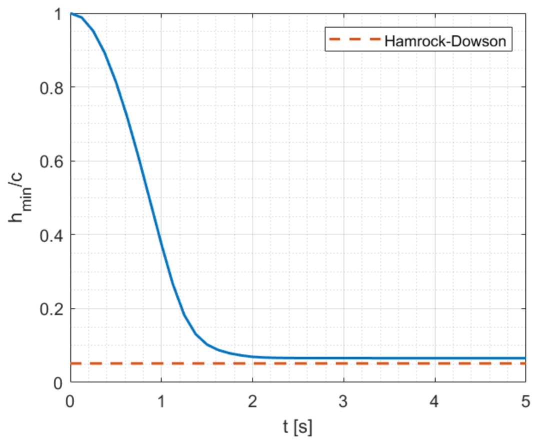

Figure 108 *Minimum film thickness of the EHL simulation*

Finally, the eventual benefit of the developed FEM deformation model stays in the possibility to entirely solve the structure equilibrium eq. (260) in a post-processing phase to find the whole set of nodal displacements $\mathbf{q}$ from which the mechanical response of the ball-in-socket bulks to the generated lubricant pressure at the interface can be analysed: for example, given the nodal displacement of each tetrahedral element, the elemental stress vector $\boldsymbol{\sigma}$, deformation vector $\boldsymbol{\varepsilon}$ and volume Ω (eq. (249)) can be evaluated to determine the internal elastic strain energy U distribution and to visualise its propagation inside the ball and the socket volumes as reported in the Figure 109.

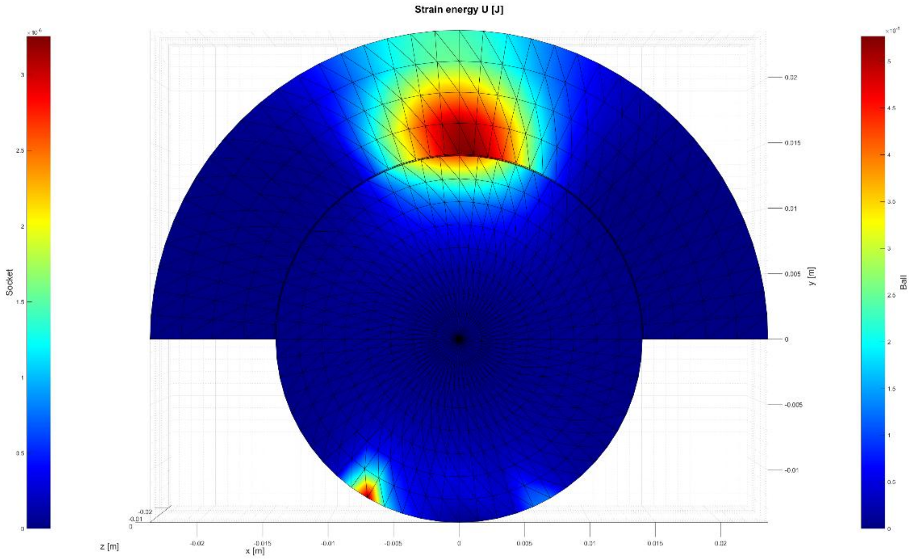

Figure 109 *Elastic strain energy of the EHL simulation by the FEM model*

2.4.3. Rectangular Mixed Lubrication and BEM deformation

Finally, the results about the ML solver devoted to the simulations of rectangular tribo-systems considered as elastic half-spaces are presented. Also in this case the input time evolution of approach and sliding velocities are supplied to the solver, so let recall in (358) the discretised Reynolds residual in cartesian coordinates **F** previously given in (305) together with the gap equation accounting for the half-space BEM compliance matrix **K** and the ML residual **G** obtained with the sigmoid transition function θ in (351).

$$\begin{gathered}
\mathrm{h_I} = \sum_{\mathrm{J}} \mathrm{K_{IJ} p_J} + \mathrm{g_I} - \delta \\
\mathrm{F_I}(\mathbf{p}) = \begin{cases} \boldsymbol{\varepsilon}_\mathrm{I}^\mathrm{T} \mathbf{D}_2 \mathbf{p}_\mathrm{I} - \mathbf{D}_\mathrm{x}^\mathrm{T} \mathbf{u}_\mathrm{I} - \mathbf{D}_\mathrm{z}^\mathrm{T} \mathbf{w}_\mathrm{I} - \mathbf{d}_\mathrm{t}^\mathrm{T} \mathbf{v}_\mathrm{t} & 2 \le \mathrm{i,j} \le \mathrm{N,M} - 1 \\ \mathrm{p_{1j}, p_{Nj}} & 1 \le \mathrm{j} \le \mathrm{M} \\ \mathrm{p_{i1}, p_{iM}} & 2 \le \mathrm{i} \le \mathrm{N} - 1 \end{cases} \\
\mathrm{G_I}(\mathbf{p}) = \theta_\mathrm{I} \mathrm{F_I}(\mathbf{p}) + (1 - \theta_\mathrm{I}) \mathrm{h_I}(\mathbf{p}) = 0
\end{gathered} \tag{358}$$

Then, the **G** residual local derivative for the non-linear Jacobi iteration is given in (359) considering the sigmoid derivative of (352) and the Reynolds residual one of (307).

$$\frac{\partial \mathrm{G_I}}{\partial \mathrm{p_I}}(\mathbf{p}) = \frac{\partial \theta_\mathrm{I}}{\partial \mathrm{h_I}} \mathrm{K_{00}} \big(\mathrm{F_I}(\mathbf{p}) - \mathrm{h_I}(\mathbf{p})\big) + \theta_\mathrm{I} \frac{\partial \mathrm{F_I}}{\partial \mathrm{p_I}}(\mathbf{p}) + (1 - \theta_\mathrm{I}) \mathrm{K_{00}} \tag{359}$$

Finally, the iterative Jacobi loop solving the presented ML problem is reported in (360) together with the cavitation constraint pressure truncation.

$$\text{while } \sum_{I} |p_I^{k+1} - p_I^k| > \text{tol}$$
$$\mathbf{p}^* = \mathbf{p}^k - \omega\, \mathbf{G}(\mathbf{p}^k) \oslash \mathbf{g_p}(\mathbf{p}^k) \;\rightarrow\; \mathbf{p}^{k+1} = \max\{0, \mathbf{p}^*\} \tag{360}$$
$$k \rightarrow k+1$$
$$\text{end}$$

Before treating a case with rough surfaces, let use the model to analyse a ball-on-plane configuration, i.e., a sphere of radius R pushing against a plane sliding along only the x direction with the velocity U_x (simulation data reported in the Table 3): in the Figure 110, the ball-on-plane coupling is shown together with the time evolution of the input approach δ and of the sliding velocities U_x and U_z.

Table 4 *Ball-on-plane input data for the ML simulation*

Data	
Ball radius R	1 cm
Plane sides L_x, L_z	2 cm
Plane Young modulus E_p	1 GPa
Plane Poisson ratio ν_p	0.4
Ball Young modulus E_b	1 GPa
Ball Poisson ratio ν_b	0.4
Barus exponent α	19.8 GPa^{-1}
Lubricant nominal viscosity μ_0	1 Pa s
Dowson-Higginson coefficient c	$5.9 \cdot 10^8$ Pa
Dowson-Higginson coefficient γ	1.34
Lubricant nominal density ρ_0	850 kg m^{-3}
Boundary limit Δ_b	10^{-4}R
Wear factor k_w	10^{-7} $mm^3 N^{-1} m^{-1}$
Dry friction coefficient μ_c	0.2
2D mesh points	$2^7 \times 2^7$
Time vector length	60
Dimensionless pressure tolerance	10^{-5}
Relaxation ω	0.01

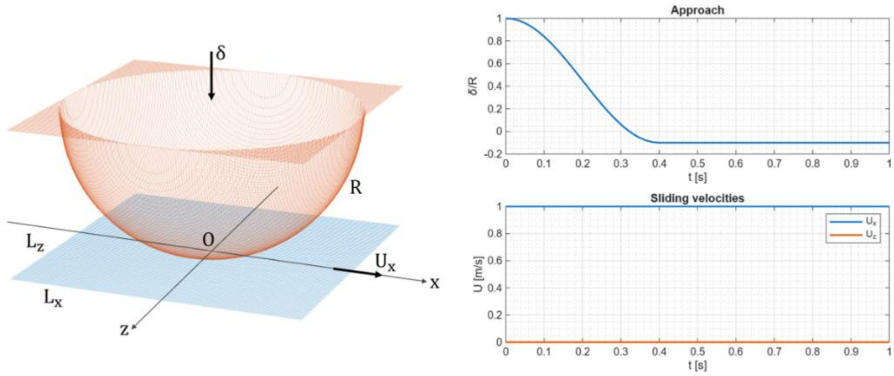

Figure 110 *Ball-on-plane relative motion for the ML simulation*

For the given operating conditions (the approach starting from the distance equal to the ball radius and pushing up to a tenth of its radius in 1 s towards the plane sliding at $1\ \mathrm{ms^{-1}}$) the resulting pressure p and gap h fields are reported in the Figure 111 at the end of the analysed time period: it can be seen that the hard ball approaching constrains the gap to close in the domain central part where the contact pressure rise shows the classical bell shape, while the surrounding fluid pressure is negligible with respect to the contact one.

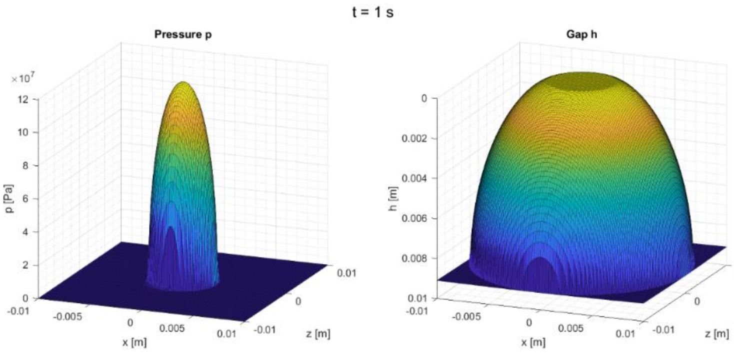

Figure 111 *Pressure and gap fields of the ML simulation*

The time evolution of the minimum gap and the maximum pressure reached at the interface are depicted in the Figure 112, where it can be seen when the contact phase occurs, i.e., when the minimum gap goes to zero.

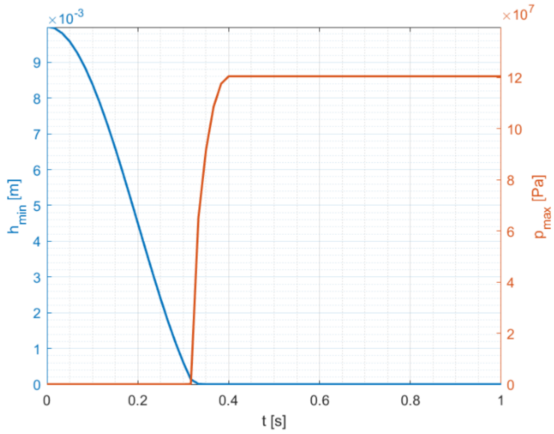

Figure 112 *Minimum gap and maximum pressure of the ML simulation*

The shear stresses τ_x and τ_z fields are shown in the Figure 106; from the eq. (169) it is known how to evaluate the viscous shear stress vector, so, in the ML regime is necessary to model it also in the contact zones: with reference to lower surface, in this work a local sliding friction Coulomb law relying on the dry friction coefficient μ_c is used and the characterization of the shear stress vector $\boldsymbol{\tau}$ over the lubricated and contact zones is managed by the sigmoid transition function θ in the eq. (361). In the Figure 113 the dry contribution of the shear stress along the x direction in the contact area is dominant (proportional to the contact pressure), while the viscous contribution is appreciable only along the z direction with an anti-symmetrical behaviour over the fluid domain.

$$\boldsymbol{\tau}(\mathbf{x},t) = \theta\left(-\frac{h}{2}\boldsymbol{\nabla}p + \mu\frac{\mathbf{V}}{h}\right) + (1-\theta)\left(\mu_c p\frac{\mathbf{V}}{\|\mathbf{V}\|}\right) \tag{361}$$

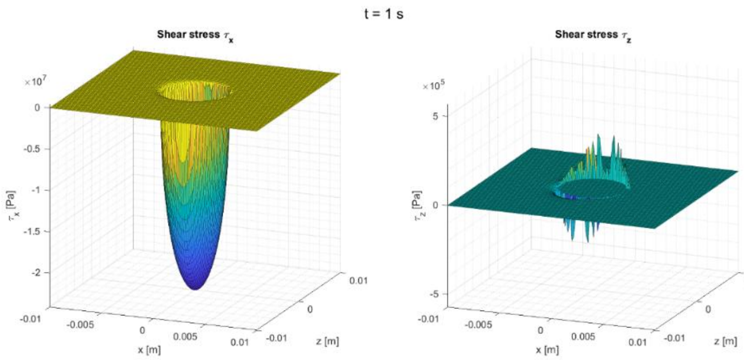

Figure 113 *Shear stress fields of the ML simulation*

The surface integration of the pressure and shear stresses fields leads to the evaluation of the load N and friction forces T_x and T_z time evolution reported in the Figure 114: basically, the only friction force felt by the lower surface is the x one.

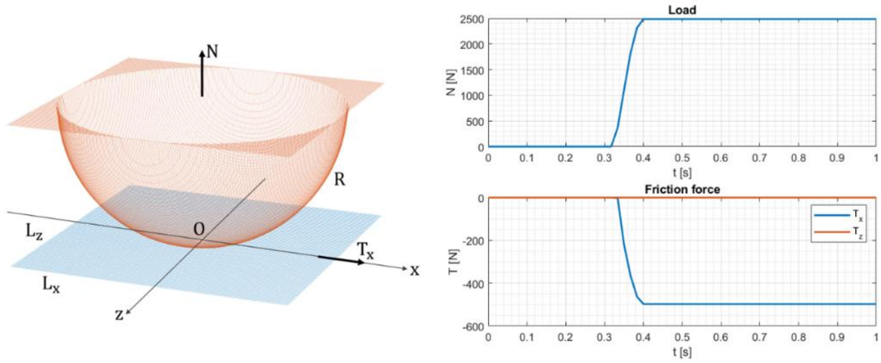

Figure 114 *Load and friction forces of the ML simulation*

The surface wear w at the end of the analysed time period is shown in the Figure 115 together with the time evolution of the wear volume V and of the Real Contact Area fraction RCA, where the latter can be easily obtained by the sigmoid θ in (362); it can be seen that the RCA reaches a stationary value of about 7.7 %, while the wear volume V increases almost linearly due to constant sliding motion.

$$\mathrm{RCA}(t) = \frac{1}{L_x L_z} \int_{\Omega} \big(1 - \theta(\mathbf{x}, t)\big)\, dA \tag{362}$$

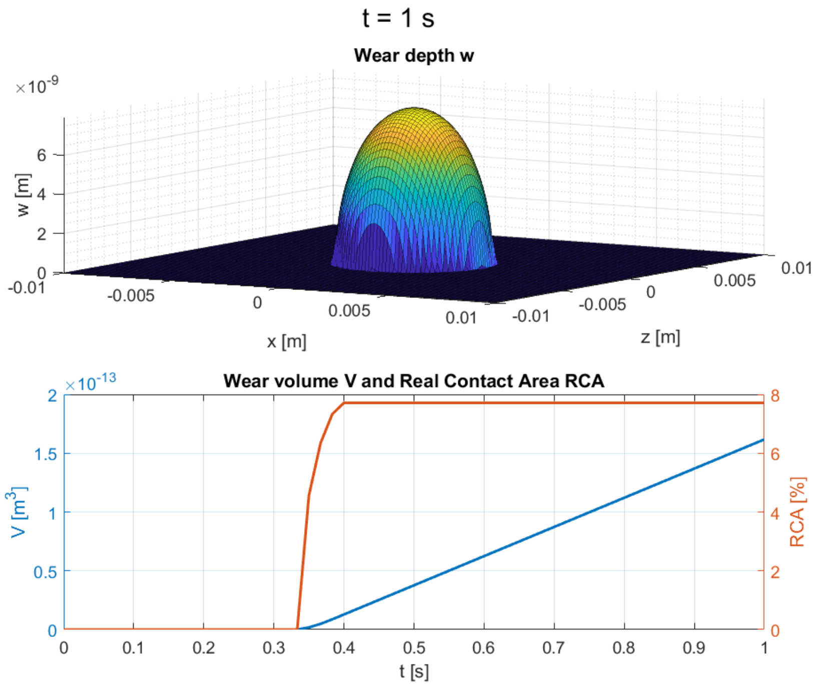

Figure 115 *Wear and Real Contact Area of the ML simulation*

Finally, the visualization of the fluid/contact pressure distribution can be obtained by the Figure 116 in which the deformed surfaces at the end of the time period are reported, together with a section view along the sliding direction at z = 0.

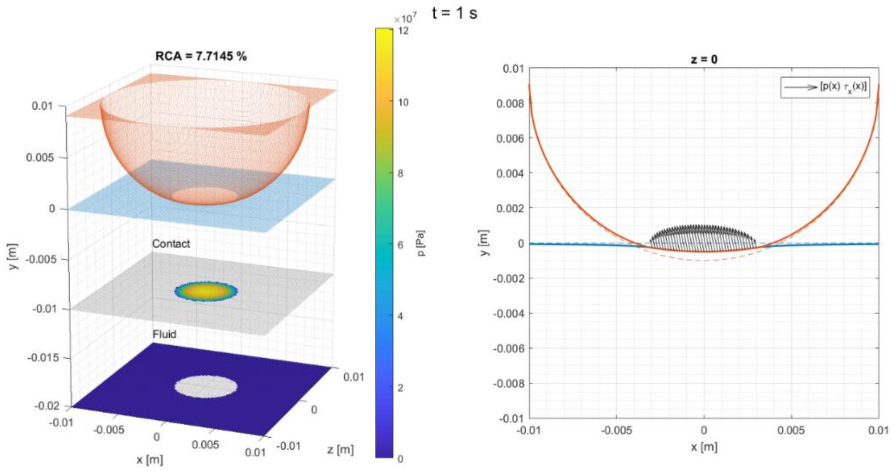

Figure 116 *Deformed surfaces and pressure distribution of the ML simulation*

In order to test the capability of the developed model to handle the ML regime that could move towards a full film EHL mode in response to a variation of the input data, now the results about the same ball-on-plane tribo-system with the same input data, except for a higher sliding velocity U_x (from $1\ \mathrm{ms}^{-1}$ to $10\ \mathrm{ms}^{-1}$) and a higher nominal viscosity μ_0 (from $1\ \mathrm{Pa\,s}$ to $10\ \mathrm{Pa\,s}$): the combined action between the more intense relative motion and the more viscous lubricant should produce a full surface separation.

The pressure p and gap fields h depicted in the Figure 117 resulted to be very similar in shape to the previous case, but, even if is not clear yet, the EHL mode takes place: the surfaces are fully separated even in the highly deformed zones, but the minimum film thickness at the meatus outlet is barely visible.

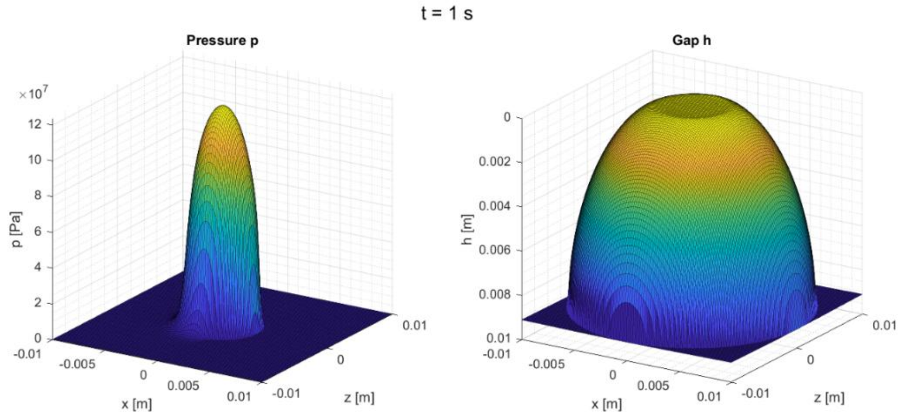

Figure 117 *Pressure and gap fields of the ML-EHL simulation*

The above is more clearly appreciable in the Figure 118, where the pressure and gap fields at the section $z = 0$ along the sliding direction are reported: while the EHL pressure spike is not appreciable for the chosen input data, a zoom on the gap allows to see the minimum film thickness at the meatus outlet; the Hamrock-Dowson empirical minimum film thickness h_{min} and also the central one h_c (Hamrock and Dowson, 1976; Lubrecht, Venner and Colin, 2009), i.e., the gap where the deformed surfaces are nearly parallel, are given in the eq. (363) and they are included in the graph in order to appreciate the reliability of the developed solver.

$$\frac{1}{R_x} = \frac{1}{R_y} = \frac{1}{R} \quad \frac{1}{E^*} = \frac{1-\nu_b^2}{E_b} + \frac{1-\nu_p^2}{E_p} \quad w = N$$
$$\frac{h_{min}}{R_x} = 3.63(2\alpha E^*)^{.49}\left(\frac{\mu_0 U_x}{2E^* R_x}\right)^{.68}\left(\frac{w}{2E^* R_x^2}\right)^{-.073}\left(1 - e^{-.68k}\right) \tag{363}$$
$$\frac{h_c}{R_x} = 2.69(2\alpha E^*)^{.53}\left(\frac{\mu_0 U_x}{2E^* R_x}\right)^{.67}\left(\frac{w}{2E^* R_x^2}\right)^{-.067}\left(1 - 0.61e^{-.73k}\right)$$

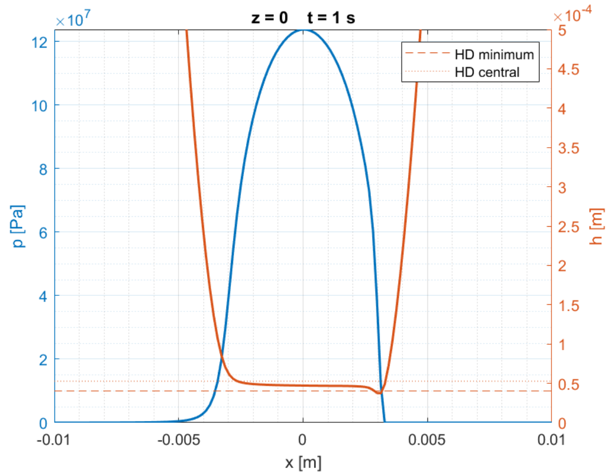

Figure 118 *Pressure and gap along the sliding direction of the ML-EHL simulation*

The viscous shear stresses field resulting from the full surface separation are reported in the Figure 119.

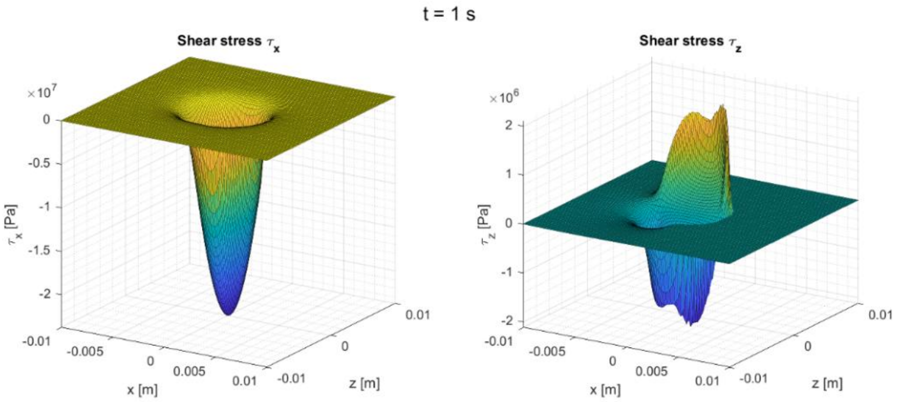

Figure 119 *Shear stresses of the ML-EHL simulation*

Then, the integration of the pressure and of shear stresses leads to the load and the friction forces depicted in the Figure 120, where similar trends can be seen with respect to the previous case, but it is evident a more smoother friction force increase.

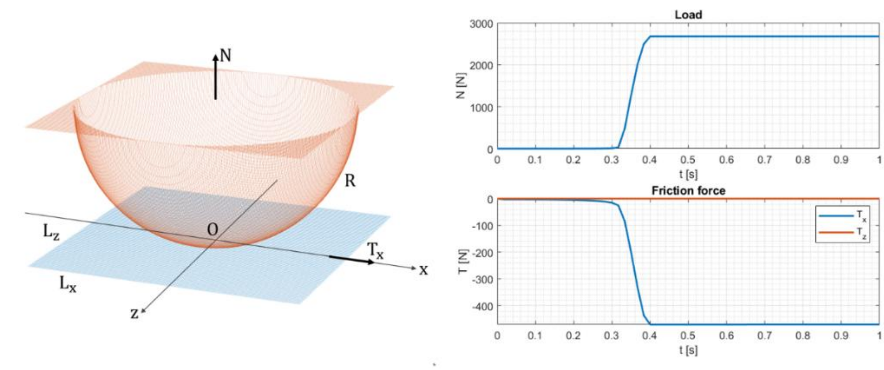

Figure 120 *Load and friction forces of the ML-EHL simulation*

Finally, the deformed surfaces together with the section $z = 0$ and the pressure distribution are given in the Figure 121 at the end of the simulated time period.

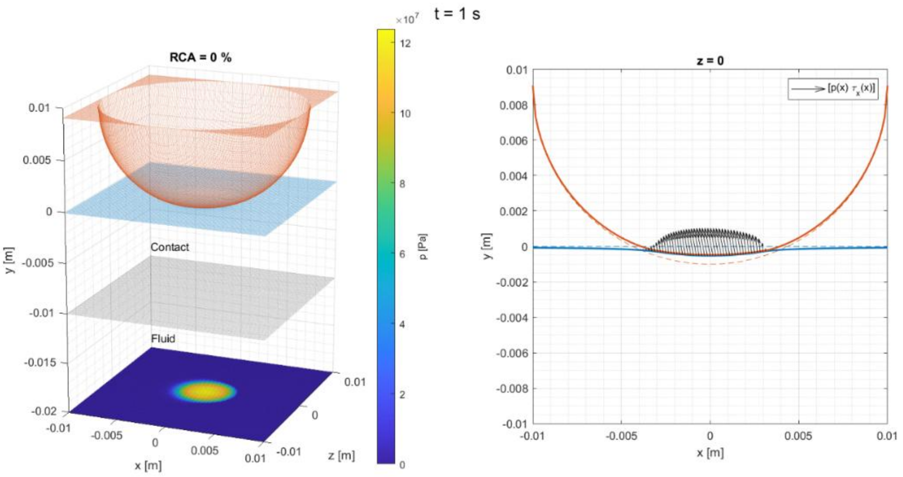

Figure 121 *Deformed surfaces and pressure distribution of the ML-EHL simulation*

Once verified the adaptability of the model to both the ML and the EHL regimes, let now discuss a case with roughness: in particular, the analysed tribo-system is composed by a rough surface pushing against a sliding plane. The input data are the same of the Table 3, but the upper surface is generated through the previously described RMP algorithm with a Hurst exponent $H = 0.8$, while realising an arithmetical roughness $R_a = 1.6$ mm calculated from the generated profile $r(\mathbf{x})$ with mean r_m as follows in the eq. (364) and a peak height $M = 1.15$ cm; for this simulation the boundary limit is chosen as $\Delta_b = 10^{-4} R_a$.

$$r_m = \frac{1}{L_x L_z}\int_{\Omega} r(\mathbf{x})\, dA \quad \rightarrow \quad R_a = \frac{1}{L_x L_z}\int_{\Omega} |r(\mathbf{x}) - r_m|\, dA \qquad (364)$$

The tribo-system is shown in the Figure 122 together with the input approach δ and sliding velocities U_x and U_z, where the former starts from an initial distance equal to the rough surface peak and pushes towards the plane until the half of its peak, while the sliding occurs only along the x direction with a constant velocity of $U_x = 1\ \mathrm{ms^{-1}}$.

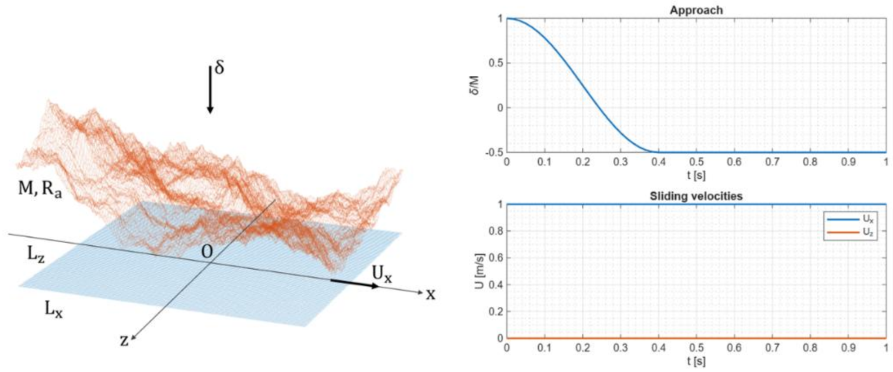

Figure 122 *Tribo-system relative motion for the rough ML simulation*

The resulting pressure and gap fields are reported in the Figure 123 at the end of the simulated time domain.

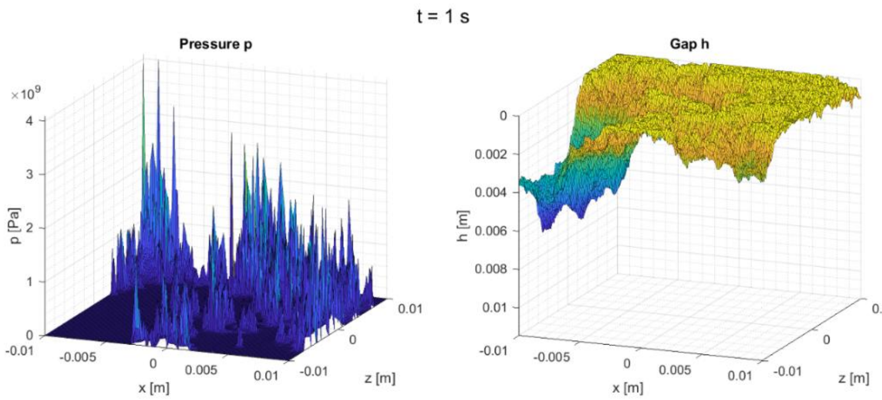

Figure 123 *Pressure and gap fields of the rough ML simulation*

In the Figure 124 the maximum pressure and the minimum gap time evolution are reported, where the dynamics of the tribo-system can be evaluated and the contact phase can be located along the time.

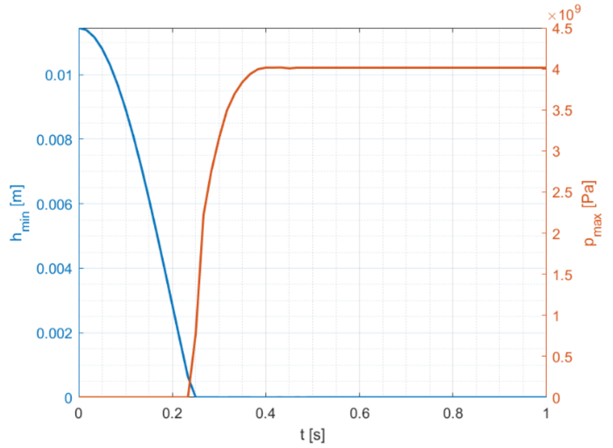

Figure 124 *Minimum gap and maximum pressure of the rough ML simulation*

The worn surface can be visualised together with the associated wear volume and the RCA in the Figure 125: the RCA shows some localised peaks probably due to suddenly occurring asperities contact that, subsequently, wear out (as demonstrated by the contemporary wear volume velocity increase), so the RCA trend settles around the 1.2 %.

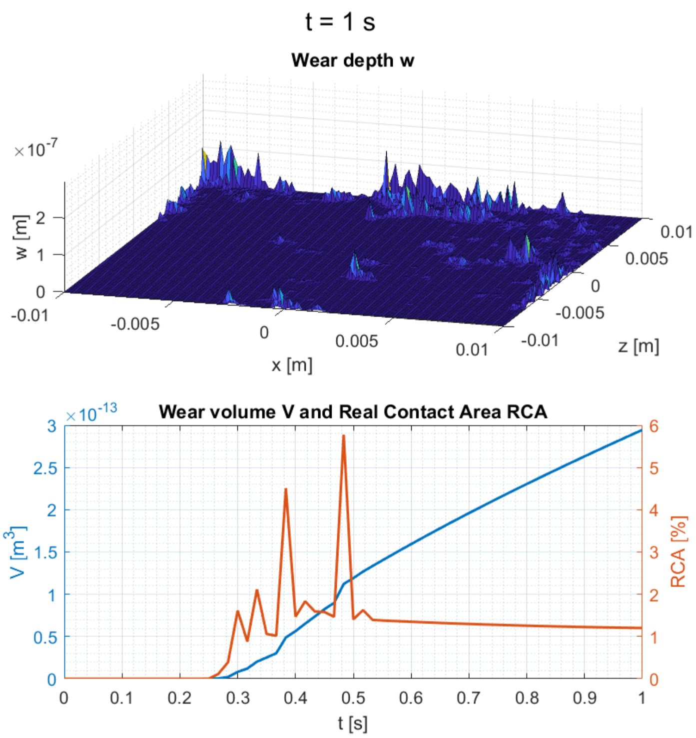

Figure 125 *Wear and Real Contact Area of the rough ML simulation*

The obtained small RCA at the end of the simulated time is better visible in the Figure 126 reporting the deformed surfaces, the fluid/contact pressure distribution and the deformed section at $z = 0$.

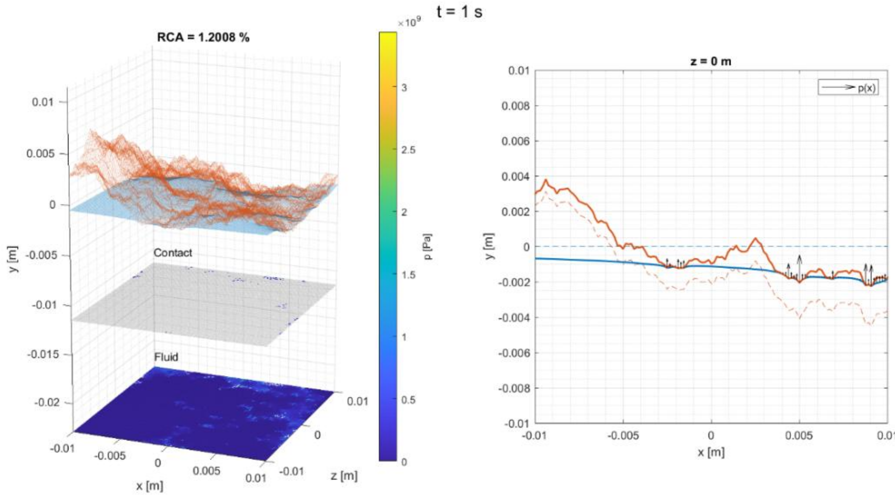

Figure 126 *Deformed surfaces and pressure distribution of the rough ML simulation*

In order to discuss about the role of the lubricant in the analysed ML regime establishing in the rough configuration, the same simulation for the same tribo-system is repeated in absence of fluid, i.e., with the DCM solver, and the results are compared; the DCM solver for a given approach and sliding velocity is obtained by simply set to zero the transition function θ all over the domain: in that way, the set of equations **G** drives the pressure (being only the contact one) to rise in the closed gap zones, while the cavitation constraint truncation will set to zero the pressure in the open gap ones respecting the LCCs.

First of all, the deformed surfaces are visualised in the Figure 127: it is evident that, in order to reproduce a pressure field similar to the ML case, the DCM regime has to demonstrate a larger RCA, in this case of about 14 %.

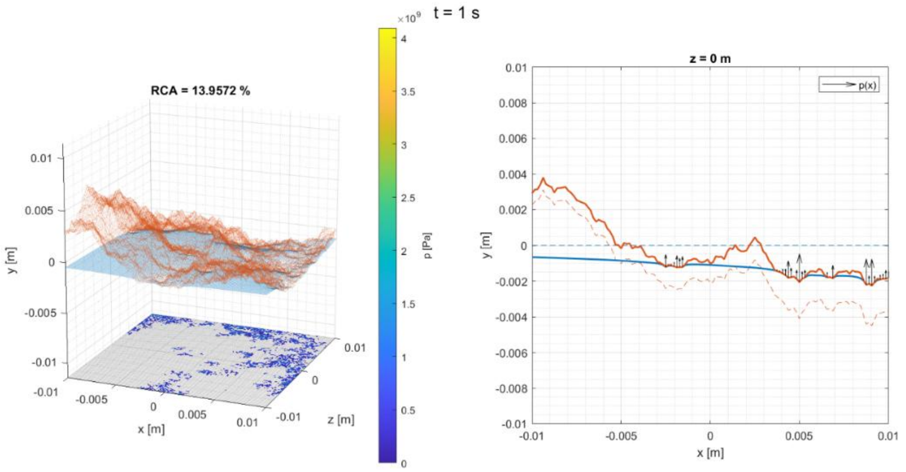

Figure 127 *Deformed surfaces and pressure distribution of the DCM rough simulation*

The DCM maximum pressure over the contact domain resulted to be slightly higher than the one shown by the ML case, while the minimum gap trend is basically identical, as reported in the Figure 128.

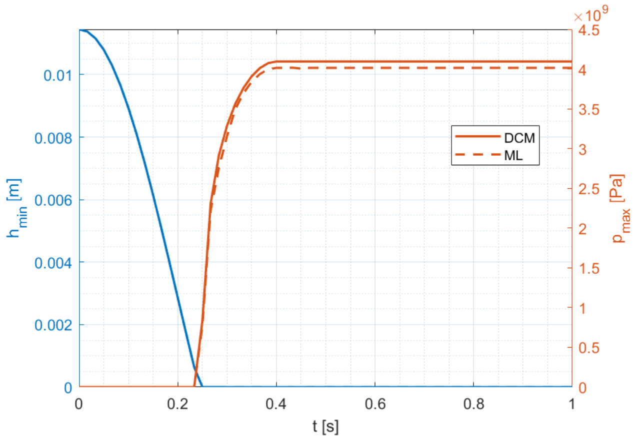

Figure 128 *Minimum gap and maximum pressure of the rough ML-DCM comparison*

While the DCM maximum pressure is higher than the ML one, the resulting load obtained by the pressure integration results to be slightly lower: this behaviour can be due to the fact that the ML pressure is composed by also a fluid contribution existing in the remaining lubricated zones, so, for the same approach δ, a more widespread pressure acting on a larger area turns into a higher load (of course for the chosen input data) as demonstrated by the Figure 129.

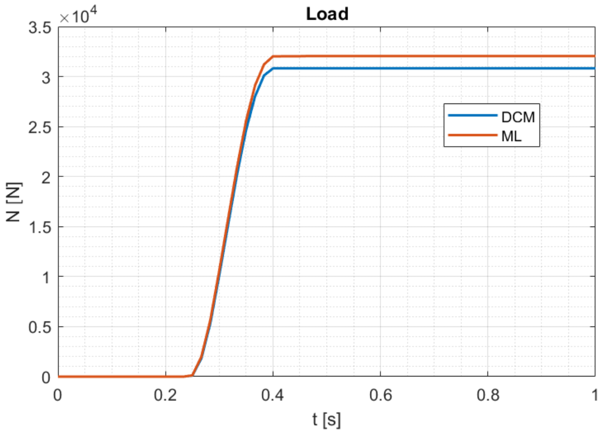

Figure 129 *Load of the rough ML-DCM comparison*

With reference to the Figure 130, the DCM RCA is not only higher than the ML one, but it also shows a smoother and regular increase, without the previous localised peaks, probably because the wear of the contacting asperities is not followed by the lubricant filling in the generated space; the DCM wear volume, even if dealing with the same sliding velocity and with a similar contact pressure with respect the ML case, is removed from a much larger contact area, so it is appreciably higher.

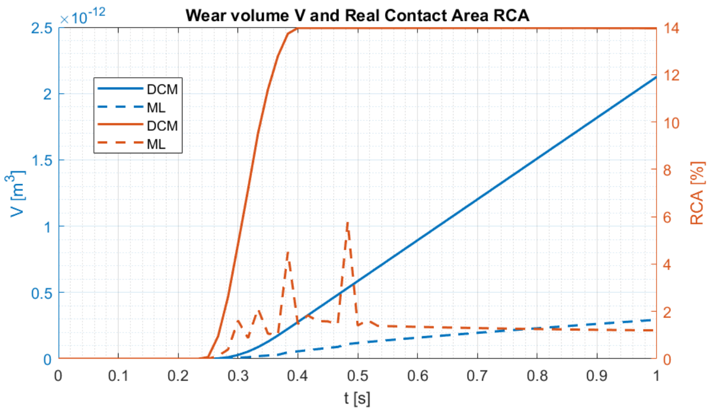

Figure 130 *Wear and Real Contact Area of the rough ML-DCM comparison*

Finally, the most interesting result (according to the author opinion) is shown in the Figure 131 reporting the pressure and gap fields for both the DCM and ML simulations; comparing the results the smoothing behaviour of the ML regime with respect to the DCM one is appreciable: the presence of the lubricant with a given viscosity and piezo-viscous rheological behaviour opens the some DCM closed gap zones imposing there a fluid pressure that resembles the contact one; this has two main effects:

- the obvious decrease of the RCA, in this case from 14 % to 1.2 %;
- the smoothing of both the pressure and the gap fields, where the former spreads over larger local areas as if the space surrounded by closed gap zones act like lubricant reservoirs ready to supply lubricant and fluid support to the imposed normal approach (or applied load), while the latter in the ML regime it's like it was filtered from the DCM configuration because of the effect of a smoother pressure field that, once convoluted by the Boussinesq deformation kernel, cuts the shortest wavelengths characterising the gap shape.

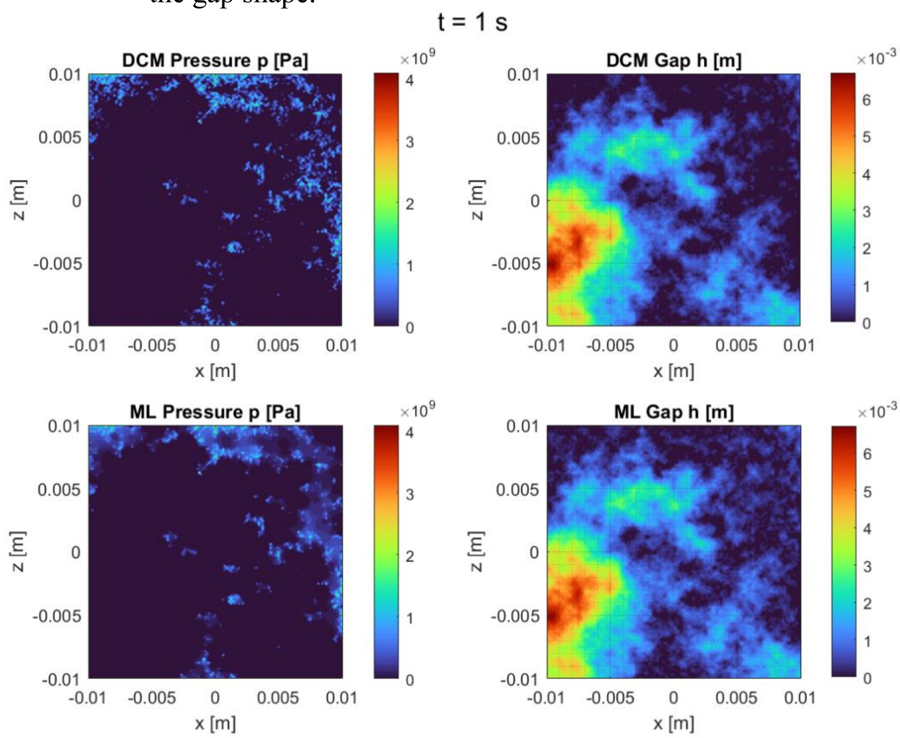

Figure 131 *Pressure and gap fields of the rough ML-DCM comparison*

At this point, all the tribological aspects studied in this work concerning the ML lubrication simulations were presented. The last topic that was addressed in this work, and presented in the next section, is the transient dynamics of the EHL tribo-systems described in the state-space dynamics form coming from the writing of a system of Differential Algebraic Equations (DAEs).

2.5. Transient Elasto-Hydrodynamic Lubrication

In this section, a computational approach to simulate the transient EHL evolution is presented: it is based on the writing of a unified system of DAEs composed by the Reynolds, the gap and the load balance governing equations that is numerically marched over time through its state-space description: this approach differs substantially from the well-established techniques based on the nested loop strategy (Venner, 1992; Huang, 2015; Habchi, 2018).

With respect to the THR framework, this developed approach is not related to a ML possibility, it does not refer to a spherical geometry nor to a 2D geometry, but it constitutes a preliminary effort to treat the EHL transient state with a more accurate approach with respect to the simple Backward Euler finite difference applied to the squeeze term and to numerically couple the lubrication, the gap and the load equations such that the lubrication states are simultaneously updated along a dynamic system marching: therefore, this approach is not ready yet to refer to a THR wear estimation, but, again, it will be deepened to make it adaptable to implants duration assessment.

Let refer to the 1D line-contact half-space tribo-system reported in the Figure 132 in which the upper cylinder of radius R is pushed by the means of the known time-varying applied load per unit length $w(t)$ against a plane moving with the known time-varying sliding velocity $U_x(t)$: the uncompressible piezo-viscous lubricant will deform the surfaces based on their elastic mechanical properties (Young moduli E_l, E_u and Poisson ratios ν_l, ν_u) and the balance between the lubricant pressure force and the applied load will govern the approach δ dynamics affected by the upper profile inertia given by its mass per unit length m.

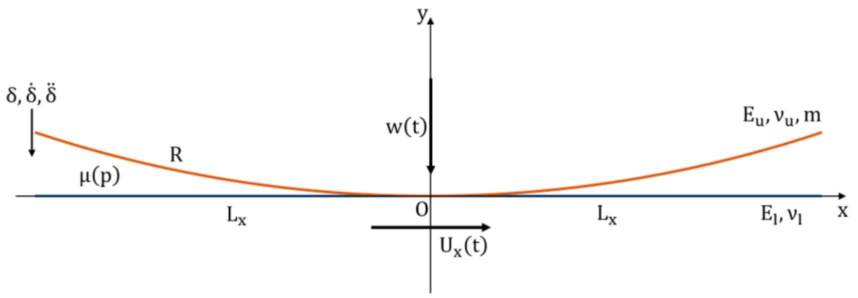

Figure 132 *Line-contact tribo-system*

The equations in (365) governing the described configuration are:

- the 1D Reynolds lubrication equations obtained by neglecting the transverse gradients and accounting for the Barus/Modulus piezo-viscous model;

- the 1D gap equation accounting for the Boussinesq convolution, the undeformed geometrical gap g and the approach δ;
- the load balance equation accounting for the upper profile inertial force.

Let note that the transient dynamical behaviour is given by both the squeeze term in the Reynolds equation and the inertial term in the load balance one (Almqvist, Almqvist and Larsson, 2004; Venner and Wijnant, 2005; Goodyer and Berzins, 2006; Hultqvist, 2020); furthermore, it is worth to realise that the assembled set of equations governs the dynamics of the unknown gap h, lubricant pressure p and approach δ for the given sliding velocity U_x and load w time inputs.

$$\mu(p) = \mu_0 e^{\frac{\alpha p}{1+\beta p}} \quad \frac{1}{E^*} = \frac{1-\nu_l^2}{E_l} + \frac{1-\nu_u^2}{E_u}$$

$$\begin{cases} \begin{cases} \dfrac{\partial}{\partial x}\left(\dfrac{h^3}{12\mu}\dfrac{\partial p}{\partial x}\right) = \dfrac{1}{2}U_x(t)\dfrac{\partial h}{\partial x} + \dfrac{\partial h}{\partial t} \\ p(-L_x, t) = p(L_x, t) = 0 \end{cases} \\ h(x,t) = -\dfrac{2}{\pi E^*}\displaystyle\int_\Omega \ln\left|\dfrac{x-\xi}{d_0}\right| p(\xi, t)\, d\xi + g(x) - \delta(t) \\ m\ddot{\delta} + \displaystyle\int_\Omega p(x,t)\, dx = w(t) \end{cases} \tag{365}$$

Knowing that the stationary EHL solution is related to the DCM one, the eqs. (365) are scaled with respect to the line-contact analytical Hertz solution (Hertz, 1882) in (366) as described in the previous chapter, where w_0 is a known nominal load.

$$a_H = \sqrt{\frac{4w_0 R}{\pi E^*}} \quad \delta_H = \frac{a_H^2}{R} \quad p_H = \frac{2w_0}{\pi a_H} \tag{366}$$

Let scale the involved quantities accordingly, with additions with respect to the DCM case reported in (367):

- the time is made dimensionless with respect to an unknown scaling time t_s;
- the viscosity is scaled with respect to its nominal value μ_0;
- the new dimensionless coefficients A and B are defined for the Barus/Modulus law;
- the dimensionless length L_X is defined as the fraction of the half domain length with respect to the contact half width.

$$\begin{aligned} &X = \frac{x}{a_H} \quad T = \frac{t}{t_s} \quad P = \frac{p}{p_H} \quad M = \frac{\mu}{\mu_0} \\ &H = \frac{h}{\delta_H} \quad G = \frac{h}{\delta_H} \quad \Delta = \frac{\delta}{\delta_H} \quad D_0 = \frac{d_0}{a_H} \end{aligned} \tag{367}$$

$$A = \alpha p_H \quad B = \beta p_H \quad L_X = \frac{L_x}{a_H}$$

The dimensionless governing equations are given in (368).

$$M(P) = e^{\frac{AP}{1+BP}}$$

$$\begin{cases} \begin{cases} \dfrac{\delta_H^2 p_H t_s}{12\mu_0 a_H^2}\dfrac{\partial}{\partial X}\left(\dfrac{H^3}{M}\dfrac{\partial P}{\partial X}\right) = U_x(t)\dfrac{t_s}{2a_H}\dfrac{\partial H}{\partial X} + \dfrac{\partial H}{\partial T} \\ P(-L_X, T) = P(L_X, T) = 0 \end{cases} \\ H(X,T) = -\dfrac{1}{\pi}\displaystyle\int_\Omega \ln\left|\dfrac{X-\Xi}{D_0}\right| P(\Xi,T)\,d\Xi + G(X) - \Delta(T) \\ \dfrac{m\delta_H}{t_s^2 p_H a_H}\ddot{\Delta} + \displaystyle\int_\Omega P(X,T)\,dX = \dfrac{\pi}{2w_0}w(t) \end{cases} \tag{368}$$

The scaling time t_s is found by imposing the dimensionless group in the load balance equation as unitary, while the remaining dimensionless group in the Reynolds equation is defined as λ; furthermore, the dimensionless sliding velocity σ and load W are given in (369).

$$t_s = \sqrt{\frac{2m}{E^*}} \quad \lambda = \frac{\delta_H^2 p_H t_s}{12\mu_0 a_H^2} \quad \sigma = U_x\frac{t_s}{2a_H} \quad W = \frac{\pi}{2}\frac{w}{w_0}$$

$$\begin{cases} \begin{cases} \lambda\dfrac{\partial}{\partial X}\left(\dfrac{H^3}{M}\dfrac{\partial P}{\partial X}\right) = \sigma(T)\dfrac{\partial H}{\partial X} + \dfrac{\partial H}{\partial T} \\ P(-L_X, T) = P(L_X, T) = 0 \end{cases} \\ H(X,T) = -\dfrac{1}{\pi}\displaystyle\int_\Omega \ln\left|\dfrac{X-\Xi}{D_0}\right| P(\Xi,T)\,d\Xi + G(X) - \Delta(T) \\ \ddot{\Delta} + \displaystyle\int_\Omega P(X,T)\,dX = W(T) \end{cases} \tag{369}$$

2.5.1. *Spatial discretization and state-space formulation*

Let spatially discretize the equations according to the 1D x-grid reported in (370) dealing with the spatial i index defining N discrete points with uniform spacing ΔX.

$$i = 0, \dots, N-1 \quad \Delta X = \frac{2L_X}{N-1} \quad X_i = -L_X + i\Delta X \tag{370}$$

The FDM discretization of the Reynolds equation (LeVeque, 2007) requires the usual stencil version of the general discrete field y_i, given by the vector $\mathbf{y}_X$, and the backward/forward mean and derivatives vector operators, i.e., $\mathbf{m}_-$, $\mathbf{m}_+$, $\mathbf{d}_{X^-}$ and $\mathbf{d}_{X^+}$, reported in (371).

$$\mathbf{y}_X = [y_{i-1} \quad y_i \quad y_{i+1}]^T \tag{371}$$

$$\mathbf{m}_- = \frac{[1 \quad 1 \quad 0]^{\mathrm{T}}}{2} \quad \mathbf{m}_+ = \frac{[0 \quad 1 \quad 1]^{\mathrm{T}}}{2}$$
$$\mathbf{d}_{\mathrm{X}^-} = \frac{[-1 \quad 1 \quad 0]^{\mathrm{T}}}{\Delta \mathrm{X}} \quad \mathbf{d}_{\mathrm{X}^+} = \frac{[0 \quad -1 \quad 1]^{\mathrm{T}}}{\Delta \mathrm{X}}$$

Let recall in (372) the second order like [3,3] derivative matrix $\mathbf{D}_{2\mathrm{X}}$ and the first order derivative vector $\mathbf{d}_{\mathrm{X}}$ considering the upwind scheme for the Couette convective term.

$$\mathbf{D}_{2\mathrm{X}} = \frac{\mathbf{m}_+ \mathbf{d}_{\mathrm{X}^+}^{\mathrm{T}} - \mathbf{m}_- \mathbf{d}_{\mathrm{X}^-}^{\mathrm{T}}}{\Delta \mathrm{X}} \quad \mathbf{d}_{\mathrm{X}} = \begin{cases} \mathbf{d}_{\mathrm{X}^-} & \sigma(\mathrm{T}) > 0 \\ \mathbf{d}_{\mathrm{X}^+} & \sigma(\mathrm{T}) < 0 \end{cases} \tag{372}$$

Then, the FDM discrete Reynolds equation is given in (373).

$$\mathrm{E} = \frac{\mathrm{H}^3}{\mathrm{M}} \rightarrow \begin{cases} \lambda \mathbf{E}_{\mathrm{X}}^{\mathrm{T}} \mathbf{D}_{2\mathrm{X}} \mathbf{P}_{\mathrm{X}} = \sigma(\mathrm{T}) \mathbf{d}_{\mathrm{X}}^{\mathrm{T}} \mathbf{H}_{\mathrm{X}} + \dfrac{\partial \mathrm{H}_{\mathrm{i}}}{\partial \mathrm{T}} \\ \mathrm{P}_0(\mathrm{T}) = \mathrm{P}_{\mathrm{N}-1}(\mathrm{T}) = 0 \end{cases} \tag{373}$$

The Boussinesq convolution in the gap equation is discretised with the BEM (Johnson, 1987) (and evaluated with the FFT approach (Wang *et al.*, 2003)) providing the compliance kernel matrix K_{ij} given in (374).

$$\mathrm{K}_{\mathrm{ij}} = -\frac{1}{\pi} \begin{bmatrix} \left(\mathrm{X}_{\mathrm{i}} - \mathrm{X}_{\mathrm{j}} + \dfrac{\Delta \mathrm{X}}{2}\right)\left(\ln\left|\mathrm{X}_{\mathrm{i}} - \mathrm{X}_{\mathrm{j}} + \dfrac{\Delta \mathrm{X}}{2}\right| - 1\right) + \cdots \\ \ldots - \left(\mathrm{X}_{\mathrm{i}} - \mathrm{X}_{\mathrm{j}} - \dfrac{\Delta \mathrm{X}}{2}\right)\left(\ln\left|\mathrm{X}_{\mathrm{i}} - \mathrm{X}_{\mathrm{j}} - \dfrac{\Delta \mathrm{X}}{2}\right| - 1\right) + \cdots \\ \ldots - \Delta \mathrm{X}(\ln|\mathrm{D}_0| + 1) \end{bmatrix} \tag{374}$$

Then, the discretised gap equation is reported in (375) where the i row of the kernel K_{ij} is denoted by the vector $\mathbf{K}_{\mathrm{i}}$.

$$\mathrm{H}_{\mathrm{i}}(\mathrm{T}) = \mathbf{K}_{\mathrm{i}}^{\mathrm{T}} \mathbf{P}(\mathrm{T}) + \mathrm{G}_{\mathrm{i}} - \Delta(\mathrm{T}) \tag{375}$$

Finally, the load balance equation is given in (376) where the lubricant pressure integral is provided by the trapezoidal integration vector $\mathbf{t}_{\mathrm{X}}$.

$$\mathbf{t}_{\mathrm{X}} = \Delta \mathrm{X} \begin{bmatrix} \dfrac{1}{2} & 1 & \cdots & 1 & \dfrac{1}{2} \end{bmatrix}^{\mathrm{T}} \rightarrow \ddot{\Delta} + \mathbf{t}_{\mathrm{X}}^{\mathrm{T}} \mathbf{P}(\mathrm{T}) = \mathrm{W}(\mathrm{T}) \tag{376}$$

The $(2\mathrm{N} + 1)$ discrete equations governing the EHL of line-contact tribo-systems are resumed in (377) in the N pressure values, N gap values and 1 approach value unknowns.

$$\begin{cases} \begin{cases} \lambda \mathbf{E}_{\mathrm{X}}^{\mathrm{T}} \mathbf{D}_{2\mathrm{X}} \mathbf{P}_{\mathrm{X}} = \sigma(\mathrm{T}) \mathbf{d}_{\mathrm{X}}^{\mathrm{T}} \mathbf{H}_{\mathrm{X}} + \dfrac{\partial \mathrm{H}_{\mathrm{i}}}{\partial \mathrm{T}} \\ \mathrm{P}_0(\mathrm{T}) = \mathrm{P}_{\mathrm{N}-1}(\mathrm{T}) = 0 \end{cases} \\ \mathrm{H}_{\mathrm{i}}(\mathrm{T}) = \mathbf{K}_{\mathrm{i}}^{\mathrm{T}} \mathbf{P}(\mathrm{T}) + \mathrm{G}_{\mathrm{i}} - \Delta(\mathrm{T}) \\ \ddot{\Delta} + \mathbf{t}_{\mathrm{X}}^{\mathrm{T}} \mathbf{P}(\mathrm{T}) = \mathrm{W}(\mathrm{T}) \end{cases} \tag{377}$$

Let defining in (378) the fluid dynamics function F_{i} devoted to the surfaces' lubrication, the solid mechanics function S_{i} devoted to the surfaces' deformation and the load function L devoted to the tribo-system normal equilibrium.

$$\begin{cases} \mathrm{F_i}(\mathbf{H}_\mathrm{X}, \mathbf{P}_\mathrm{X}, \mathrm{T}) = \begin{cases} \lambda \mathbf{E}_\mathrm{X}^\mathrm{T} \mathbf{D}_{2\mathrm{X}} \mathbf{P}_\mathrm{X} - \sigma(\mathrm{T}) \mathbf{d}_\mathrm{X}^\mathrm{T} \mathbf{H}_\mathrm{X} \\ \mathrm{P_0}, \mathrm{P_{N-1}} \end{cases} \\ \mathrm{S_i}(\mathrm{H_i}, \mathbf{P}, \Delta) = \mathrm{H_i} - \mathbf{K}_\mathrm{i}^\mathrm{T} \mathbf{P} - \mathrm{G_i} + \Delta \\ \mathrm{L}(\mathbf{P}, \mathrm{T}) = \mathrm{W}(\mathrm{T}) - \mathbf{t}_\mathrm{X}^\mathrm{T} \mathbf{P} \end{cases} \tag{378}$$

Substituting the (378) in (377), the 1D EHL DAE system in vector form is given in (379), where:

- the fluid function $\mathbf{F}$ governs the dynamics of the gap $\mathbf{H}$ differential variable (the $[\mathrm{N}, \mathrm{N}]$ identity matrix $\mathbf{I}_\mathrm{H}$ is introduced in order to respect the algebraic equations devoted the null lubricant pressure boundary conditions);
- the solid function $\mathbf{S}$ governs the dynamics of the pressure $\mathbf{P}$ algebraic variable;
- the load function L governs the dynamics of the approach Δ differential variable.

The obtained DAE system is semi-explicit and has index 1 (Wanner and Hairer, 1996), meaning that the algebraic equations have to be differentiated once to obtain the algebraic variable derivative and, as a consequence, a system of Ordinary Differential Equations (ODEs).

$$\mathbf{I}_\mathrm{H} = \begin{bmatrix} 0 & & \cdots & & 0 \\ & 1 & \cdots & 0 & \\ \vdots & \vdots & \ddots & \vdots & \vdots \\ & 0 & \cdots & 1 & \\ 0 & & \cdots & & 0 \end{bmatrix} \rightarrow \begin{cases} \mathbf{I}_\mathrm{H} \dfrac{\partial \mathbf{H}}{\partial \mathrm{T}} = \mathbf{F}(\mathbf{H}, \mathbf{P}, \mathrm{T}) \\ \mathbf{0} = \mathbf{S}(\mathbf{H}, \mathbf{P}, \Delta) \\ \ddot{\Delta} = \mathrm{L}(\mathbf{P}, \mathrm{T}) \end{cases} \tag{379}$$

Let write the (379) in the space-state form in (380), defining the states vector $\mathbf{u}$ composed by the gap $\mathbf{H}$, the pressure $\mathbf{P}$, the approach Δ and the approach velocity $\dot{\Delta}$, the fluid-solid-load source function of the states and of the time $\mathbf{\Phi}$ and the singular identity matrix $\mathbf{C}$ identifying the differential equations and the algebraic ones: the obtained system is now a singular ODE set (Wanner and Hairer, 1996).

$$\begin{bmatrix} \mathbf{I}_\mathrm{H} & \mathbf{0} & \mathbf{0} & \mathbf{0} \\ \mathbf{0} & \mathbf{0} & \mathbf{0} & \mathbf{0} \\ \mathbf{0}^\mathrm{T} & \mathbf{0}^\mathrm{T} & 1 & 0 \\ \mathbf{0}^\mathrm{T} & \mathbf{0}^\mathrm{T} & 0 & 1 \end{bmatrix} \frac{\partial}{\partial \mathrm{T}} \begin{bmatrix} \mathbf{H} \\ \mathbf{P} \\ \Delta \\ \dot{\Delta} \end{bmatrix} = \begin{bmatrix} \mathbf{F}(\mathbf{H}, \mathbf{P}, \mathrm{T}) \\ \mathbf{S}(\mathbf{H}, \mathbf{P}, \Delta) \\ \dot{\Delta} \\ \mathrm{L}(\mathbf{P}, \mathrm{T}) \end{bmatrix} \rightarrow \quad \mathbf{C}\dot{\mathbf{u}} = \mathbf{\Phi}(\mathbf{u}, \mathrm{T}) \tag{380}$$

Let find in (381) the fluid-solid-load functions in (378) derivatives with respect to the states.

$$\begin{gathered} \frac{\partial \mathrm{F_i}}{\partial \mathbf{H}_\mathrm{X}}(\mathbf{H}_\mathrm{X}, \mathbf{P}_\mathrm{X}, \mathrm{T}) = \begin{cases} \lambda \mathbf{P}_\mathrm{X}^\mathrm{T} \mathbf{D}_{2\mathrm{X}}^\mathrm{T} \dfrac{\partial \mathbf{E}_\mathrm{X}}{\partial \mathbf{H}_\mathrm{X}} - \sigma(\mathrm{T}) \mathbf{d}_\mathrm{X}^\mathrm{T} \\ 0 \end{cases} \\ \frac{\partial \mathrm{F_i}}{\partial \mathbf{P}_\mathrm{X}}(\mathbf{H}_\mathrm{X}, \mathbf{P}_\mathrm{X}) = \begin{cases} \lambda \left(\mathbf{E}_\mathrm{X}^\mathrm{T} \mathbf{D}_{2\mathrm{X}} + \mathbf{P}_\mathrm{X}^\mathrm{T} \mathbf{D}_{2\mathrm{X}}^\mathrm{T} \dfrac{\partial \mathbf{E}_\mathrm{X}}{\partial \mathbf{P}_\mathrm{X}} \right) \\ 1 \end{cases} \\ \frac{\partial \mathrm{S_i}}{\partial \mathrm{H_i}} = 1 \quad \frac{\partial \mathrm{S_i}}{\partial \mathbf{P}} = -\mathbf{K}_\mathrm{i}^\mathrm{T} \quad \frac{\partial \mathrm{S_i}}{\partial \Delta} = 1 \quad \frac{\partial \mathrm{L}}{\partial \mathbf{P}} = -\mathbf{t}_\mathrm{X}^\mathrm{T} \end{gathered} \tag{381}$$

The derivatives in (382) in vector form constitute the Jacobian of the source function $\mathbf{\Phi}$, i.e., $\mathbf{\Phi_u}$, with the following structure reported in (382):

- the blocks referred to the fluid function derivatives with respect to the gap and to the pressure, i.e., $\mathbf{F_H}$ and $\mathbf{F_P}$, are $[\mathrm{N},\mathrm{N}]$ tridiagonal matrices;
- the block referred to the solid function derivative with respect to the gap is the $[\mathrm{N},\mathrm{N}]$ identity matrix;
- the block referred to the solid function derivative with respect to the pressure is the negative kernel compliance matrix $\mathbf{K}$;
- the block referred to the solid function derivative with respect to the approach is a $[\mathrm{N},1]$ vector full of ones;
- the block referred to the load function derivative with respect to the pressure is the negative transposed trapezoidal integration vector $\mathbf{t}_\mathrm{X}$.

$$\mathbf{\Phi_u}(\mathbf{u},\mathrm{T}) = \begin{bmatrix} \mathbf{F_H}(\mathbf{H},\mathbf{P},\mathrm{T}) & \mathbf{F_P}(\mathbf{H},\mathbf{P}) & \mathbf{0} & \mathbf{0} \\ \mathbf{I} & -\mathbf{K} & \mathbf{1} & \mathbf{0} \\ \mathbf{0}^\mathrm{T} & \mathbf{0}^\mathrm{T} & 0 & 1 \\ \mathbf{0}^\mathrm{T} & -\mathbf{t}_\mathrm{X}^\mathrm{T} & 0 & 0 \end{bmatrix} \tag{382}$$

Before proceeding with the transient simulative formulation of the assembled DAE system, let realise the computational advantages of the state-space approach even in the stationary case: the EHL stationarity in correspondence of a feasible time instant T^* is given by switching off the squeeze term in the Reynolds equation and the inertial term in the load balance equation, i.e., by switching off the states $\mathbf{u}$ time derivative, leading to the non-linear system of equations reported in (383) represented by the source function $\mathbf{\Phi}$.

$$\mathbf{\Phi}(\mathbf{u},\mathrm{T}^*) = \mathbf{0} \tag{383}$$

The stationary 1D EHL problem in (383) can be solved with the Newton iterative method (damped by the relaxation factor ω) in (384) by updating simultaneously the states $\mathbf{u}$ avoiding the expensive and possibly unstable nested loop strategy; the main computational difficulty stays in the Jacobian block related to the solid function derivative with respect to the pressure, i.e., the full dense compliance matrix $\mathbf{K}$ (easy to assemble due to its Toeplitz form, but giving troubles during the Jacobian $\mathbf{\Phi_u}$ inversion): in order to overcome that issue, in this work this sub-block is replaced by its diagonal form, since, as explained during the BEM formulation, the main diagonal of $\mathbf{K}$ is composed by the maximum value of the kernel matrix K_{00} providing the major contribution to the solid function $\mathbf{S}$ variation in response to the lubricant pressure $\mathbf{P}$ one; basically, it is a computational strategy that adopts the faster local Jacobi approach in correspondence of the solid function variation with respect to the pressure, while keeping the more robust Newton update elsewhere. It is worth to note that the most useful starting state trial is the one referred to the stationary DCM solution (explained in the related chapter), since it is the solution closest to the stationary EHL one. The structure of the mostly diagonal Jacobian is reported in the Figure 133.

$$\boldsymbol{\Phi}_{\mathbf{u}}(\mathbf{u},\mathrm{T}^*) = \begin{bmatrix} \mathbf{F}_{\mathbf{H}}(\mathbf{H},\mathbf{P},\mathrm{T}^*) & \mathbf{F}_{\mathbf{P}}(\mathbf{H},\mathbf{P}) & \mathbf{0} & \mathbf{0} \\ \mathbf{I} & -\mathrm{K}_{00}\mathbf{I} & \mathbf{1} & \mathbf{0} \\ \mathbf{0}^{\mathrm{T}} & \mathbf{0}^{\mathrm{T}} & 0 & 1 \\ \mathbf{0}^{\mathrm{T}} & -\mathbf{t}_{\mathrm{X}}^{\mathrm{T}} & 0 & 0 \end{bmatrix} \tag{384}$$

$$\mathbf{u}^{(\mathrm{k}+1)} = \mathbf{u}^{(\mathrm{k})} - \omega\left[\boldsymbol{\Phi}_{\mathbf{u}}\left(\mathbf{u}^{(\mathrm{k})},\mathrm{T}^*\right)\right]^{-1}\boldsymbol{\Phi}\left(\mathbf{u}^{(\mathrm{k})},\mathrm{T}^*\right)$$

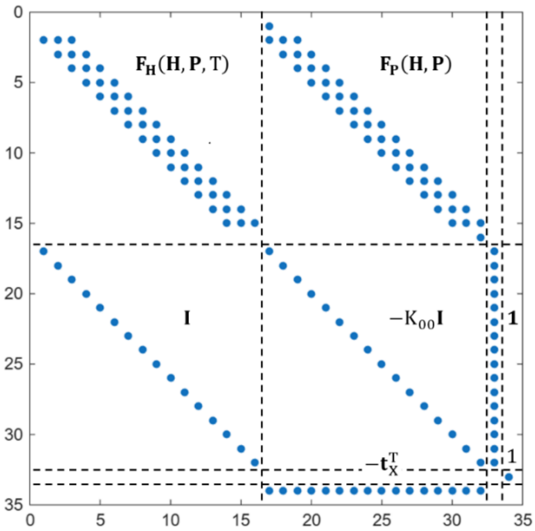

Figure 133 *1D EHL source function Jacobian*

The same computational strategy is adopted in the context of the transient EHL simulation; first of all, the singular ODE system in (380) has to be coupled with the states Initial Conditions (ICs) $\mathbf{u}_0$: in a system of DAEs the ICs have to respect the algebraic equations at the initial instant $\mathrm{T} = 0$ in order to achieve numerical consistency (Wanner and Hairer, 1996); in this case, the algebraic constraints are the null lubricant pressure at the boundaries and the gap equation reported in (385).

$$\begin{cases} \mathrm{P}_0(0) = \mathrm{P}_{\mathrm{N}-1}(0) = 0 \\ \mathbf{S}\big(\mathbf{H}(0),\mathbf{P}(0),\Delta(0)\big) = 0 \end{cases} \rightarrow \mathbf{u}_0 = \begin{bmatrix} \mathbf{H}(0) \\ \mathbf{P}(0) \\ \Delta(0) \\ \dot{\Delta}(0) \end{bmatrix} \rightarrow \begin{cases} \mathbf{C}\dot{\mathbf{u}} = \boldsymbol{\Phi}(\mathbf{u},\mathrm{T}) \\ \mathbf{u}(0) = \mathbf{u}_0 \end{cases} \tag{385}$$

In order to respect the EHL DAE system consistency, the ICs $\mathbf{u}_0$ can be of two types reported in (386):

- the rest ICs $\mathbf{u}_\mathrm{r}$ given by zero pressure, a chosen starting approach Δ_0 and a null approach velocity;
- the stationary ICs $\mathbf{u}_\mathrm{s}$ coming from a steady-state phase, respecting then, by definition, the algebraic constraints.

$$\mathbf{u}_\mathrm{r} = \begin{bmatrix} \mathbf{G} - \Delta_0 \\ \mathbf{0} \\ \Delta_0 \\ 0 \end{bmatrix} \qquad \boldsymbol{\Phi}(\mathbf{u}_\mathrm{s}, 0) = \mathbf{0} \tag{386}$$

2.5.2. *Time discretization and DAE marching*

Let proceed now to the time discretization to start the time marching, noting that, until now, the time derivative operator was a simple Backward Euler finite difference applied to the Reynolds equation squeeze term; in this work the multi-stage Runge-Kutta marching methods are chosen (Wanner and Hairer, 1996; LeVeque, 2007). The uniform time grid is given in (387) by the temporal index n, the uniform step size $\Delta\mathrm{T}$ and the discrete instants T^n, together with the general s-stages Runge-Kutta intermediary steps $\mathbf{u}^{\mathrm{n}+\mathrm{c}_\mathrm{i}}$ and the solution one $\mathbf{u}^{\mathrm{n}+1}$: the Runge-Kutta method divides the time step $\Delta\mathrm{T}$ in s nodes c_i in which the solution $\mathbf{u}$ derivative is assumed to be a linear combination of the source function $\boldsymbol{\Phi}$ evaluated in that intermediary nodes through the coefficients a_{ij}, then it evaluates the solution derivative around the whole time step by averaging the intermediary stages source function with the weights b_i.

$$\mathrm{n} = 0, \dots, \mathrm{M}-1 \quad \Delta\mathrm{T} = \frac{\mathrm{L}_\mathrm{T}}{\mathrm{M}-1} \quad \mathrm{T}^\mathrm{n} = \mathrm{n}\Delta\mathrm{T}$$
$$\begin{cases} \mathbf{C}\dfrac{\mathbf{u}^{\mathrm{n}+\mathrm{c}_\mathrm{i}} - \mathbf{u}^\mathrm{n}}{\Delta\mathrm{T}} = \displaystyle\sum_{\mathrm{j}=1}^{\mathrm{s}} \mathrm{a}_{\mathrm{ij}} \boldsymbol{\Phi}\left(\mathbf{u}^{\mathrm{n}+\mathrm{c}_\mathrm{j}}, \mathrm{T}^\mathrm{n} + \mathrm{c}_\mathrm{j}\Delta\mathrm{T}\right) \qquad \mathrm{i} = 1, \dots, \mathrm{s} \\ \mathbf{C}\dfrac{\mathbf{u}^{\mathrm{n}+1} - \mathbf{u}^\mathrm{n}}{\Delta\mathrm{T}} = \displaystyle\sum_{\mathrm{i}=1}^{\mathrm{s}} \mathrm{b}_\mathrm{i} \boldsymbol{\Phi}(\mathbf{u}^{\mathrm{n}+\mathrm{c}_\mathrm{i}}, \mathrm{T}^\mathrm{n} + \mathrm{c}_\mathrm{i}\Delta\mathrm{T}) \end{cases} \tag{387}$$

Let focus on the s intermediary stages: due to the impossibility to invert the singular matrix $\mathbf{C}$, only the Implicit Runge-Kutta (IRK) methods can be used in the context of DAE simulations, meaning that the Runge-Kutta coefficients a_{ij} matrix cannot be lower triangular with zero main diagonal, i.e., an explicit Runge-Kutta method: then, the two possible solutions are represented by the general full IRKs and by the Diagonal IRKs (DIRKs) reported in the Table 4 in their Butcher tableau form (Alexander, 1977; Kennedy and Carpenter, 2016).

Table 5 *Full and Diagonal IRK tableaus*

Full IRK	Diagonal IRK

$$
\begin{array}{c|ccccc}
c_1 & a_{11} & \cdots & a_{1i} & \cdots & a_{1s} \\
\vdots & \vdots & & \vdots & & \vdots \\
c_i & a_{i1} & \cdots & a_{ii} & \cdots & a_{is} \\
\vdots & \vdots & & \vdots & & \vdots \\
c_s & a_{s1} & \cdots & a_{si} & \cdots & a_{ss} \\
\hline
 & b_1 & \cdots & b_i & \cdots & b_s
\end{array}
\qquad
\begin{array}{c|ccccc}
c_1 & a_{11} & & & & \\
\vdots & \vdots & \ddots & & & \\
c_i & a_{i1} & \cdots & a_{ii} & & \\
\vdots & \vdots & & \vdots & \ddots & \\
c_s & a_{s1} & \cdots & a_{si} & \cdots & a_{ss} \\
\hline
 & b_1 & \cdots & b_i & \cdots & b_s
\end{array}
$$

Starting from the full IRK case, due to the dense Runge-Kutta coefficients a_{ij} matrix, the intermediary stages have to be solved at once: defining as $\mathbf{x}$ the unknown vector composed by the intermediary stage increments $\mathbf{x}_i$ from the previous states $\mathbf{u}^n$, the $s(2N+2)$ long set of equations $\mathbf{f}$, composed by the intermediary residuals $\mathbf{f}_i$ to be simultaneously solved, is reported in (388).

$$
\begin{aligned}
&\mathbf{x} = \begin{bmatrix} \vdots \\ \mathbf{x}_i = \mathbf{u}^{n+c_i} - \mathbf{u}^n \\ \vdots \end{bmatrix} \\
&\mathbf{f}(\mathbf{x}) = \begin{bmatrix} \vdots \\ \mathbf{f}_i(\mathbf{x}) = \mathbf{C}\dfrac{\mathbf{x}_i}{\Delta T} - \displaystyle\sum_{j=1}^{s} a_{ij}\boldsymbol{\Phi}\left(\mathbf{x}_j + \mathbf{u}^n, T^n + c_j\Delta T\right) \\ \vdots \end{bmatrix} = \mathbf{0}
\end{aligned}
\tag{388}
$$

The solution of (388) can be obtained by the Newton method relying on the Jacobian $\mathbf{f}_\mathbf{x}$, which is assembled by its subblocks reported in (389) accounting for the Kronecker delta δ_{ij} and the source function Jacobian $\boldsymbol{\Phi}_\mathbf{u}$.

$$
\begin{aligned}
&\frac{\partial \mathbf{f}_i}{\partial \mathbf{x}_j}(\mathbf{x}) = \mathbf{C}\frac{1}{\Delta T}\delta_{ij} - a_{ij}\boldsymbol{\Phi}_\mathbf{u}\left(\mathbf{x}_j + \mathbf{u}^n, T^n + c_j\Delta T\right) \\
&\mathbf{f}_\mathbf{x}(\mathbf{x}) = \begin{bmatrix} & \vdots & \\ \cdots & \dfrac{\partial \mathbf{f}_i}{\partial \mathbf{x}_j} & \cdots \\ & \vdots & \end{bmatrix} \\
&\mathbf{x}^{(k+1)} = \mathbf{x}^{(k)} - \omega\left[\mathbf{f}_\mathbf{x}\left(\mathbf{x}^{(k)}\right)\right]^{-1}\mathbf{f}\left(\mathbf{x}^{(k)}\right)
\end{aligned}
\tag{389}
$$

The inversion of the big $[s(2N+2), s(2N+2)]$ Jacobian matrix $\mathbf{f}_\mathbf{x}$ can be avoided in the case of a DIRK method: the triangularity of the Runge-Kutta coefficients a_{ij} matrix allows to split the $\mathbf{f}$ simultaneous problem into the $\mathbf{f}_i$ sequential problems with size $(2N+2)$ in the unknown current stage increment $\mathbf{x}_i$, since the previous stages $\mathbf{x}_{j<i}$ are already solved and the coefficients $a_{i,j>i}$ are zero; the DIRK intermediary stage is reported in (390), together with the related Newton solver.

$$
\mathbf{C}\frac{\mathbf{u}^{n+c_i} - \mathbf{u}^n}{\Delta T} = \sum_{j=1}^{i} a_{ij}\boldsymbol{\Phi}\left(\mathbf{u}^{n+c_j}, T^n + c_j\Delta T\right) \tag{390}
$$

$$\mathbf{f}_i(\mathbf{x}_i) = \mathbf{C}\frac{\mathbf{x}_i}{\Delta T} - \sum_{j=1}^{i} a_{ij}\mathbf{\Phi}\left(\mathbf{x}_j + \mathbf{u}^n, T^n + c_j\Delta T\right)$$
$$\frac{\partial \mathbf{f}_i}{\partial \mathbf{x}_i}(\mathbf{x}_i) = \mathbf{C}\frac{1}{\Delta T} - a_{ii}\mathbf{\Phi}_{\mathbf{u}}(\mathbf{x}_i + \mathbf{u}^n, T^n + c_i\Delta T)$$
$$\mathbf{x}_i^{(k+1)} = \mathbf{x}_i^{(k)} - \omega\left[\frac{\partial \mathbf{f}_i}{\partial \mathbf{x}_i}\left(\mathbf{x}_i^{(k)}\right)\right]^{-1}\mathbf{f}_i\left(\mathbf{x}_i^{(k)}\right)$$

Let move to the solution stage which explicitly provides the new states $\mathbf{u}^{n+1}$ by the previously described weighted sum: also in this case, the invertibility of the singular matrix $\mathbf{C}$ does not allow to proceed, unless the following two conditions are met.

The first condition is verified when the Runge-Kutta coefficients a_{ij} matrix is non-singular: in that case the intermediary stage can be inverted by introducing in (391) the inverse of a_{ij}, i.e., ω_{ij}, to evaluate the source function $\mathbf{\Phi}$ in the i node as a linear combination of the states $\mathbf{u}$ derivatives on all the intermediary nodes (Wanner and Hairer, 1996).

$$\begin{gathered}\mathbf{C}\frac{\mathbf{u}^{n+c_i} - \mathbf{u}^n}{\Delta T} = \sum_{j=1}^{s} a_{ij}\mathbf{\Phi}\left(\mathbf{u}^{n+c_j}, T^n + c_j\Delta T\right)\\ \sum_{j=1}^{s}\omega_{ij}\mathbf{C}\frac{\mathbf{u}^{n+c_j} - \mathbf{u}^n}{\Delta T} = \mathbf{\Phi}(\mathbf{u}^{n+c_i}, T^n + c_i\Delta T)\end{gathered} \tag{391}$$

Then, the found source function in the i node can be substituted in the explicit step in (392) allowing to simplify the singular matrix $\mathbf{C}$ and the time step ΔT.

$$\begin{gathered}\mathbf{C}\frac{\mathbf{u}^{n+1} - \mathbf{u}^n}{\Delta T} = \sum_{i=1}^{s} b_i \sum_{j=1}^{s}\omega_{ij}\mathbf{C}\frac{\mathbf{u}^{n+c_j} - \mathbf{u}^n}{\Delta T}\\ \mathbf{u}^{n+1} - \mathbf{u}^n = \sum_{j=1}^{s}\left(\sum_{i=1}^{s} b_i\omega_{ij}\right)(\mathbf{u}^{n+c_j} - \mathbf{u}^n)\end{gathered} \tag{392}$$

The remaining summation in parenthesis is defined as a new set of weights d_j obtained in (393) from the inversion of the non-singular Runge-Kutta coefficients matrix $\mathbf{A}$ and the original weights vector $\mathbf{b}$.

$$d_j = \sum_{i=1}^{s} b_i\omega_{ij} \quad \rightarrow \quad \mathbf{d}^T = \mathbf{b}^T\mathbf{A}^{-1} \tag{393}$$

At this point, the IRK explicit step allows to evaluate the next states $\mathbf{u}^{n+1}$ as the simple linear combination of the intermediary stages increment (Wanner and Hairer, 1996) given in (394).

$$\mathbf{u}^{n+1} = \mathbf{u}^n + \sum_{j=1}^{s} d_j\mathbf{x}_j \tag{394}$$

The second condition is met when the last row of the Runge-Kutta coefficients matrix **A** is equal to the weights vector **b**: in this case, the next states $\mathbf{u}^{n+1}$ actually are the last intermediary stage; in fact, due to the Runge-Kutta method consistency, the sum of the matrix **A** rows has to be equal to the nodes vector **c** and, of course, the sum of the weights **b** has to be unitary, meaning that a so-called stiffly accurate method last node corresponds to the new time instant (Wanner and Hairer, 1996). In the Table 5, the structure of a stiffly accurate IRK tableau is reported. The advantage of a stiffly accurate IRK method for DAE simulations stays in the possibility to impose the algebraic equations exactly on the used time grid discrete instants.

Table 6 *Stiffly accurate IRK tableau*

$$
\begin{array}{c|ccccc}
c_1 & a_{11} & \cdots & a_{1i} & \cdots & a_{1s} \\
\vdots & \vdots & & \vdots & & \vdots \\
c_i & a_{i1} & \cdots & a_{ii} & \cdots & a_{is} \\
\vdots & \vdots & & \vdots & & \vdots \\
1 & b_1 & \cdots & b_i & \cdots & b_s \\
\hline
 & b_1 & \cdots & b_i & \cdots & b_s
\end{array}
$$

In the stiffly accurate case, the new step can be evaluated as reported in (395).

$$\mathbf{u}^{n+1} = \mathbf{u}^n + \mathbf{x}_s \tag{395}$$

The (395) simplification can be adopted whether the Runge-Kutta matrix **A** is singular or not: the class of IRKs that can be adopted in this context with a singular **A** matrix is characterised by stiffly accurate methods with a null first row of **A**, for both the full and the diagonal IRKs reported in the Table 6.

Table 7 *Stiffly accurate full and diagonal IRKs tableaus with singular Runge-Kutta matrix*

Full IRK	Diagonal IRK
$\begin{array}{c\|ccccc} 0 & 0 & \cdots & 0 & \cdots & 0 \\ \vdots & \vdots & & \vdots & & \vdots \\ c_i & a_{i1} & \cdots & a_{ii} & \cdots & a_{is} \\ \vdots & \vdots & & \vdots & & \vdots \\ 1 & b_1 & \cdots & b_i & \cdots & b_s \\ \hline & b_1 & \cdots & b_i & \cdots & b_s \end{array}$	$\begin{array}{c\|ccccc} 0 & 0 & & & & \\ \vdots & \vdots & \ddots & & & \\ c_i & a_{i1} & \cdots & a_{ii} & & \\ \vdots & \vdots & & \vdots & \ddots & \\ 1 & b_1 & \cdots & b_i & \cdots & b_s \\ \hline & b_1 & \cdots & b_i & \cdots & b_s \end{array}$

It is worth to note that, due to the method consistency, a null first row of **A** leads to a zero first node, meaning that the first stage actually is the previous states vector $\mathbf{u}^n$, so the first intermediary stage increment is a zero vector as reported in (396).

$$\mathbf{x}_1 = \mathbf{0} \tag{396}$$

A last note about the singular IRKs with full tableau is given: in this case, once set to zero the first intermediary stage increment $\mathbf{x}_1$, the simultaneous problem $\mathbf{f}$ reported in (388) can be reduced to the last $(s-1)$ intermediary stages, reducing the size of the problem to $(s-1)(2N+2)$.

Before resuming all the feasible IRKs able to march the transient EHL problem in its DAE form, the following DIRK properties are discussed. The stiffness and the numerical burden of the DAE systems computation could provide instabilities during the marching that can be addressed with DIRK methods showing two particular characteristics (the related tableaus are reported in the Table 7):

- the first one is represented by the Runge-Kutta matrix with a constant element γ on the main diagonal; the so-called Singly Diagonally IRKs (SDIRKs) are very useful when the $\mathbf{f}_i$ Jacobian is not assembled at each iteration, but it is assumed to be constant along a chosen number of iterations, leading to the possibility to factorizing it less frequently (Alexander, 1977; Kennedy and Carpenter, 2016);
- the second one is represented by singular SDIRKs (so with null first row and a single element on the main diagonal, while stiffly accurate) with a Crank-Nicolson-like second intermediary stage; due the explicit first stage zero setting, these are called Explicit SDIRKs (ESDIRKs) and a huge research is given in literature because of their stability properties (Kværnø, 2004).

Table 8 *SDIRK and ESDIRK tableaus*

SDIRK	ESDIRK
$\begin{array}{c\|ccccc} \gamma & \gamma \\ \vdots & \vdots & \ddots \\ c_i & a_{i1} & \cdots & \gamma \\ \vdots & \vdots & & \vdots & \ddots \\ c_s & a_{s1} & \cdots & a_{si} & \cdots & \gamma \\ \hline & b_1 & \cdots & b_i & \cdots & b_s \end{array}$	$\begin{array}{c\|cccccc} 0 & 0 \\ 2\gamma & \gamma & \gamma \\ \vdots & \vdots & \vdots & \ddots \\ c_i & a_{i1} & a_{i2} & \cdots & \gamma \\ \vdots & \vdots & \vdots & & & \ddots \\ 1 & b_1 & b_2 & \cdots & b_i & \cdots & \gamma \\ \hline & b_1 & b_2 & \cdots & b_i & \cdots & \gamma \end{array}$

An ESDIRK with different elements on the main diagonal is simply indicated as EDIRK; a famous stiffly accurate EDIRK in the context of both the ODE and DAE simulation is the TRapezoidal-Backward Differentiation Formula with second order accuracy (TR-BDF2) reported in (397) for an ODE system (Wanner and Hairer, 1996; LeVeque, 2007) (so without the singular matrix $\mathbf{C}$): going from the previous time n to the next one $(n+1)$, the TR-BDF2 executes a Crank-Nicolson step between n and the step mid-point, followed by a BDF2 at the next step involving the three nodes, i.e., n, the mid-point and $(n+1)$.

$$\begin{cases} \dfrac{\mathbf{u}^{n+1/2}-\mathbf{u}^{n}}{\Delta T/2} = \dfrac{1}{2}\left[\mathbf{\Phi}(\mathbf{u}^{n},T^{n}) + \mathbf{\Phi}\left(\mathbf{u}^{n+1/2},T^{n}+\Delta T/2\right)\right] \\ \dfrac{3\mathbf{u}^{n+1}-4\mathbf{u}^{n+1/2}+\mathbf{u}^{n}}{\Delta T} = \mathbf{\Phi}(\mathbf{u}^{n+1},T^{n}+\Delta T) \end{cases} \tag{397}$$

Evaluating $\mathbf{u}^{n+1/2}$ from the Crank-Nicolson step and substituting it in the BDF2 one, leads to the Runge-Kutta form of the TR-BDF2 reported in (398).

$$\begin{cases} \dfrac{\mathbf{u}^{n+1/2}-\mathbf{u}^{n}}{\Delta T} = \dfrac{1}{4}\mathbf{\Phi}(\mathbf{u}^{n},T^{n}) + \dfrac{1}{4}\mathbf{\Phi}\left(\mathbf{u}^{n+1/2},T^{n}+\Delta T/2\right) \\ \dfrac{\mathbf{u}^{n+1}-\mathbf{u}^{n}}{\Delta T} = \dfrac{1}{3}\mathbf{\Phi}(\mathbf{u}^{n},T^{n}) + \cdots \\ \ldots + \dfrac{1}{3}\mathbf{\Phi}\left(\mathbf{u}^{n+1/2},T^{n}+\Delta T/2\right) + \dfrac{1}{3}\mathbf{\Phi}(\mathbf{u}^{n+1},T^{n}+\Delta T) \end{cases} \tag{398}$$

The tableau related to the (398) is given in the Table 8, revealing the stiffly accurate EDIRK nature of the TR-BDF2 multi-stage method.

Table 9 *TR-BDF2 EDIRK tableau*

$$\begin{array}{c|ccc} 0 & & & \\ 1/2 & 1/4 & 1/4 & \\ 1 & 1/3 & 1/3 & 1/3 \\ \hline & 1/3 & 1/3 & 1/3 \end{array}$$

Resuming, all the IRK methods feasible to solve the 1D EHL DAE system are reported: the Tables 9-14 collect the general, stiffly accurate and singular methods tableaus for both the IRKs and the DIRKs, highlighting the related stage number s and accuracy order p (Alexander, 1977; Wanner and Hairer, 1996; Kværnø, 2004; LeVeque, 2007; Ying, Henriquez and Rose, 2009; Kennedy and Carpenter, 2016).

Table 10 *Full IRKs*

Name	Stage number s	Accuracy order p
Gauss-Legendre	2	4
Gauss-Legendre	3	6
Radau IA	2	3
Radau IA	3	5

Table 11 *Stiffly accurate full IRKs*

Name	Stage number s	Accuracy order p
Lobatto IIIC	2	2
Lobatto IIIC	3	4
Lobatto IIIC	4	6
Radau IIA	2	3

Radau IIA	3	5

Table 12 *Singular stiffly accurate full IRKs*

Name	Stage number s	Accuracy order p
Lobatto IIIA	2	2
Lobatto IIIA	3	4

Table 13 *DIRKs*

Name	Stage number s	Accuracy order p
Implicit midpoint	1	2
Kraaijevanger-Spijker	2	2
Qin-Zhang	2	2
Pareschi-Russo	2	2
Crouzeix	2	3
Crouzeix	3	4

Table 14 *Stiffly accurate DIRKs*

Name	Stage number s	Accuracy order p
Backward Euler	1	1
IM-CBDF2	2	2
IM-CBDF3	3	3
SDIRK	4	3

Table 15 *Singular stiffly accurate DIRKs*

Name	Stage number s	Accuracy order p
Crank-Nicolson	2	2
TR-BDF2	3	2
TR-CBDF2	3	2
TR-CBDF3	4	3

2.5.3. Stationary simulation

In the following, the conducted simulations are presented: the input were selected from the Hamrock-Dowson EHL dimensionless parameters of material G^*, velocity U^* and load W^* reported in (399), that will be useful also to have a benchmark to compare with the stationary minimum and central film thickness h_{min} and h_c (Dowson, 1967).

$$G^* = 2\alpha E^* \quad U^* = \frac{\mu_0 U_0}{4E^* R} \quad W^* = \frac{w_0}{2E^* R} \tag{399}$$

$$\frac{h_{min}}{R} = 2.65\ G^{*0.54} U^{*0.7} W^{*-0.13}$$
$$\frac{h_c}{R} = 3.06\ G^{*0.56} U^{*0.69} W^{*-0.1}$$

For a given lubricant and tribo-system materials and geometry, i.e., fixed α, μ_0, E^* and R, the nominal load w_0 and the nominal velocity U_0 are extracted from the related dimensionless parameters in (400): they will be used to characterize the time-varying inputs supplying the state-space EHL problem, i.e., the dimensionless load $W(T)$ and sliding velocity $\sigma(T)$.

$$\begin{gathered} w_0 = (2E^*R)W^* \quad U_0 = \left(\frac{4E^*R}{\mu_0}\right)U^* \\ \begin{matrix} W(T) \\ \sigma(T) \end{matrix} \ \rightarrow \ \begin{cases} \mathbf{C}\dot{\mathbf{u}} = \boldsymbol{\Phi}(\mathbf{u}, T) \\ \mathbf{u}(0) = \mathbf{u}_0 \end{cases} \ \rightarrow \ \mathbf{u}(T) \end{gathered} \tag{400}$$

Let start by validating the stationary EHL simulation with respect to the DCM one and to the empirical Hamrock-Dowson benchmarks: the DCM solver based on the variational principle (Tian and Bhushan, 1996) and the stationary EHL one given by the zeros of the source function $\boldsymbol{\Phi}$ are reported in (401), while the input data are collected in the Table 15.

$$\begin{cases} \min\limits_{\mathbf{P},\Delta} \frac{1}{2}\mathbf{P}^T\mathbf{K}\mathbf{P} + \mathbf{G}^T\mathbf{P} - \frac{\pi}{2\Delta X}\Delta \\ \mathbf{P} \geq \mathbf{0} \quad \mathbf{H} \geq \mathbf{0} \quad \mathbf{P} \circ \mathbf{H} = \mathbf{0} \\ \mathbf{t}_X^T\mathbf{P} = \frac{\pi}{2} \end{cases} \quad \boldsymbol{\Phi}(\mathbf{u}, T^*) = \mathbf{0} \tag{401}$$

Table 16 *Stationary 1D EHL simulation input data*

Data	
Cylinder radius R	1 cm
Cylinder mass m	$1\ \mathrm{kg\ m^{-1}}$
Plane Young modulus E_l	210 GPa
Plane Poisson ratio ν_l	0.3
Cylinder Young modulus E_u	210 GPa
Cylinder Poisson ratio ν_u	0.3
Lubricant nominal viscosity μ_0	1 Pa s
Barus exponent α	$21.9\ \mathrm{GPa^{-1}}$
Modulus coefficient β	$1.59\ \mathrm{GPa^{-1}}$
Hamrock-Dowson load parameter W^*	$4.3 \cdot 10^{-3}$
Hamrock-Dowson velocity parameter U^*	$2.17 \cdot 10^{-10}$
Domain half length L_x	3.1 mm
Grid points number N	2^9
Relaxation factor ω	10^{-2}
Tolerance tol	10^{-6}

First of all, the resulting gap-pressure shapes are depicted in the Figure 134: it can be verified that both the DCM and the EHL shapes insist on the contact area with half width a_H and the dimensionless peak pressure is unitary, meaning that its dimensional value is equal to the Hertzian pressure p_H; the EHL pressure shape overlaps to the DCM one, while clearly showing the pressure spike at the meatus outlet and the consequent pressure drop in order to keep the line integral to respect the load balance; the EHL gap shape clearly demonstrates the minimum film thickness at the meatus outlet at the same height of the Hamrock-Dowson empirical one, providing the same matching that can be retrieved for the central film thickness.

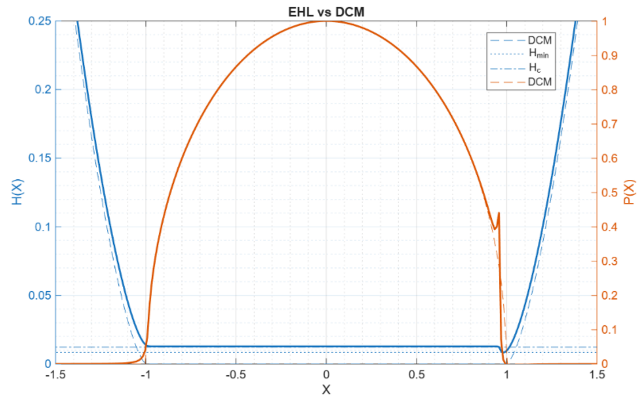

Figure 134 *Stationary EHL-DCM gap and pressure shapes*

The deformed surfaces for both the EHL and DCM simulations are shown in the Figure 135: due to the analogy between the two tribological modes, the shapes of the deformed surfaces are very similar.

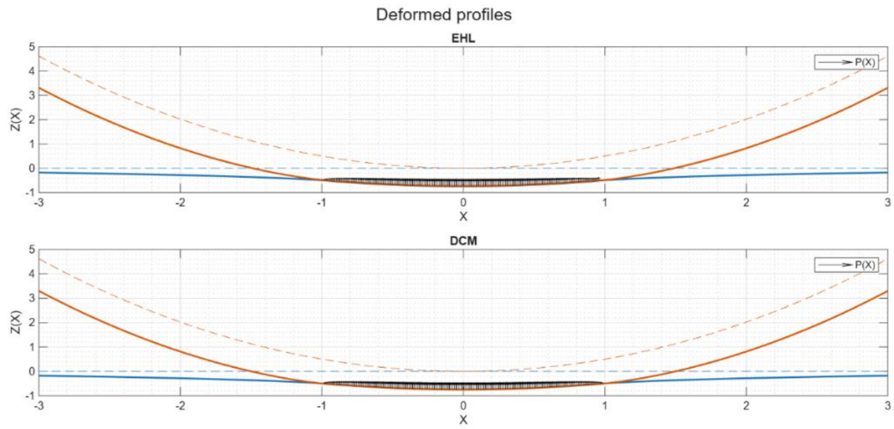

Figure 135 *Stationary EHL-DCM deformed surfaces*

An interesting EHL output is represented by the lubricant flow velocity field u and the consequent lubricant shear stress τ reported in the eq. (402).

$$\begin{aligned} u(x,y,t) &= -\frac{1}{2\mu}\frac{\partial p}{\partial x}(hy-y^2)+U_x\left(1-\frac{y}{h}\right) \\ \tau(x,y,t) &= \mu\frac{\partial u}{\partial y} = -\frac{1}{2}\frac{\partial p}{\partial x}(h-2y)-\mu\frac{U_x}{h} \end{aligned} \tag{402}$$

In their dimensionless form, respectively, U and T_X, the (402) fields are given in (403) scaling the normal coordinate y with the Hertzian approach δ_H.

$$\begin{aligned} U(X,Y,T) &= u\frac{t_s}{2a_H} = -\frac{3\lambda}{M}\frac{\partial P}{\partial X}(HY-Y^2)+\sigma\left(1-\frac{Y}{H}\right) \\ T_X(X,Y,T) &= \tau\frac{\delta_H}{\mu_0}\frac{t_s}{2a_H} = -3\lambda\frac{\partial P}{\partial X}(H-2Y)-M\frac{\sigma}{H} \end{aligned} \tag{403}$$

The lubricant flow and shear stress fields related to the stationary EHL simulations are depicted in the Figure 136, overlapped to the gap-pressure shapes: the fluid carried by the moving plane and constrained to flow across the highly deformed narrow gap generates a high shear stress.

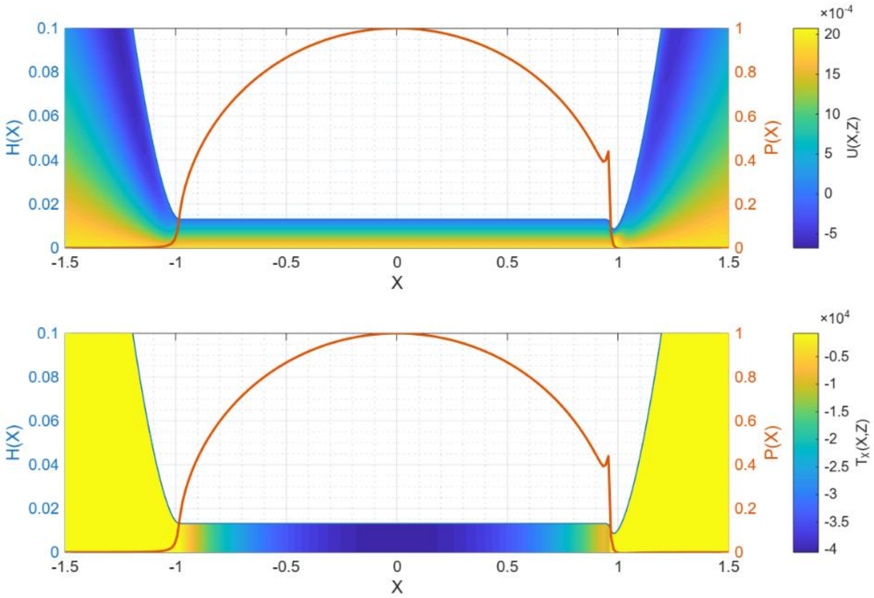

Figure 136 *Stationary EHL flow velocity and shear stress*

2.5.4. Transient simulation

Given the good results of the stationary simulation, let move to the transient ones.

2.5.4.1. Step inputs

First, the constant loading and sliding inputs from rest ICs simulation is conducted: with reference to (404), the constant inputs come from the Hamrock-Dowson parameters in the Table 15, while the rest ICs are characterised by a negative unitary initial approach Δ_0; the time period L_T simulated is chosen to be 2000 times the scaling time t_s in order to evaluate the transient dynamics extinction towards the stationary phase, where the comparison with respect to the Hamrock-Dowson empirical benchmark can be performed, while the marching is executed with the 4-stage SDIRK in the Table 13 on a time grid with $M = 100$ points.

$$\mathbf{u}_0 = \mathbf{u}_r = \begin{bmatrix} \mathbf{G}+1 \\ \mathbf{0} \\ -1 \\ 0 \end{bmatrix} \qquad \begin{aligned} W(T) &= \frac{\pi}{2} \\ \sigma(T) &= \frac{t_s}{2a_H} U_0 \end{aligned} \tag{404}$$

The states time evolution of the described simulation is depicted in the Figure 137: starting from the rest conditions and for constant inputs, the applied load imposes a fast increase of the approach Δ which reaches its stationary value after the transient; the approach dynamics leads the surfaces to come close fast, generating a lubricant pressure P bump which travels along the sliding direction and turns into the stationary EHL pressure shape with the exit spike; the generated wave has the analogous effect on the gap H which shows a decreasing socket of lubricant moving towards the meatus outlet, so that the establishing central film thickness turns into the minimum gap at the meatus outlet once reached the stationary phase.

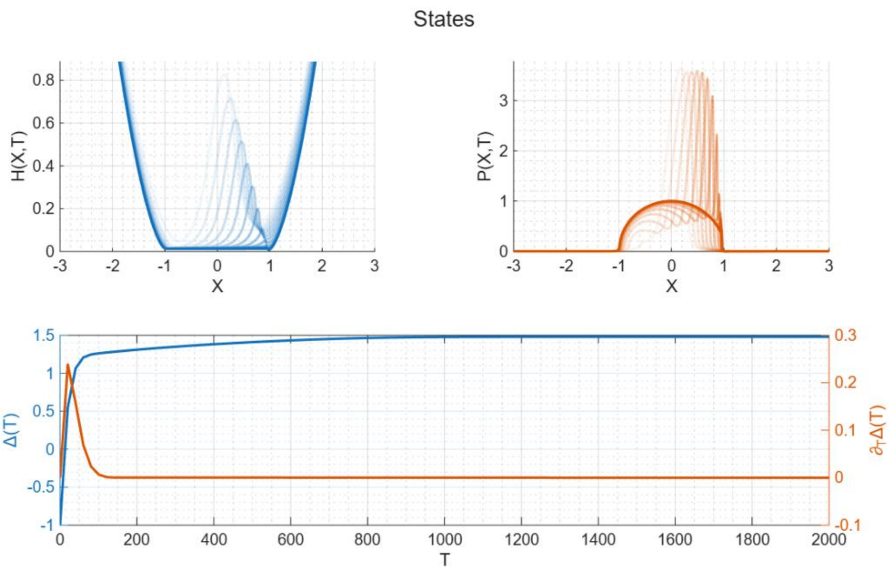

Figure 137 *Constant inputs simulation states*

The very interesting wave characteristic of the transient EHL simulation for constant inputs can be verified in the Figure 138 showing the minimum film thickness time evolution for all the IRKs demonstrating convergence up to a maximum time points M equal to 500: it is evident the minimum film thickness evolution towards the empirical Hamrock-Dowson central gap, turning into the minimum one after the transient phase; no IRK with full Runge-Kutta matrix **A** worked, while the majority of the DIRKs did, showing instabilities at the very initial transient phase for the IM-CBDF2 and the IM-CBDF3 and a little delay for the Kraaijevanger-Spijker and the Backward Euler. Anyway, all the functioning IRKs demonstrate the reaching of the stationary phase with the same characteristics described for the steady-state simulation, revealing the reliability of the developed code justified by the comparison with respect to the empirical Hamrock-Dowson benchmark.

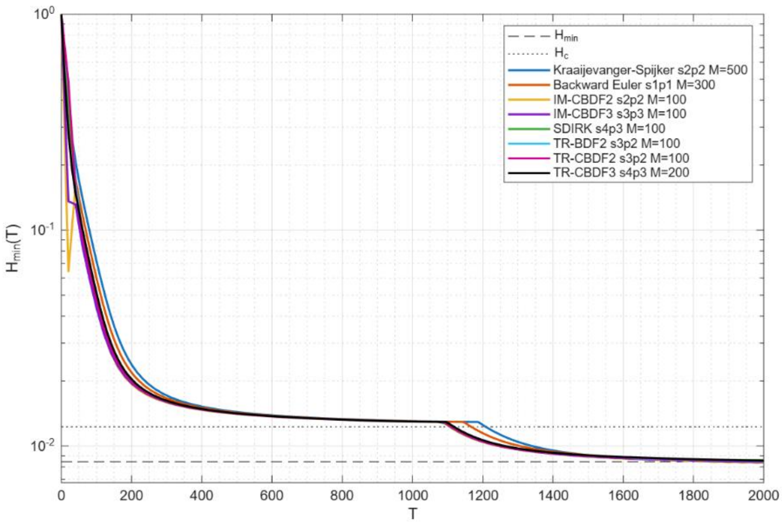

Figure 138 *Minimum gap for converging IRKs vs Hamrock-Dowson*

2.5.4.2. Pure squeeze

Further interesting lubrication contexts can be simulated: the next one is the pure squeeze lubrication obtained with the same input data reported in the Table 15, from the same rest ICs, same DIRK method and same the constant inputs simulation but with a null sliding velocity (eq. (405)).

$$W(T) = \frac{\pi}{2} \quad \sigma(T) = 0 \tag{405}$$

The Figure 139 reports the states evolution during the pure squeeze simulation: due to the null sliding, the EHL pressure P shape is symmetrical and it is governed by the constant applied load; then, as demonstrated by the gap H, the realised lubricant socket tends to decrease, together with the symmetrical pressure bell, resulting in the approach Δ behaviour very similar to the previous simulation; this time, once the fluid within the highly deformed zone escapes the meatus, the minimum film thickness will go to zero, since there is no stationary lubricant effect in absence of sliding.

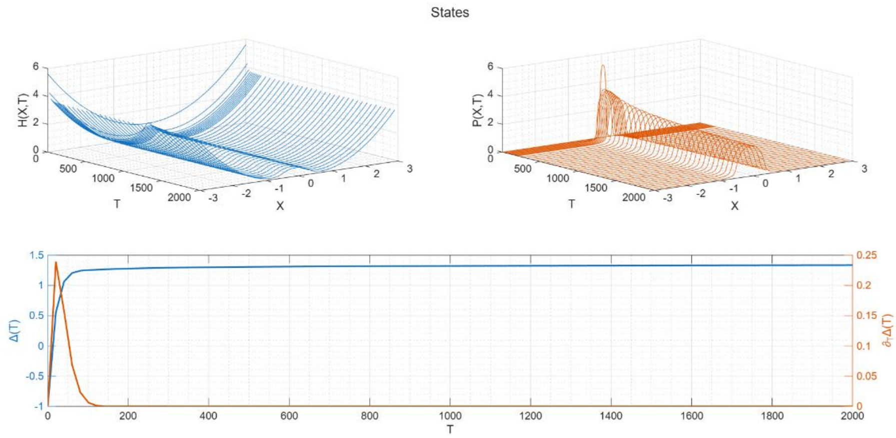

Figure 139 *Pure squeeze simulation states*

The lubricant flow escaping the meatus is clearly visualised in the Figure 140 showing the described flow velocity field and the associated anti-symmetrical shear stress with a closer look at the highly deformed zone.

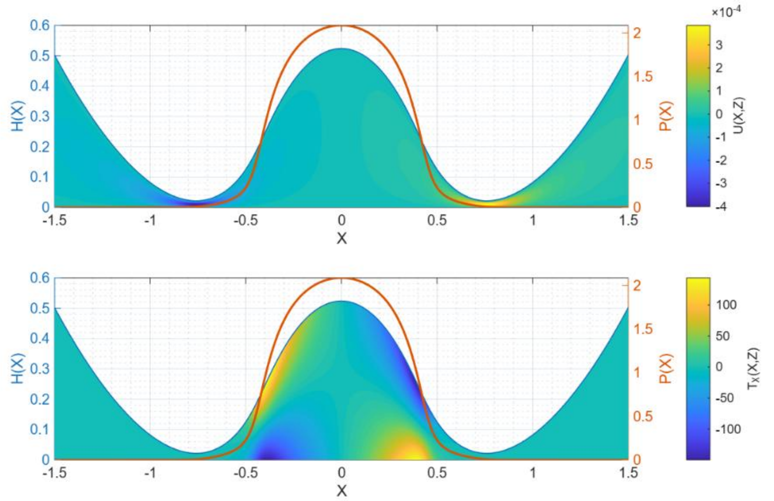

Figure 140 *Pure squeeze simulation flow and shear stress*

2.5.4.3. Harmonic inputs

Two final interesting applications could be the tribo-system response to harmonic inputs. Starting from harmonic sliding and constant loading conditions (4 sliding cycles over the simulation time L_T equal to 10000, as reported in (406)), the states evolution over time is given in the Figure 141: with reference to the gap H, the wave travelling back and forth across the meatus and decaying over time is representative of what happens in fully lubricated reciprocating tribometer; the pressure P bell, after the initial transient phase, turns into the classical EHL shape changing its verse based on the varying sliding direction; the approach Δ, once the fast initial surface approaching, demonstrates oscillations with a certain delay with respect to sliding.

$$W(T) = \frac{\pi}{2} \quad \sigma(T) = \frac{t_s}{2a_H} U_0 \sin\left(4\frac{2\pi T}{L_T}\right) \tag{406}$$

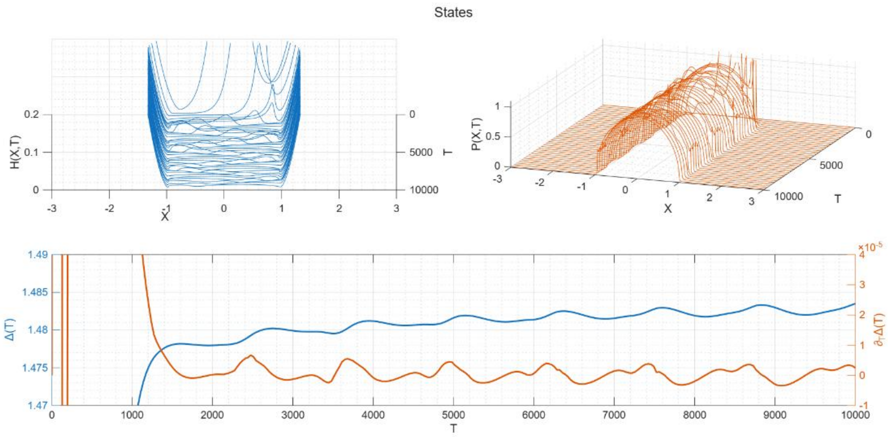

Figure 141 *Harmonic sliding simulation states*

Finally, the tribo-system response to a harmonic loading and null sliding (4 load oscillations around the w_0 mean value with a fifth half amplitude over a simulated time L_T equal to 2000, which results are reported in the Figure 142), could be of interest in the context of dynamically loaded bearings, where it could be useful to analyse the approach Δ response in terms of amplitude and phase with respect to the input load; it is interesting to visualise the symmetrical pressure P bell shape with oscillating magnitude creating little bumps that travel out from the highly deformed zone.

$$W(T) = \frac{\pi}{2}\left[1 + \frac{1}{5}\sin\left(4\frac{2\pi T}{L_T}\right)\right] \quad \sigma(T) = 0 \tag{407}$$

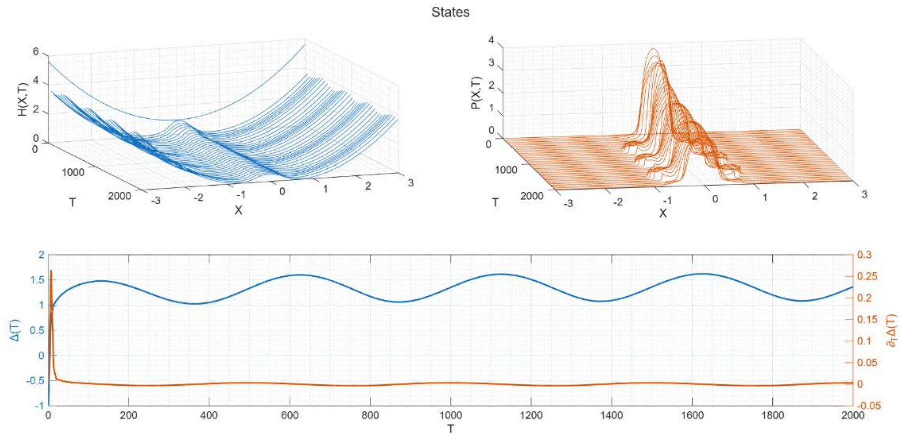

Figure 142 *Harmonic loading simulation states*

The developed code resulted to be very efficient and adaptable to several operating conditions, reason why it will be generalised to 3D configuration and to the compressible lubricant fluid case in future works.

The proposed approach is based on the manuscript produced by the author (Sicilia and Ruggiero, 2026).

Conclusions

In this work several numerical strategies to simulate the dynamics of Multi-Body systems and the tribology of conjugated surfaces were studied, implemented, tried and improved in the context of biomechanical systems to estimate the wear of its joints; the main application was referred to the wear estimation of the hip joint replacement involved in the lower limb musculoskeletal system moving following a gait cycle, but the presented developed models and related simulations referred also to rectangular tribo-systems in both dry and lubricated conditions, where the latter were characterised in both full-film and mixed regimes.

In the first part of the thesis the Multi-Body formulation adopted to characterise the inverse dynamics of musculoskeletal system was presented; in particular, the topics covered were:

- the rigid body kinematics to describe its configuration in the 3D space, with a focus on its orientation that in this work was addressed with the unit quaternion;
- the Multi-Body constrained kinematics relying on the writing of a set of equations that rule the relative motion between the bodies linked by joints in terms of mobility and constraints, creating a topology network that relates the Multi-Body system Lagrangian coordinates to its DoF;
- the characterization of the above joint equations for the coupling considered in this work, i.e., revolute joint, cam joint, spherical joint and free joint;
- the Multi-Body dynamics Lagrangian formulation allowing to obtain the system EoM that, along the inverse dynamics verse, is a closed linear system in the unknown Lagrange multipliers, i.e., generalised forces that acts on the bodies at the joint level in order to respect instant by instant the joint constraint and mobility equations;

  the characterization of Multi-Body system driving forces as generated by the muscular system, then, the development of a tool that uses the muscles attachment points kinematics to link the generalised driving forces to the real generated muscle forces, with the possibility to evaluate curved muscle path wrapping around bony surfaces through a developed geodesic curve generation algorithm; next, the muscle forces were related to their activation level through the Hill muscle model considering both the contractile and the passive force contributions, allowing the writing of the musculoskeletal Multi-Body system EoM in the unknowns muscle activations and Lagrange multipliers, wherethe latter are composed also by the joint reactions playing a determinant role in the context of the joint tribology;

- the description of the minimization strategy to solve the above EoM in the redundant unknowns, i.e., the static optimization that minimizes the system driving effort to follow the selected kinematics; furthermore, the inverse kinematics minimization algorithm was introduced to elaborated the Multi-Body system DoF due to the knowledge of the trajectories of a set of markers applied to the musculoskeletal system: the latter upgrade allows the author to have both inverse kinematics and inverse dynamics solvers, so to obtain a tool that starting from the musculoskeletal system marker kinematics is able to evaluate its muscle activations and joint reactions produced during that selected motion.

The developed Matlab® code was used to evaluate the inverse kinematics and the inverse dynamics of two musculoskeletal systems, i.e., an upper limb with 2 DoF and 6 muscles and a lower limb with 23 DoF and 92 muscles which input data are taken from the open-source OpenSim® software: the lower limb simulation for the selected gait kinematics provided the time evolution of the hip joint reactions that were compared to the associated *in vivo* loads coming from the Bergmann measurements (Bergmann *et al.*, 2016) obtaining a good qualitative matching, so the assembled code resulted to be a reliable generator of tribological inputs, i.e., joint load and relative motion, to be supplied to a tribological simulator; furthermore, the lower limb system simulation outputs were compared to the ones obtained by the related OpenSim® software routine, providing acceptable error metrics with high correlation coefficients, returning little deviations that can be devoted to different numerical strategies adopted by the open-source calculator.

Then, the tribological and numerical concepts to simulate the joint lubrication and contact regimes were addressed, assembling a series of algorithms differentiating in terms of lubrication regime, deformation models, numerical solving strategies; in particular:

- the Reynolds lubrication equation, the gap equation and the load balance equation were introduced in the case of HL mode, together with the elliptic Reynolds PDE FDM discretization resulting in the linear algebraic equations set solved by the means of the Jacobi, Gauss-Seidel and SOR iterative methods;

- then, the same HL FDM discretization was adapted to the spherical geometry of the hip joint identifying the femoral head relative motion with respect to the acetabular cup with its eccentricity and angular velocity vectors; furthermore, the input of hip loads and angular velocities coming from the Multi-Body simulation were rotated in the spherical Reynolds equation reference frame fixed to the acetabular cup;
- the adjustments to make the Reynolds lubrication equation valid for the EHL regime were presented by introducing the lubricant pressure-varying rheological models and characterising the deformation models bringing non-linearities to the new unsteady advection/diffusion Reynolds PDE;
- three deformation models were introduced, i.e., a local spring deformation model in the context of the lubricated spherical joint allowing to solve the Reynolds equation with the iterative Newton method, a FEM deformation model of the spherical joint defining a dense compliance matrix that constrained to adopt a free derivative iterative method to solve the Reynolds equation, a half-space BEM deformation model referred to both 2D and 3D rectangular tribo-systems which the resulting convolution was addressed by the FFT, while the associated Reynolds equation iterative solver was based on the nonlinear local Jacobi method.

Proceeding with the lubrication mode numerical characterization, the ML regime was introduced:

- basic concepts about the DCM simulations of both line-contact and point-contact tribo-systems based on the variational principle were described;
- a fractal surface generator based on the extension of the Brownian motion properties was assembled to take into account the roughness in the gap between the conjugated surfaces;
- the surfaces' wear was included in the gap equation by the means of the Archard wear model in order to consider the progressive surface deterioration in the contact zone and to have a wear volume estimator for the given tribological operating conditions;
- the LCCs related to the DCM regime were adapted to the ML regime in two ways, i.e., by the fluid/contact pressure splitting referred to the spherical joint case in which the contact deformation rises to avoid the surfaces' interpenetration and by the definition of a smooth transition function referred to the rectangular tribo-system case that continuously imposes the null gap equation in the contact zones and the Reynolds one elsewhere.

Consequently, the simulation results were presented in the framework of 4 cases:

- the spherical Reynolds equation in the ML regime with the splitting pressures method and equipped with the local spring deformation model was solved for the hip joint supplied by gait cycle loading and motion conditions coming from the musculoskeletal inverse dynamics solver, obtaining reliable results in terms of the implant wear volume with respect to *in vitro* measurements and realising the main applicative objective of this work, i.e., the coupling between the Multi-Body and the tribological models;
- the spherical Reynolds equation in the full-film EHL regime with the developed FEM deformation model was solved for a given set of ball-in-socket eccentricities and angular velocities, showing results about the lubricant pressure/gap EHL shapes, shear stresses, loads and viscous friction torques and verifying the validity of the developed code by comparing the resulting minimum film thickness with respect to the empirical Hamrock-Dowson one (Hamrock and Dowson, 1976; Lubrecht, Venner and Colin, 2009);
- the rectangular Reynolds equation in the ML regime with the half-space BEM deformation model was solved for a ball-on-plane configuration with the smooth transition technique for a given set of approach and sliding velocity, providing a reliable behaviour in both the ML condition and the EHL one reached by increasing the lubricant viscosity (also in this last case the minimum film thickness was compared to the Hamrock-Dowson empirical benchmark);
- the same previous case was repeated in the case of a rough surface obtained with the fractal generator on a sliding a plane, which results were compared to the analogous DCM solution and discussing the role of the lubricant presence with respect to the variation of the RCA, the wear volume and others tribological aspects.

Lastly, a numerical approach to simulate the transient full film 1D EHL was proposed: it is based on the writing of unified system of equations composed by the Reynolds equation, the gap equation and load balance equation accounting for inertial effects.

The resulting DAE system, in which the transient effects are stimulated by the squeeze term in the Reynolds equation and by the inertia in the load balance equation while the gap equation acts as an algebraic constraint, was spatially discretised by the means of the FDM for the fluid part (Reynolds) and with the BEM for the solid part (deformation), so it is rewritten its state-space form to obtain a singular ODE system.

The above was numerically marched over time by the means of several IRKs and DIRKs methods able to handle the DAE nature of the multi-physics EHL problem, and a series of simulations was conducted:

- the model was firstly tested in the stationary case, obtaining an optimal matching with respect to the associated DCM solution and to the Hamrock-Dowson empirical central and minimum film thickness (Dowson, 1967);
- the same above stationary results were obtained by the transient simulation for constant loading and sliding time inputs, providing a selection among the DIRK methods succeeding in the loop convergence;
- the transient simulation was then conducted in the pure squeeze conditions, for the harmonic sliding case and for the harmonic load one, discussing the effects of the resulting transient waves that, travelling along the meatus, drew the lubricant gap/pressure shapes and govern the approach dynamics.

All the developed codes, in both the biomechanics and the tribology part of this work, were based on several numerical and modelling strategies and are in continuous deepening and evolution, so the proceedings of this studies is strongly stimulating the author perspectives, which the main one is the merging of the Multi-Body and the DAE solvers in the context of a global simulator for the ML regime for both the rectangular and the spherical geometries.

Finally, as reported in the related sections, the developed codes refer to the author’s publications (Ruggiero and Sicilia, 2020b, 2020a, 2021a, 2021b, 2022a, 2022c, 2022b, 2024; Ruggiero, Sicilia and Affatato, 2020; Sicilia, De Stefano and Ruggiero, 2024; Sicilia and Ruggiero, 2025, 2026).

Bibliography

Abdullah, M. *et al.* (2024) 'Multibody dynamics-based musculoskeletal modeling for gait analysis: a systematic review', *Journal of neuroengineering and rehabilitation*, 21(1), p. 178.

Affatato, S. *et al.* (2009) 'Mixing and matching in ceramic-on-metal hip arthroplasty: an in-vitro hip simulator study', *Journal of biomechanics*, 42(15), pp. 2439–2446.

Aherwar, A., Singh, A. and Patnaik, A. (2015) 'Current and future biocompatibility aspects of biomaterials for hip prosthesis', *AIMS Bioeng*, 3(1), pp. 23–43.

Alexander, R. (1977) 'Diagonally Implicit Runge–Kutta Methods for Stiff ODE's', *SIAM J. Numer. Anal*, 14(6), pp. 1006–1021.

Almqvist, T., Almqvist, A. and Larsson, R. (2004) 'A Comparison Between Computational Fluid Dynamic and Reynolds Approaches for Simulating Transient EHL Line Contacts', *Tribol. Int*, 37(1), pp. 61–69.

Anderson, F.C. and Pandy, M.G. (1999) 'A Dynamic Optimization Solution for Vertical Jumping in Three Dimensions', *Comput. Methods Biomech. Biomed. Eng*, 2(3), pp. 201–231.

Anderson, F.C. and Pandy, M.G. (2001) 'Dynamic Optimization of Human Walking', *ASME J. Biomech. Eng*, 123(5), pp. 381–390.

Archard, J.F. (1953) 'Contact and rubbing of flat surfaces', *Journal of Applied Physics*, 24(8), pp. 981–988.

Archard, J.F. and Hirst, W. (1956) 'The wear of metals under unlubricated conditions', *Proc. R. Soc. Lond. Ser. A. Math. Phys. Sci*, 236, pp. 397–410.

Arnold, E.M. *et al.* (2010) 'A Model of the Lower Limb for Analysis of Human Movement', *Ann. Biomed. Eng*, 38(2), pp. 269–279.

Askari, E. *et al.* (2014a) ‘Nonlinear vibration and dynamics of ceramic on ceramic artificial hip joints: a spatial multibody modelling’, *Nonlinear Dyn*, 76(2), pp. 1365–77.

Askari, E. *et al.* (2014b) ‘Study of the Friction-Induced Vibration and Contact Mechanics of Artificial Hip Joints’, *Tribol. Int*, 70, pp. 1–10.

Bair, S. (2022) ‘The unresolved definition of the pressure-viscosity coefficient’, *Sci Rep*, 12(1).

Bergmann, G. *et al.* (2016) ‘Standardized Loads Acting in Hip Implants’, *PLoS One*, 11(5), p. 0155612.

Chand, T.J. (2011) ‘Complete Description of the Thelen 2003 Muscle Model’. OpenSim, Stanford, CA.

Cheraghalizadeh, J. *et al.* (2024) ‘Fractional brownian motion as a rough surface’, *Physica A Statistical Mechanics Applications*, 129907.

Ciccarelli, P. *et al.* (2024) *Italian Arthroplasty Registry. Annual Report 2023 – Addendum*. Rome: Il Pensiero Scientifico Editore.

Cooley, J., Lewis, P. and Welch, P. (1969) ‘The finite Fourier transform"’, *IEEE Transactions on Audio and Electroacoustics*, 17(2), pp. 77–85.

Cooley, J.W. and Tukey, J.W. (1965) ‘An algorithm for the machine calculation of complex Fourier series"’, *Mathematics of Computation*, 19(90), pp. 297–301.

Cosenza, C., Niola, V. and Savino, S. (2018) ‘A mechanical hand for prosthetic applications: Multibody model and contact simulation’, *Proc. Inst. Mech. Eng. Part H J. Eng. Med*, 232, pp. 819–825.

Curtis, N. (2010) ‘Craniofacial biomechanics: An overview of recent multibody modelling studies’, *J. Anat*, 218, pp. 16–25.

Delp, S.L. *et al.* (1990) ‘An Interactive Graphics-Based Model of the Lower Extremity to Study Orthopaedic Surgical Procedures’, *IEEE Trans. Biomed. Eng*, 37(8), pp. 757–767.

Di Puccio, F. and Mattei, L. (2015) ‘Biotribology of artificial hip joints’, *World J. Orthop*, 6, p. 77.

Dowson, D. (1967) ‘Paper 10: Elastohydrodynamics’, *Proc. Inst. Mech. Eng*, 182(1), pp. 151–167.

Dowson, D. and Higginson, G.R. (1966) *Elastohydrodynamic lubrication*. 1st edn. Oxford: Pergamon.

Dumbleton, J.H. (1981) *Tribology of Natural and Artificial Joints*. Amsterdam, the Netherlands: Elsevier.

Duprey, S. *et al.* (2017) 'Kinematic models of the upper limb joints for multibody kinematics optimisation: An overview', *J. Biomech*, 62, pp. 87–94.

Essner, A., Schmidig, G. and Wang, A. (2005) 'The clinical relevance of hip joint simulator testing: In vitro and in vivo comparisons', *Wear*, 259(7–12), pp. 882–886.

Evans, H.P. and Hughes, T.G. (2000) 'Evaluation of deflection in semi-infinite bodies by a differential method', *Proc. Inst. Mech. Eng. Part C J. Mech. Eng. Sci*, 214, pp. 563–584.

Felippa, C.A. (2004) *Introduction to finite element methods*. University of Colorado.

Fisher, J. and Dowson, D. (1991) 'Tribology of total artificial joints', *Proc Inst Mech Eng H J Eng Med*, 205(2), pp. 73–9.

Flores, P., Ambrosio, J. and Claro, J.P. (2004) 'Dynamic Analysis for Planar Multibody Mechanical Systems With Lubricated Joints', *Multibody Syst. Dyn*, 12(1), pp. 47–74.

Fregly, B.J., Bei, Y. and Sylvester, M.E. (2003) 'Experimental evaluation of an elastic foundation model to predict contact pressures in knee replacements', *J. Biomech*, 36, pp. 1659–1668.

Gao, F. *et al.* (2002) 'Computational method for muscle-path representation in musculoskeletal models', *Biol. Cybern*, 87, pp. 199–210.

Gao, L. *et al.* (2009) 'Effect of 3D physiological loading and motion on elastohydrodynamic lubrication of metal-on-metal total hip replacements', *Med Eng Phys*, 31(6), pp. 720–9.

Gao, L., Dowson, D. and Hewson, R.W. (2015) 'Predictive wear modeling of the articulating metal-on-metal hip replacements', *J. Biomed. Mater. Res. Part B Appl. Biomater*, 105, pp. 497–506.

Goodyer, C.E. and Berzins, M. (2006) 'Adaptive Timestepping for Elastohydrodynamic Lubrication Solvers', *SIAM J. Sci. Comput*, 28(2), pp. 626–650.

Greenwood, J.A. (2020) ‘Elastohydrodynamic lubrication’, *Lubricants*, 8(5), p. 51.

Habchi, W. (2018) *Finite Element Modeling of Elastohydrodynamic Lubrication Problems*. New York: John Wiley & Sons.

Hada, M., Yamada, D. and Tsuji, T. (2007) ‘An analysis of equivalent impedance characteristics by modeling the human musculoskeletal structure as a multibody system’, *Proceedings of the ECCOMAS Thematic Conference*. Milano, Italy, pp. 1–20.

Halloran, J.P. *et al.* (2005) ‘Comparison of deformable and elastic foundation finite element simulations for predicting knee replacement mechanics’, *J. Biomech. Eng*, 127, pp. 813–818.

Hamrock, B.J. and Dowson, D. (1976) *Isothermal Elastohydrodynamic Lubrication of Point Contacts: Part III– Fully Flooded Results*. Cleveland, OH: National Aeronautics and Space Administration Technical Note.

Hamrock, B.J., Schmid, S.R. and Jacobson, B.O. (2004) *Fundamentals of fluid film lubrication*. CRC press.

Hertz, H. (1882) ‘Uber die Beruhrung Fester Elastischer Korper (on the Contact of Elastic Solids’, *J. Reine Angew. Math*, 92, p. 156171.

Holzbaur, K.R.S., Murray, W.M. and Delp, S.L. (2005) ‘A Model of the Upper Extremity for Simulating Musculoskeletal Surgery and Analyzing Neuromuscular Control’, *Ann. Biomed. Eng*, 33, pp. 829–840.

Hu, Y.Z. *et al.* (2001) ‘A computer model of mixed lubrication in point contacts’, *Tribology Int*, 34(1), pp. 65–73.

Huang, P. (2015) *Numerical Calculation of Elastohydrodynamic Lubrication: Methods and Programs*. New York: John Wiley & Sons.

Hultqvist, T. (2020) *Transient Elastohydrodynamic Lubrication: Effects of Geometry, Surface Roughness, Temperature, and Plastic Deformation*. Ph.D. dissertation,. Luleå University of Technology.

Huynh, K. *et al.* (2013) ‘Development and validation of a discretised multi-body spine model in LifeMOD for biodynamic behaviour simulation’, *Comput. Methods Biomech. Biomed. Eng*, 18, pp. 175–184.

Jacobson, A. (2024) ‘Optimized Dual-Volumes for Tetrahedral Meshes’, *Computer Graphics Forum*, 43(5), p. 15133.

Jagatia, M. and Jin, Z. (2001) 'Elastohydrodynamic lubrication analysis of metal-on-metal hip prostheses under steady state entraining motion', *Proc. Inst. Mech. Eng. Part H J. Eng. Med*, 215, pp. 531–541.

Jalali-Vahid, D. *et al.* (2001a) 'Prediction of lubricating film thickness in a ball-in-socket model with a soft lining representing human natural and artificial hip joints', *Proc. Inst. Mech. Eng. PartJ J. Eng. Tribol*, 215, pp. 363–372.

Jalali-Vahid, D. *et al.* (2001b) 'Prediction of lubricating film thickness in UHMWPE hip joint replacements'.

Jalali-Vahid, D. and Jin, Z.M. (2001) 'Transient elastohydrodynamic lubrication analysis of ultra-high molecular weight polyethylene hip joint replacements', *Proc. Inst. Mech. Eng. Part C J. Mech. Eng. Sci*, 216, pp. 409–420.

Jalali-Vahid, D., Jin, Z.M. and Dowson, D. (2003) 'Elastohydrodynamic lubrication analysis of hip implants with ultra high molecular weight polyethylene cups under transient conditions', *Proc. Inst.Mech.Eng.PartCJ.Mech.Eng.Sci.,217,767–777*. CrossRef.

Jin, Z.M. and Dowson, D. (1999) 'A full numerical analysis of hydrodynamic lubrication in artificial hip joint replacements constructed from hard materials', *Proc Inst Mech Eng C J Mech Eng Sci*, 213(4), pp. 355–70.

Johnson, K.L. (1987) *Contact Mechanics*. Cambridge University Press, UK.

Jovanovic, K., Vranic, J. and Miljkovic, N. (2015) 'Hill's and Huxley's Muscle Models: Tools for Simulations in Biomechanics', *Serbian J. Elect. Eng*, 12(1), pp. 53–67.

Ju, Y. and Farris, T.N. (1996) 'Spectral analysis of two-dimensional contact problems', *Transactions of the ASME. Journal of Tribology*, 118(2), p. 8,.

Kalker, J.J. (1977) 'Variational Principles of Contact Elastostatics', *IMA J Appl Math*, 20(2), pp. 199–219.

Kennedy, C.A. and Carpenter, M.H. (2016) 'Diagonally implicit Runge-Kutta methods for ordinary differential equations'.

Kværnø, A. (2004) 'Singly Diagonally Implicit Runge–Kutta Methods With an Explicit First Stage', *BIT Numer. Math*, 44(3), pp. 489–502.

van Leeuwen, H. (2009) ‘The determination of the pressure–viscosity coefficient of a lubricant through an accurate film thickness formula and accurate film thickness measurements’, *Proc. Inst. Mech. Eng. Part J: J. Eng. Tribol*, 223, pp. 1143–1163.

LeVeque, R.J. (2007) ‘Finite Difference Methods for Ordinary and Partial Differential Equations: Steady-State and Time-Dependent Problems, Society for Industrial and Applied Mathematics’. Philadelphia, PA.

Li, J. and Berger, E.J. (2001) ‘A Boussinesq–Cerruti solution set for constant and linear distribution of normal and tangential load over a triangular area’, *J Elast Phys Sci Solids*, 63, pp. 137–51.

Liu, F. *et al.* (2021) ‘Enhanced computational modelling of UHMWPE wear in total hip joint replacements: The role of frictional work and contact pressure’, *Wear*, 482–483, p. 203985. Available at: https://doi.org/10.1016/j.wear.2021.203985.

Liu, S. and Wang, Q. (2002) ‘Studying contact stress fields caused by surface tractions with a discrete convolution and fast fourier transform algorithm’, *Transactions of the ASME*, 124, pp. 36–45.

Liu, S., Wang, Q. and Liu, G. (2000) ‘A versatile method of discrete convolution and FFT (DC-FFT) for contact analyses’, *Wear*, 243(1–2), p. 11,.

Lombera Rodríguez, H. and Tello, J.I. (2019) ‘On the Reynolds equation and the load problem in lubrication: Literature review and mathematical modelling’, *Mathematics Applied to Engineering, Modelling, and Social Issues*, pp. 1–43.

Love, A.E.H. (1929) ‘Stress produced in a semi-infinite solid by pressure on part of the boundary’, *Philosophical Transactions of the Royal Society of London*, 377, pp. 54–59.

Lubrecht, A.A., Venner, C.H. and Colin, F. (2009) ‘Film Thickness Calculation in Elasto-Hydrodynamic Lubricated Line and Elliptical Contacts: The Dowson, Higginson, Hamrock Contribution’, *Proc. Institution Mech. Eng. Part J J. Eng. Tribol*, 223(3), pp. 511–515.

Ludema, K.C. (1996) *Friction, wear, lubrication: a textbook in tribology*. Boca Raton, Fla: CRC Press, cop.

Mattei, L. *et al.* (2011) ‘Lubrication and wear modelling of artificial hip joints: a review’, *Tribol Int*, 44(5), pp. 532–49.

Mattei, L., Di Puccio, F. and Ciulli, E. (2013) ‘A comparative study of wear laws for soft-on-hard hip implants using a mathematical wear model’, *Tribol. Int*, 63, pp. 66–77.

Meng, H.C. and Ludema, K.C. (1995) ‘Wear models and predictive equations: their form and content’, *Wear*, 181-183(PART 2):443–457.

Merola, M. and Affatato, S. (2019) ‘Materials for hip prostheses: a review of wear and loading considerations’, *Materials*, 12(3).

Millard, M. *et al.* (2013) ‘Flexing Computational Muscle: Modeling and Simulation of Musculotendon Dynamics’, *ASME J. Biomech. Eng*, 135(2), p. 021005.

Mukras, S.M. *et al.* (2010) ‘Evaluation of contact force and elastic foundation models for wear analysis of multibody systems’, *Proceedings of the International Design Engineering Technical Conferences and Computers and Information in Engineering Conference*. Montreal, QC, Canada, pp. 1565–1577.

Nikravesh, P.E. and Gim, G. (1993) ‘Systematic Construction of the Equations of Motion for Multibody Systems Containing Closed Kinematic Loops’, *J. Mech. Des*, 115, pp. 143–149.

Nordin, M. and Frankel, V.H. (2001) *Basic Biomechanics of the Musculoskeletal System*. Philadelphia, PA, USA: Lippincott Williams & Wilkins.

Oliveira, H. (2016) ‘Inverse Dynamic Analysis of the Human Locomotion Apparatus for Gait; Instituto Superior Técnico’. Lisbon, Portugal.

Patel, R. *et al.* (2022) ‘A review of mixed lubrication modelling and simulation’, *Tribology Ind*, 44(1), pp. 150–68.

Pérez-González, A. *et al.* (2008) ‘A modified elastic foundation contact model for application in 3D models of the prosthetic knee’, *Med. Eng. Phys*, 30, pp. 387–398.

Pohrt, R. and Li, Q. (2014) ‘Complete boundary element formulation for normal and tangential contact problems’, *Phys Mesomech*, 17, pp. 334–40.

Polonsky, I.A. and Keer, L.M. (1999) ‘A numerical method for solving rough contact problems based on the multi-level multi-summation and conjugate gradient techniques’, *Wear*, 231(2), p. 19,.

Popov, V.L., Hefl, M. and Willert, E. (2019) *Handbook of contact mechanics*. Springer.

Quental, C. *et al.* (2013) 'Multibody System of the Upper Limb Including a Reverse Shoulder Prosthesis', *J. Biomech. Eng*, 135, p. 111005.

Quental, C. *et al.* (2018) 'Influence of the Musculotendon Dynamics on the Muscle Force-Sharing Problem of the Shoulder—A Fully Inverse Dynamics Approach', *ASME J. Bio mech. Eng*, 140(7), p. 071005.

Quental, C., Folgado, J. and Ambrosio, J. (2016) 'A Window Moving Inverse Dynamics Optimization for Biomechanics of Motion', *Multibody Syst. Dyn*, 38(2), pp. 157–171.

Ramjee, S. (2008) 'Numerical analysis of lubrication in an artificial hip joint'.

Reynolds, O. (1886) 'IV. On the Theory of Lubrication and Its Application to Mr. Beauchamp Tower's Experiments, Including an Experimental Determination of the Viscosity of Olive Oil', *Philos. Trans. R. Soc. London*, 177, pp. 157–234.

Romero, F. and Alonso, F. (2016) 'A Comparison Among Different Hill-Type Contraction Dynamics Formulations for Muscle Force Estimation', *Mech. Sci*, 7(1), pp. 19–29.

Ruggiero, A. and Sicilia, A. (2020a) 'A mixed elasto-hydrodynamic lubrication model for wear calculation in artificial hip joints', *Lubricants*, 8(7), p. 72.

Ruggiero, A. and Sicilia, A. (2020b) 'A novel explicit analytical multibody approach for the analysis of upper limb dynamics and joint reactions calculation considering muscle wrapping', *Applied Sciences*, 10(21), p. 7760.

Ruggiero, A. and Sicilia, A. (2021a) 'Development of a multibody biomechanical model of the human upper limb', *Biotribology*. CRC Press, pp. 91–121.

Ruggiero, A. and Sicilia, A. (2021b) 'Mathematical development of a novel discrete hip deformation algorithm for the in silico elasto-hydrodynamic lubrication modelling of total hip replacements', *Lubricants*, 9(4), p. 41.

Ruggiero, A. and Sicilia, A. (2022a) 'A musculoskeletal multibody algorithm based on a novel rheonomic constraints definition applied to the lower limb', *Journal of Biomechanical Engineering*, 144(8), p. 081010.

Ruggiero, A. and Sicilia, A. (2022b) ‘Implementation of a finite element deformation model within an elasto-hydrodynamic lubrication numerical solver for a ball in socket tribopair’, *Frontiers in Mechanical Engineering*, 8, p. 909156.

Ruggiero, A. and Sicilia, A. (2022c) ‘Synovial Lubrication Modeling of Total Hip Replacements Using Musculoskeletal Multibody Dynamics’, *Industrial Tribology*. CRC Press, pp. 167–207.

Ruggiero, A. and Sicilia, A. (2024) ‘Total Hip Replacement Response to a Variation of the Radial Clearance Through In Silico Models’, *Mechanical Engineering in Biomedical Applications* [Preprint].

Ruggiero, A., Sicilia, A. and Affatato, S. (2020) ‘In silico total hip replacement wear testing in the framework of ISO 14242-3 accounting for mixed elasto-hydrodynamic lubrication effects’, *Wear*, 460, p. 203420.

Scholz, A. *et al.* (2014) *Improved Muscle Wrapping Algorithms Using Explicit Path-Error Jacobians*. Dordrecht: Computational Kinematics, Springer.

Schwarze, M. *et al.* (2013) ‘Loads on the prosthesis–socket interface of above-knee amputees during normal gait: Validation of a multi-body simulation’, *J. Biomech*, 46, p. 1201 1206.

Shabana, A. (2020) *Dynamics of Multibody Systems*. Cambridge, UK: Cambridge University Press.

Sharif Shourijeh, M. (2013) ‘Optimal control and multibody dynamic modelling of human musculoskeletal systems’.

Sicilia, A., De Stefano, M. and Ruggiero, A. (2024) ‘From Marker Trajectories to Muscular Activations: A Musculoskeletal Multibody Model Considering Compliant Tendon Behaviour’, *International Tribology Symposium of IFToMM*. Cham: Springer Nature Switzerland, pp. 468–478.

Sicilia, A. and Ruggiero, A. (2025) ‘A Fractal Rough surfaces’ Mixed Lubrication model considering Boundary Element Method deformation’, *Tribology International*, 111210.

Sicilia, A. and Ruggiero, A. (2026) ‘Simulating the transient dynamics of line-contact Elasto-Hydrodynamic Lubricated systems by solving a Differential Algebraic Equation set’, *Journal of Tribology*, 148(4), p. 044102.

Silva, M.T. and Ambrósio, J. (2003) 'Solution of Redundant Muscle Forces in Human Locomotion with Multibody Dynamics and Optimization Tools', *Mech. Based Des. Struct. Mach*, 31, pp. 381–411.

Silva, M.T., Pereira, A.F. and Martins, J. (2011) 'An efficient muscle fatigue model for forward and inverse dynamic analysis of human movements', *Procedia IUTAM*, 2, pp. 262–274.

Srivastava, G., Christian, N. and Higgs, C.F., III (2021) 'A predictive framework of the tribological impact of physical activities on metal-on plastic hip implants', *Biotribology*, 25, p. 100156.

Stanley, H.M. and Kato, T. (1997) 'FFT-based method for rough surface contact', *Journal of Tribology, Transactions of the ASME*, 119(3), p. 485,.

Stavness, I., Sherman, M. and Delp, S. (2012) *A General Approach to Muscle Wrapping Over Multiple Surfaces*. Gainesville, FL: America Society for Biomechanics Conference.

Takenaka, S. (1988) *On pathwise projective invariance of Brownian motion"*. I.

Thelen, D.G. (2003) 'Adjustment of Muscle Mechanics Model Parameters to Simulate Dynamic Contractions in Older Adults', *ASME J. Biomech. Eng*, 125(1), pp. 70–77.

Tian, Q. *et al.* (2009) 'Dynamics of Spatial Flexible Multibody Systems With Clearance and Lubricated Spherical Joints', *Com put. Struct*, 87(13–14), pp. 913–929.

Tian, X. and Bhushan, B. (1996) 'A numerical three-dimensional model for the contact of rough surfaces by variational principle', *Journal of Tribology*, 118(1), pp. 33–42.

Udofia, I. and Jin, Z. (2003) 'Elastohydrodynamic lubrication analysis of metal-on-metal hip-resurfacing prostheses', *J. Biomech*, 36, pp. 537–544.

Venner, C.H. (1992) *Multilevel Solution of the EHL Line and Point-Contact Problems"*. Ph.D. Dissertation,. Universiteit Twente.

Venner, C.H. and Wijnant, Y.H. (2005) 'Validation of EHL Contact Predictions Under Time Varying Load', *Proc. Inst. Mech. Eng., Part J: J. Eng. Tribol*, 219(4), pp. 249–261.

Wang, F. and Jin, Z. (2004a) 'Lubrication Modelling of Artificial Hip Joints: From Fluid Film to Boundary Lubrication Regimes', *Eng. Syst. Des. Analysis*, 417731, pp. 605–611. Available at: https://doi.org/10.1115/esda2004-58077.

Wang, F. and Jin, Z. (2004b) 'Prediction of elastic deformation of acetabular cups and femoral heads for lubrication analysis of artificial hip joints', *Proc. Inst. Mech. Eng. Part J J. Eng. Tribol*, 218, pp. 201–209.

Wang, F. and Jin, Z. (2008) 'Transient Elastohydrodynamic Lubrication of Hip Joint Implants', *J. Tribol*, 130, p. 6200. Available at: https://doi.org/10.1115/1.2806200.

Wang, F., Wang, L. and Sun, M. (2010) 'Tribological modelling of spherical bearings with complex spherical-based geometry and motion', *WIT Trans. Eng. Sci*, 66, pp. 3–15.

Wang, H.R. *et al.* (2010) 'An improving algorithm for generating real sense terrain and parameter analysis based on fractal', *International Conference on Machine Learning and Cybernetics, 2*. IEEE, pp. 686–91.

Wang, W.Z. *et al.* (2003) 'A Comparative Study of the Methods for Calculation of Surface Elastic Deformation', *Proc. Inst. Mech. Eng., Part J: J. Eng. Tribol*, 217(2), pp. 145–154.

Wang, W.-Z. *et al.* (2009) 'Numerical Lubrication Simulation of Metal-On-Metal Artificial Hip Joint Replacements: Ball-In-Socket Model and Ball-On-Plane Model', *Proc. Institution Mech. Eng. Part J J. Eng. Tribol*, 223(7), pp. 1073–1082. Available at: https://doi.org/doi:10.1243/.

Wanner, G. and Hairer, E. (1996) *Solving Ordinary Differential Equations II*. Berlin, Heidelberg, DE: Springer.

Yamaguchi, G.T. and Zajac, F.E. (1989) 'A Planar Model of the Knee Joint to Characterize the Knee Extensor Mechanism', *J. Biomech*, 22(1), pp. 1–10.

Yang, J. and Zhao, W. (2016) 'Numerical simulations for G-Brownian motion', *Front Math China*, 11, pp. 1625–43.

Ying, W., Henriquez, C.S. and Rose, D.J. (2009) 'Composite Backward Differentiation Formula: an Extension of the TR-BDF2 Scheme', *Appl. Numer. Math* [Preprint].

Zarifi, O. and Stavness, I. (2016) 'Muscle wrapping on arbitrary meshes with the heat method', *Comput. Methods Biomech. Biomed. Eng*, 20, pp. 1–11.

Zhang, H. *et al.* (2016) ‘A mixed lubrication model for studying tribological behaviors of surface texturing’, *Tribology Int*, 93, pp. 583–92.

Zhang, S. *et al.* (2019) ‘Numerical simulation of mixed lubrication considering surface forces’, *Tribology Int*, 140(105878).

Zhu, D. (2007) ‘On some aspects of numerical solutions of thin-film and mixed elastohydrodynamic lubrication’. Proc Inst Mech Eng Part J J Eng Tribology.

Zhu, D. and Hu, Y.Z. (1999) ‘The study of transition from elastohydrodynamic to mixed and boundary lubrication’. Adv Front Eng Tribology Proc STLE/ASME HS Cheng Tribology Surveill.

Zivic, F. *et al.* (2017) *Biomaterials in clinical practice: advances in clinical research and medical devices*. Springer.

List of main symbols

Chapter 1 - Biomechanics

$Oxyz$	Reference frame
t	Time
$\mathbf{q}$	Lagrangian coordinates vector
$\mathbf{t}$	Rigid body translation vector (global position)
$\boldsymbol{\theta}$	Rigid body orientation vector (unit quaternion)
α, β, γ	Euler angles
$\hat{\mathbf{v}}$	Unit vector
Θ	Rotation angle
$\tilde{\mathbf{u}}$	Skew matrix
$\mathbf{R}$	Rotation matrix
$\bar{\mathbf{u}}$	Local position vector
$\boldsymbol{\omega}$	Angular velocity vector
$\mathbf{H}$	Hamiltonian product matrix
$\bar{\mathbf{C}}$	Quaternion conjugation matrix
$\mathbf{r}$	Global position vector
$\mathbf{d}$	Degrees of Freedom vector
$\mathbf{C}$	Constraint equations
$\mathbf{D}$	Mobility equations
$\mathbf{B}$	Body equations
$\boldsymbol{\Phi}$	Position problem equations
T	Kinetic energy
ρ	Rigid body density
V	Rigid body volume
m	Rigid body mass
$\bar{\mathbf{I}}$	Rigid body inertia tensor
$\mathbf{M}$	Rigid body mass matrix
$\mathbf{Q}_v$	Quadratic velocity generalised force vector
$\boldsymbol{\Phi}_{\mathbf{q}}$	Constraint Jacobian
$\boldsymbol{\lambda}$	Lagrange multipliers
$\mathbf{F}_e, \mathbf{T}_e$	External force/torque vectors
δW	Virtual work
$\mathbf{u}$	Surface parameters

s	Curvilinear coordinate
$\mathbf{x}(\mathbf{u})$	Surface explicit function
$\mathbf{c}(s)$	Geodesic curve
$\hat{\mathbf{t}}, \hat{\mathbf{n}}, \hat{\mathbf{b}}$	Tangent, normal and binormal unit vectors triplet
$\mathbf{A}$	Actuation matrix
$\mathbf{f}$	Muscles' force vector
l_t	Tendon length
l_m, v_m, α_p	Muscle length, deformation velocity and pennation angle
$\mathbf{a}$	Muscles' activation vector

Chapter 2 - Tribology

t	Time
$\mathbf{x}$	2D contact domain
h	Lubricant gap
p	Lubricant pressure
μ	Lubricant viscosity
$\mathbf{U}$	Surfaces' entraining velocity vector
$\mathbf{V}$	Surfaces' sliding velocity vector
g	Geometrical undeformed gap
δ	Surfaces' rigid approach
N, w	Load applied to the surfaces
$\mathbf{u}, \boldsymbol{\tau}$	Lubricant flow and shear stress vectors
$\mathbf{T}$	Friction force
i, j, I	Grid indices
$\mathbf{m}, \mathbf{d}, \mathbf{D}$	Finite Difference vector/matrix operators
θ, φ	Spherical angles
$\hat{\mathbf{t}}_\theta, \hat{\mathbf{t}}_\varphi, \hat{\mathbf{r}}$	Spherical tangent and radial unit vectors
$\mathbf{e}$	Eccentricity vector
$\boldsymbol{\omega}$	Angular velocity vector
ρ	Lubricant density
u	Surfaces' normal deformation
$\mathbf{F}$	Discretised Reynolds equation residual vector
$\mathbf{F_p}$	Discretised Reynolds equation Jacobian
$\mathbf{q}$	FEM nodal displacements
$\boldsymbol{\varepsilon}$	FEM strain vector
$\boldsymbol{\sigma}$	FEM stress vector
$\mathbf{C}$	FEM compliance matrix
K	BEM convolution kernel
$\mathbf{K}$	BEM compliance matrix
$\mathrm{DFT}, \mathrm{FFT}$	Discrete and Fast Fourier Transform
a_H, δ_H, p_H	Hertzian contact half-width, approach and peak pressure
$\mathcal{N}(\mu, \sigma^2)$	Normal distribution with given mean and variance

B	Brownian motion
r	Fractal roughness
H	Hurst exponent
w	Wear depth
V	Wear volume
p_c	Contact pressure
θ	Mixed Lubrication transition function
h_{min}, h_c	Hamrock-Dowson minimum and central film thickness
RCA	Real Contact Area
$\mathbf{F}, \mathbf{S}, L$	Fluid, Solid and Load EHL functions
$\mathbf{u}$	States vector
$\mathbf{\Phi}$	Source function vector
$\mathbf{\Phi_u}$	Source function Jacobian
n	Time index
a_{ij}, b_i, c_i	Runge-Kutta coefficients, weights and nodes